THE UNIVERSITY OF HULL

157nm F_2 LASER CHARACTERIZATION AND APPLICATION TO POLYMER ABLATION

being a Thesis submitted for the Degree of

Doctor of Philosophy (Physics)

in the University of Hull

by

Rozalina Zakaria

M.Sc (Malaya)

May 2009

Acknowledgements

I would like to express a million thanks to Professor Peter E. Dyer for all the guidance and help throughout this research, also to Dr Chris. D. Walton in helping in the practical work and to all the departmental staff who gave support in many ways.

To my entire course mates especially Robin Scott in sharing all the moments during my studies here.

And I would like to express my gratitude to my one and only Mum, for her never ending kindness, support and encouragement.

157nm F_2 laser characterization and application to polymer ablation

Abstract

The work in this thesis focuses on applications and characterization studies of the vacuum ultra-violet (VUV) 157nm F_2 laser. The laser ablation properties of various polymeric materials, namely polydimethylsiloxane (PDMS), the photo-resist SU-8, nylon 66, ultra-high molecular weight polyethylene (UHMWPE), Lexan polycarbonate and CR-39 polymer have been investigated. The main priority was given to Lexan polycarbonate and CR-39 polymer as new potential materials to explore using this laser.

A considerable component of the work is directed at gaining a better understanding of the underlying physics of the laser interaction in relation to surface modification, in particular the possible limitations on surface roughness set by mode coherence effects. White light interferomety, and optical and scanning electron microscopy (SEM) measurements are carried out to identify the processing conditions for micron scale size structures (cones) produced on the surface, and the realization of 'smooth' and in some instances intentionally 'roughened' surfaces after ablation. It is shown that exceptionally well defined conical structures can be formed on Lexan polycarbonate and CR-39 polymer with certain laser processing conditions. These cones produce a circular interference fringe system with sub-micron period adjacent to their base as a result of walls reflections. An ablation model is used to analyse these fringes, and from the range of fringe visibility it is shown possible to estimate the spatial coherence properties of the F_2 laser beam.

A preliminary investigation of ablating CR-39 that had been exposed to an alpha particle source is described. This polymer is widely used for detecting ionizing particles by use of chemical etching to reveal their damage tracks. 157nm laser ablation of chemically etched, radiation exposed samples showed the etched track 'pores' tended to be smoothed by ablation and also appeared to act as nucleation sites for cones.

A fluorescence technique using Lumilass G9 glass plate and a CCD camera was applied in this work to analyze the VUV laser beam. This required knowledge of using optical systems, a CCD camera, and capturing and analyzing bmp images for analysis in MathCAD. Measurements made in this way permit divergence to be found for the direct and the weakly focussed (asymmetric) laser output beam. Spatial coherence derived in this way is shown to be in reasonable agreement with that based on the cone interference result. The fluorescence method is also applied to characterizing small-scale beam fluctuations on the direct F_2 laser output beam. These are found to have a magnitude of a few %, a value that compares quite well earlier theoretical predictions and a simulation of spatial mode fluctuations in the narrow line-width, highly multimode F_2 laser.

TABLE OF CONTENT

CHAPTER 1

CHAPTER 2

RESEARCH OVERVIEW

CHAPTER 3

SURFACE MODIFICATION OF POLYMER MATERIALS INDUCED BY 157nm F_2 LASER IRRADIATION

3.2 Experimental Arrangement

3.3 Results and Discussion

3.3.1 PDMS

3.3.2 SU-8

3.3.3 Nylon 66

3.3.4 UHMWPE

CHAPTER 4

157nm F_2 LASER INTERACTION WITH CR-39 POLYMER

CHAPTER 5

SURFACE QUALITY OF POLYMERS ABLATED WITH THE 157nm F_2 LASER

CHAPTER 6

157nm F_2 BEAM CHARACTERIZATION

CHAPTER 7

CONCLUSIONS

CHAPTER 1

INTRODUCTION

The interaction of ultraviolet (UV) radiation with organic polymers has been the subject of investigation for decades, including photodegradation mechanisms, gaseous products of UV laser ablation, surface measurements before, during and after ablation and the theory of polymer ablation [1-4].

A vast number of studies have used physical and chemical techniques to characterise the surface of organic polymers prior to and during the onset of ablation. One of the factors that are important is the effects prior to the onset of the ablation. These effects could include bond-breaking, radical generation and trapping/recombination and thermal heating [5]. These would be expected to produce a surface layer which has physical and chemical properties that are modified from the original pristine material.

The work in this thesis was focussed on the interaction of the VUV F_2 laser emitting at a wavelength of 157nm with various organic polymers i.e. Lexan polycarbonate, allyl-diglycol carbonate (CR-39), polydimethylsiloxane (PDMS), SU-8, nylon 66, and ultra-high molecular weight polyethylene (UHMWPE). The investigation was carried out on the laser ablation characteristics and the surface quality of the ablated materials. Typically, UV laser ablation was carried out with a succession number of pulses. The etching of the surface is a linear function of the number of pulses when the polymer is a strong absorber at the laser wavelength. For example; for weak absorbers like polymethylmethacrylate (PMMA) at 248nm and polyethylene at 193nm [6]. A microscopic model for ablative photodecomposition using variety of organic polymers at fluence as little as 10mJcm^{-2} was studied [2], where a model based on a process in order to see if a change in specific volume will lead to ablation without melting and determine the velocity and angular distributions of the ablated material. The value of etch depth per pulse is usually averaged over hundreds of pulses in order to minimize the uncertainties in the measurement of the etch depth. The average values for the etch depth per pulse are reproducible to within the uncertainties in the measurement of the fluence provided the absorption characteristics are well-controlled [6]. At the early stage of ablation research, the work was focussed on basic scientific understanding of the process but later more works were concentrated on the application of the polymer ablation.

Recent developments in cavity design and gas lifetime, together with improved output energy and reliability, have brought the VUV F_2 lasers [7] to a position where it can be considered for industrial applications. The move from ArF lasers (λ=193nm) to shorter wavelength F_2 lasers (λ=157nm), coupled with high purity VUV CaF_2 optics to operate over extended time periods, allows the realization of sub 100nm feature resolution to be produced [8]. This high spatial resolution capability obtained at this wavelength makes it an interesting source for machining applications, especially for producing micro-optic and micro-mechanical devices.

During the course of the research presented in this thesis, the following new and important aspects were discovered and are described:

1. Research on the interaction of 157nm F_2 laser radiation with Lexan polycarbonate discovered cones developed on the surface and these led to interference effects in the form of fringe adjacent region of the base of the cones. The ablation threshold can be determined from the apex angle of the cones allowing a comparison with the value obtained from etch rate measurements. The characteristics of the interference fringes are related with the divergence of the laser amongst other things and this as will be shown has allowed the spatial coherence be determined.

2. For the first time, the interaction of 157nm laser radiation with allyl-diglycol carbonate (CR-39) was investigated from the point of view of its ablation characteristics and the quality of the VUV processed surfaces. It was observed that exceptionally well defined cones with sharp tips developed on the ablated surface of this polymer.

3. CR-39 is a well known polymer used for recording the tracks of ionizing particles, and here the interaction of 157nm laser radiation with the alpha irradiated CR-39 was studied. Surfaces on which chemically etched damage tracks were formed were found to initiate cone formation when ablated with the VUV laser.

4. An F_2 beam characterisation technique based on converting from the VUV to visible radiation through the fluorescence of a glass plate has been developed. Two-dimensional beam profiles could then be recorded using a CCD camera and subsequently analyzed using MathCAD software allowing indirect measurements of spatial coherence, and beam fluctuations to be assessed.

The following outlines the organization of the thesis;

After the introduction in Chapter 1, Chapter 2 goes on to provide a short review of the past research on the laser ablation development using 157nm laser with organic polymers. Chapter 3 describes the 157nm laser ablation characteristics of the polymers used i.e. polydimethylsiloxane (PDMS), SU-8, nylon 66, UHMWPE and Lexan polycarbonate. The ablation characterisation focussed more on the Lexan polycarbonate as this found to develop micro-scale cones on the ablated surfaces. The etch depth per pulse versus logarithmic fluence plots have been used to determine the ablation threshold of the polymers. The linear region of the plot can be fitted according to the Beer's Law. This has given rise to the suggestion that the absorptivity can be actually measured from the gradient line to give an effective absorption coefficient [9]. The ablation threshold obtained using this method has been compared to the threshold obtained by calculating the apex angle of the cones [10] produced in polycarbonate at 157nm laser. The examples of the capability of 157nm F_2 laser in micro-machining organic polymers as nylon 66, polymethylmethacrylate (PMMA), and Lexan polycarbonate has been explored.

Chapter 4 describes the interaction of 157nm laser with the polymer CR-39. Here, the laser ablation characteristics and the measurements of ablation threshold from etch rate and cone apex angles are reported and the methods compared for pristine material. Additional work on material that was chemically etched following alpha particle exposure is then described, where the 157nm laser was used to ablate these physically modified surfaces.

Chapter 5 describes the surface characterization in terms of roughness of ablated PDMS, Lexan polycarbonate and CR-39. An attempt is made to link theoretical estimates of fluctuations in the highly multimode F_2 laser beam with the experimental roughness results for these materials. The experimental results obtained from white light interferometry were analyzed on selected cone free regions of the surface of Lexan polycarbonate and CR-39.

F_2 laser beam characterisation is described in Chapter 6, where the beam profile of the laser was captured and recorded using a CCD camera. The VUV radiation was converted to visible fluorescence using a Tb^{3+} doped glass (Lumilass G9). The properties of the beam profiles captured in this way were then analyzed in MathCAD. This chapter provides experimental information on the optical set up, the CCD camera calibration and its capability to record the beam image, and fluorescence saturation effects. The fluorescence technique used here, will provides the spatial coherence and fluctuations measurements from full-width half maximum (FWHM) of the beam.

The final Chapter (Chapter 7) presents a summary of conclusions drawn from the research conducted and also outlines some possible avenues for future work that have grown out of these activities throughout this work.

References

[1] R.Srinivasan and V.Mayne-Banton, Applied Physics Letters 41 (1982) 576.

[2] B.J.Garrison and R.Srinivasan, Applied Physics Letters 44 (1984) 849.

[3] P.E.Dyer and R.Srinivasan, Applied Physics Letters 48 (1986) 445.

[4] T.Lippert and J.T.Dickinson, Chem.Rev 103 (2003) 453.

[5] W.W.Duley, UV Lasers: effects and applications in materials science, Cambridge University Press, *United Kingdom*, 1996.

[6] R.Srinivasan, *Interaction of Laser Radiation with Organic Polymers* in Laser Ablation-Principles and Applications, Springer Verlag Heidelberg, 1994.

[7] M.Fiebig, M.Kauf, J.Fair, H.Endert, M.Rahe, and D.Basting, Applied Physics A 69 (1999) S305.

[8] A.K.Bates, M.Rothschild, T.M.Bloomstein, T.H.Fedynyshyn, R.R.Kunz, V.Liberman, and M.Switkes, IBM J.Res & Dev 45 (2001) 605.

[9] R.Srinivasan, Emile Sutcliffe, and B. Braren, Laser Chem 9 (1988) 147.

[10] H.R.Philipp, D.G.Legrand, H.S.Cole, and Y.S.Liu, Polymer Engineering and Science 27 (1987) 1148.

CHAPTER 2

RESEARCH OVERVIEW

2.1 Introduction

Since 1960 when the demonstration of the first laser emission in ruby at 694.3nm was reported by Maiman [1], attention rapidly shifted to obtain emission at other wavelengths. Much research has been conducted on laser emission at visible, near infrared and infrared, and UV (excimer) wavelengths but extension to the vacuum ultraviolet (VUV), at 157nm is quiet recent.

Ultraviolet laser emission can be generated from numerous atoms, ions and molecules in pulse and CW gaseous discharges. The emission by a short-lived molecule that is bound in an upper state but dissociative in its ground state is termed excimer emission. An important class of lasers is made up of transient rare gas halide molecules consisting of one rare gas atom (e.g. argon, krypton, or xenon) and one halogen atom (e.g. fluorine, chlorine, or bromine). These are called rare gas halide excimer lasers. Excimer lasers can be operated with different gas mixtures to produce different output wavelengths. The most important excimer lasers are listed in Table 2.1 [2]:

Type	Wavelength
F_2	157nm
ArF	193nm
KrF	248nm
XeCl	308nm
XeF	351nm

Table 2.1: Excimer lasers with output wavelengths showing the wavelength from 157nm to 351nm.

Excimer lasers were first demonstrated in the mid-1970's where they became progressively important to many applications and the most powerful practical source of ultraviolet laser radiation. In the present work, the focus was on the so-called F_2 'excimer' laser emitting principally on the 157nm VUV transition.

Studies of radiative relaxation of excited rare gas atoms and halogen or rare gas halide (RGH) molecules started as early as 1975 when Velazco [1] confirmed the electronic states in excimer laser emission and led to the suggestion that RGH molecules might be the source of efficient laser emission at UV wavelengths. These lasers provided output ranging from near-UV through the vacuum ultraviolet (VUV), short duration emission pulses, energy measured at tens to hundreds of millijoules per pulse, and pulse repetition rates sufficient enough to produce useful average power [3]. Advantages of RGH lasers also include [1]:

i) low density in the cavity medium, which can support high intensities without self-focussing effects,
ii) that they are scalable to operate in active cavity,
iii) operation at UV wavelengths,
iv) low spatial and temporal coherence minimizing laser speckle and fringe formation on imaging,
v) operation at high repetition rates,
vi) high pulse energies available from large volume devices (10^4J).

The earliest work using the F_2 laser was published as early as 1977 by Rice *et al* [4]. They reported the observation of two new emission features following electron-beam excitation of He/F_2 and Ne/F_2 gas mixtures. They obtained both a spontaneous and stimulated emission band system between 1500 and 1600°A attributed to transitions in molecular fluorine. A microdensitometer band of spontaneous –emission spectrum of the 1500-1600°A molecular fluorine band observed in the electron-beam-excited Ne/F_2 and He/F_2 mixtures.

It has now been nearly thirty years since the first publication reported using UV excimer lasers to process polymers in the form of conventional resist and as 'self-developing' resist [5-7]. Srinivasan and Mayne-Banton [6] have reported ablation of polyethylene terephthalate (PET) using a 193nm ArF laser. Self-developing photoresist using a vacuum ultraviolet F_2 excimer laser exposure was reported as early as 1985 by Henderson *et al* [8], where the performance of the self-developing resist nitrocellulose was studied with energy density greater than 25mJcm^{-2}. Scanning electron microscopy (SEM) indicated little or no residue was produced on the ablation area and it was possible to produce a clean, fine line approximately 200nm wide. This pattern was created by exposing a 180nm thick, 13.25% nitrogen content nitrocellulose film on Si substrate with two pulses at fluence of ~100mJcm^{-2}.

A number of reviews have appeared over the past decade on the progress of research and development on polymer ablation with UV lasers. For example, as first reported during 1980's by Srinivasan [9], the ablation process is believed to be a volume explosion in which small molecules are expelled from the polymer surface. In 1990's era, a review of various polymer ablation studies using excimer lasers was reported by Dyer [10]. For example, the interaction of ArF excimer laser irradiation with polyethylene was reported by Dyer and Karnakis [11] where a phenomenon called incubation was observed [12] on low density polyethylene (LDPE) , where the first few pulses were applied to the material gives no etching. However, after these first few pulses depending upon the fluence, a constant etch depth per pulse can be seen. At this stage of development a broad field of scientific applications for laser polymer ablation had evolved and processing, including material removal, surface modification and film deposition [3], reported.

2.2 Laser Ablation Studies

Studies of laser ablation of the polymer materials started in the early 1980's with Srinivasan's work that used a 193nm ArF excimer laser to etched directly polymeric materials. Since then [7, 12, 13], research devoted to understanding the science and developing the technology behind UV laser ablation of polymeric materials has grown to be surprisingly broad. Emphasis has been placed on the measurement of the ablation rate X as a function of fluence. A simple analysis based on Beer-Lambert law then leads to the prediction that:

$$X = \frac{1}{\alpha_{eff}} \ln\left(\frac{F}{F_T}\right) \tag{2.1}$$

where α_{eff} is the effective absorption coefficient at the laser wavelength. Equation 2.1 predicts that X should be linearly related to ln F and that the gradient of the line will be α_{eff}^{-1}. F_T is the ablation threshold found from the intercept with the $\ln F$ axis.

Among conventional polymers that are often used in laser ablation studies are polymethylmethacrylate (PMMA), polyimide (PI), polytetrafluoroethylene (PTFE), polyethylene (PE), and polycarbonate (PC). UV photo-ablation of organic polymers has two important characteristics that form parts of on-going research; first, the investigation about fundamental mechanisms involved in ablation, whether bond breaking proceeds through direct photochemical or by highly localized thermal reaction [10]. Secondly, the potential of laser-processed polymeric materials for applications in micro-electronics, opto-electronics and micromechanical machining [10].

The fundamental characteristics of laser photo-ablation of polymers can be summarized as [10];

i) A highly localized spatial interaction;
ii) An ablation threshold for significant removal of material;
iii) Minimum heat-affected zone (HAZ)

The first point describes the contact or projection techniques experiment from the range of laser wavelength (λ=193nm-350nm, 157nm for the F_2 laser) with appropriate optics to produce submicron definition. The third, fourth, and fifth harmonics of the Q-switch Nd:YAG laser provide potentially alternative wavelength for the same objective. A very shallow depth of material removal is possible for UV or VUV ablation of many polymers because of their high absorption coefficient (of order 10^4-10^5 cm^{-1}). It is possible to modify the surface in a highly controllable way, usually with etch rates of $\leq$100nm per pulse [10]. This spatial localization gives a unique advantage to UV lasers for many polymer micromachining applications.

The ablation threshold F_T (energy per unit area per pulse) (Figure 2.1) is dependent on the polymer involved and the laser wavelength. The ablation threshold F_T for many polymers is reported to be in a range of a few tens to a few hundred millijoules (mJ) per square centimetre (cm^2). The absorbed energy density needed to produce ablation can be expressed as the product of ablation threshold (F_T) and effective absorption (α_{eff}). For example; ablation threshold of polyimide using 157nm laser is found to be 25mJcm^{-2}, with α_{eff}= 13μm^{-1} [14].

The surface modification of polymer materials will clearly be restricted to a depth of order α_{eff}^{-1}. There are thus benefits in having a large coefficient α_{eff} since [10];

i) This reduces the thermal loading on the polymer surface ($F_T \alpha \alpha_{eff}^{-1}$)

ii) The initial depth α_{eff}^{-1} heated to a high temperature is small, as is any radiation modified zone

iii) Conduction cooling to the bulk polymer is fast, since $t \propto \alpha_{eff}^{-2}$.

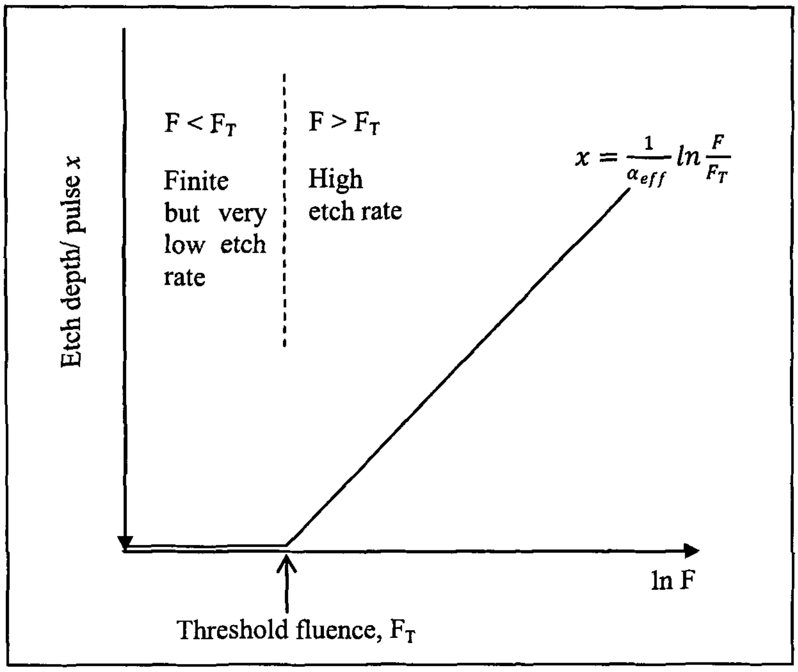

Figure 2.1: Etch depth per pulse x as a function of ln (Fluence) for ablation of polymer when Beer's Law is applicable. F_T *is the ablation threshold of the polymer and the gradient of the line defines the inverse of the effective absorption coefficient* (α_{eff}).

2.3 Interaction of UV Lasers with Polymer Materials

It was first reported in 1982 [12], that when a pulsed UV-laser irradiated organic polymer, the material spontaneously etched away to a depth of 0.1μm to several microns. Where the starting process is to measure the depth of the material removed from the polymer surface by each of laser pulse, that is so-called etch rate per pulse. Results are now available on the variation of the etch rate (x) with fluence (F) for a wide range of polymers and laser wavelengths. The depth of ablation per pulse can be derived by measuring the depth of ablation crater d, and dividing this by the number of exposure pulses n, giving $x = d/n$ as the average value.

Srinivasan *et al* [9] analyzed the etching of several polymers by ultraviolet pulse laser radiation. Ablation is believed to be a volume explosion, and ablation threshold which is expressed in terms of 'useful' photon density in the ablation volume falls within a narrow range (±50%). Experimental data which relates the etch depth per pulse to the fluence of the pulse have been analyzed, where the first attempt to take the temporal width of the laser pulse was published by Keyes *et al* [15].

Short pulses of far-ultraviolet (<200nm) laser radiation are capable of etching organic polymer films without melting the remaining sample. When a pulse of laser radiation (<200nm) wavelength with a fluence above threshold value irradiates the polymer films, the material at the irradiation site is spontaneously etched away to a depth of 1000°A or more, in a process termed ablative photodecomposition [13]. The mechanism proposed for this ablative photodecomposition occurs in a variety of organic polymers, and attributes ablation in volume that accompanies the photolysis of the polymer.

2.4 Surface Modification During and Prior to Ablation

A number of studies have been reported characterizing the physical and chemical properties of the surface of polymers prior to and after the onset of ablation at UV laser wavelengths. Photoetching can produce a variety of morphological features on the ablation surface. These include conical structures that have been seen on a variety of polymers under UV laser ablation, and in polyimide, PET, polyethylene and nylon 66 exposed using the 157nm VUV laser [14]. The ablation threshold can be determined from the formation of the cones that develop on the surface. To do so the full apex angle θ_m of the cone is related to the ablation threshold, (F_T) and applied fluence (F) according to:

$$\theta_m = 2\sin^{-1}\left[\frac{F_T(1-R_0)}{F(1-R(\theta_m)}\right] \tag{2.2}$$

where R_0 is the reflectivity at normal incidence to the polymer surface whereas $R(\theta_m)$ is the reflectivity loss on the cone wall at the half cone angle ($\theta_m/2$).The threshold obtained from this method is often less than ablation threshold by up to a factor of two. Table 2.2 shows the comparison threshold obtained from measured cone apex angle (F_T) and thermocouple measurements for polyimide, polyethylene terephthalate (PET), polyethylene, and nylon 66 using the 157nm laser.

Polymer	F_T	F'_T
Polyimide	23±7	36±7
Polyethylene terephthalate (PET)	19±6	29±6
Polyethylene	25±7	67±14
Nylon 66	33±7	

Table 2.2: Comparison of thresholds measured by cone apex angle (F_T) and thermocouple measurements (F'_T) [14].

It has been suggested [14] that this discrepancy is due to the difficulty in measuring etching depths near threshold compared to the high sensitivity required for thermocouple measurements. Figure 2.2 shows the scanning electron microscopy images of the cone formation; 300 pulses at 0.11Jcm^{-2} for nylon 66 and PET using 157nm laser.

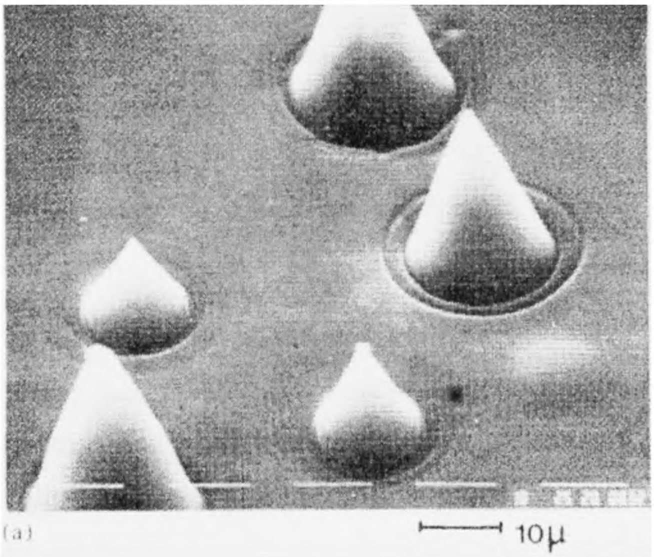

(a)

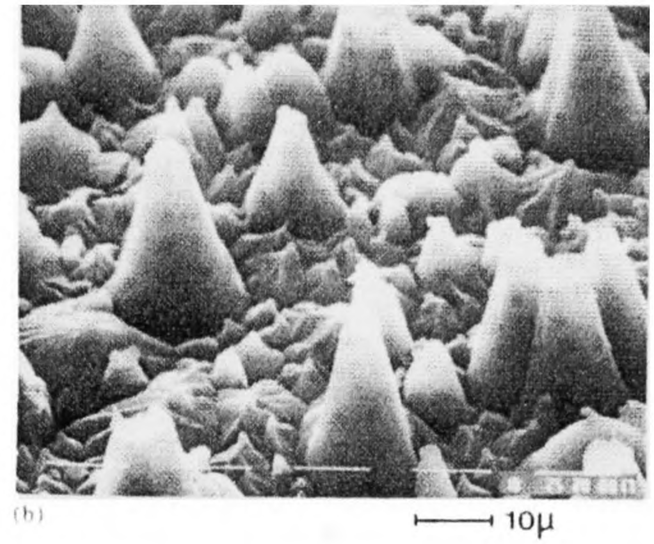

(b)

Figure 2.2: Cones structures produced in (a) nylon 66 and (b) PET using 300 pulses at 0.11Jcm^{-2} with 157nm F_2 laser [14].

The ablation of PET using the 157nm laser produced gaseous products consisting of CO, CO_2, CH_4, C_2H_2, C_2H_4, C_4H_2, C_4H_4, benzene and CH_3CHO, similar to those found in the case of exposure with the XeCl laser and ArF laser [16]. The ablation threshold can be determined by measurements of the thermal loading of thin films and of the apex angles of particulate-induced cone structures. The value of threshold obtained by thermal loading measurement gives 29±6 mJcm^{-2}. From this work, it was notably that using F_2 laser produces relatively higher CO/CO_2 and C_2H_2/C_2H_4 ratios than other excimer lasers i.e. XeCl (308nm) and ArF (193nm).

Since the work reported earlier [14, 17] on cones and the threshold fluence derived from the apex angle of the cone using XeCl and F_2 laser, it can be seen that particulate-induced surface microstructures arise from small particles that are redeposited on the surface from ablation products or deliberately added on the polymer substrates. It has been reported that the symmetry of cones can be influence by the polarization dependence of reflection at their walls. A change from circular cross-section with unpolarized radiation to an elliptical elongation when linearly polarized radiation is used has been reported by Hopp *et.al* [18] on the polycarbonate surfaces ablated using the 193nm ArF excimer laser. Several published studies on the cones formed on ablated polycarbonate using the 193nm ArF excimer laser have appeared [18, 19]. The optical properties of bisphenol-A polycarbonate at wavelengths down into the VUV have been reported by Philipp *et al* [20], so that optical constants obtained by applying Kramers-Kronig analysis are available for modelling wall reflections effects. Lexan polycarbonate is used in micro-optical applications because of its superior resistance to impact and heat and its relatively high refractive index for a commercially available thermoplastic. There appear to be no previous reports of cone formation on polycarbonate ablated surfaces at the 157nm F_2 laser wavelength; this phenomenon is discussed further in this thesis.

An application using the 157nm F_2 laser for the fabrication of microstructures in polymer substrates has been studied by Stuke *et al* [21] using silicon membrane contact mask. This process allowed the flexible and rapid prototyping of micro-reactors and micro-channel system for applications in genome analysis and biotechnology. Polymers used were polymethylmethacrylate (PMMA), polycarbonate (PC) and polystyrene; with fluence applied $\approx$100mJcm^{-2} etch rates were 140nm per pulse for polycarbonate and very smooth surfaces with a roughness in the nanometre range was reported on a micrometer lateral scale. Glass miroarrays have also been fabricated using 157nm laser ablation [22]. These serve as templates for replication using polydimethylsiloxane (PDMS), with possible applications in printing arrays of molecules. PDMS itself has also been micromachined using 157nm and 193nm lasers [23, 24], because of its importance in many microdevice applications. An ablation threshold of 115±30 mJcm^{-2} is reported for this material at 157nm laser [23].

No published data was found on the 157nm laser ablation characteristics of the CR-39 polymer in a pristine state or when it had been exposed as a track detector. Allyl-diglycol carbonate (CR-39) is a useful polymer for etched track detection because of its sensitivity and resolution [25]. However, there are a number of studies reporting etching characteristics of CR-39 with ultraviolet laser irradiation e.g. by Dwaikat *et al* [26] using a pulse ultraviolet Indium-doped Yttrium Aluminium Garnet (UV-In:YAG) laser (λ=266nm, pulse energy of 42mJ/pulse at repetition rate of 10Hz), Shahid *et al* [27] using a 10.6μm CO_2 laser with multiple pulses of energy 1-3J, and Tse *et al* [28] reported the effects of CR-30 irradiated with UV at 257nm at atmosphere for 10hours at a distance of 5cm with various the conditions of experiments .Studies of the ablation threshold for CR-39 by Kukreja [29] found this to be 25Jcm^{-2} when treated with a CW-CO_2 laser.

2.5 Micromachining with F_2 Lasers

Microlithography can be described as lithography in manufacturing integrated circuits. Microlithography started as optical lithography, using lamps for generating the image of a mask pattern in the photo resist on a wafer [30] but progressed to UV laser sources in the search for additional resolution. The demands of excimer laser technology are unique for the lithography technique and the need for shorter exposure wavelengths spurred important developments in F_2 excimer lasers that have in turn benefited other areas. In particular reliable, high repetition rate devices have become available for use not only in scientific studies but also in technological applications. As well as the potential advantage in conventional resist processing [31], the short wavelength and high photon energy (7.9eV) at 157nm, make possible high-resolution micromachining of many materials [32], notably polymers and glasses, by ablation.

Micromachining can be implemented by patterning using contact-masks or preferably, non-contact projection techniques, where a mask containing the required pattern is imaged on the surface to be ablated. The choice of the laser wavelength used plays an important role, as thermal loading on the surface can be minimised by using a wavelength that is strongly absorbed and consequently has a low ablation threshold. This can minimise softening (melting) effects that may well act to degrade microstructures [10].

Many published results confirmed the micromachining capability of the 157nm laser in various materials such as glasses [33], insulators [34], and in polymers such polytetrafluoroethylene (PTFE) [35]. The relatively strong absorption at this wavelength leads to low ablation thresholds allowing depth removal at nanometre level and production of sub-micron features with no evidence of surface micro-cracking, confirming that with appropriate optical systems the VUV F_2 laser is suitable for machining applications [36].

Stuke *et al* [37] demonstrated prototype microstructures using an absorbing liquid as a mask in the evacuated chamber at 157nm. The absorbing liquid was applied directly to the surface of PMMA in the pattern administered by a micro syringe. The fluence was set to $0.4mJcm^{-2}$ on the image plane.

In many cases it has been found that 157nm laser micromachining of polymers, ceramics and glass that are difficult to process at other laser wavelengths, yields cleaner and better defined ablation features. This is so even in tough or high-band-gap materials such as PTFE, and fused silica. The choice of laser wavelength use in the micromachining application is crucial as appropriate laser will minimize thermal loading on the film reported earlier [10].

The capabilities for machining microstructures on polymethylmethacrylate (PMMA) with sub-micron period [33], with 157nm F_2 laser, and in other material systems such as chrome films on CaF_2 and SiO_2 (fused silica) substrates was reported by Herman *et al* [38]. A projection system was used with $30mJcm^{-2}$ fluence at image plane. The 157nm F_2 laser was applied to exploit the strong interaction of 7.9eV photons and it was indicated that there was promise for generating high resolution micro-patterns on Cr-on-CaF_2 and Cr-on-SiO_2 photomasks.

2.6 Characterisation of UV Beam Profile

To optimize the laser beam characteristics, a measurement of beam profile is fundamental to many material interactions processes. Ideally, the measurement of beam profile will provide quantitative output throughout the beam at a usefully high sampling rate. This is relatively easy for continuous wave (CW) laser outputs with intensity distributions at visible, near IR and near UV wavelengths. However, the measurement of beam profile in the deep UV offers additional difficulties because of the low UV sensitivity of standard CCD cameras. The small aperture of CCD cameras is also incompatible with the large beam size of the most of excimer lasers, unless the lens arrangements are used. A more general solution in the beam profile measurement of the VUV laser, involves using a fluorescent material to convert the VUV radiation into visible radiation, which can be detected with a conventional CCD camera. Transparent materials such as MgO or in present work, Lumilass G9 glass, are ideal as fluorescent converters because of these materials can be doped with a low level of transitions metal ions such as Tb^{3+} and Ni^{2+}. In the simple arrangement shown in Figure 2.3 an image of the aperture is created on a fluorescent glass as a conversion medium, and a CCD camera in-line monitors the fluorescence. A video frame grabber with image analysis software is used to capture the image.

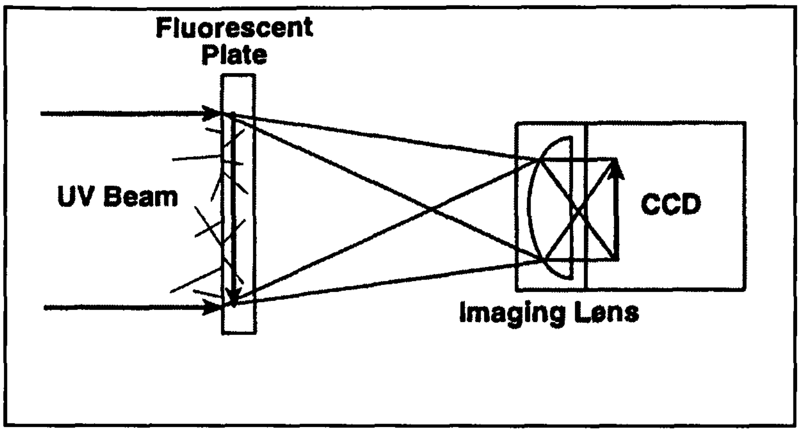

Figure 2.3: An example of beam profiler using a fluorescent glass to convert UV to visible radiation, and use of CCD camera to record the intensity [39].

Whilst the output power (energy) of the beam can easily be measured accurately with for example, a calorimeter or joulemeter, there are often problems pertaining to the absolute spatial dimensions of the output beam. In recent years, these problems in measuring spatial profile of the output beam has been solved, albeit at considerable expense, using vidicon and reticon detectors and also photodiode arrays which can be used to detect and record the two-dimensional beam profile at various wavelengths [40].

The simplest approach to profiling and recording the output beam, involves looking directly at the laser beam and recording the radiation with a CCD camera. This is often not practical at UV laser radiation because of the low UV sensitivity of the CCD cameras itself. Hence, use of fluorescent material to convert UV laser radiation into visible emission, which practically can be detected with a conventional CCD camera. In 1990, Davis [1] reported, the use of a UV sensitive film with a resolution exceeding 10^3 lines mm^{-1} to image the beam from excimer lasers, with a range of 0.1-200mJcm^{-2}. As an alternative, systems consisting of a fluorescent crystal which the host is glass with low levels (ppm) of transient metal ions such as Tb^{3+} was used recently [41, 42] for the imaging the output beams at 157nm [42] and 308nm [42] respectively. Using this technique gives better characterization compared to simple conventional methods like burn paper which has limitations, in that it only offers a convenient way to view a single shot or aid laser alignment. These papers have small dynamic range, non-linear thermal properties and are unable to provide a quantitative intensity distribution for the beam.

References

[1] W.W.Duley, UV Lasers: effects and applications in materials science, Cambridge University Press, *United Kingdom*, 1996.

[2] J. Hecht, Understanding laser, Howard W.Sams & Company, *Indiana, United State of America*, 1988.

[3] P.E.Dyer, Applied Physics A 77 (2003) 167.

[4] J.K.Rice, K.Hays, and J.R.Woodworth, Applied Physics Letters 31 (1977) 31.

[5] Y.Kawamura, K.Toyoda, and S.Namba, Applied Physics Letters 40 (1982) 374.

[6] R.Srinivasan and V.Mayne-Banton, Applied Physics Letters 41 (1982) 576.

[7] P.E.Dyer, J.E.Andrew, D.Forster, and P.H.Key, Applied Physics Letters 43 (1983) 717.

[8] D.Henderson, J.C.White, H.G.Craighead, and I.Adesida, Applied Physics Letters 46 (1985) 900.

[9] R.Srinivasan, Emile Sutcliffe, and B. Braren, Laser Chem 9 (1988) 147.

[10] P.E.Dyer, *Laser Ablation of Polymers* in Photochemical processing of electronic materials, Academic Press, *London*, 1992.

[11] P.E.Dyer and D.M.Karnakis, Applied Physics Letters 64 (1993) 1344.

[12] R.Srinivasan, *Interaction of Laser Radiation with Organic Polymers* in Laser Ablation-Principles and Applications, Springer Verlag Heidelberg, 1994.

[13] B.J.Garrison and R.Srinivasan, Applied Physics Letters 44 (1984) 849.

[14] P.E.Dyer, S.D.Jenkins, and J.Sidhu, Applied Physics Letters 52 (1988) 1880.

[15] T.Keyes, R.H.Clarke, and J.M.Isner, Journal Physics Chemistry 89 (1985) 4194.

[16] P.E.Dyer, G.A.Oldershaw, and D.Schudel, Journal Physics D:Applied Physics 25 (1992) 323.

[17] P.E.Dyer, S.D.Jenkins, and J.Sidhu, Applied Physics Letters 49 (1986) 453.

[18] B.Hopp, Zs.Bor, E.Homolya, and E.Mihalik, Applied Surface Science 109 (1997) 232.

[19] B.Jaleh, P.Parvin, N.Sheikh, Z.Zamanipour, and B.Sajad, Nuclear Instruments and Methods in Physics Research B 265 (2007) 330.

[20] H.R.Philipp, D.G.Legrand, H.S.Cole, and Y.S.Liu, Polymer Engineering and Science 27 (1987) 1148.

[21] Markus Lapezyna and M. Stuke, *Rapid prototype fabrication of smooth microreactor channel system in PMMA by VUV laser ablation at 157nm for applications in genome analysis and biotechnology,* Materials Research Society Symposium proceedings 526 (1998) 143.

[22] P.E.Dyer, S.M.Maswadi, C.D.Walton, M.Ersoz, P.D.I.Fletcher, and V.N.Paunov, Applied Physics A 77 (2003) 391.

[23] K.Rubahn, J.Ihlemann, G.Jakopic, A.C.Simonsen, and H.G.Rubahn, Applied Physics A 79 (2004) 1715.

[24] V.M.Graubner, N.Oskar, L.Thomas, H.Marc, S.Bernard, and W.Alexander, Applied Surface Science 197 (2002) 786.

[25] L.M.Kukreja, V.B.Joshi, A.M.Bhagwat, U.K.Chatterjee, and D.D.Bhawalkar, Applied Physics Letters 49 (1986) 181.

[26] Nidal Dwaikat, Toshiyuki Iida, Fuminobu Sato, Yushi Kato, Ippei Ishikawa, Wataru Kada, Atsuya Kishi, Makoto Sakai, and Y. Ihara, Nuclear Instruments and Methods in Physics Research A 572 (2007) 826.

[27] Shazia Shahid, M.Shahid Rafique, M.Khaleeq-ur-Rahman, I.M.Ghauri, and Faizan-ul-Haq, in *31st EPS Conference on Plasma Physics*, London, 2004.

[28] K.C.C.Tse, D.Nikezic, and K.N.Yu, Radiation Measurements 43 (2008) S98.

[29] L. M. Kukreja, Bull.Mater.Sci 11 (1988) 225.

[30] R.Patzel and U.Stamm, Excimer lasers for microlithography, Springer Berlin Heidelberg, *New York*, 2005.

[31] A.K.Bates, M.Rothschild, T.M.Bloomstein, T.H.Fedynyshyn, R.R.Kunz, V.Liberman, and M.Switkes, IBM J.Res & Dev 45 (2001) 605.

[32] M.Fiebig, M.Kauf, J.Fair, H.Endert, M.Rahe, and D.Basting, Applied Physics A 69 (1999) S305.

[33] P.E.Dyer, A.M.Johnson, S.Maswadi, and C.D.Walton, Lasers in Manufacturing (2003) 27.

[34] P.E.Dyer and C.D.Walton, Applied Physics A 79 (2004) 721.

[35] E.E.Mayer, D.A.Gillett, J.H.Fair, M.J.Scaggs, H.Endert, and D.Basting, in *ICALEO 98*, Orlando, 1998.

[36] P.E.Dyer, S.M.Maswadi, H.V.Snelling, and C.D.Walton, Proceeding SPIE 4637 (2002)

[37] M.Lapczyna and M.Stuke, Applied Physics A 66 (1998) 473.

[38] Peter R.Herman, Jianzhao Li, and A. Yick, in Laser Applications in Microelectronic and Optoelectronic Manufacturing VIII, Vol. SPIE 4977, Photonic West, San Jose, 2003, p. 400.

[39] http://www.ophiropt.com/user_files/laser/beam_profilers/UV-Lasers.pdf.

[40] I. W.Boyd, Laser Processing of Thin Films and Microstructures, Springer-Verlag Berlin Heidelberg New York, 1987.

[41] Y.Otani, M.Takahashi, L.Jin, H.Kowa, and N.Umeda, Proceeding SPIE 5188 (2003) 134.

[42] B.B.Shrivastava, N.S.Benerji, P.Bhatnagar, HS Vora, and U.Nundy, in International Conference in Photonics, Institute of Photonics, Cochin University,Cochin (Kerala),India, 2004.

CHAPTER 3

SURFACE MODIFICATION OF POLYMER MATERIALS INDUCED BY 157nm F_2 LASER IRRADIATION

This chapter describes the polymer surface modification and ablation induced by 157nm F_2 laser irradiation, discusses the experimental system arrangement and the analysis of the results obtained from optical micrographs and scanning electron microscopy. The results were analyzed from the experimental point of view and supported with simulations in MathCAD.

3.0 Introduction

There is currently considerable interest in exploiting the unique source properties of the 157nm VUV F_2 laser in applications such as lithography [1] and in micromachining [2] various materials, including glasses [3] and various types of organic polymers [4].

The capabilities of this short wavelength laser for producing high spatial resolution, combined with its high average power and good lifetime, make it now a viable tool for use in industrial processes.

In this chapter, the surface modification of various organic polymers induced by 157nm laser has been investigated and the potential of sub-micron feature definition on the polymer materials by ablation is demonstrated. Polymers have potential in many practical applications including micro-electronics and micromechanical devices [4] and there are now also many biopolymers that find use in medical technologies [5].

Though most previous effort has been concentrated on polyimide and polymethylmethacrylate (PMMA) which find use in semiconductor packaging technologies and as a resist base respectively, many other organic polymers have been investigated, for example; polyethylene terephthalate (PET), polytetrafluoroethylene (PTFE), polycarbonate (PC) and nylon 66 exposed at various laser wavelengths. In the present research, several polymers have been exposed to 157nm laser radiation, including polydimethylsiloxane (PDMS), the photo-resist SU-8, nylon 66, ultra-high molecular weight polyethylene (UHMWPE), Lexan polycarbonate (PC) and allyl diglycol carbonate (CR-39). The CR-39 polymer will be explained details in Chapter 4.

In this chapter, the basic parameters characteristic of the laser ablation process were determined for these materials i.e., the etch rate versus fluence, and hence the ablation threshold and the effective absorption coefficient, with the 157nm F_2 laser. Additionally, the ablation threshold for the polycarbonate (PC) sample was obtained from the apex angle cones formed induced at this wavelength. Interference effects arising from reflection off the walls of microns sized cones were also studied experimentally and using modelling.

3.1 Polymer Characteristics

The nylon 66 and UHMWPE samples used were obtained through the collaborative work with the Engineering Department at the University of Loughborough.

Most of this research concentrated on the interaction of the VUV 157nm F_2 laser with polycarbonate Lexan (PC) and CR-39. These materials have interesting potential in various applications, e.g. polycarbonate is used to make microlenses in large and super-large area optical films [6] and CR-39 finds optical use as well as being suitable for 'track-etch' radiation detectors.

3.1.1 Polydimethylsiloxane (PDMS)

Polydimethylsiloxane (PDMS) is a polymer that has important applications, and in particular, is widely used for replication, allowing micro-structures for use in, for example, micro-fluidics to be moulded from masters that have surface relief. It has useful properties including good thermal stability; resistance to UV radiation and relative chemical inertness, low surface energy, a good dielectric strength (making a good insulator), and maintains physical properties over a useful wide range of temperatures [7] .There is interest in ablation patterning this material using UV and VUV lasers and also in using UV radiation to modify its surface properties. The latter may permit the polymer surface to be altered from hydrophobic to hydrophilic without etching or physical structuring. PDMS has a specific heat of c =1100Jkg^{-1}K^{-1}, a density of ρ =1030kgm^{-3}) and refractive index to normal incident of light of n (1.445) [8] at ~430nm.

The chemical formula of PDMS is $(H_3C)_3SiO[Si(CH_3)_2O]_nSi(CH_3)_3$, n being the number of repeating monomer $[SiO(CH_3)_2]$ units. The silicon atoms will generally have two carbon based pendant groups (R) to complete its octet, R referring to the methyl group (CH_3) as shown in Figure 3.1.

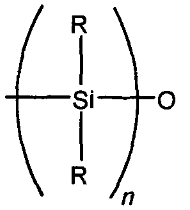

Figure 3.1: Siloxane repeat unit ($R=CH_3$)

3.1.2 Photo-resist SU-8

Negative photo-resist SU-8 is a very viscous polymer that can be spun or spread over a thickness ranging from 1 µm up to 2 mm. This resist has been specifically developed for ultra-thick, high-aspect-ratio MEMS (Micro-Electro-Mechanical-Systems) type applications using standard lithography equipment. A well-known technology for this applications is LIGA (Lithographie, Galvano-formung, Abformung), which includes three processes; X-ray lithography, micro electroplating, and micro embossing [9]. SU-8 negative type photoresist can easily be patterned using UV photolithography. SU-8 has a density of ρ=1190kgm^{-3}. SU-8 is based on an epoxy; a term is referring to a bridge consisting of an oxygen atom and two other atoms, usually carbon. Such a structure is called 1, 2-epoxide. An epoxy resin is defined as a molecule containing one or more 1, 2-epoxy groups, as shown in Figure 3.2 below.

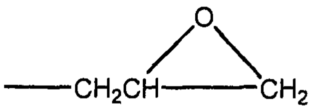

Figure 3.2: 1, 2-epoxy ring.

3.1.3 Nylon 66

Nylons are versatile polymer materials and have been used in various commercial products ranging from carpet fibres, ropes and parachutes to gears, casings and even spatulas. Nylon 66 is highly crystalline, chemically resistant material with good mechanical strength, good abrasion resistant and self-lubricating properties. Nylon has a density of $\rho = 1140 kgm^{-3}$ and specific heat of $c = 1670 Jkg^{-1}K^{-1}$ [10]. Nylon 66 is often referred to as poly(hexamethylene adipamide) and has the repeat structure shown in Figure 3.3.

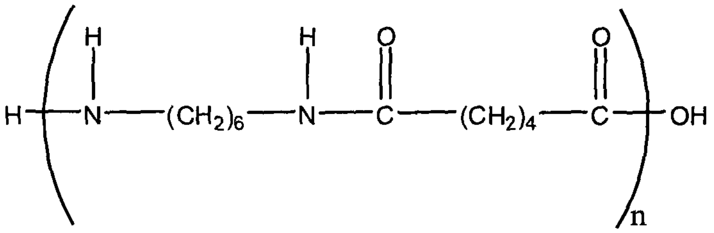

Figure 3.3: Poly(hexamethylene adipamide) or Nylon 66.

3.1.4 Ultra-high molecular weigh polyethylene (UHMWPE)

Ultra high molecular weight polyethylene (UHMWPE) has a high degree of both linearity and crystallinity, and a molecular weight of the order of 6-7 million atomic mass units. Because of its high degree of chain entanglement it has a very high melt viscosity. UHMWPE is also insoluble in all organic solvents at room temperature, and even at elevated temperature is only sparingly soluble in a limited range of solvents (e.g. decalin). The UHMWPE used was pure, and had average molecular weight of 5×10^6 g/mol and a density of $930 kgm^{-3}$ [11]. The UHMWPE used was in sheet form of $200 mm^2$ surface area.

UHMWPE (Figure 3.4) with the repeat monomer unit of $-CH_2-$, is a material employed in many scientific fields, such as bio-medicine and the micro-engineering[11].

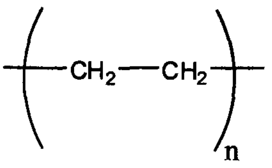

Figure 3.4: Structure of repeat monomer (UHMWPE) with n greater than 100,000.

3.1.5 Lexan Polycarbonate (PC)

Polycarbonates are a particular group of thermoplastic polymers that have attractive properties in terms of temperature resistance, impact resistance and optical quality and find use because of these and their process ability and reasonable cost. They are the group of polymers having functional groups linked together by carbonate groups (-O-(C=O)-O-) in a long molecular chain. The functional group of Lexan polycarbonate (PC) polymer is shown in Figure 3.5 below.

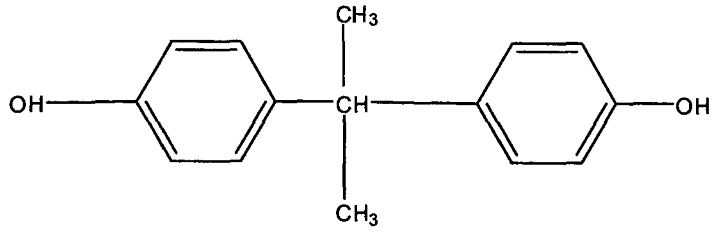

Bisphenol A

Figure 3.5: Functional group of polycarbonate lexan (PC)

The characteristics of polycarbonate are similar to those of polymethylmethacrylate (PMMA; acrylic), but polycarbonate is stronger and more highly transparent to visible light and has in fact better light transmission characteristics than many kinds of glass. The polycarbonate (PC) used in this work was Lexan from Goodfellow Cambridge Limited in the form of 3mm thick sheets. It has a density of $\rho = 1130\ \text{kgm}^{-3}$ and specific heat of $c = 1170\text{Jkg}^{-1}\text{K}^{-1}$ [12].

3.2 Experimental Arrangement

3.2.1 Sample preparation

In this work, only PDMS bulk samples need a preparation set-up and these were prepared by mixing a base of PDMS precursor (Dow Corning Sylgard Elastomer 184 base) and a curing agent in proportions of 10:1. The liquid mixture was placed in an evacuated chamber to discharge bubbles and to eliminate oxygen in the samples. PDMS siloxane base oligomers contain a vinyl group and curing agent that contains a proprietary platinum-based catalyst to produce addition of SiH bonds across the vinyl group. Mixing the base and curing agent leads to the formation of $Si\text{-}CH_2\text{-}CH_2\text{-}Si$ polymeric linkages. Raman spectroscopy can be used to study bond groups in PDMS and will be discussed further in this chapter. Following mixing the base and curing agent it was poured into a master that was to be moulded and was then cured at 80°C for 24 hours. The resulting material formed in this way was highly transparent, colourless, and homogenous in its bulk and could be peeled away from the master leaving a surface replica.

3.2.2 Experimental set-up

A 157nm VUV F_2 laser (Lambda Physik LPF 200) which produced output energy of up to 35mJ in an 11ns pulse (full-width at half-maximum) was used to expose the various polymer samples. The charging voltage of the laser may could be varied in 1kV steps from 21kV to 26kV and this allowed the laser energy and hence fluence at the target to be varied. The full-angle beam divergence of the direct output beam was ~3mrad in its narrow dimension and ~8mrad in its long dimension.

The polymer samples were held on a motorized stage, which was capable of movements in the x-y-z directions in increments from 1mm to 1μm under computer control. Due to the high absorption of the 157nm wavelength in oxygen in air, the laser output had to be delivered either in vacuum or in a rare gas such as Argon. In these experiments the target was placed in a chamber that was capable of being evacuated down to 1×10^{-5} mbar. The chamber was evacuated using a dry pump and the pressure was measured using Edwards

Pirani/Penning 1005 pressure gauges. The chamber could also be purged with He or Ar gas as an alternative for beam delivery but in these experiments this was not used. Figure 3.6 shows a schematic diagram of the F_2 laser experimental set-up.

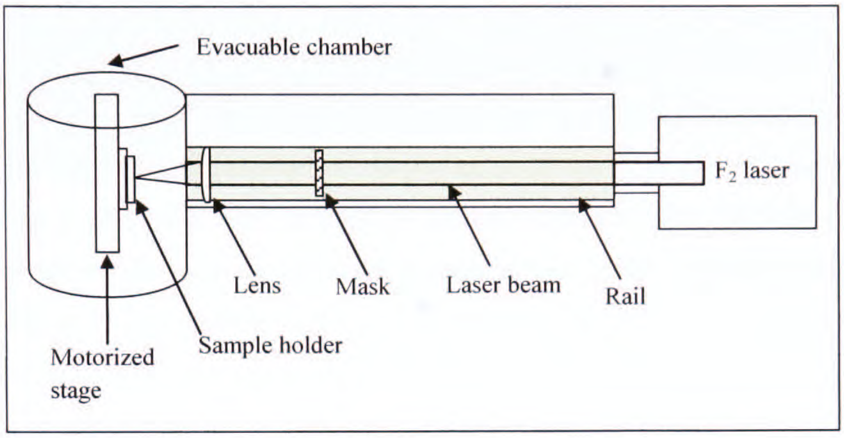

Figure 3.6: F_2 laser experimental set-up

The laser pulse energy was measured using a Molectron pyroelectric joulemeter (calibration factor = 34mJ/V) coupled to an oscilloscope (Hewlett Packard Infinium SCOP07). Using the joulemeter calibration, the fluence was calculated from

$$Fluence(mJ/cm^2) = \frac{V \times 34}{A} \tag{3.1}$$

where V (volts) is the measured voltage and A (cm^2) is the irradiated area of the sample. In this experiment, the joulemeter was positioned in the evacuated chamber between the lens and target area, before and after the experiment in order to determine and average value for the energy. A rectangular aperture placed in the beam path was used to select the region of quasi-uniform fluence from the laser output. A calcium fluoride lens (CaF_2) with a focal length f ≈ 90mm was then used to project a de-magnified image of this aperture to increase the fluence at the sample. The magnification M and object to lens distance, S_0, and image to lens distance, S_I, are related using (3.2);

$$M = -\frac{S_I}{S_0} \tag{3.2}$$

and the Gaussian lens equation (3.3);

$$\frac{1}{S_1}+\frac{1}{S_0}=\frac{1}{f} \tag{3.3}$$

M must be chosen with the constraint that distances S_I and S_O should fit within in the chamber. An objective aperture of dimensions of 2mm by 4mm was positioned in the most uniform part of the output beam of the F_2 laser. A magnification of ~0.1x to ~0.15x was chosen as this gave adequate fluence gain and was consistent with the chamber dimensions. It was important to determine the location of the image plane for this optical system. This was done by ablating a polyimide film located at various distances from the lens. Polyimide (0.125mm thick sheet) was used as the target because it was readily available and has a low ablation threshold at 157nm. Following a sequence of exposures the lens was cleaned in order to minimize the build up of contaminants on its surface. In this experiment, as the depth-of-field for this demagnification was ≈ ±0.05mm, redefining an image plane was important as it could change up to 0.5mm when the lens is re-positioned. The best image plane was determined by moving the film in increments of 0.01mm over a range of 1.0mm. Thirty sites were irradiated with 50pulses each at a laser charging voltage of 26kV and 10Hz repetition rate. The ablation sites on the polyimide were then viewed using an optical microscope (Leica DMLM) with ±2μm depth resolution. The clearest and sharpest image found in this way was taken to define the best image plane and the sample surfaces were then positioned in this plane. An example of the 'best image' is seen in Figure 3.7. The ablated area was found to be 0.18 mm × 0.37 mm (±0.002 mm resolution), and was used in equation 3.1 for fluence calculations.

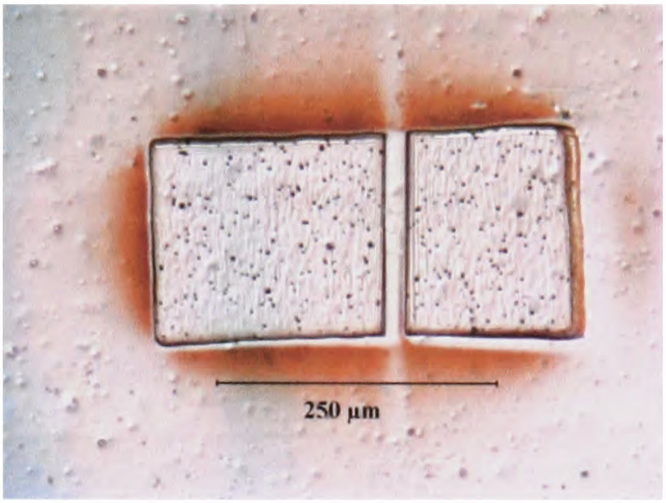

Figure 3.7: The best 'ablation' image on polyimide sample for image plane determination. The line in the middle is due to a wire place on the aperture to assist focussing.

A white light interferometer (VEECO-WYKO NT1100) was used to quantitatively characterize the ablation sites produced in the samples. This optical profiler gave ablation depth information allowing estimates of the threshold and etch rate for samples exposed at 157nm to be made. It also permitted an examination and quantification of surface roughness produced by ablation and the influence that fluence and number of pulses had on this. Raman spectroscopy of the PDMS ablation sites was used in an effort to determine to what extent vibration peaks of the vinyl group were changed. The investigation of Raman shift used an Olympus BH2-UMA microscope coupled to a Renishaw 1000 Ramascope. As the excitation source, a diode laser was used at 780nm. The Raman microscope, prior to use, was calibrated using silicon, which has a known peak at 521.09cm^{-1}. The PC samples were characterized further using Scanning Electron Microscopy (SEM) for the morphology of the samples after being irradiated using the 157nm laser. SEM images were obtained using a Zeiss Evo 60 Scanning Electron Microscopy (SEM).

3.3 Results and Discussion

3.3.1 PDMS

3.3.1.1 UV-VIS spectra

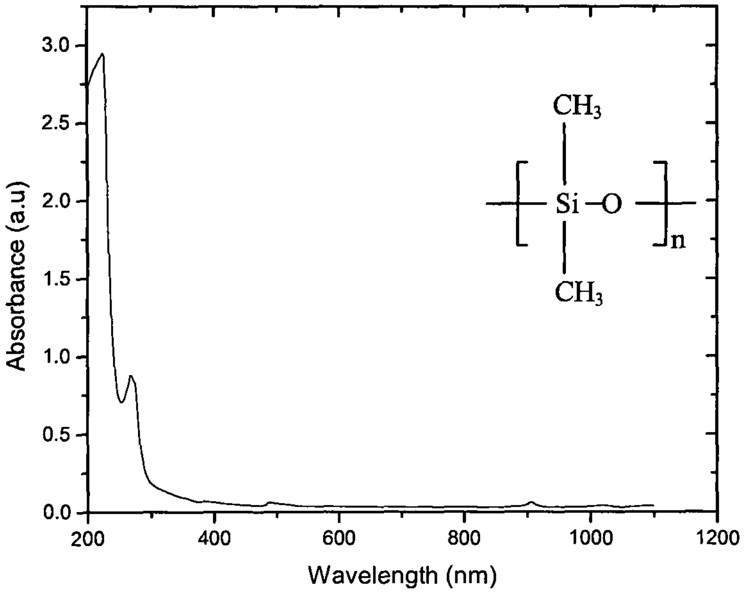

Figure 3.8: UV absorption spectrum of PDMS in the range 200 to 1200nm.

UV absorption spectra of PDMS in the wavelength range 200 to 1200nm were found using a UNICAM 5625 UV-VIS spectrophotometer. The absorbance versus wavelength for a 5mm thick sample prepared by moulding is seen in Figure 3.8. PDMS evidently has low absorption at wavelengths in the range 300 -1100nm but significant absorption below ~300nm as can be seen from Figure 3.8. At ~200nm the absorption coefficient is estimated to be 12.7cm^{-1} suggesting PDMS is not strongly absorbing even in the deep UV. Although the spectrophotometer cuts-off below 200nm it can be conjectured from the spectrum in Figure 3.8 that it has an absorption coefficient of similar magnitude at a wavelength of 157nm. As will be seen later PDMS can be ablated with fluences greater than 100mJ cm^{-2} at 157nm. For ablation at the longer wavelength of the frequency quadrupled Nd: YAG laser at 266nm, where PDMS has weak absorption (estimated at ~3.5cm^{-1}), incubation effects are involved in ablation [13].

3.3.1.2 Etch depth analysis

PDMS was irradiated with the 157nm laser at various fluences between ~100mJcm^{-2} and 900mJcm $^{-2}$. The depth per pulse of PDMS removed from the samples subjected to one 1, 2, 3, 4 and 5 pulses is seen in Figure 3.9. Each set leads to a reasonably well-defined line and as expected the depth increases with increasing numbers of pulses and increasing fluence. It is noted that using the white light interferometer it was possible to record very small changes in surface height, in this case down to ~2nm with one pulse at ~100mJcm^{-2}.

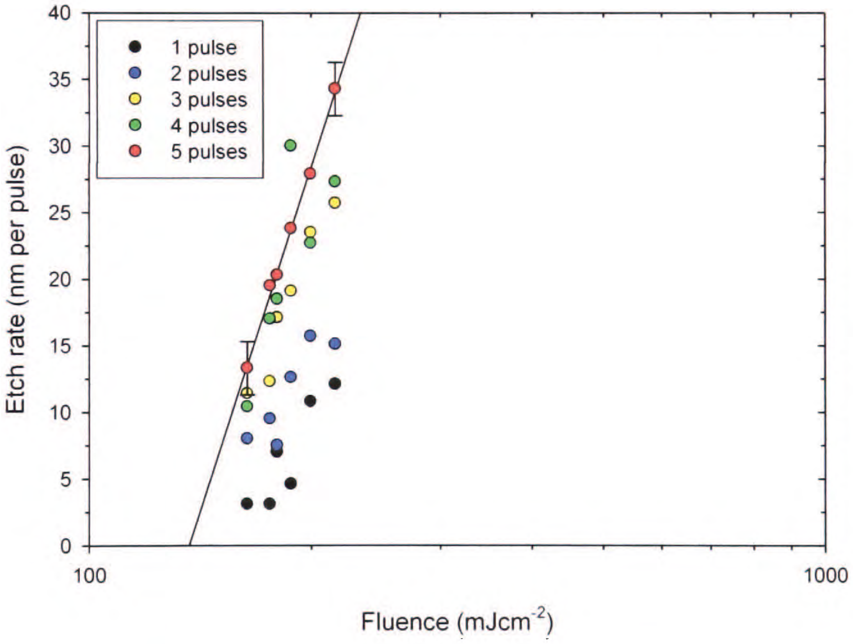

Figure 3.9: Etch depth per pulse for one, two, three, four and five pulses versus the fluences in 100mJcm^{-2} and linear regression line for PDMS exposed using the 157nm laser.

A fit to material removal in ablation can be derived by using Beer-Lamberts law. In this model the etch rate $d(F)$ versus fluence, F, becomes a function of the threshold fluence, F_T and the effective absorption coefficient, α_{eff}, and is described as

$$d(F) = \frac{1}{\alpha_{eff}} \ln\left(\frac{F}{F_T}\right) \tag{3.4}$$

This was applied in this experiment to determine the ablation threshold and effective absorption coefficient for PDMS. The experimental data used are shown in Figure 3.10 where the etch rate-fluence for exposure sets comprising 1, 5, 10 50 and 100 pulses are shown. By using linear regression line to cover the data for each group of exposures the ablation threshold was found to be approximately constant for 1-100 pulses, falling in the range 100 - 110mJcm^{-2}. It is noted that the etch rate per pulse is larger for a single pulse exposure than the average gained from multiple exposure of a single site. This may be because of the surface properties of the PDMS sample differ from the bulk so that the first pulse sees, for example, a different threshold and effective absorption coefficient to the subsequent pulses. It is also possible that surface modification effects play a role e.g. through roughening, or photochemical-induced structural changes.

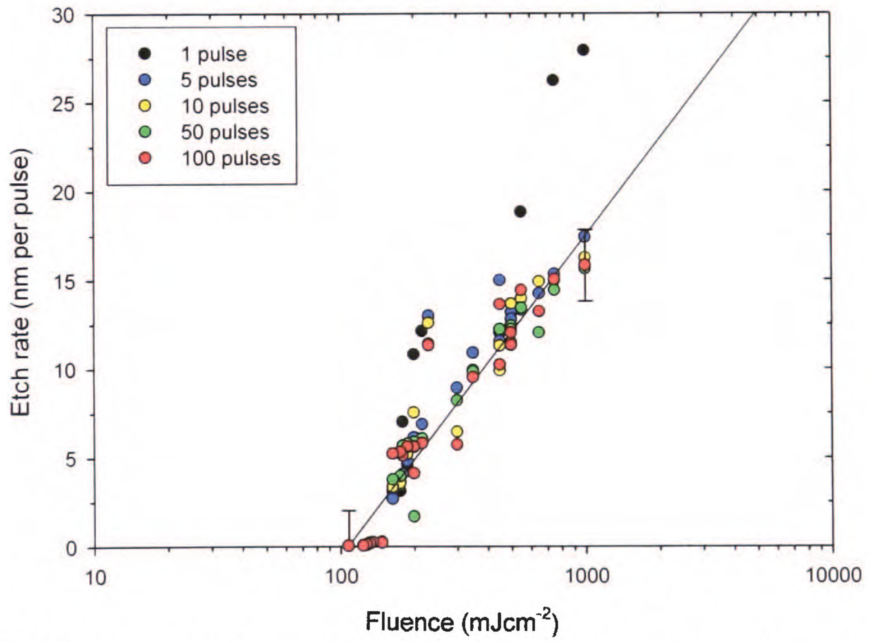

Figure 3.10: Etch rate per pulse versus fluence for PDMS exposed at 157nm. Best fit line for 100 pulses is shown.

The threshold of 105 ± 10 $mJcm^{-2}$ obtained for the 5mm thick PDMS sample here, appears similar to that reported for thin films (694nm thick), where the ablation threshold at 157nm was 115 ± 30 $mJcm^{-2}$ [14].

From the slope of the lines used to fit the data in Figure 3.10, the effective absorption coefficient (α_{eff}) was calculated to be in the range of 3.5 x $10^4 cm^{-1}$ and 6.4 x 10^4 cm^{-1}. There is some evidence from Figure 3.10 that the effective absorption coefficient slightly increases in value when 10 or more pulses are used on each site. This may be indicative of a weak incubation effect or possibly differences in properties between the surface and the bulk PDMS. At this VUV ablation wavelength PDMS exhibits a relatively high effective absorption coefficient and is comparable to the value of α_{eff} ~1x10^5 cm^{-1} reported for polymethylmathacrylate (PMMA). We assume now that we can use α_{eff} to determine an extinction coefficient k using equation:

$$\alpha = \alpha_{eff} = \frac{4\pi k}{\lambda} \tag{3.5}$$

where λ = 157nm. With α_{eff} = 3.5 x 10^4 cm^{-1}, this gives a k value is estimated to be 0.044.

Etch depth should become greater as the number of exposure pulses increased, (Figure 3.10), but apparently the etch rate for single pulse is greater than for larger numbers of pulses thus the threshold value cannot be estimated from Figure 3.9. This behaviour possibly could be related to the preparation of the sample, where a dense skin layer may be formed. It would be of interest to investigate this further.

3.3.1.3 Raman spectroscopy

A Raman microscope system (Renishaw, Laser Diode NIR 780/50) consisting of a light microscope (Leica DL-LM) coupled to a Raman spectrometer was used to investigate the exposed PDMS surface. The microscope was equipped with four objectives with 5x, 20x, 50x, and 100x magnification and an LMPLAN FL 50x.0.5NA eyepiece. The microscope optics was used to focus the excitation laser onto the target and collect the backscattered light (180°). The excitation source was a diode laser emitting at 780nm and the instrument was calibrated against the Stokes Raman signal of pure Si at 521cm^{-1} using a (111) silicon wafer.

The Raman line obtained for silicon is seen in Figure 3.11. The microscope was focused onto the sample surface by using a white light source; this was then replaced by the laser beam and Raman spectra were recorded at Stokes Raman shifts of 200 to 3000cm^{-1}.

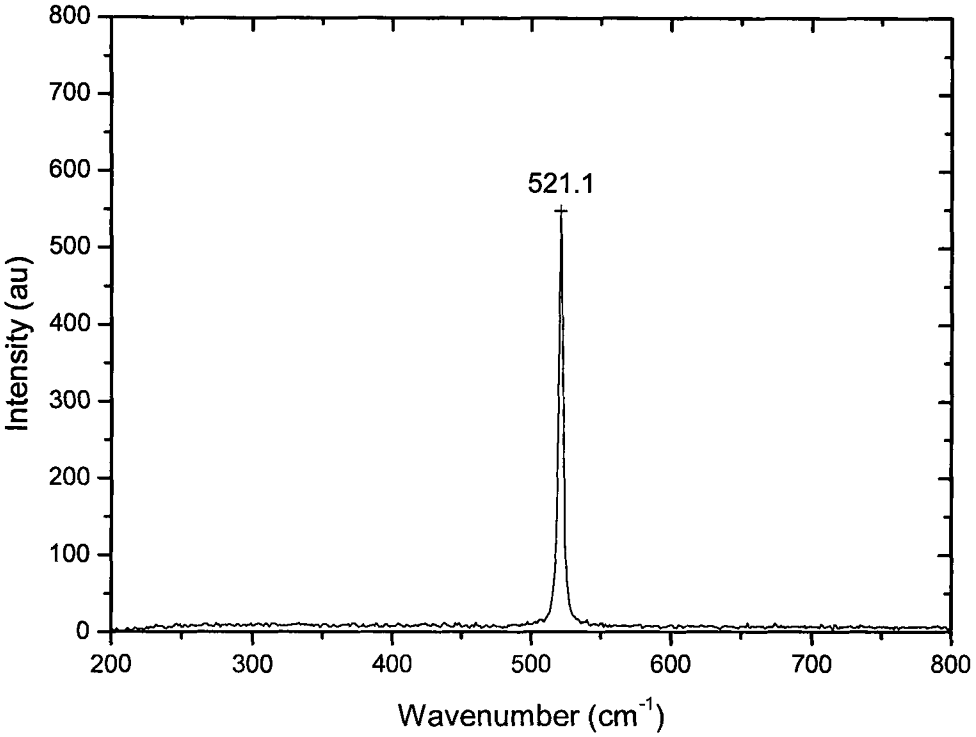

Figure 3.11: Raman spectrum calibration for pure silicon wafer at 521.1cm^{-1}.

Raman spectroscopy was used to study how the 157nm laser exposure alters the conformations of the PDMS polymer. Advantages of the Raman spectroscopy in this experiment include direct experimental observation, orientational information and chemical bond information from peak position and bandwidth analysis [15], Figures 3.12 and Figure 3.13 show a spectrum comparison between unirradiated PDMS and PDMS exposed to the 157nm laser respectively. In Figure 3.12, for unirradiated PDMS, no prominent peaks are seen except a weak feature at 488cm^{-1} attributable to the Si-O-Si vibration.

In previous studies of PDMS using an Ar^+ laser at 488nm, and 514.5nm [16] as the Raman excitation source, intense stretching vibrations of methyl groups appear at 2965 and 2907 cm^{-1}, methyl bending vibrations appear at 1412 and 1262 cm^{-1}, Si-CH_3 rocking vibrations appear at 862, 787, and 687cm^{-1}, and Si-O-Si stretching vibrations appear at 488 cm^{-1} [16].

Figure 3.13, shows the vibration peaks identified in the present experiments for PDMS ablated using the 157nm laser. The peaks are poorly resolved possibly because the ~700nm excitation laser used is less suitable for this than the Ar$^+$ laser. Vibration peaks at 488cm^{-1}(Si-O-Si symmetric stretching), 687 cm^{-1} (Si-CH_3 symmetric rocking), 708cm^{-1} (Si-C symmetric stretching), and 1262 cm^{-1} (CH_3 symmetric bending) are tentatively identified. The formation of Si-CH_3 and Si-C is suggested from the intensity peaks between 600cm^{-1} to ~700cm^{-1} and is indicative of the formation of the new silicon species. Studies by Lippert *et al* [17] concluded that the oxygen radical transformed the Si-C bond to create a new Si-O-Si which resulted in cross-linking. The silicon radical also reacts with the hydroxyl radical when exposed using a 172nm lamp in air, forming the silanol-group (Si-OH). However, in this experiment, no silanol group (Si-OH) was formed after irradiation with the 157nm laser because high absorption meant it was not possible to perform irradiation at significant pressures of oxygen (or air). Bond breaking of the backbone of the PDMS chain (Si-O) or side groups of the polymer (Si-C and C-H) is the more likely contribution to chemical modification of its surface with the high photon energy (7.9eV) 157nm laser.

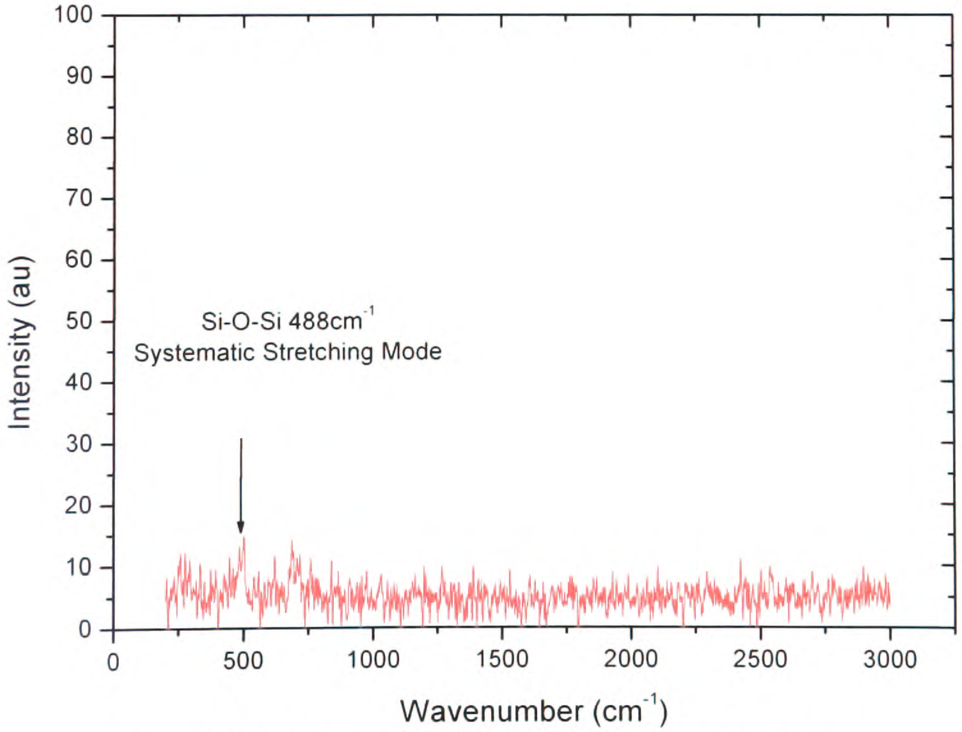

Figure 3.12: Raman spectrum of unirradiated PDMS surface

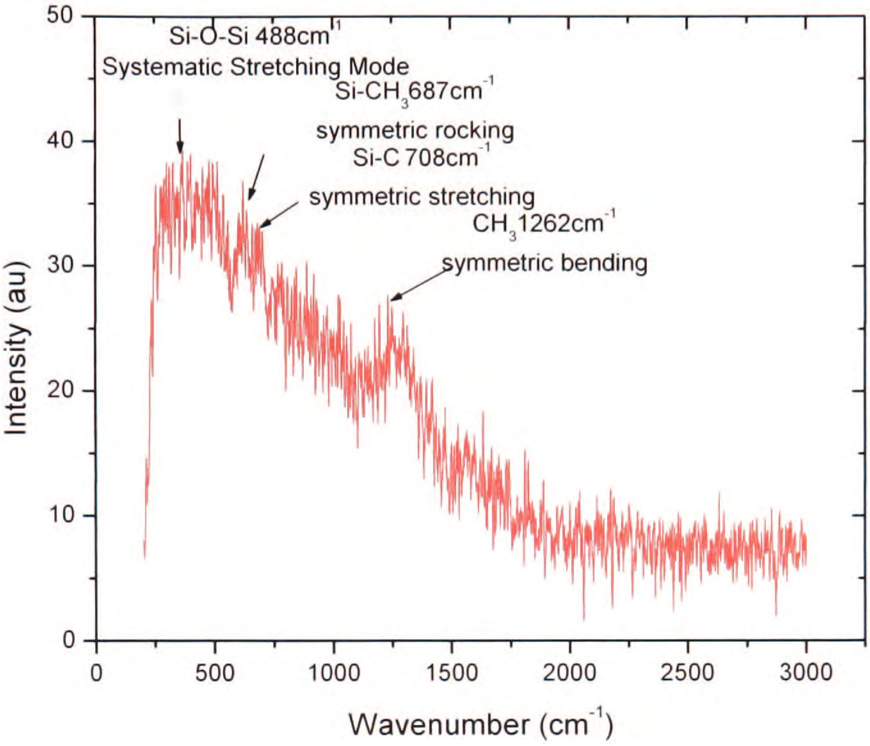

Figure 3.13: Raman spectrum over range of wave numbers to 3000cm^{-1} for PDMS surface ablated at 157nm. Si-O-Si symmetric stretching at 488cm^{-1}, Si-CH3 symmetric rocking at 687cm^{-1}, Si-C symmetric stretching at 708cm^{-1} and CH3 symmetric bending at 1262cm^{-1} are indicated.

3.3.1.4 Calculation of surface temperature

An estimate of surface temperature, T_s was made by neglecting thermal diffusion during ablation pulse and assuming absorbed laser energy on the target material has been transformed to heat. The temperature rise on the ablated material can be characterized by δ, the ratio of absorption length ($1/\alpha$) to thermal diffusion length, L, over the laser pulse duration, t. D is thermal diffusivity and L can be derived from the equation (3.6):

$$L = \sqrt{Dt} \tag{3.6}$$

and the value of δ can be calculated by equation (3.7):

$$\delta = 1 / \alpha\sqrt{Dt} \tag{3.7}$$

For $\delta >> 1$ negligible heat flow occurs and the temperature rise profile ΔT_S is as shown in equation (3.8):

$$\Delta T_S = (1-R)\frac{\alpha}{\rho C}Fe^{-\alpha x} \tag{3.8}$$

The surface temperature (i.e. at $x = 0$) is then given as

$$T_S = T_R + (1-R)\alpha F / C \tag{3.9}$$

where $C = \rho c$ is the volume specific heat, ρ being the PDMS density and c its specific heat and T_R=300K is the initial temperature. F is the fluence and R is the surface reflection coefficient at 157nm,

The following properties of PDMS are found from reference [8]:

Specific heat, c	=	1100	$\mathrm{Jkg^{-1}K^{-1}}$
Density, ρ	=	1030	$\mathrm{kgm^{-3}}$

By assuming the refractive index n is 1.445 after exposure, the normal incidence reflection coefficient of PDMS can be calculated using equation (3.10):

$$R = \frac{(n-1)^2 + k^2}{(n+1)^2 + k^2} \tag{3.10}$$

Using n =1.445 and k = 0.044 gives R ≈ 0.033. Then using equation 3.9 we get a temperature rise for PDMS at the threshold fluence F_T = 100mJcm^{-2} of 4694K corresponding to a surface temperature of ~ 4994K. This estimate suggests a high surface temperature could be reached when PDMS is exposed at 157nm.

3.3.2 SU-8

3.3.2.1 Etch rate analysis

SU-8 was irradiated at 157nm with various fluences between ~300mJcm^{-2} and ~1600 mJcm^{-2}. The depth of SU-8 removed from the samples subjected to 1, 5, 10, 50 and 100 pulses was measured. The extrapolation lines give an estimated threshold value of ~50-100 mJcm^{-2} as shown in Figure 3.14. Data presented in Figure 3.14 considerably shown uncertainty as there is no consistency for the etch depth against fluence for this material. From the slope of the 50 pulses line, the effective absorption coefficient calculated was α_{eff} =7.4 x 10^4 cm^{-1} and the extinction coefficient estimated as k = 0.092. The ablation characteristics of the SU-8 photoresist spun on Si wafers under 248 KrF excimer pulsed laser had been studied by Muralidhar *et.al* [18]. The threshold fluence for ablation of SU-8 was measured to be about 50mJcm^{-2} and reveal very smooth morphology of the etched surfaces; they hence concluded that SU-8 is one of the suitable polymer materials for excimer ablation lithography.

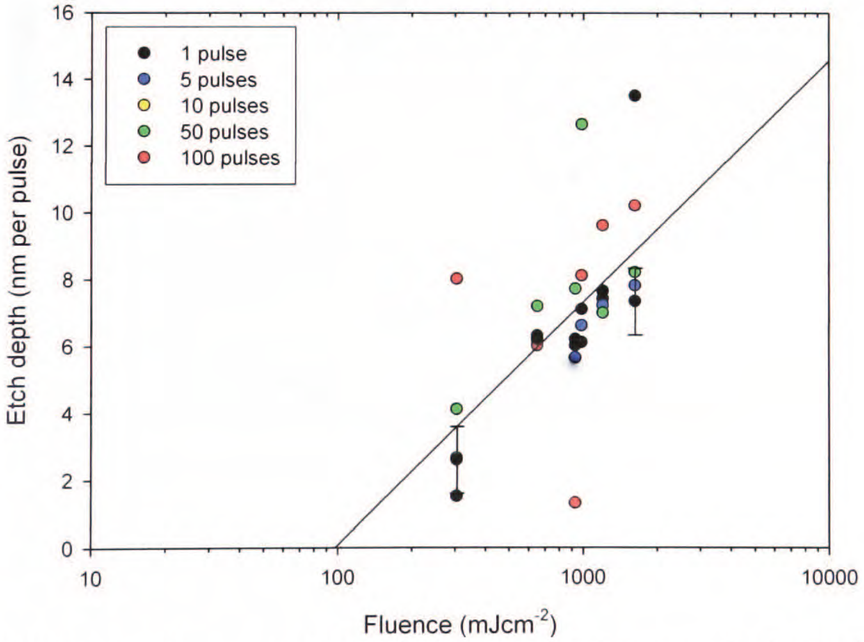

Figure 3.14: Etch depth per pulse for 1, 5, 10, 50 and 100 pulses versus the fluence for SU-8 exposed using the 157nm F_2 laser with best regression line shown.

3.3.3 Nylon 66

3.3.3.1 Etch rate analysis

Figure 3.15 shows the etch rate per pulse as a function of fluence for Nylon 66 polymer at the 157nm laser wavelength. The ablation threshold for this polymer from the data in Figure 3.15 is (27±3) $mJcm^{-2}$. A previous study by Dyer *et al* [19] on Nylon 66 at the 157nm laser wavelength gave a value of (33±7) $mJcm^{-2}$ by the calculation based on the apex angle of cones formed in the ablation. From the gradient line shown in Figure 3.15, an effective absorption coefficient of $\alpha_{eff} \approx 1.1 \times 10^5$ cm^{-1} is calculated.

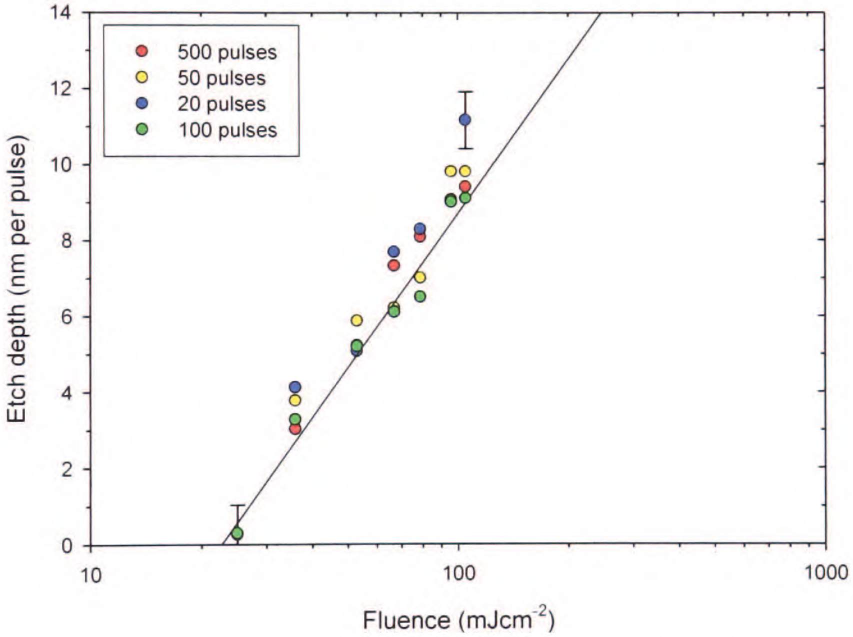

Figure 3.15: Etch rate as a function of fluence for Nylon 66 ablated at 157nm laser wavelength based on average obtained for differing numbers of pulses.

3.3.4 UHMWPE

3.3.4.1 Etch rate analysis

Figure 3.16 shows the etch depth per pulse of laser ultra-high molecular weight polyethylene (UHMWPE) at the 157nm laser wavelength. The data show considerable scatter making a meaningful extraction of useful values for α_{eff} and the threshold fluence difficult. Ablation persists at least down to fluences of ~27mJcm^{-2} for a surface exposed to 50 or more pulses. For the 20 pulse series the results fall on a reasonably well defined plot with corresponding values of $\alpha_{eff} \approx 4\times10^5$ cm^{-1} and threshold fluence = (28 ± 3) mJcm^{-2}. Previous work on (UHMWPE) has yielded a threshold of (29±6)mJcm^{-2} [20], with CO, CO_2, CH_4, C_2H_2, C_2H_4, C_4H_2, C_4H_4, benzene and CH_3CHO being detected as the gaseous products of ablation.

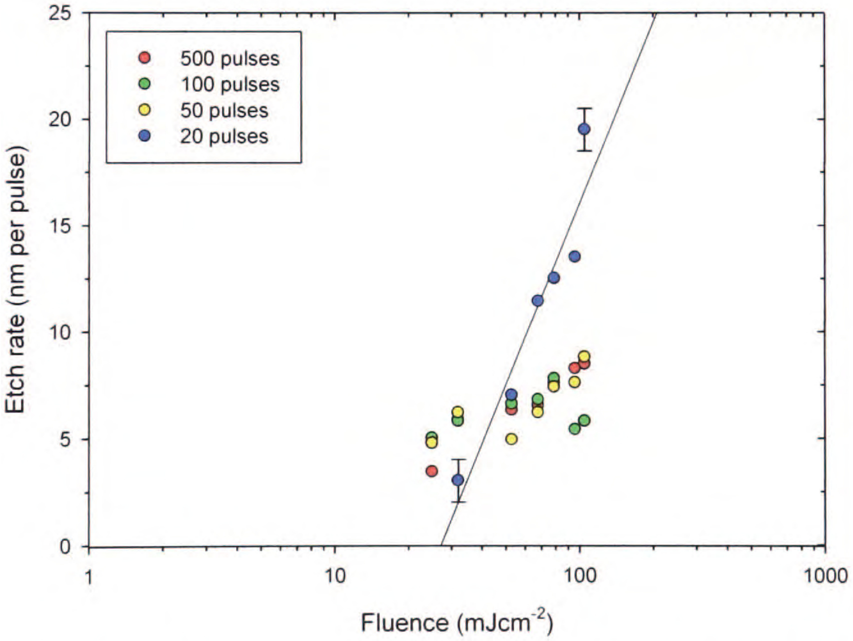

Figure 3.16: Etch rate of ultra high molecular weigh polyethylene (UHMWPE) ablated at the 157nm laser wavelength based on average for various numbers of pulses.

3.3.5 Lexan Polycarbonate (PC)

3.3.5.1 Ablation sites after irradiation

Polycarbonate samples exposed to various numbers of ablation pulses at differing fluences were viewed using an optical microscope. A series of images obtained for a fluence of 55mJcm^{-2} with 50, 100 and 500 pulses is seen in Figure 3.17. The rectangular ablations sites are seen to contain dark spots that become progressively more intense but fewer in numbers, as the number of exposure pulses increases. These 'spots' are cones that develop on the surface and appear dark because they reflect little light back into the microscope. Also evident from Figure 3.17 is a patterning effect outside of the main ablation site that is a result of re-deposition of material from the ablation plume. This shows up relatively faintly in the 50 and 100 pulse exposures but becomes more marked with 500 pulses where this debris extends beyond 100μm from the crater margin. In the 100 pulse micrograph (Figure 3.17b) the deposited layer has apparently just become thick enough to produce visible fringes as a result of interference between light reflected from the film surface and the film-substrate interface. In Figure 3.17c the thickness of this layer has grown to a sufficiently large value that multiple coloured fringes are seen.

The formation of debris surrounding the ablation sites of polyimide (PI), polyethylene terephthalate (PET), polymethylmethacrylate, polystyrene and polyethylene has been studied in some detail by Singleton *et al* [21]. Hydrodynamic models describing the form of the patterns produced by re-deposition from polymer ablation plumes have been reported by Miotello *et al* [22]. These are based on a one-dimensional outwards expansion of the plume being coupled to a sideways expansion and explain quite well how the shape of re-deposition zone is governed by ablation crater on the wider sideways. This is confirmed in Figure 3.17c, where re-deposition of debris evidently extends considerably further in the vertical compared with the horizontal direction.

In studies of glass ablation using a 266nm laser, Singh *et al* [23] have used the interference fringes produced by the re-deposited layer to determine its thickness and the material mass involved. A similar approach can be used here if it is assumed the layer decreases monotonically in thickness from the edge of the crater and has a refractive index μ

that is lower than bulk polycarbonate so the phase change at the air-layer and layer-substrate interfaces is the same. Interference maxima would then appear at a thickness

$$t = m\lambda / 2\mu \tag{3.11}$$

where λ is the vacuum wavelength and m an integer [23]. For the upper fringe system in Figure 3.17c there are about three red fringes on moving inward to the crater rim, which using $m = 3$ and taking $\lambda = 600$nm and $\mu \leq 1.58$ for a polycarbonate-like layer gives $t \geq 570$nm. This would correspond to deposition at a rate of about 1.1nm/pulse immediately beyond the crater rim.

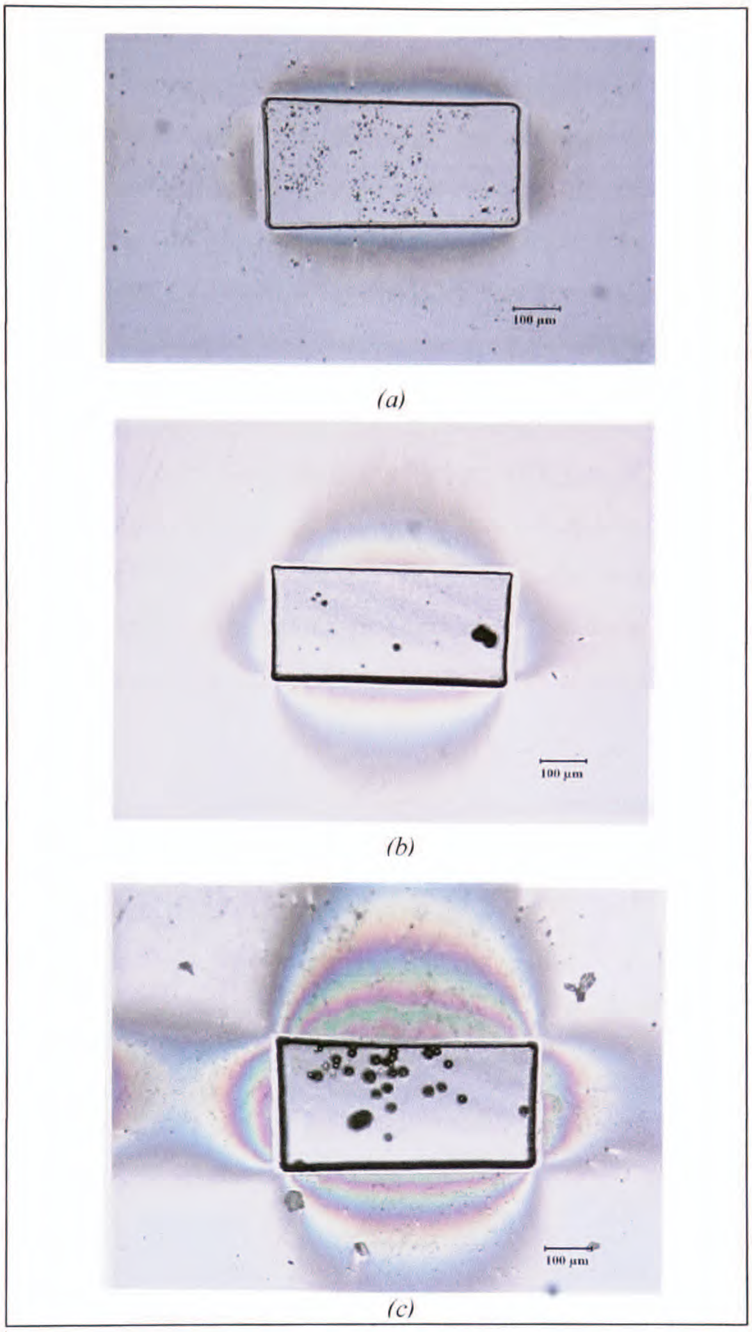

Figure 3.17: Optical microscope images of polycarbonate ablated at ~55mJcm^{-2} with various numbers of 157nm pulses (a) 50 pulses (b) 100 pulses and (c) 500 pulses, (a) 50 pulses showing multiple black 'spots' due to cones in the ablation crater and faint indication of darkening due debris layer outside of crater (b) With 100 pulses the cones extend in size but become smaller in number. The extent of debris re-deposition becomes clearer through the appearance optical interference fringes in the layer (c) With 500 pulses a few large-scale size cones remain in the crater. The debris layer becomes more pronounced and is clearly revealed by the interference fringes produced by the polychromatic light source.

3.3.5.2 Etch rate analysis

The etch rate for PC was determined by subjecting samples to various number of pulses and fluences and then measuring the depth of the ablation site using the white light interferometer. Figure 3.18 shows the average etch rate per pulse as the function of fluence at 157nm for various numbers of pulses. From the extrapolation of the regression line, a distinct threshold for ablation of PC of 10mJcm^{-2} is obtained. Based on the gradient of the line at 100 pulses shown in Figure 3.19 below, an effective absorption coefficient α_{eff} of $\approx 3 \times 10^5$ cm^{-1} is calculated.

The value of the effective absorption coefficient indicates PC is a strongly absorbing organic polymer at 157nm. Using α_{eff}, a volume specific heat of 1440kJm^{-3}and assumed surface reflection loss of 5% [3], the surface temperature rise calculated by using equation (3.9) is 1649K at the ablation threshold of 10mJcm^{-2}. This large temperature rise on the surface suggests that material removal is driven by thermal degradation and vaporization [14].

Over a certain range of fluence, the formation of the cones occurred on the PC surface, allowing measurement of the cones angle to be used to estimate the ablation threshold. The value obtained in this way could then be compared with the etch rate measurements. The results obtained from the cones will be explained in the section below.

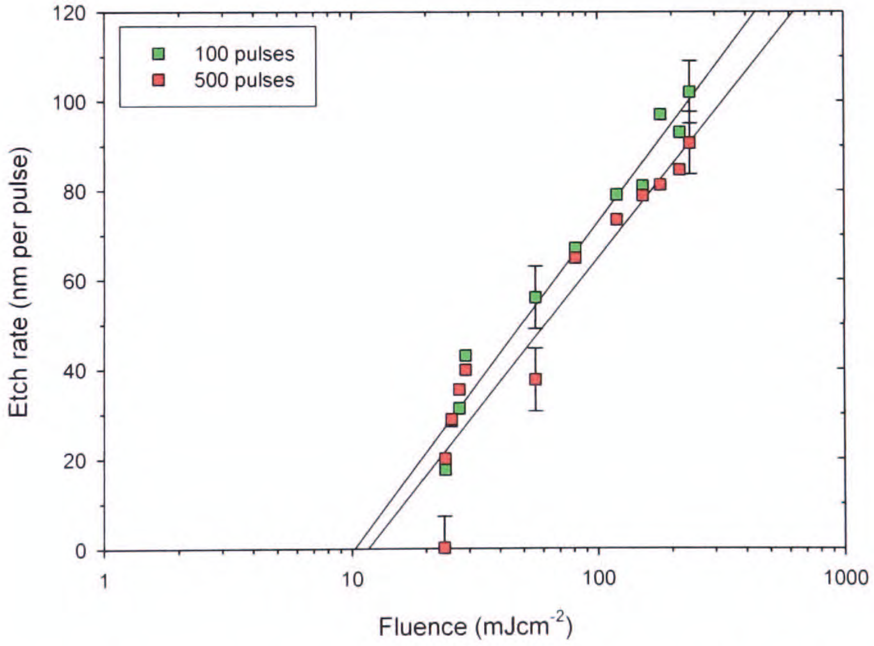

Figure 3.18: Etch rate as a function of fluence for polycarbonate (PC) ablated at 157nm.

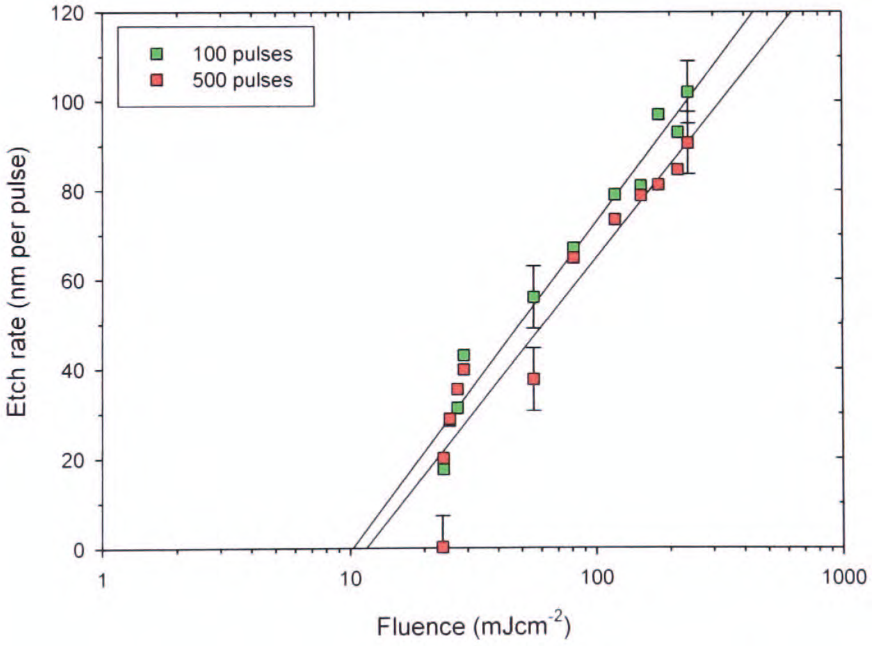

Figure 3.19: Etch rate as a function of fluence for polycarbonate (PC) for 100 and 500 pulses (data extracted from Figure 3.18).

3.3.5.3 Formation of cones

To determine the ablation threshold of materials, various methods have been used in the research previously [20] . The most common method is the measurements of the etch depth per pulse or etch rate obtained from the ablation over a range of fluence. These are fitted using equation (3.4) to give the value of ablation threshold F_T. An alternative method employs the measurements of the thermal loading of thin films, and generally gives similar results to the etch rate method. Another technique, based on the apex angle of particle-induced cone structures, is sensitive to very small levels of etching and often gives appreciably lower values of threshold compared to the two methods stated above.

Values of the ablation threshold determined from the apex angle of the stable, well-defined conical structures on polyimide, polyethylene terephthalate (PET) and Nylon 66 at 157nm are reported in [19] as (23±7) mJcm^{-2}, (19±6) mJcm^{-2}, and (33±7) mJcm^{-2} respectively.

In the present work the form of particle-induced cone structures was studied on the PC after ablation using the 157nm laser over a range of fluence. Previous research reported by Stuke *et al* [24] on the fabrication of microchannel using polymers PMMA, polystyrene and polycarbonate using 157nm, gave the result of ablation threshold of ~18mJcm^{-2} for PC.

Interestingly, the cone structures that developed on the PC surface after ablation give a well defined interference pattern surrounding the region around the base of the cones, which provides information on the spatial coherence width of the beam.

(a) Unseeded samples

Cone formation on PC was observed on both clean surfaces (unseeded) and on surfaces that were deliberately seeded with particles to induce their formation.

Samples of PC without deliberate particulate seeding were exposed over a range of pulse number from 10 to 500 pulses and a range of fluences from ~10mJcm^{-2} to ~250mJcm^{-2} at 10Hz using the 157nm laser. The morphology of the ablated surface was investigated by scanning electron microscopy (SEM). Figure 3.20a shows the cones that developed on PC subjected to 100 pulses at a fluence of ~55mJcm^{-2} and Figure 3.20b at the higher fluence of 81mJcm^{-2}.

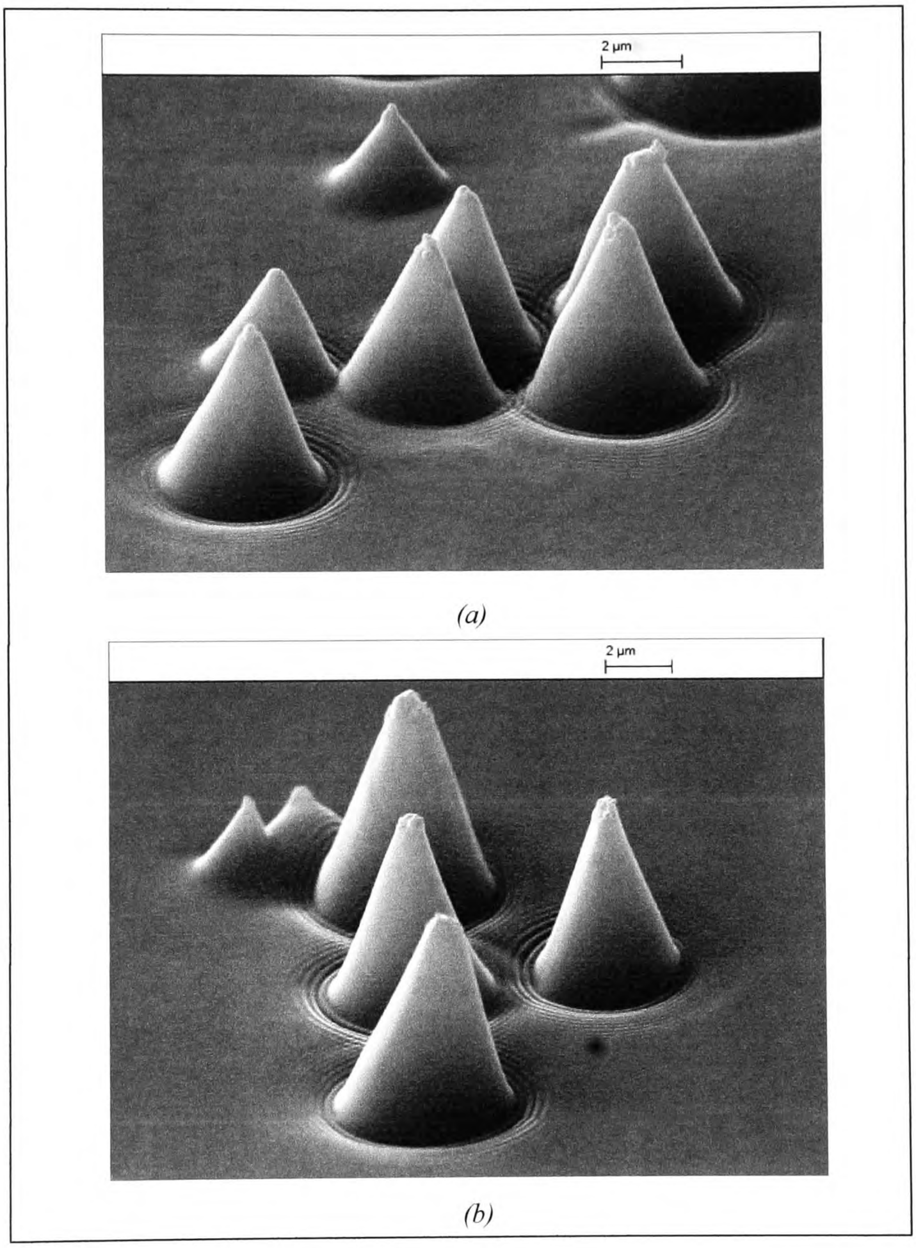

(a)

(b)

Figure 3.20: Conical structures produced using 100 pulses applied to polycarbonate (157nm laser); (a) ~55mJcm^{-2} (b) 81mJcm^{-2}.

Using the 'Ruler MB' software, the full apex angle, $(2\theta_t)$ (see Figure 3.29) became smaller at higher fluence, for example at same pulse number (100pulses) $2\theta_t$ is 51° at 55mJcm^{-2} decreased to 41.7° at ~81mJcm^{-2}. The apex angle of the cones decreased at higher fluence and this is turn gives smaller base radius. The SEM images shown were for the stage tilted at 60°, apex angle will be taking in the account as true half-angle viewing at 90° (θ_t) where a correction factor must be applied.

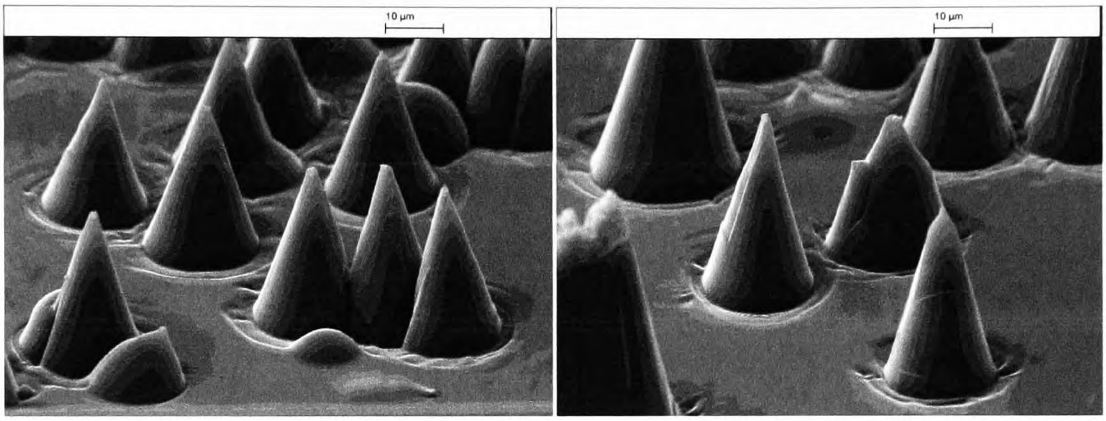

Figure 3.21 (a) Conical structures at ~55.8mJcm^{-2} and (b) at ~81mJcm^{-2}, when 500 pulses were applied to polycarbonate (PC) using the 157nm laser.

The areal density of cones appearing on the ablated PC surface varied with fluence and number of exposure pulses. In general, a high fluence and greater numbers of pulses led to fewer cones and reduction in apex angle as is illustrated by Figure 3.21 (a and b) where at 500 pulses, fluence ~56mJcm^{-2} gives half cone apex angle as 22° and reduced to 21° at ~81mJcm^{-2}. Here 500 pulses applied at a fluence of 230mJcm^{-2}, results in a dramatic reduction in cones compared to Figure 3.22, the surface is essentially devoid of such structures aside from two in the corner of the crater.

In contrast in the near-threshold fluence regime, cones were quite dense over the surface and in many cases only partially developed even when a large number of exposure pulses was used e.g. Figure 3.23; (a) 25mJcm^{-2} , 100pulses and (b) 29mJcm^{-2}, 500pulses shows the cone structures are small, not straight walls, wider base indicating not define cones formed.

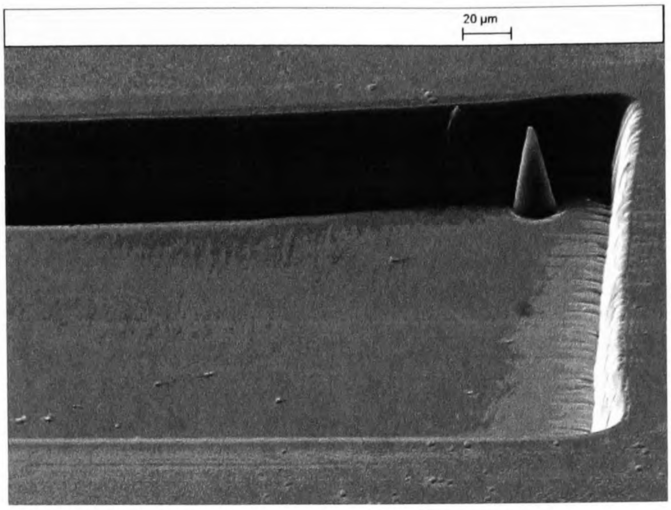

Figure3.22: Conical structures at ~230mJcm^{-2} with 500 pulses applied to polycarbonate (PC) using the 157nm laser.

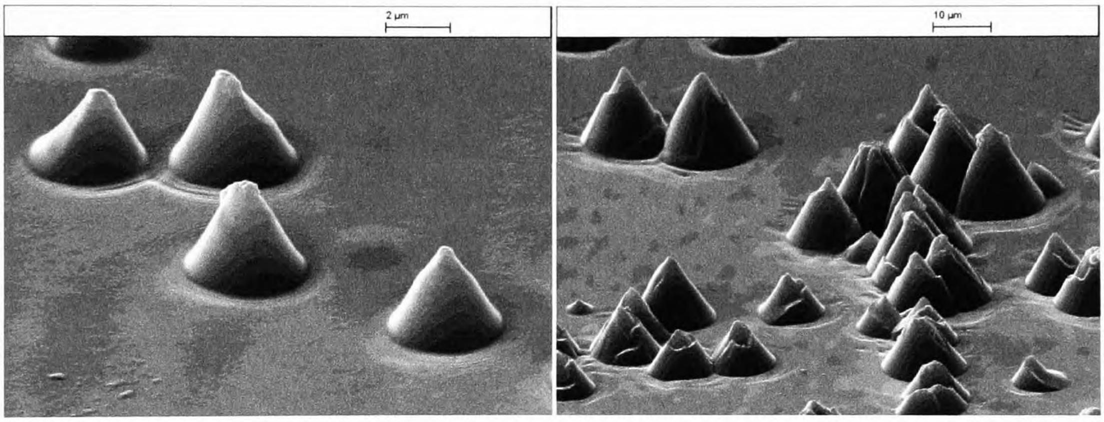

Figure 3.23: Conical structures on polycarbonate at (a) ~25mJcm^{-2} with 100 pulses and (b) ~29mJcm^{-2} with 500 pulses, 157nm laser exposure.

(b) Seeded samples

This experiment has been done by deliberately seeding fine particles of alumina (~0.05µm, Gallenkamp Griffin PSR-350-D grade 5/20) on the clean sample of polycarbonate (PC). The seeded PC was then etched using various numbers of 157nm pulses at different laser fluences. The morphology of the seeded samples were viewed under the SEM. Figure 3.24 shows comparison images of the conical structures at a fluence of ~81mJcm^{-2} for 10, 50, 100 and 500 pulses. Cones are only partially formed with 10 pulses applied but essentially fully formed at 100 pulses (Figure 3.24a and c). Figure 3.24d shows the formation of the cones covering the ablated surface at 500 pulses.

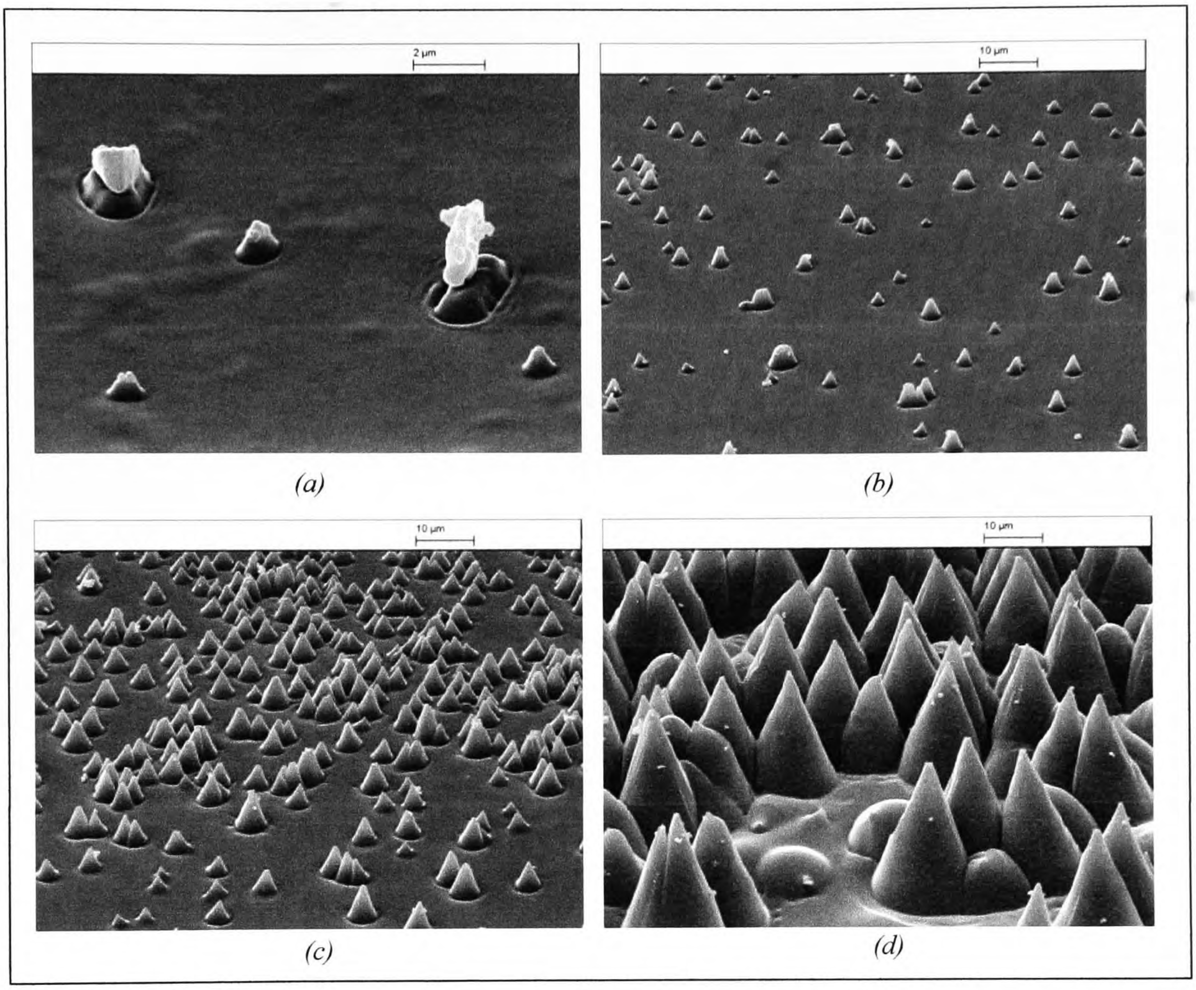

(a) (b)

(c) (d)

Figure 3.24: Evolution of conical structures on the seeded polycarbonate (PC) ablated surface with (a) 10 pulses (b) 50 pulses (c) 100 pulses and (d) 500 pulses at ~81mJcm^{-2}.

It can be seen from this experiment that cones develop under impurity particles. The density of the cones covering the surface depends on the particles layered on the surface. An impurity particle sitting on top of the cone can be clearly seen in Figure 3.25, and this produces shielding as shown schematically in Figure 3.26. If the particles on the surface are resistant to ablation they act to shield underlying polymer, leading to the development of well defined and stable conical structures as etching process proceeds (Figure 3.24a-d).

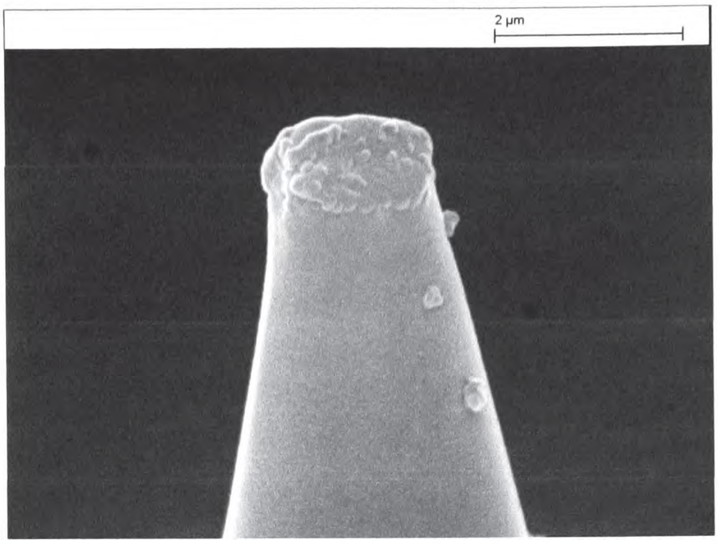

Figure 3.25: Top of the conical structure shows the effect of the impurity particle on the ablated polycarbonate (PC) surface.

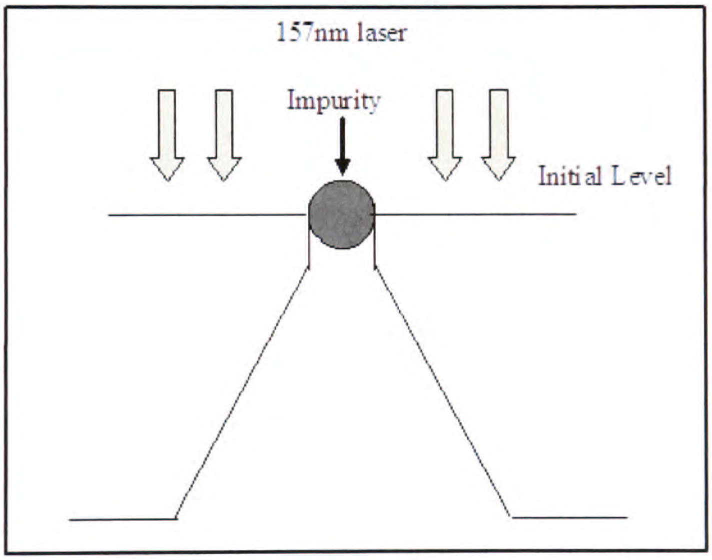

Figure 3.26: Illustration of the impurity effects on the polycarbonate (PC) ablated surfaces.

(c) Areal density of cones

The areal density of the cones on the ablated PC surface using the 157nm laser has been studied for the seeded and unseeded condition. Figure 3.27a and b shows the areal cone density after deliberately seeding with alumina particles (0.05μm) and unseeded PC sample at 100 pulses, ~81mJcm^{-2}. Figure 3.27b shows a high density of developed cones on the seeded sample compared to unseeded sample (Figure 3.27a).

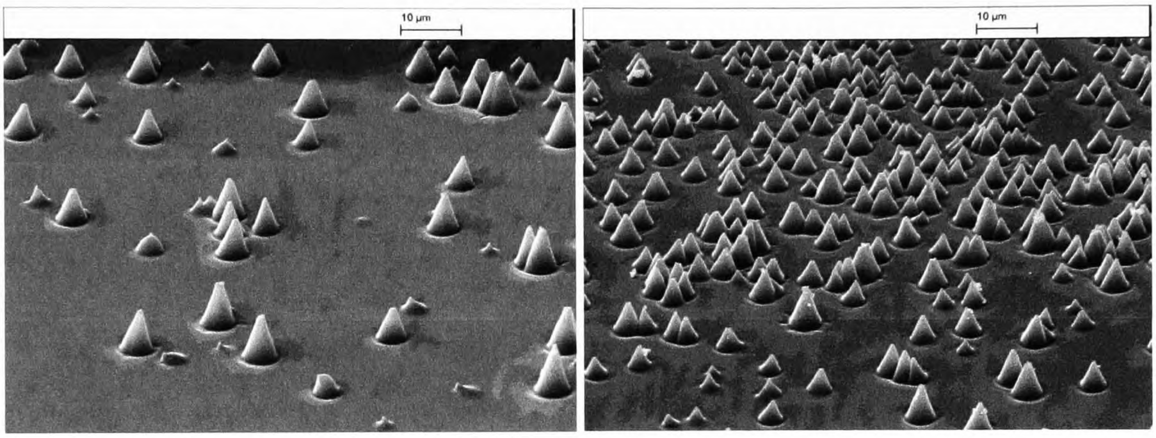

Figure 3.27: Cone formation for (a) unseeded PC, (b) PC with ~0.05μm particle surface seeding, exposed to ~81mJcm^{-2}at 157nm.

The areal density of cones was estimated by counting the number within a given area of the SEM image (typically over a 100μm x 70μm field). The results are shown in Figure 3.28 where $\log_{10}$ (areal density) versus fluence is plotted for the seeded and unseeded cases. It is evident that seeding significantly increase the areal density (a factor of nearly ten times more near to threshold) and that the number of cones per unit area falls as the fluence is raised.

Simple considerations [25] show that the ablation removal of 'particulates' through optical undercutting will occur if etch depth per pulse x satisfies $x \geq d$ where $x=\alpha_{eff}^{-1} \ln F/F_T$ and d is approximate shadowing depth of the particles. The latter is given approximately by:

$$d \approx 2r^2 / \lambda \qquad (3.12)$$

for $r \geq \lambda$

where r is the particle radius. This leads to a condition that ablation removal of the particle will occurs if its radius satisfies $r \leq r_{max}$ where:

$$r_{\max} = \sqrt{\frac{\lambda}{2\alpha_{eff}} \ln \frac{F}{F_T}} \tag{3.13}$$

r_{max} is seen to increase as the fluence raised, the effective absorption coefficient is decreased or λ increased. The fall in areal density seen in Figure 3.28 can thus tentatively be explained if the added particles have a range of sizes and increasing fluence progressively removes the larger of these so that they are unavailable for 'shielding'. It is noted that as 0.05μm (50nm) particles were used and more complicated shadowing model would be required.

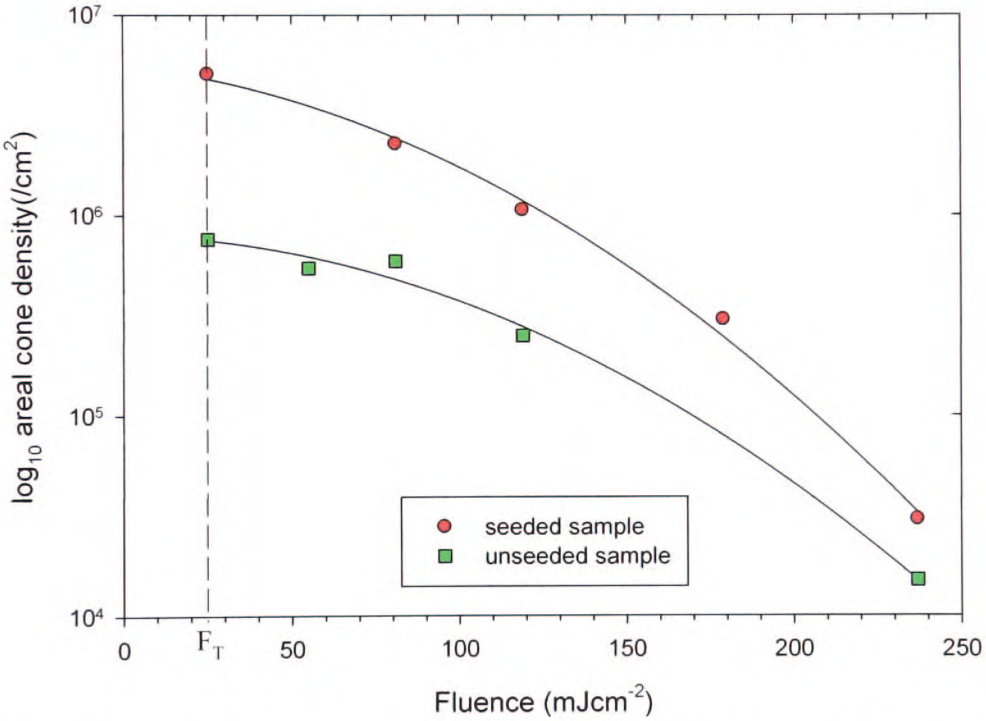

Figure 3.28: Variation of areal cone density for 157nm F_2 laser exposed polycarbonate (PC) showing results for 100 pulses on unseeded sample and seeded sample.

(d) Correction factor for cone angle

Figure 3.29 shows the view direction of cones when the SEM stage is tilted. Under these conditions it is necessary to determine a correction factor to get the true angle value $2\theta_t$ of the cone apex angle when $\theta_v \neq 90^\circ$. To this end a series of SEM images was obtained for the same group of cones with the viewing angle θ_v varying from 0 - 75°. These are shown in Figures 3.30. The perceived cone apex angle θ_p (see Figure 3.29) was measured for each image using the MB-Ruler software and also by calculating it from the measured cone base diameter and effective cone height.

The perceived full angle of the cone apex $2\theta_p$ determined in this way is plotted in Figure 3.31 versus the stage viewing angle θ_v. As expected and can be seen from the fit here, the true cone apex angle i.e. at $\theta_v = 90^\circ$ is smaller than when measured on a tilted stage. For $\theta_v = 60^\circ$ the correction factor needed is from Figure 3.31 ~ 0.83.

Straightforward geometrical considerations for a tilted cone lead to a simple theoretical expression relating the perceived angle θ_p, the viewing angle θ_v and true half-angle θ_t (refer Appendix A for a cone profile). This gives

$$\theta_t = \tan^{-1}\left[\tan(\theta_p)\cos\{\pi/2-\theta_v\}\right] \tag{3.14}$$

This expression is plotted in Figure 3.31 and shows a good fit with the experimental results; hence corrections can be easily applied using this expression.

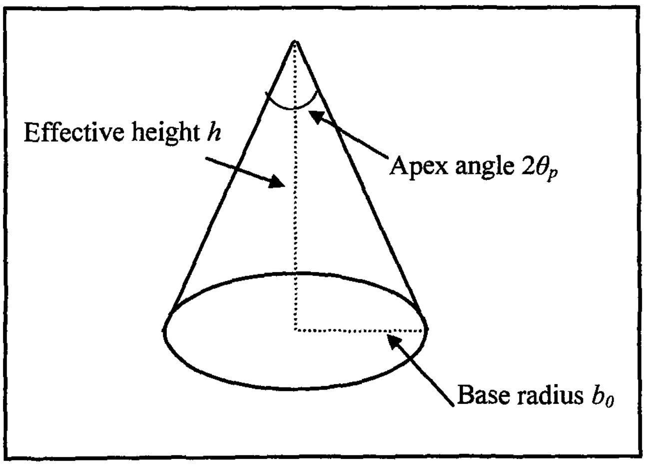

Figure 3.29: Showing effective height, h and base radius b. The perceived angle $\theta_p = \tan^{-1} b_0/h$

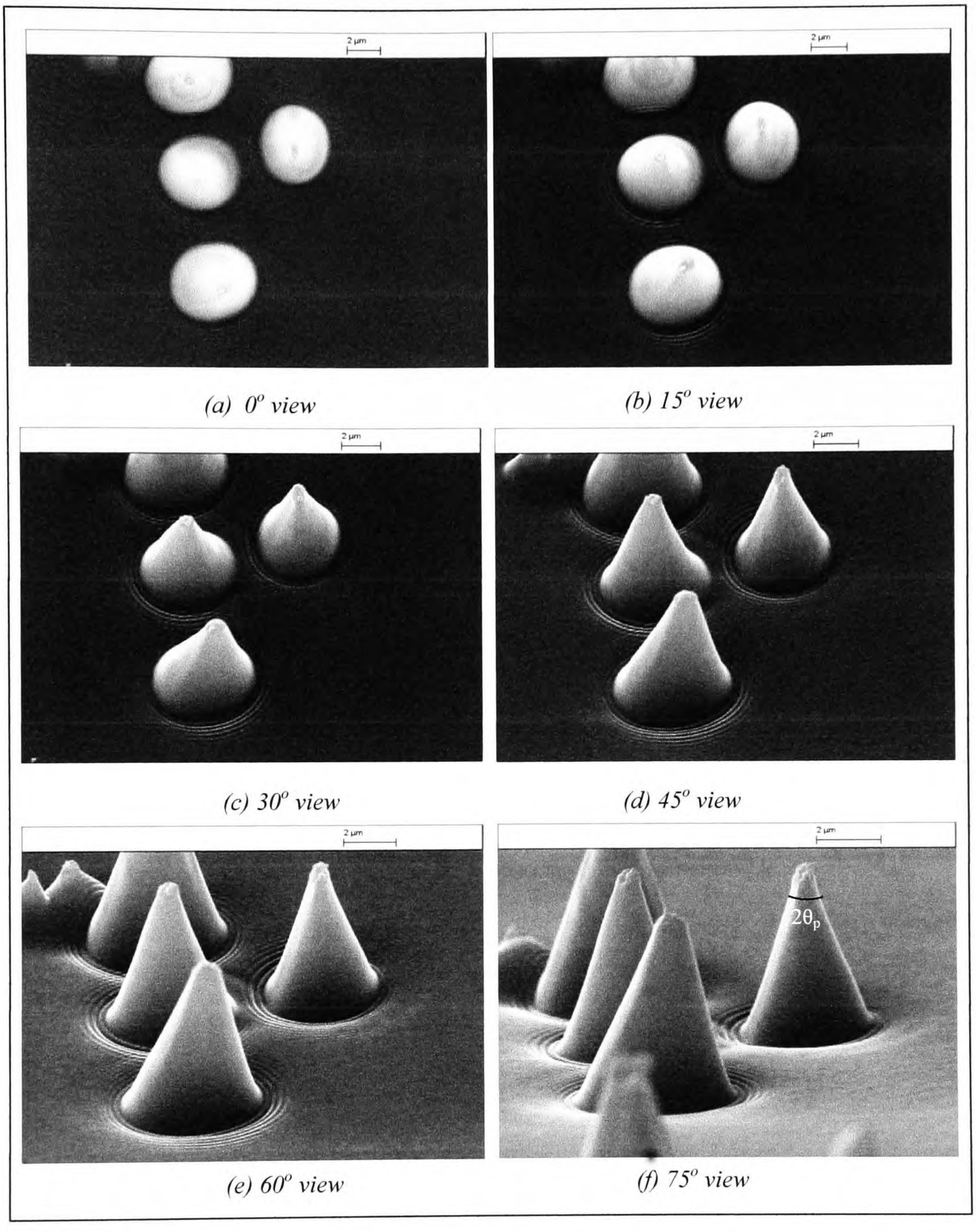

(a) 0° view

(b) 15° view

(c) 30° view

(d) 45° view

(e) 60° view

(f) 75° view

Figure 3.30: Group of cones viewed with stage angles from the vertical of (a) $\theta_v = 0^o$ (b) 15^o (c) 30^o (d) 45^o (e) 60^o (f) 75^o.

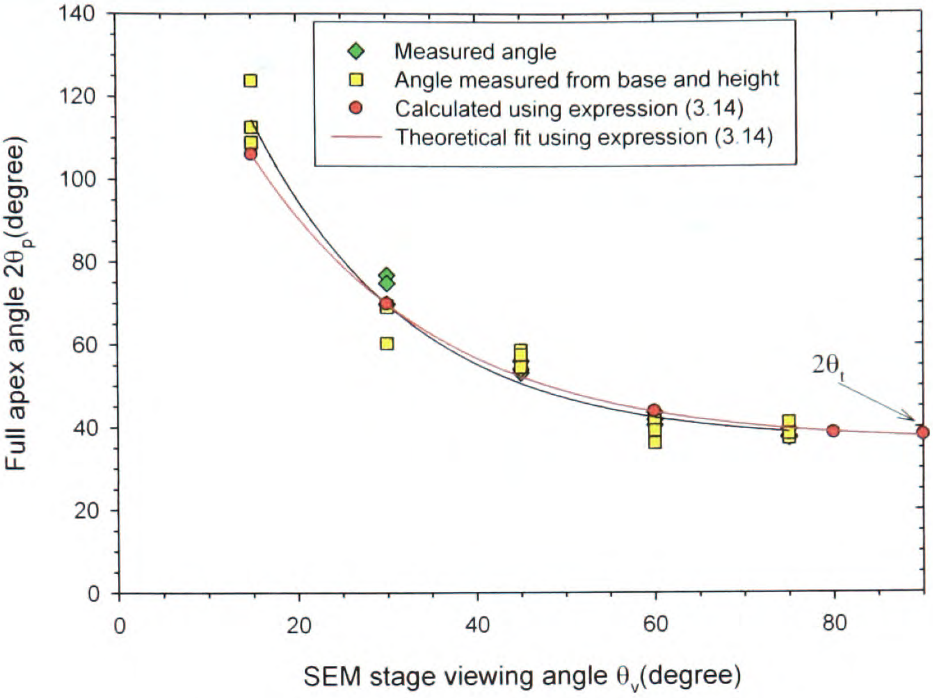

Figure 3.31: Perceived cone full apex angle $2\theta_p$ from direct angle measurement and that determined from measured height and base size of the cone as a function of the stage viewing angle θ_v. The theoretical plot is based on equation 3.14 with a true half-angle of $\theta_t = 19°$.

(e) Ablation characterization from the cones

An ablation threshold for Lexan polycarbonate (PC) can be obtained from the half apex true angle of cones from the formula [25] ,

$$\theta_t = \sin^{-1}(F_T / F) \tag{3.15}$$

Here F_T is the fluence at threshold and F is the incident fluence. Rearranging equation (3.15), gives:

$$F_T / F = \sin\theta_t \tag{3.16}$$

This simple model indicates that a plot of $\sin\theta_t$ versus $1/F$ should be linear passing through the origin, in principle allowing the threshold fluence to be derived from the slope of the line. Figure 3.32 shows that the results for cones on polycarbonate plotted in this way are not in good agreement with the expectations of this simple model.

The expression in equation 3.16 neglects surface reflection loss and that the energy density loading at the surface may change with the angle of incidence of the laser beam.

To take account of this the energy loading E_L (joules per unit volume) on the surface at normal incidence is expressed as:

$$E_L = \alpha_{eff}(1 - R_0^{\,2})F_T \qquad (3.17)$$

where α_{eff} is the effective absorption coefficient, R_o is reflection loss at normal incidence and F_T the threshold fluence.

It is now assumed that ablation on an inclined surface occurs when the same energy loading is reached. The amplitude reflection loss at the inclined surface is taken to be R_p and R_s for s and p polarisation components respectively and for an unpolarized beam the average of $R_p^{\,2} + R_s^{\,2}$ is taken i.e. $\frac{R_p^{\,2} + R_s^{\,2}}{2} = R_m^{\,2}$. Now due to refraction the transmitted beam is not normal to the surface but is refracted at an angle r. The effective penetration depth (normal to surface) is then smaller by a factor cos r so the effective energy loading is

$$(\alpha_{eff}/\cos r)\;(1 - R_m^{\,2}).F\cos i \qquad (3.18)$$

where F is fluence at normal incidence. On the assumption that ablation commences when the energy loading E_L is attained, the corresponding threshold for the inclined surface is found by equating equations (3.17) and (3.18)

$$(1 - R_0^{\,2})F_T = \frac{F}{\cos r}(1 - R_m^{\,2})\cos i \qquad (3.19)$$

Here F is now the fluence at threshold for the surface when irradiated at an angle of incidence i and F_T that at normal incidence. Now

$$\cos i = \sin\theta_t \qquad (3.20)$$

where θ_t is cone apex half-angle.

Thus, by taking the cone wall angle to be defined by reaching the (inclined) threshold energy loading on the surface, the fluence and cone angle are related by

$$F = \frac{F_T \cos r\,(1 - R_0^{\,2})}{(1 - \frac{R_p^{\,2} + R_s^{\,2}}{2})\sin\theta_t} \qquad (3.21)$$

The angle of refraction and cone apex angle are linked through the polymer refractive index μ by $\sin r = \cos\theta_t / \mu$

It is noted that if angle dependence of reflection loss is neglected i.e. $(R_p^2+R_s^2)/2 = R_o^2$ and the effective absorption coefficient remains unchanged when refraction occurs i.e. $\cos r = 1$, then equation 3.21 simplifies to

$$F_T / F = \sin\theta_t$$

which is equation 3.16.

Equation 3.21 was evaluated using the Fresnel equations [30] to determine R_s and R_p as described in more detail in section 3.4.1 (see equations 3.25 and 3.26) with a value of $\mu = 1.463$ for polycarbonate taken from reference [31]. A plot of the cone half-angle versus the normalised fluence F/F_T using equation 3.21 is shown in Figure 3.33, along with experimental data for cones on polycarbonate. The experimental fluence has been normalised using values of $F_T = 20$, 25 and 30mJcm^{-2} in an attempt to get a fit to the theoretical line. Though there is considerable uncertainty, a value of $F_T = 25$mJcm^{-2} brings the data in reasonable accord with the theoretical curve. This is considerably larger than deduced from etch rate versus fluence measurements (Figure 3.19), though in that case there is again considerable uncertainty in extrapolating the data to determine the threshold.

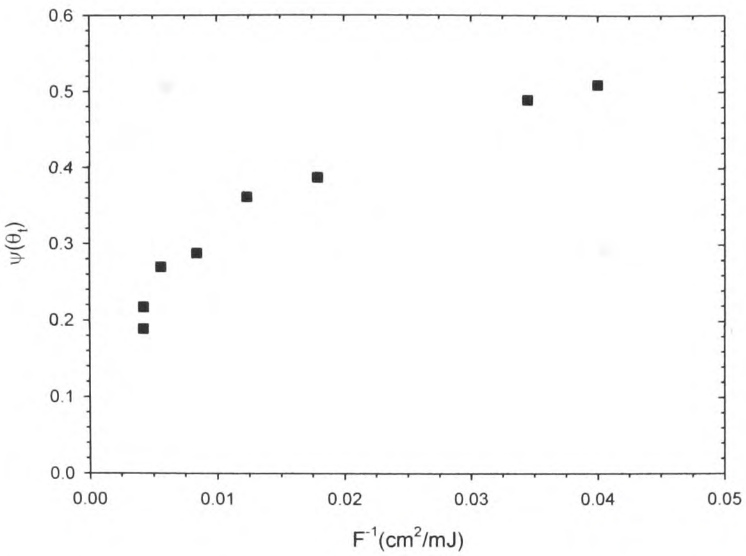

Figure 3.32: $\Psi(\theta)$ as a function of F^{1}, where $\Psi(\theta)=\sin(\theta_t)$ based on the corrected angle for polycarbonate using 157nm laser.

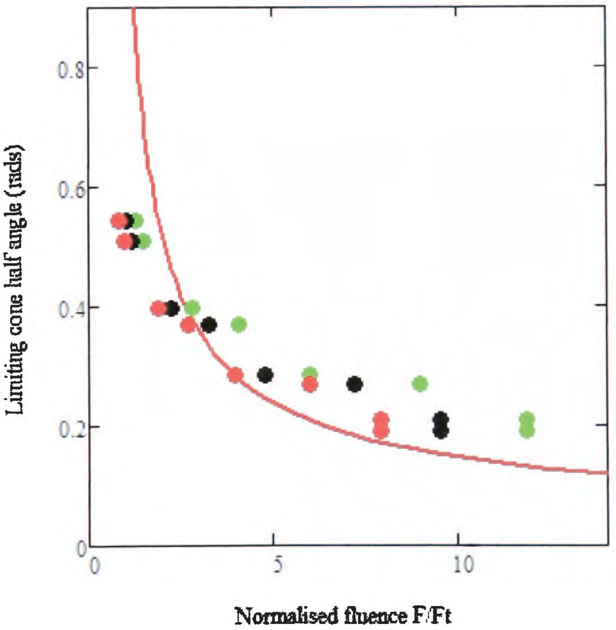

Figure 3.33: Cone half-angle as a function of normalised fluence. The solid line shows the theoretical result for polycarbonate based on energy loading at non-normal laser incidence on the cone wall for a refractive index $\mu=1.463$. The experimental results shown are normalised to ablation thresholds of $F_T = 20mJcm^{-2}$(green points), $25mJcm^{-2}$(black points) and $30mJcm^{-2}$(red points). A reasonable fit is obtained for $F_T = 25mJcm^{-2}$though there is evidently considerable uncertainty in this estimate.

3.4 Interference Fringes

The cones developed on the ablated surfaces of polycarbonate exhibit a ring-like system of interference fringes surrounding the region at the bottom of the cones, which originate from the interference of the incident laser light with that reflected from the cone wall. These interference fringes can be clearly seen under the observations using Scanning Electron Microscopy (SEM). The formation of the cones in polycarbonate has been reported by Hopp *et al* [26] in the range of fluence about 20-60mJcm^{-2} for 193nm laser exposure and they observed the cones symmetry was dependent on the laser polarization. In the present work, experimental and modelling studies have been applied for the appropriate cones with apex angles that produce a distinct fringe system surrounding the base of the cones. The cones seen in the present work are essentially symmetric which is consistent with the F_2 laser beam being unpolarized. Development of the conical structures on the PC surface is thought to be initiated by the shadowing and diffraction effect of particulate impurities and the interference effect then occur because of the reflection from the cone wall.

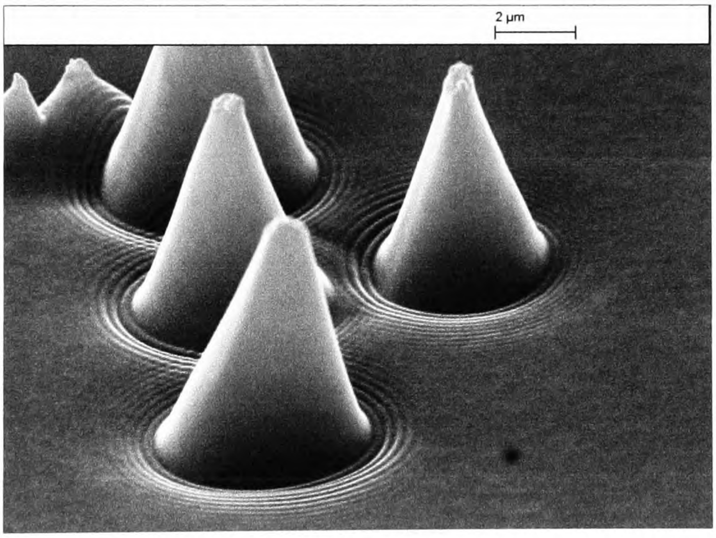

Figure 3.34: A group of cones on the ablated polycarbonate (PC) showing interference fringes with fringe period of 250nm.

Figure 3.34 shows a group of cones seen at a viewing angle of 60° for polycarbonate (PC) subjected to 100 pulses at 81mJcm^{-2}. The surface of ablated area outside of the region of fringes is seen to be smooth and devoid of significant debris, indicating the good quality surface that can be produced when ablating this material with the 157nm laser. Figure 3.35 shows a magnified view near the base of a cone where a set of well-defined circular fringes has been produced through interference of the incident beam and that reflected from the cone wall. From Figure 3.35 the fringes are seen to have an essentially constant spacing and, based on a spacing of 1.67µm for six fringes as determined from the SEM, their period is ~278nm.

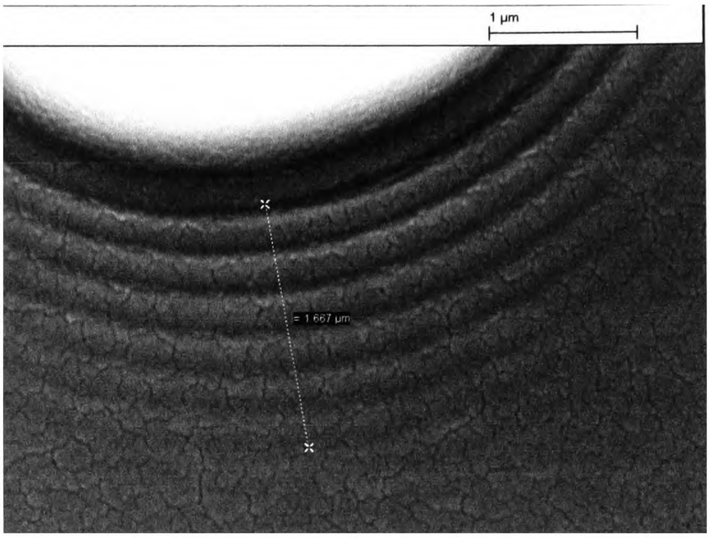

Figure 3.35: Fringes around the base of a cone in polycarbonate viewed at 0°. Six fringes here have a spacing of 1.67µm giving a fringe period ~278nm.

When a further and careful examination of the fringes was made, viewing them from above (i.e. at 0°), it was noted that they exhibited a degree of asymmetry around the base of the cones. They were seen to be visible over a greater distance along the direction of the narrow dimension (*Y*) of the F_2 laser output beam than in the orthogonal direction (*X*). This arises because of the difference in the spatial coherence widths in the low and high divergence directions of the beam, a finding that is supported by the modelling discussed below. This asymmetry is evident in the fringes seen in the group of cones in Figure 3.36, which are viewed at normal incidence to the surface. Cones A, B, and C, which approximately lie along the high coherence direction of the beam, imprint fringes on the walls of their neighbour. In contrast, cone D, lying to the right of cone B, which is displaced along the low coherence direction, has no fringes on its wall, neither does it appear to produce fringes on B. In Figure 3.36b the SEM micrographs have been enhanced using image processing software (convolution filtering) to more clearly reveal the fringes surrounding the cones and on their walls.

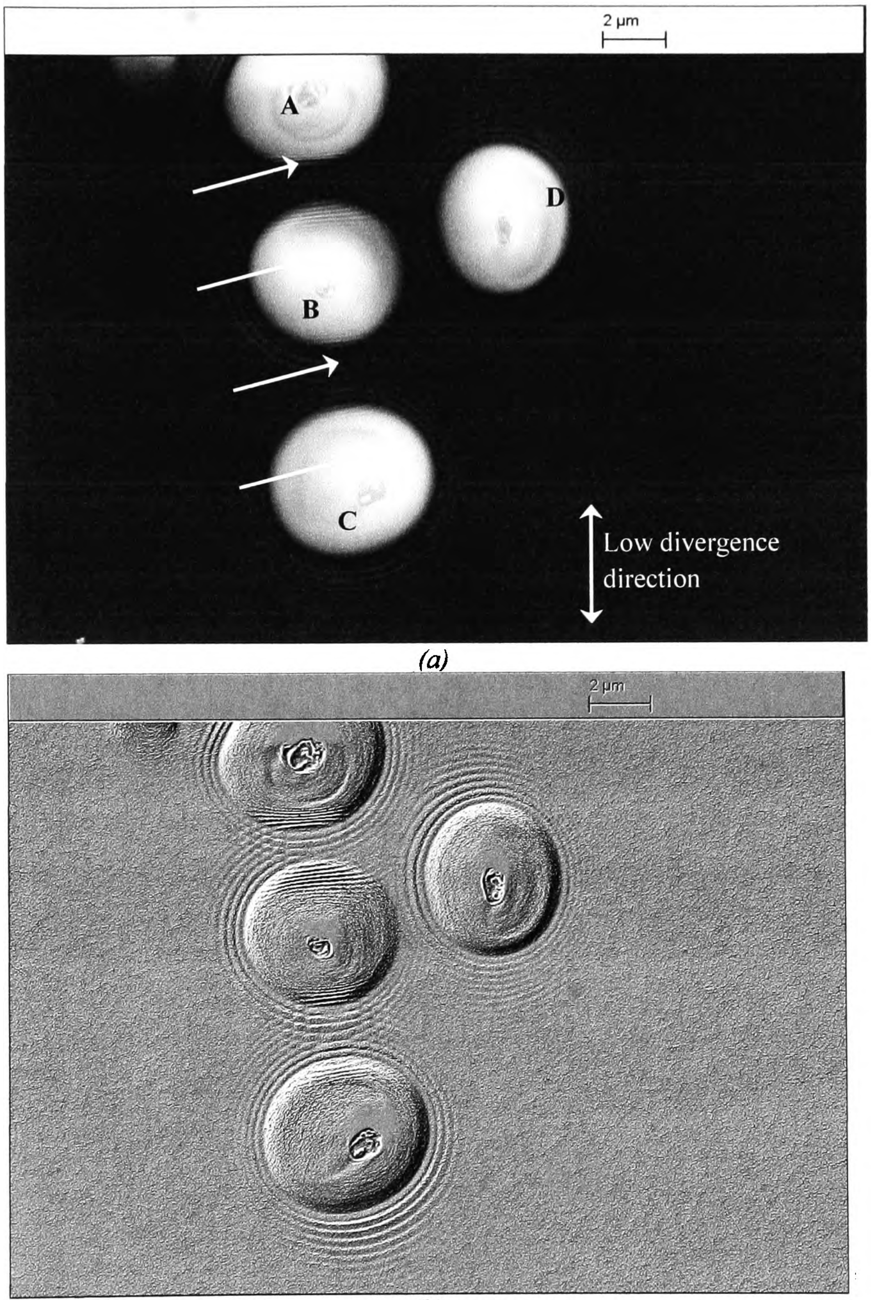

(a)

(b)

Figure 3.36: (a) A group of cones with asymmetry in the ranges over which fringes are visible. SEM viewing angle = 0° from vertical. The direction of the narrow dimension of the F_2 laser which has low divergence is as indicated. The arrows designate fringes on the walls of cones (b) Viewing angle = 0° with convolution bas-relief filter applied to enhance fringes.

The cones effectively form a micro-conical mirror that produces circular fringes in a fashion similar to the linear fringes with the Lloyds mirror arrangement (Figure 3.37). Here, interference is between the light reflected from one long mirror and the light coming directly from the source without reflection.

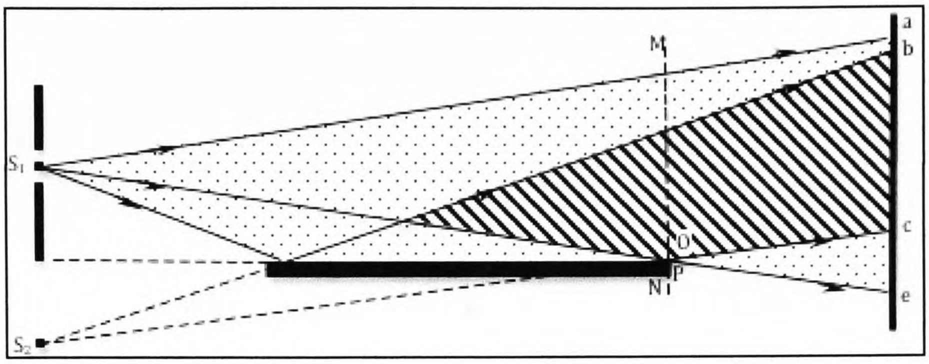

Figure 3.37: Lloyd's mirror arrangement

3.4.1 Model for the cone interference

The beam reflected from the cone wall interferes with direct beam producing a set of circular fringes on the flat surface beyond the cone base. Figure 3.38 shows a schematic diagram of the reflected beam from the cone wall, which is used in the model of the cone interference. From this figure the reflected beam and direct beam intersect at an angle $2\theta_t$ producing fringes of period:

$$\Lambda = \frac{\lambda}{2\sin\theta_t} \tag{3.22}$$

along the direction perpendicular to the bisector of the two beams.

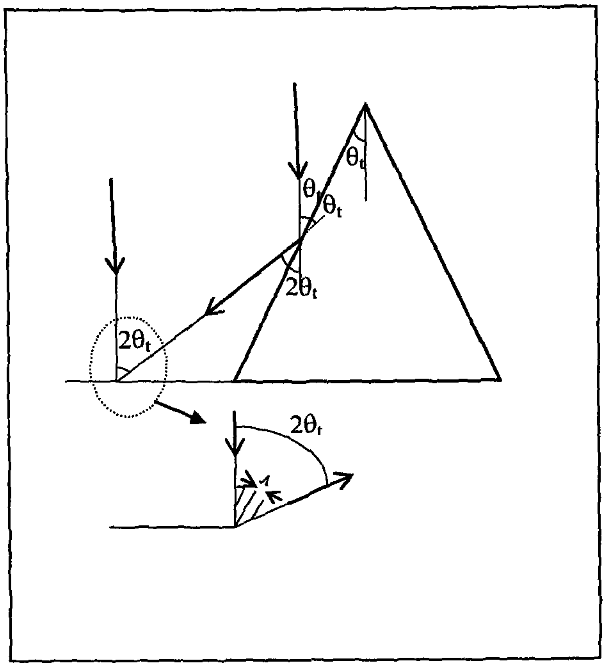

Figure 3.38: Schematic diagram of the light beam reflected from the cone wall

These fringes when projected onto the horizontal surface lead to a periodicity Λ_S given by:

$$\Lambda_S = \frac{\Lambda}{\cos\theta_t} \tag{3.23}$$

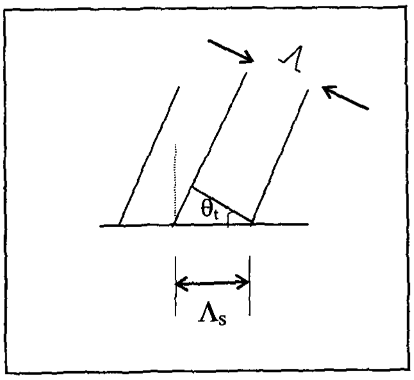

Figure 3.39: Fringe projection onto horizontal space.

Combining equations (3.22) and (3.23);

$$\Lambda_S = \frac{\lambda}{2\sin\theta_t \cos\theta_t} = \frac{\lambda}{\sin 2\theta_t} \qquad (3.24)$$

where λ is the laser wavelength and θ_t is cone half angle. θ_t here refers to the true angle with the view angle correction applied.

Basically, to quantify the fringe system, the amplitude reflection coefficients for the cone wall were calculated using Fresnel equations [27]:

$$R_p = \frac{\mu \cos i - \cos r}{\mu \cos i + \cos r} \qquad (3.25)$$

$$R_s = \frac{\cos i - \mu \cos r}{\cos i + \mu \cos r} \qquad (3.26)$$

where R_p and R_s (p-polarized and s-polarized) denotes the amplitude reflection coefficients for the light parallel and perpendicular to the plane of incidence. The angle of incidence is $i=(90-\theta_t)$ and $\sin r = \sin i/\mu$. Equations (3.25) and (3.26) were evaluated using a real value for the refractive index of Lexan polycarbonate of $\mu = 1.463$ at 157.4nm wavelength [28]. The incident laser beam was assumed to be unpolarized i.e. to have equal components of s and p-polarised radiation.

From the schematic diagram (Figure 3.40) the sum of incident and reflected fields for s-polarized and p-polarized radiation is given by [29]:

$$E_s = \frac{\exp - i(kx\sin\delta\phi + kz\cos\delta\phi)}{\sqrt{2}} + \frac{R_s\sqrt{\cos(2\theta_t - \delta\phi)}\sqrt{I_x}\,\exp - i(kx\sin[2\theta_t - \delta\phi] + kz\cos[2\theta_t - \delta\phi])}{\sqrt{2}} \qquad (3.27)$$

$$E_p = \begin{pmatrix} \frac{1}{\sqrt{2}} \\ 0 \end{pmatrix} \exp - i(kx\sin\delta\phi + kz\cos\delta\phi) + \begin{pmatrix} R_p\cos(2\theta_t - \delta\phi)\sqrt{I_x}/\sqrt{2} \\ R_p\sin(2\theta_t - \delta\phi)\sqrt{I_x}/\sqrt{2} \end{pmatrix} \exp - i(kx\sin[2\theta_t - \delta\phi] + kz\cos[2\theta_t - \delta\phi]) \qquad (3.28)$$

The sum of the incident and reflected fields in equations 3.27 and 3.28 is based on a plane wave description as in Figure 3.40:

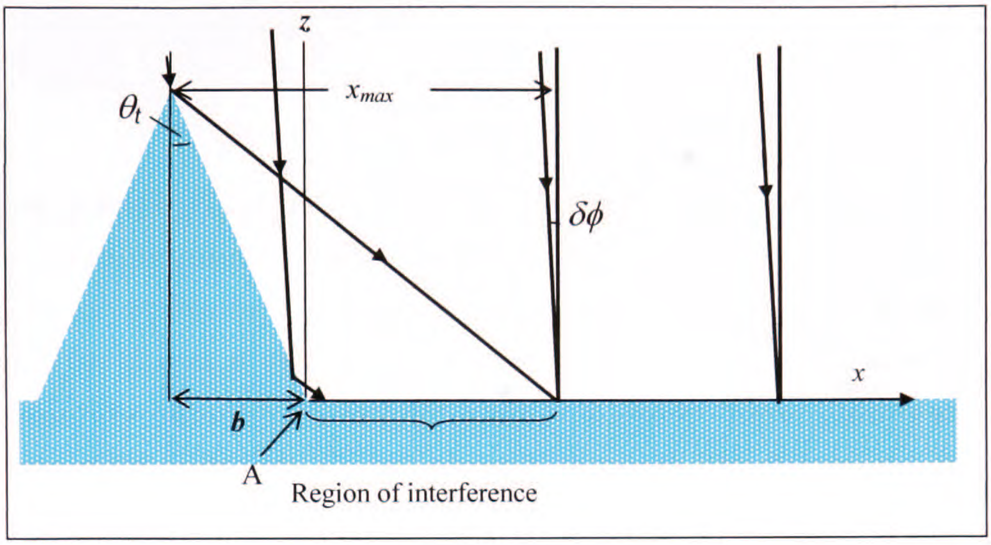

Figure 3.40: Schematic diagram showing region of interference of the incident light with that reflected from the cone wall.

A correction factor is included in these expressions to account for the irradiance reduction at x produced by expansion of the reflected beam from the cone wall. The irradiance reduction can be written as:

$$I_x = \frac{(b - x\cos 2\theta_t)\cos[2\theta_t - \delta\phi]}{(x+b)} \tag{3.29}$$

where b is the radius of the cone base. The incident beam is nominally perpendicular to the surface with a small but finite spread of angles, $\delta\varphi$, with respect to z axis (Figure 3.40) to allow the beam divergence to be taken in account.

The fluence F is given by the product of irradiance and pulse duration and hence proportional to the scalar product [29]:

$$F_{s,p} \propto E_{s,p} \cdot \overline{E_{s,p}} \tag{3.30}$$

For finite spatial coherence $F_{s,p}$ was integrated over $\Delta\varphi$, the full divergence angle of the laser, with the simplifying assumptions that the source was spatially incoherent and had a uniform irradiance distribution:

$$F_{full,s,p} = \int_{-\Delta\phi/2}^{\Delta\phi/2} F_{s,p} \frac{d\delta\phi}{\Delta\phi} \qquad (3.31)$$

The top view scanning electron microscopy image (Figure 3.36), shows the fringe system is limited in its radial extent. The maximum size is defined by reflection from the tip of the cone and under multiple pulse exposure the cone height and base radius progressively increase and the location of fringe maxima moves. Assuming the cone height increases at uniform rate from pulse-to-pulse and that a simple log-linear fluence dependence with effective absorption coefficient, α_{eff}, and threshold fluence F_T, describes the etch rate per pulse, the removed depth of surface d_m for m pulses is [29]:

$$d_m = \sum_{n=1}^{m} \frac{1}{\alpha_{eff}} \ln[F_{tot}(x,n)\gamma]$$

Here, $F_{tot}(x,n) = F_{full,s}(x + b(m) - b(n)) + F_{full,p}(x + b(m) - b(n)) \quad for \quad 0 \le x \le x_{\max}$

$$F_{tot} = 1 \qquad for \quad x > x_{\max} \qquad (3.22)$$

and $x_{max} = b(n)/\cos 2\theta_v$ is the maximum value of x for which the reflected beam overlaps the incident beam on the n^{th} pulse when the cone has a base radius $b(n)$. γ is the ratio of the fluence applied to the threshold fluence for etching, F/F_T.

Figure 3.41 shows the calculated profile in the vicinity of the base of a cone on ablated polycarbonate with m = 100 pulses at an incident fluence of 81mJcm^{-2} with F_T=15mJcm^{-2} (γ=5.4) and α_{eff}= 0.024nm^{-1}. The threshold was set at this value as a compromise between the etch rate value of ~11mJcm^{-2} and that of 25mJcm^{-2} estimated from the cone angle. The effective absorption coefficient, cone angle (θ_f=19.3°) and the pulse number were chosen to produce a cone base radius of 2.5μm to allow comparison with the experimental result shown in Figure 3.34 and 3.36. This value of α_{eff} was chosen to provide a cone depth consistent with experiment. It is some 20% lower than determined from Figure 3.19, but is essentially within the experimental uncertainty.

The etch depth modelled in Figure 3.41 is carried out for divergences of 3mrad and 8mrad as estimated for the narrow and wider dimension of the rectangular output beam of the 157nm laser. In the model, the divergences have been increased by 15x because of the demagnification used in the projection imaging system. The calculated fringes show good quantitative agreement with the experimental results in Figure 3.36, where the fringes in the direction of low spatial coherence extend over a significantly smaller distance than those in orthogonal direction.

Figure 3.42 shows etch profiles in the region adjacent to the base of a cone in polycarbonate calculated at various stages of growth. Figures 3.42 a-d show 10, 20, 50 and 80 applied pulses. The fluence-to-threshold fluence ratio is again $\gamma = 5.4$, effective absorption coefficient $\alpha_{eff} = 0.024\text{nm}^{-1}$ and cone half angle $\theta_t = 19.3°$.

The peak-to-peak depth modulation reaches ~95nm near the base edge for 100 pulses and is not significantly different to that for 10pulses (Figure 3.42a). An interference minimum is placed at $x = 0$ as there is a π phase shift for the reflected s-component, and, with $\mu = 1.463$, when $\theta_t < 34.4°$ for the p-component. This minimum location likely plays a role in [30]the cone development that is not being investigated further here. The fringes have a period of ~ 252nm in good agreement with equation (3.22). The etch depth outside of the reflected beam zone with 100 pulses is ~7031nm, but is deeper by ~ 150 – 195nm at the edge of the cone base (depending on beam divergence) because of the reflected contribution. The radial extent of fringes increases as the cone gets deeper (Figure 3.42) but their amplitude is limited by the spatial shift they experience as the cone grows from pulse-to-pulse. From the modelling results, the maximum fringe amplitude stays approximately constant at ~100nm for 10 -100 pulses (Figures 3.41 and 3.42). The fringe modulation (visibility) falls as x increases i.e. at greater radial extent, both because of the finite spatial coherence of the beam and the reflected beam expansion factor I_x.

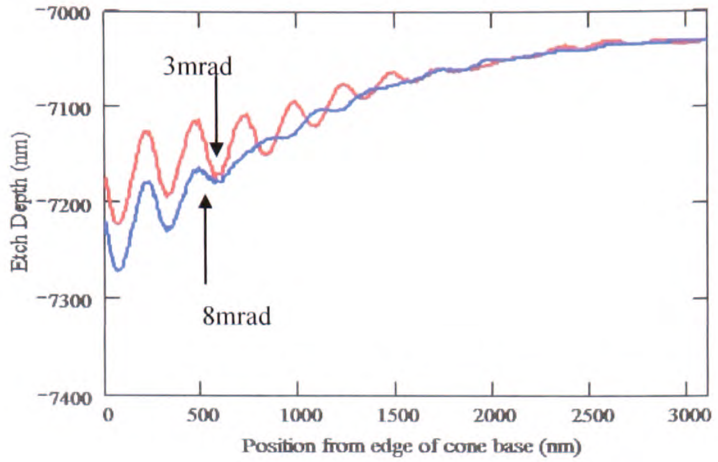

Figure 3.41: Modelled interference fringes produced in the region on the base of the cone in polycarbonate with cone half-angle=0.337rad (19.3°), 100 pulses at 81mJcm^{-2}, F_T=15mJcm^{-2}, μ=1.463.

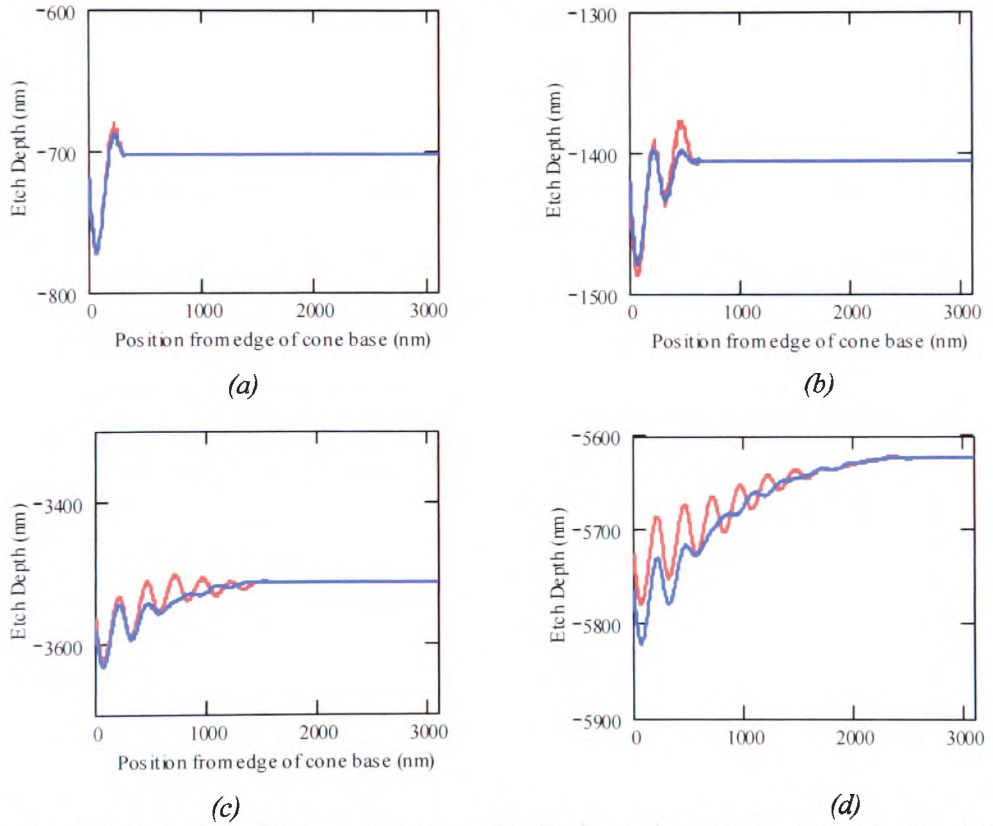

(a) *(b)*

(c) *(d)*

Figure 3.42: Etch profile in region adjacent to the base of a cone in polycarbonate calculated taking account of interference due to reflection from cone wall. Fluence-to-threshold fluence ratio γ = 5.4, effective absorption coefficient k = 0.024nm^{-1} and cone half-apex angle of 19.3°. Development of interference as etching proceeds is seen for;

(a) 10 pulses, cone base radius = 246nm, (b) 20 pulses, cone base radius = 492nm (c) 50 pulses, cone base radius = 1230nm (d) 80 pulses, cone base radius = 1968nm.

The etch-depth curves in Figures 3.41 and 3.42 are for intrinsic beam divergences of 3mrad and 8mrad as estimated for the narrow and wider dimension respectively of the rectangular output beam of the 157nm laser. In the simulation these divergences have been increased by 15× because of the projection image demagnification factor of the system. The range over which fringe visibility is maintained is lower for the larger divergence as the corresponding spatial coherence width is reduced. This is borne out by the experimental results in Figures 3.36a and b, where the fringes in the direction of low spatial coherence are seen to extend over a considerably smaller distance than those in the orthogonal direction.

In the low coherence direction an estimate of the spatial coherence width l can be made from the observation that fringes in Figure 3.36 persist out to $x_i \sim$ 800 - 900nm from the cone edge. The direct and reflected rays that meet at this limiting point are spaced laterally by $w = 2x_i\cos^2\theta_t$ giving $w \approx$ 1.43 - 1.6μm for a cone half angle $\theta_t = 19.3^\circ$. Multiplying this by the image reduction factor of 15 the spatial coherence width in the wider dimension of the 157nm laser beam is $l \approx$ 21 - 24μm. This is consistent with a value of $l = \lambda/\Delta\phi \approx 20\mu m$ based on the full-angle divergence of $\Delta\phi$ = 8mrad. For the narrow beam dimension a similar estimate based on the fringes in Figure 3.36 gives a value for spatial coherence of $l \approx 54\mu m$. This is considerably larger because of the lower beam divergence in this direction.

3.5 F_2 Laser Micromachining on Materials

3.5.1 Introduction and applications

Micromachining of polymers is an important field that has both potential in immediate and future applications in diverse areas such as medicine, microelectronic systems and photonics. Lasers have been proven as effective tools in micromachining; enabling high-resolution structures to be defined in a variety of materials [3, 31]

The high quantum energy of 7.9eV of 157nm photons from the F_2 laser makes it a unique source for use in areas such as lithography [31] and micromachining [3]. At this wavelength most polymeric materials exhibit very strong absorption, implying low ablation threshold with the concomitant benefits of reduced thermal loading and minimal thermal damage to the machined surface [2]. These advantages, coupled with a sub-micron spatial resolution capability (resulting from the short laser wavelength), make the use of the VUV laser increasingly attractive as a tool for producing microstructures and modifying material surfaces [2].

To illustrate the micromachining capability of the 157nm F_2 laser, work was carried out on the following polymers; Nylon 66, PMMA and Lexan polycarbonate.

With low spatial coherence excimer lasers patterning can be conveniently implemented by use of contact masks or preferably, non contact projection methods, in which a mask containing the desired pattern is imaged on the surface of the polymer sample as shown in Figure 3.43. The projection technique allows image reduction (with fluence gain) to be built in and avoids mask fouling by the ablation products.

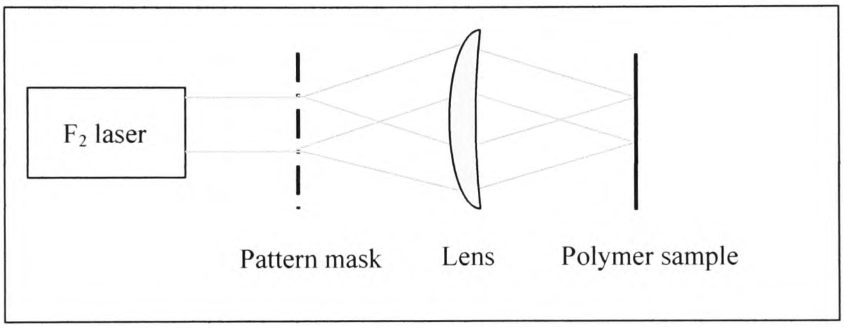

Figure 3.43: Simple projection etching arrangement for non-contact pattern definition by ablation

3.6 Material Considerations

3.6.1 Nylon 66

For the micromachining of Nylon 66 using the 157nm F_2 laser, the projection etching technique was used using a SS316 foil. The mask used was (30mm x 30mm) size and consisted of an array of five circular apertures with a diameter of 0.5mm in a straight line arrangement spaced by 1mm centre to the centre (Figure 3.44). This mask allowed 0.5mm spaced trenches to be etched on the polymer surface with the 157nm F_2 laser using a projection system with a projection system image reduction of 10x.

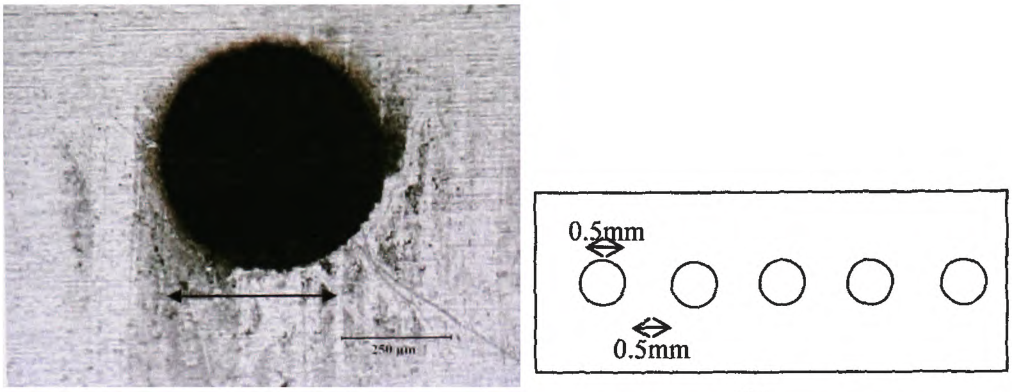

(b)

Figure 3.44: (a) 0.5mm diameter aperture in SS316 foil for the patterning trenches (b) Mask geometry

The trenches were produced on the Nylon 66 sample by traversing the controllable stage by using OWIS software monitored by the computer. Two sets of sample with the trenches of approximately 1µm and 10µm deep were produced. In order to obtain these depths, each site required 1000 and 10000 pulses respectively before the mask was moved on. By using OWIS software, the traverse velocity of the stage can be set based on equation (3.23):

$$v_t = \frac{dR}{N} \tag{3.23}$$

Here *d* is the diameter of one of the apertures; *R* is repetition rate used which is was 20Hz and *N* is number of pulses. From equation (3.23), for the 1µm and 10µm deep trenches, velocities of 0.01 and 0.001mms^{-1} for the stage were set by the computer.

Optical microscopy image (Figure 3.45) shows the trenches machined on the Nylon 66 sample. Along the trenches, 'black features' are clearly seen compared to the non-ablated surface, these 'black features' are believed to be cones as confirmed in earlier work on VUV laser ablation of Nylon [19].

Figure 3.45: Optical microscope image of Nylon 66 after ablation using 157nm laser and projection mask. This picture shows the irradiated area as a series of trenches. This sample has received 1000 pulses at a fluence of 40mJcm^{-2}.

Figure 3.46a shows the trenches formed in Nylon 66 when imaged using the white light interferometer viewed in 3D image; and Figure 3.46b shows profile across X of the trenches showing the depth of the ablated trenches of 0.6-0.8μm.

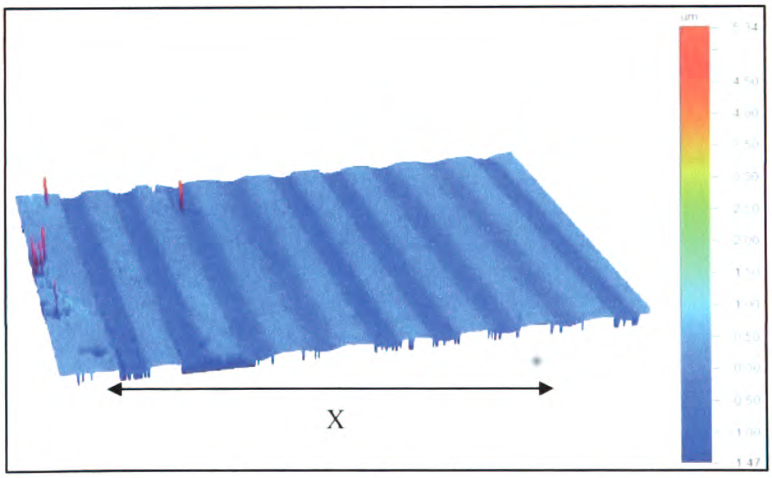

(a)

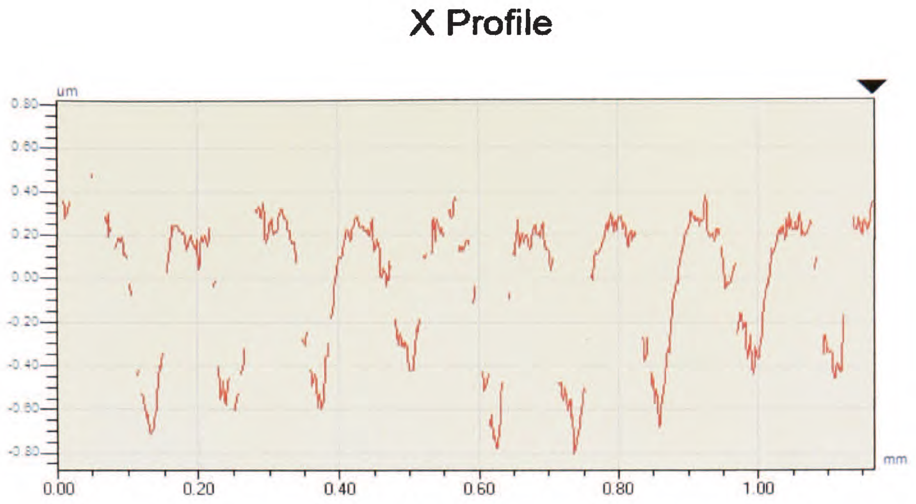

(b)

Figure 3.46: (a) White light interferometer image of trenches formed in Nylon 66 after ablation using the 157nm laser and projection mask (b) X profile result on the ablated Nylon 66 from white light interferometer analysis showing the depth of the ablated trenches to be ~0.6μm to 0.8μm.

Machining of the Nylon 66 with the 157nm F_2 laser has been studied in comparison with using a 10.6μm wavelength from a 10W CO_2 laser [32]. In comparison with CO_2, the 157nm F_2 laser produces well defined trenches indicating the good potential of using the 157nm laser as a source to minimize thermal loading on the surface that is crucial in the various application. The comparative study of surface modification of the Nylon 66 has been conducted in order to vary the parameters driving biocompatibility (surface topography, hydrophobic reactions, hydrophilic reactions and surface chemistry).

3.6.2 Polymethylmethacrylate (PMMA)

The capability for patterning micron scale-size features was tested by exposing PMMA using a metal proximity mask (copper mesh) with 8μm x 8μm hexagonal openings. Hexagonal cross section structures were machined by using contact mask technique at an exposure fluence of ~135mJcm^{-2}, and a laser repetition rate of 20Hz.

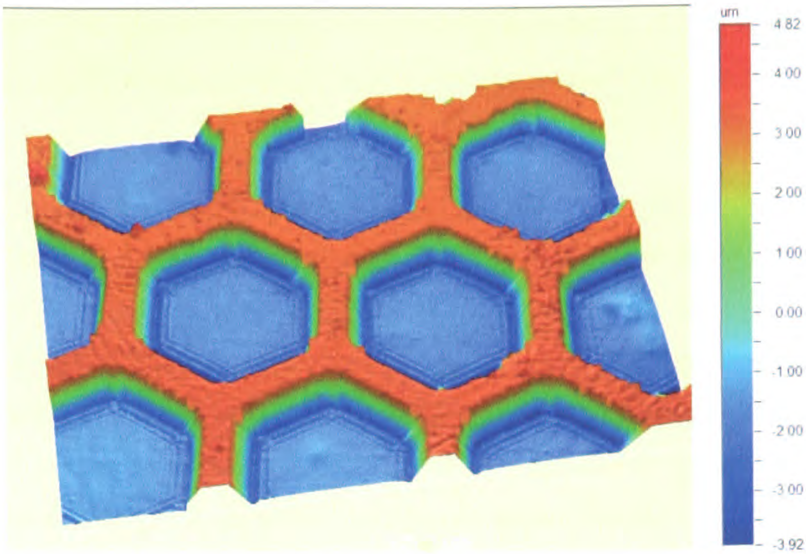

Figure 3.47: An image obtained from the white light interferometer of PMMA ablated at 157nm. A contact masks with an array of hexagonal openings and fluence ~135mJcm^{-2}was used.

Figure 3.47 shows hexagonal features machined into PMMA by the 157nm laser using a fluence of ~135mJcm^{-2} and the contact mask technique. The edges of the craters are well defined and the bottom surfaces are seen to be smooth and are deep compared to the surface indicating using 157nm laser to machine this material leads to very clean results with no evidence of debris or thermal damage for example using other material like glass [2] or insulators [33]. The ablated hexagonal produced with this mask show clearly resolved diffraction sub-structures at the edges of the exposed area. Similar structures effect have been observed on N-BK7 glass patterned with the 157nm F_2 laser using proximity masks and have been exploited for replication and micro-contact printing application [34].

3.6.3 Lexan polycarbonate (PC)

There is a considerable amount of published work on excimer laser ablation of polycarbonate [26, 35] as this material has excellent optical properties and has micro-optical device applications. The sub-micron resolution ablation behaviour of polycarbonate enables so-called Synchronised Image Scanning (SIS) mask design to control the shape and form of 3D features only a few times bigger than the resolution limit of the laser ablation mask projection system [30]. The SIS technique reported by Boehlen *et al* [30] at Exitech uses a 248nm KrF with pulse energy of 400mJ and a maximum repetition rate of 200Hz as the photon source.

In the present work, contact-mask patterning of polycarbonate (PC) ablation was carried out with the F_2 laser, at a fluence of ~100mJcm^{-2} and the focal length lens (*f*=83mm) on the manoeuvrable stage in the evacuable chamber. The thickness of the PC used was 3mm. A mask of in the form of a nickel mesh with 7.5μm x 7.5μm square openings was placed in contact on the polymer surface. A projection imaging of a rectangular aperture was used for illuminated with a reduction of ~15x employed. Here, irradiation in vacuum with 100 laser pulses, repetition rate at 20Hz, produced an array of square features. The SEM and white light interferometer images below show the good potential of the polycarbonate to be machined with the 157nm F_2 laser.

Observation of the ablated area with the optical microscope was unable to reveal anything about the base of the etched holes due to their depth and shadowing caused by a combination of depth and width. The accurate 7.5μm square holes produced can be seen from the scanning electron microscope (SEM) image shown in Figure 3.48 (a-c). Figure 3.48a shows the view at normal incidence; Figure 3.48b shows detail from Figure 3.48a but viewed from 60° on the tilted SEM stage and Figure 3.48c shows one magnified single square machined in the PC. This has a dark base due to the depth of the crater and a faint diffraction pattern can also be seen on the wall of the square. High magnification SEM images of these micro-features Figure 3.48b and c, revealed no evidence of crack formation on or adjacent to the ablation site, a result that is similar to that found when machining of soda lime glass and BK7 by contact and non-contact projection [3] using this laser wavelength.

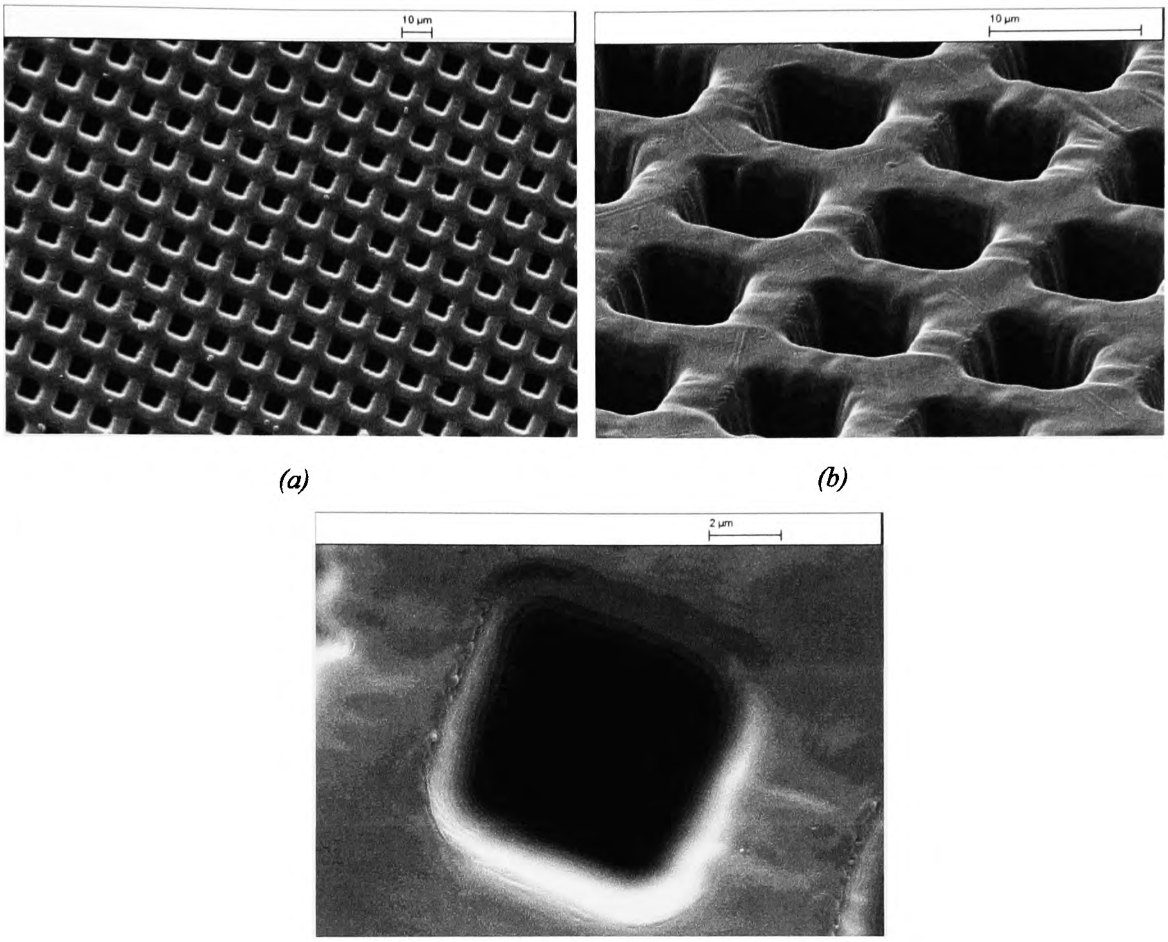

(a) *(b)*

(c)

Figure 3.48(a): Scanning electron microscope (SEM) image showing (a) normal incidence view of array of square micro-features (b) like (a) but viewed at a tilt angle of 60° from SEM stage and (c) magnified view of a single square machined in Lexan polycarbonate. F_2 laser ablation through a proximity metal contact mask with 7.5µm x 7.5µm apertures, 100 pulses at ~100mJcm^{-2}.

References

[1] T.Suganuma, H.Kubo, O.Wakabayashi, H.Mizoguchi, and K.Nakao, Optics Letters 27 (2002) 46.

[2] P.E.Dyer, A.M.Johnson, S.Maswadi, and C.D.Walton, Lasers in Manufacturing (2003) 27.

[3] P.E.Dyer, S.M.Maswadi, C.D.Walton, M.Ersoz, P.D.I.Fletcher, and V.N.Paunov, Applied Physics A 77 (2003) 391.

[4] P.E.Dyer, Laser Ablation:Processes and Applications:"XI International Symposium on gas flow and chemical lasers and high power laser conference" Proceeding SPIE 3092 (1997)

[5] S. E. San, Journal of Radiological Protection 25 (2005) 93.

[6] Karl L.Boehlen, Phil T.Rumsby, Neil Sykes, and C. Lefevre, Proceeding SPIE 62611F (2006)

[7] J.M.N.Ng, A.D.Stroock, and G.M.Whitesides, Electrophoresis 23 (2002) 3461.

[8] D.Erickson, D.Sinton, and D. Li, Lab On A Chip 3 (2003) 141.

[9] J.Liu, B.Cai, J.Zhu, G.Ding, X.Zhao, C.Yang, and D.Chen, Microsystem Technologies 10 (2004) 265.

[10] H. http://www.goodfellow.com/E/Polyamide - Nylon 6.

[11] L.Torrisi, S.Gammino, A.M.Mezzasalma, A.M.Visco, J.Badziak, and P.Parys, Applied Surface Science 227 (2004) 164.

[12] Giulio Croce, Paola D'Agaro, and F. D. Mora, in International Symposium on Advances in Computational Heat Transfer, Norway, 2004.

[13] V.M.Graubner, N.Oskar, L.Thomas, H.Marc, S.Bernard, and W.Alexander, Applied Surface Science 197 (2002) 786.

[14] K.Rubahn, J.Ihlemann, G.Jakopic, A.C.Simonsen, and H.G.Rubahn, Applied Physics A 79 (2004) 1715.

[15] John R, Kazuo Nakamoto, and C. W. Brown, Introductory to raman spectroscopy, Academic Press, 2003.

[16] Sung Chul Bae, Hyunjung Lee, Zhiqun Lin, and S. Granick, Langmuir 21 (2005) 5685.

[17] T.Lippert, Plasma Processes Polymers 2 (2005) 525.

[18] Muralidhar K Ghantasala, Jason P Hayes, E.C.Harvey, and D. K.Sood, Journal of Micromechanics and Microengineering 11 (2001) 133.

[19] P.E.Dyer, S.D.Jenkins, and J.Sidhu, Applied Physics Letters 52 (1988) 1880.

[20] P.E.Dyer, G.A.Oldershaw, and D.Schudel, Journal Physics D:Applied Physics 25 (1992) 323.

[21] Donald L.Singleton, George Paraskevopoulos, and R. S.Irwin, Journal Applied Physics 66 (1989) 3324.

[22] Antonio Miotello, Roger Kelly, Bodil Braren, and C. E.Otis, Applied Physics Letters **61** (1992) 2784.

[23] S.Singh, M.Argument, Y.Y.Tsui, and R.Fedosejevs, Journal of Applied Physics 98 (2005) 1.

[24] Markus Lapezyna and M. Stuke, *Rapid prototype fabrication of smooth microreactor channel system in PMMA by VUV laser ablation at 157nm for applications in genome analysis and biotechnology,* Materials Research Society Symposium proceedings 526 (1998) 143.

[25] P.E.Dyer, S.D.Jenkins, and J.Sidhu, Applied Physics Letters 49 (1986) 453.

[26] B.Hopp, Zs.Bor, E.Homolya, and E.Mihalik, Applied Surface Science 109 (1997) 232.

[27] E. Hecht, Optics, Addison Wesley, *United State of America*, 2002.

[28] H.R.Philipp, D.G.Legrand, H.S.Cole, and Y.S.Liu, Polymer Engineering and Science 27 (1987) 1148.

[29] P.E.Dyer, C.D.Walton, and R.Zakaria, Applied Physics A 95 (2009) 319.

[30] Karl L.Boehlen, Neil Sykes, and C. Lefevre, in SPIE, 2005.

[31] A.K.Bates, M.Rothschild, T.M.Bloomstein, T.H.Fedynyshyn, R.R.Kunz, V.Liberman, and M.Switkes, IBM J.Res & Dev 45 (2001) 605.

[32] D.G.Waugh, J.Lawrence, C.D.Walton, and R.Zakaria, in *Investigation into the efficiacy of CO_2 lasers for modifying the factors influencing biocompatibility of an polymeric biomaterial in comparison with F_2 excimer laser*
(ICALEO 2008), Los Angeles,USA, 2008.
[33] P.E.Dyer and C.D.Walton, Applied Physics A 79 (2004) 721.
[34] P.E.Dyer, J.Mackay, and C.D.Walton, Optics Communications **240** (2004) 391.
[35] M.Devalckenaere, A.Jadin, K.Kolev, and L.D.Laude, Nuclear Instruments and Methods in Physics Research B 151 (1999) 263.

CHAPTER 4

157nm F_2 LASER INTERACTION WITH CR-39 POLYMER

This chapter describes the interaction of the 157nm F_2 laser with the polymer CR-39 allyl-diglycol carbonate (CR-39). It covers studies made of the ablation and surface modification of CR-39 under 157nm laser exposure of pristine surfaces. Some preliminary work has also been carried out on ablating surfaces of CR-39 that had been exposed to alpha particles and subsequently chemically etched to reveal micron-scale size tracks.

4.1 Allyl-diglycol Carbonates (CR-39)

CR-39, or allyl-diglycol carbonate, is a polymer commonly used in the manufacture of eyeglass lenses. It has excellent properties that make it suitable for other applications such as an excellent recorder for nuclear tracks, possessing as it does a high degree of isotropy and uniformity of response. CR-39 will record nuclear tracks with $Z/\beta > 6$ which indicates, for example, that it will easily record all natural α particles at full energy up to 18MeV [1]. CR-39 is transparent in the visible spectrum and almost completely opaque in the ultraviolet range. It has high abrasion resistance, half the density of glass and has an index of refraction that is slightly lower than that of crown glass, making it the most suitable material for eyeglasses and sunglass lenses. CR-39 has a density of $\rho = 1300\text{kgm}^{-3}$ and a specific heat of $c = 2300\text{Jkg}^{-1}\text{K}^{-1}$ [2]. CR-39 is also resistant to most of the solvents and other chemicals, to gamma radiation, to aging and to material fatigue.

In the radiation detection application, pure CR-39 material is exposed to ionizing charged particles (e.g. α-particles). These transfer energy to electrons creating tracks of damaged polymer which are revealed by an etching process in a caustic solution of sodium hydroxide (chemical etching).

CR-39 is made by polymerization of diethyleneglycol bis allylcarbonate (ADC) in presence of diisopropyl peroxydicarbonate (IPP) catalyst. The presence of the allyl groups allows the polymer to form cross-links; thus, it is a thermoset resin. The monomer structure of CR-39 is shown in Figure 4.1. The CR-39 used was 1mm thick and was purchased from Page Mouldings Limited (Pershore, UK).

$$CH_2{=}CH{-}CH_2{-}O{-}CO{-}O{-}CH_2{-}CH_2{-}O{-}CH_2CH_2{-}O{-}CO{-}O{-}CH_2{-}CH{=}CH_2$$

Figure 4.1: Functional group of allyl-diglycol carbonate, CR-39

4.2 Ablation Sites

Ablation experiments were carried out on samples of CR-39, and optical microscopy, scanning electron microscopy and white light interferometer measurements performed to assess its response to the 157nm laser radiation.

A set of optical micrographs obtained for ablation at three fluencies is seen in Figure 4.2. A rectangular object aperture and an image de-magnification of ×10 was used. Unlike for polycarbonate (see Figures 3.17 in Chapter 3), there appears to be little or no visible evidence for re-deposited material being present around the ablation site, even when as many as 500 pulses are applied at relatively high fluence (Figure 4.2c). Debris-free ablation is an attractive property especially in applications such as micro-optics or MEMS fabrication where contamination by films or particulates is undesirable. Although further work is needed to study this in more depth, if confirmed it would point to CR-39 being a useful substrate material for 157nm ablation.

Although Figure 4.2a is essentially clean in the ablation site, the exposures made at higher fluence and with more pulses exhibit dark spots as a result of cones developing on the surface. The cones increase in diameter as the ablation depth increases, Figures 4.2b and c, and in Figure 4.2c, where 500 pulses at 180mJcm^{-2} have been used for ablation, are seen to produce prominent darkened spots on the surface.

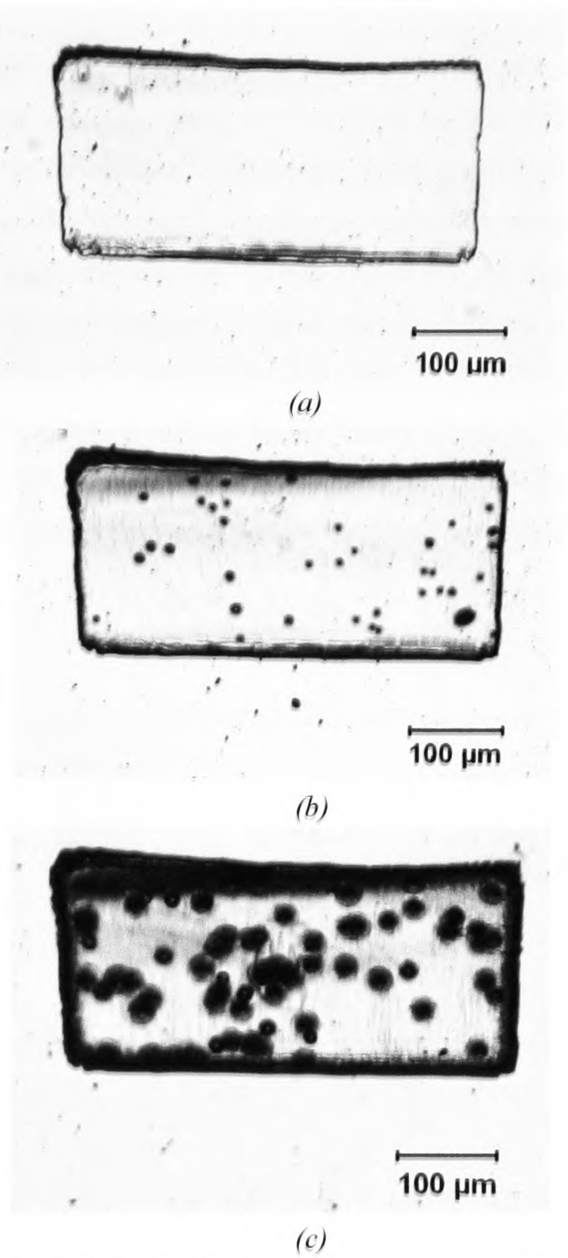

Figure 4.2: Optical microscope images of CR-39 ablated at 157nm (a) 100 pulses at 50mJcm^{-2} (b) 200 pulses at 140mJcm^{-2} (c) 500 pulses at 180mJcm^{-2}

4.3 Etch Rate Analysis

Figure 4.3 shows a plot of the etch rate per pulse versus fluence for CR-39 as derived from the white light interferometer; based on the linear fits for ≥10 pulse exposure the estimated ablation threshold is ~60mJm^{-2}. However, Figure 4.2 shows there is still a small level of etching at a fluence of ~50mJcm^{-2}, and thus the estimated ablation threshold for CR-39 is taken to lie in the range ~50-60mJcm^{-2}. From Figure 4.3, the etch rate per pulse for a single pulse reached ~100nm at ~120mJcm^{-2}, higher than for multiple exposure. The data for 50 pulse exposure gave reasonably consistent values and the gradient of the corresponding line in Figure 4.3, gave an effective absorption coefficient of $\alpha_{eff} \approx 2.9 \times 10^5$ cm^{-1}. This is similar to polycarbonate and indicates CR-39 is a strongly absorbing organic polymer at 157nm. No data relating to the optical constants in the VUV spectral region could be found for this material.

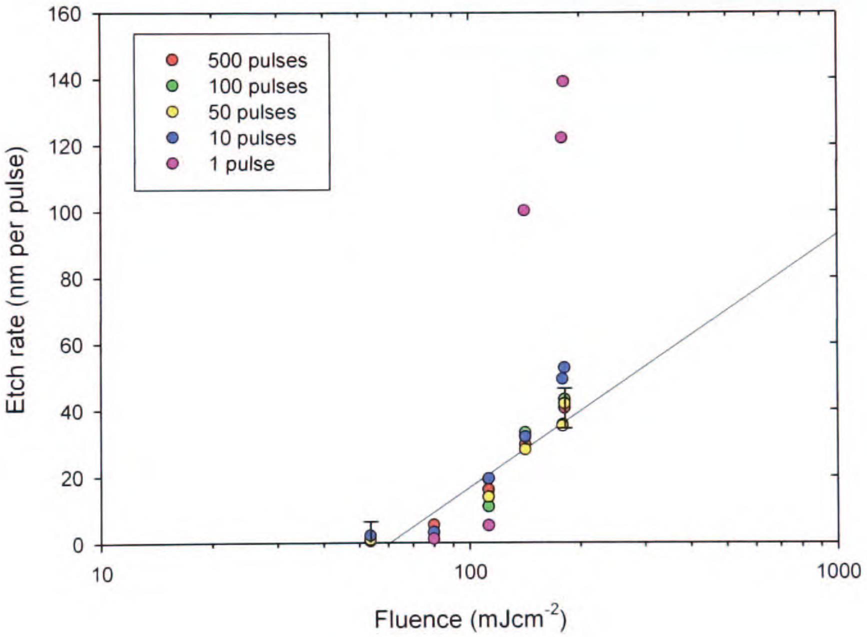

Figure 4.3: Etch rate as a function of fluence for CR-39 polymer using the 157nm laser. Results for the average etch rate per pulse for various numbers of pulses are shown.

4.4 Formation of Cones

For this experiment, clean CR-39 samples (unseeded) were irradiated using 157nm laser radiation over a range of pulse number from a single pulse to thousands of pulses and over a range of fluences from ~50mJcm^{-2} to ~180mJcm^{-2}. The dark spots that were seen under optical microscopy in the previous section were confirmed by scanning electron microscopy to be cones on the CR-39 surface. These had very well-defined structures and, in general, appeared to have even better definition than those on the irradiated polycarbonate surface. In particular, the cones on CR-39 were found to have extremely straight walls and to be extremely sharp at their tips as can be seen from the results shown in Figure 4.4. From the SEM images of the ablation sites, small particles appeared to be on the surface though it is difficult to make out if these reside on the top of the cone as 'initiating' sites.

Figure 4.4a and b show the cones that developed at fluences of 112mJcm^{-2} and 180mJcm^{-2} with 500 pulses. The cones appear to have a similar size and shape at the same fluence. A comparison of Figures 4.4 a and b shows as expected that the cone apex angle is larger at the lower fluence i.e. the full apex angle is ~70° at 112mJcm^{-2} and ~55° at 180mJcm^{-2} when corrected for the 60° viewing angle. It also appears that the cone tips get sharper as the fluence is raised. Exposure the CR-39 surface to a higher number of pulses, Figures 4.4c and d, led to an increase in the areal density of the cones compared to that at lower pulse number, Figures 4.4a and b.

Figure 4.5 shows a group of cones produced with 500 pulses at a fluence of ~80mJcm^{-2}. In this case, the cone full apex angle is 83° corrected for the viewing angle of 60° on the SEM. At this fluence of ~80mJcm^{-2}, the cones have not fully developed and are not as well defined as those seen at higher fluences (Figure 4.5b and c), where the full apex angle is 66° and 51° respectively, again illustrating that the angle is reduced at higher fluence. Here they are fully developed, with sharp tips and very well defined structure.

In Figure 4.5a the ablated surface of this polymer well away from the cone bases is seen to be relatively smooth and devoid from significant debris indicating the good surface quality of this material when ablated with the 157nm laser. The fringes around the bottom of the cones can be clearly seen in Figure 4.6a with 100 pulses at ~60mJcm^{-2} and Figure 4.6b with 100 pulses at ~180mJcm^{-2}.

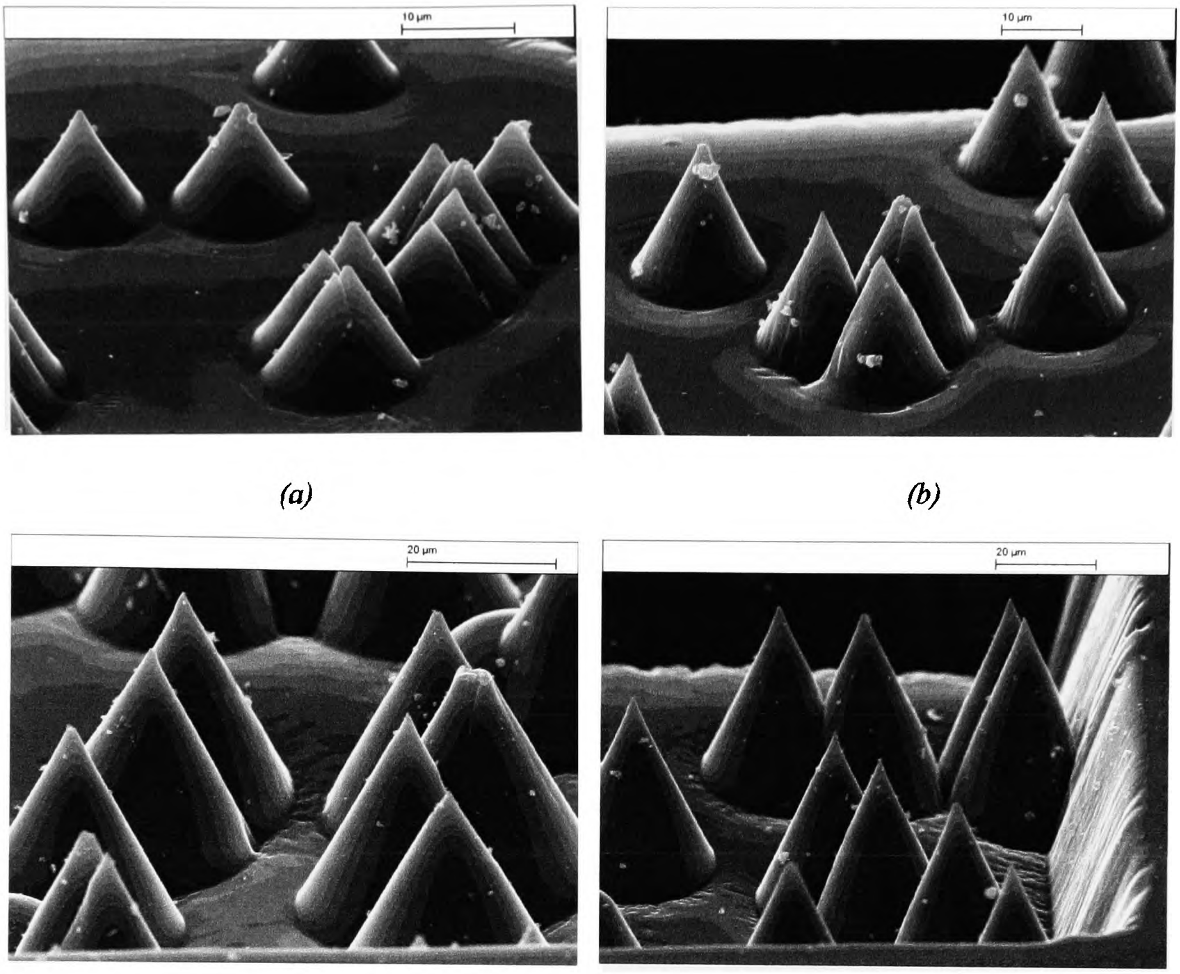

(a) (b)

(c) (d)

Figure 4.4: Examples of cone formation on the CR-39 surface using the 157nm laser (a) 500 pulses at 112mJcm^{-2} (b) 500 pulses at 180mJcm^{-2} (c) 1000 pulses at 142mJcm^{-2} and (d) 1000 pulses at 182mJcm^{-2}.

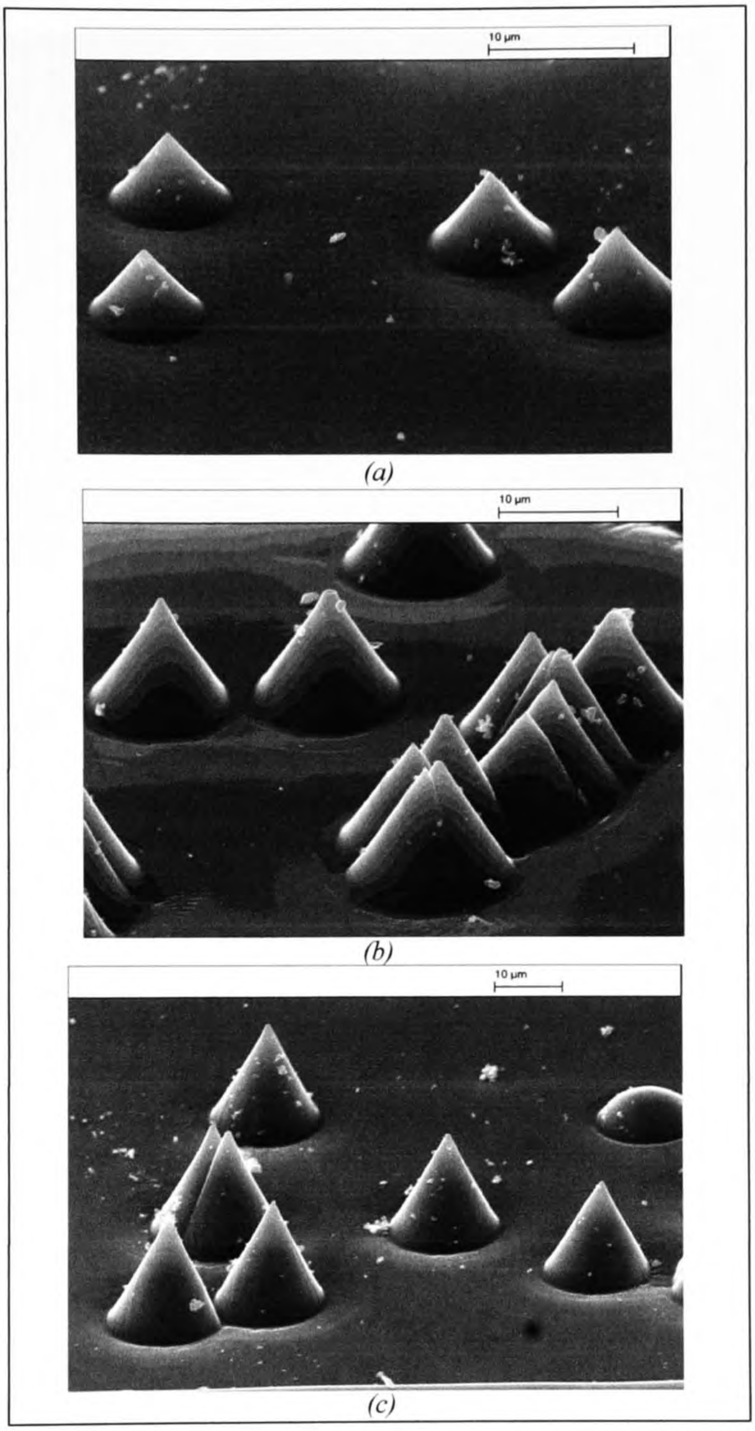

(a)

(b)

(c)

Figure 4.5: Evolution of conical structures developed on CR-39 using the 157nm laser (a) 500 pulses at ~80mJcm^{-2} (b) 500 pulses at ~112mJcm^{-2}(c) 500 pulses at ~140mJcm^{-2}

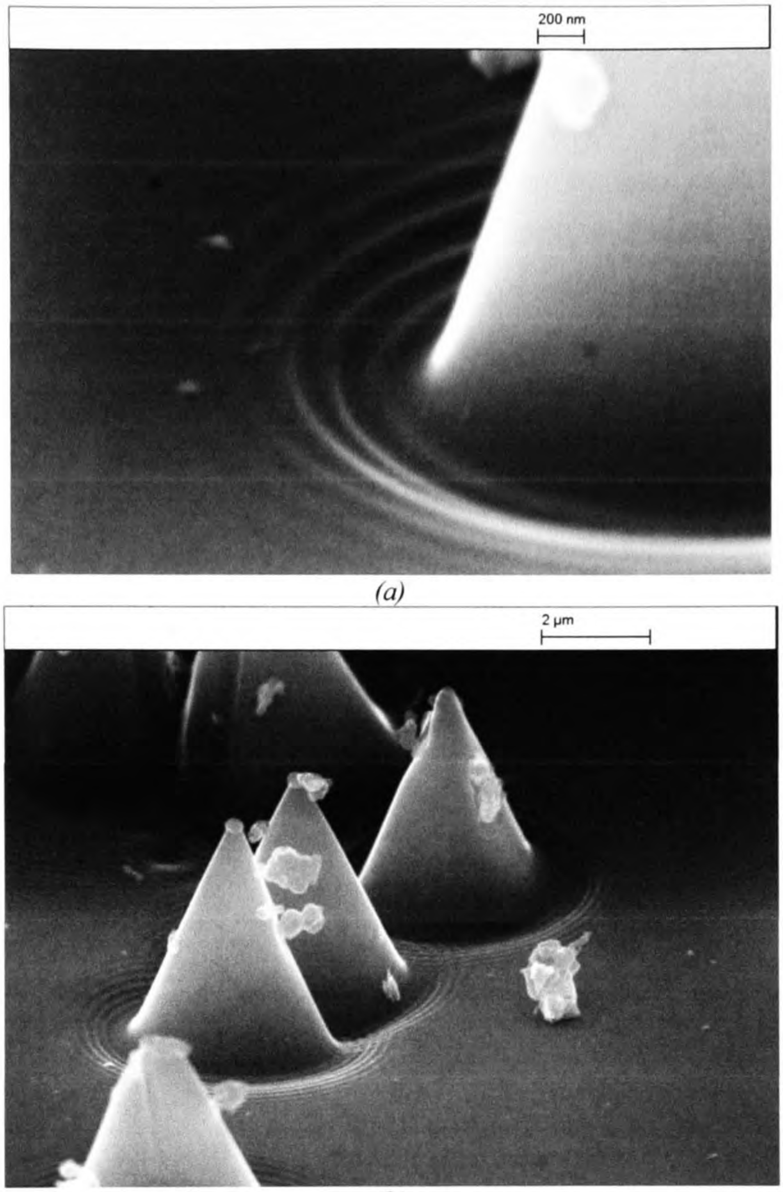

(a)

(b)

Figure 4.6: Fringes seen at the region of the bottom of the cones on CR-39 (a) 100 pulses at ~60mJcm^{-2} and (b) 100 pulses at ~182mJcm^{-2}.

4.5 Ablation Characterisation from the Cones

The ablation threshold of CR-39 was calculated from the apex angle of the cones developed on the irradiated surface. Using equation 3.15 in Chapter 3, a graph of $\psi(\theta_t) = \sin\theta_t$ versus inverse fluence, F^{-1}, should give a straight line with a slope related to the threshold F_T. The measured cone angle was corrected by a similar method to that applied to polycarbonate (expression 3.14) to account for viewing angle, but angle-dependent reflection loss on the cone wall was neglected. Figure 4.7 shows the resulting data. At the higher fluences the cone angles showed quite a small spread in value. The gradient obtained from the slope linearized by fitting a plot of $\psi(\theta)$ versus F^{1} through the origin in Figure 4.7 gives a threshold of 58mJcm^{-2} which seems broadly consistent with that deduced from the etch rate. It is interesting to observe that in previous work on ablating CR-39 using a CO_2 laser at 10.6µm [3], a threshold of 25Jcm^{-2} was found and its was concluded that the ablated surface was free from micro-cracks, vents or chips. This threshold is much higher than obtained here, the difference principally arising from the greater absorption in the VUV spectral region.

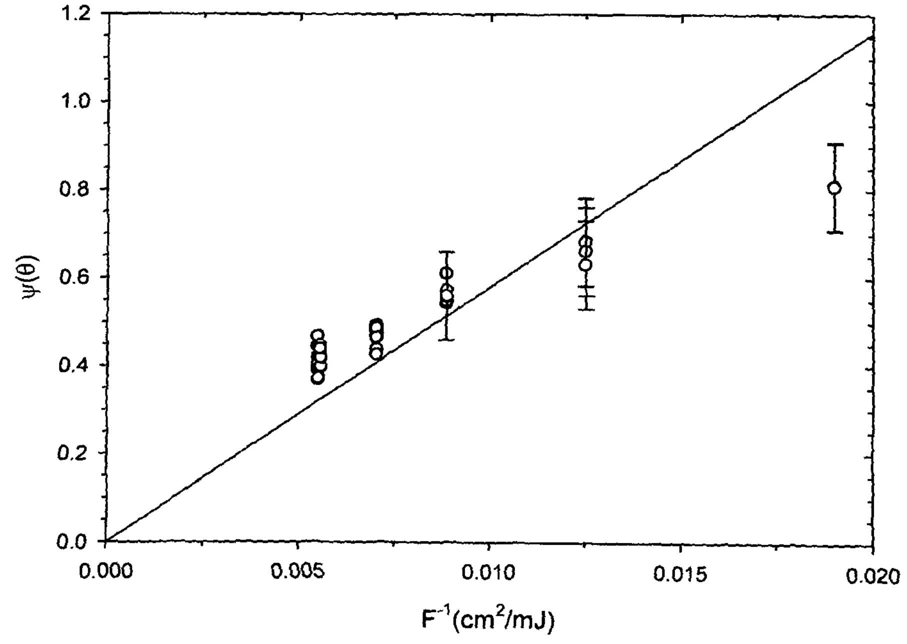

Figure 4.7: Experimental results for $\psi(\theta) = \sin\theta_t$ where θ_t is the true cone half-angle as a function of inverse fluence (F^{-1}), for CR-39 ablated at 157nm. The line is a fit that gives a threshold fluence of 58mJcm^{-2}.

4.6 Track Etching on the CR-39

This section describes preliminary studies of ablating CR-39 that had been pre-exposed to ionizing radiation in the form of alpha particles of a few MeV energy. Radiation tracks were produced by exposing it to a ^{226}Ra source (1.6×10^3 yr half-life) with an activity of 5microcurie. This radium isotope decays principally by alpha emission with energies of 4.87 and 4.61MeV. The alpha particles pass through the material, transfer energy to electrons resulting in a trail of damaged molecules along the particle track. The track can be made visible upon etching with the strong acid or base solution, as the radiation damaged polymer along the particle track etches about 10 times faster [4] than the parent polymer surface.

Irradiation of polymeric material with ionizing particles may cause many types of changes and produce chemical products in the system. It has been reported earlier that irradiation of CR-39 with X-rays produces CO_2 in the polymer [5]. A clearer understanding of bond breaking by ionizing particles and, thus, the changes in the track registration properties of CR-39, may require further analysis of the kinetics of the bond breaking.

According to Tse *et al* [6], when CR-39 is exposed to ionizing radiation, two alkyl radicals and a polycarbonate-ended radical is dissociated into 2,2-oxydiethanol diradical and carbon dioxide during the process of decarboxylation. Irradiation of CR-39 with alpha particles in the presence of oxygen in the air prevents the recombination of free radical pairs and as a result permanent damage is formed along the alpha-particle trajectory. The damage created by the incident particle can be through collision by the particle itself or from the ionizing particles created along its track. A qualitative diagram showing how the tracks are produced by solution etching is sketched in Figure 4.8(a-c). In this diagram the assumption is made [4] that the undamaged surface is eroded away at a velocity V_G orthogonal to the surface. If the etching velocity along the damaged track is V_T, the angle of incidence on the surface must exceed a critical angle θ_c to avoid the track disappearance due to the progressive etching of the normal surface. This critical angle can be express as:

$$\theta_c = \sin^{-1}\left(\frac{V_G}{V_T}\right) \tag{4.1}$$

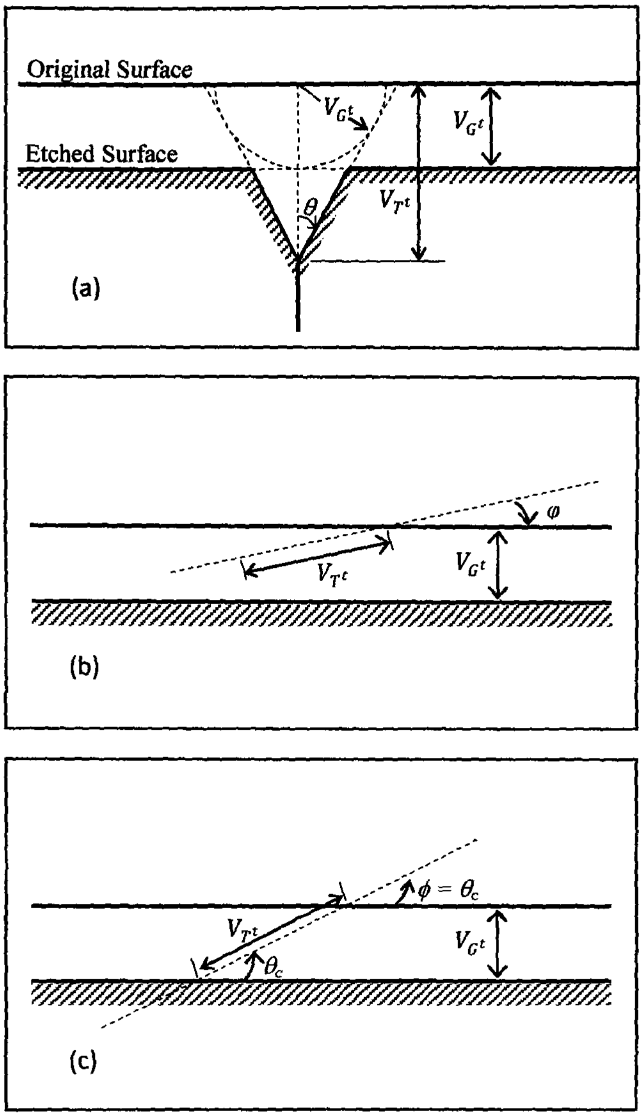

Figure 4.8: (a) Model of track etching in which the normal surface is removed at a velocity V_G by chemical reaction and the damaged track at a velocity V_T, leading to a cone-shaped pit. (b) Track formed at an angle φ less than critical angle (c) The case is where particle enters at the critical angle θ_c, tracks formed at angle greater than θ_c with respect to the surface will be visible after etching [4].

4.6.1 Experimental procedure

Samples of dimensions 25 x 25 mm^2 were cut from the 1mm thick sheet of CR-39 and taken to Castle Hill Hospital where they were exposed to the ^{226}Ra alpha source. As ~5MeV alpha particles penetrate only about 8mm of air the samples were placed directly on the source window and exposed for ~1s, 5s or 10s. One sample remained unexposed in order to provide a control measurement.

Following exposure the samples were etched by placing them in a 6.25N sodium hydroxide (NaOH) solution in a glass vessel that was held in a stirred water bath that maintained the temperature at 70°C. They were held under these conditions for 1.5h and then removed, washed with distilled water and dried in air. According to the literature these etching conditions typically produce tracks ~7μm in diameter and ~150μm long for alpha particles of 4-5MeV energy [7]. Studies were then carried out using optical microscopy and scanning electron microscopy (SEM) on samples that had been subjected to the following treatments.

- Chemical etching but unexposed ('control' sample).
- ~1s exposure to alpha particles and chemically etched.
- 5s exposure to alpha particles and chemically etched.
- 10s exposure to alpha particles and chemically etched.
- Unexposed to alpha particles, chemically etched and irradiated using 157nm laser radiation.
- 10s exposure to alpha particles, chemically etched and treated with 157nm laser radiation.
- 10s exposure to alpha particles, no chemical etching but treated with 157nm laser radiation.

Ablation of the samples was carried out in vacuum (10^{-5}mbar) using the F_2 laser set-up described in Chapter 3 (Section 3.2.2) at a laser repetition rate of ~10Hz with an imaged aperture demagnification of 10x. Following exposure to a given number of pulses, the effects of 157nm laser irradiation were assessed.

4.6.2 Result and discussion

The etch tracks produced by alpha particles in CR-39 are seen in Figure 4.9 (a-d), as revealed by optical microscopy. Figure 4.9a shows the sample unexposed to the alpha particles, and Figures 4.9b and c the samples exposed for 1 and 5 seconds respectively. Though little change in the sample is evident for the 1second case, the 5 second exposure is seen to produce copious tracks in the chemically etched sample. These are revealed by the dark spots in the optical micrograph which are regions where material has been etched away. It is evident from Figure 4.9d that the density of tracks increases further when CR-39 is exposed to alpha particles for 10 seconds. As noted in the previous section, each sample was chemically etched in sodium hydroxide solution under the same conditions.

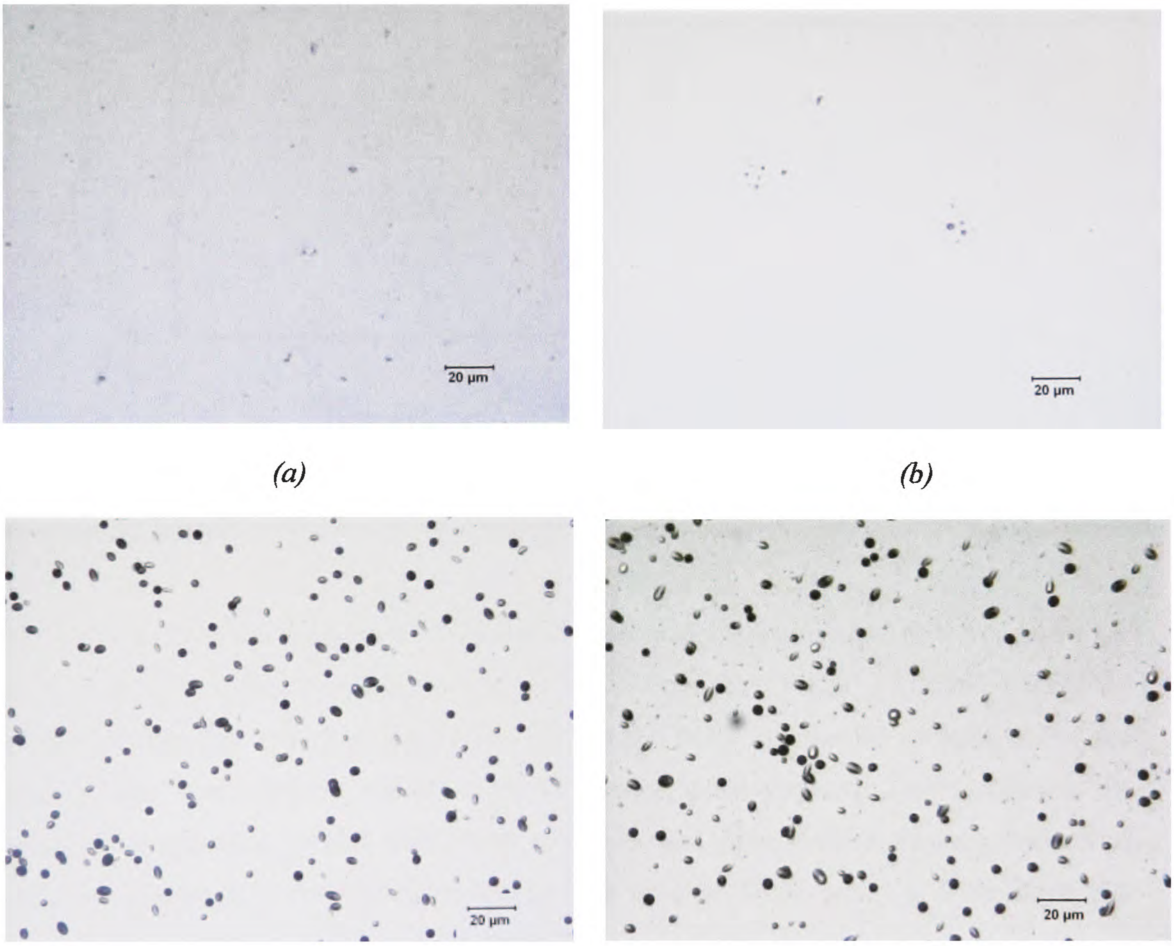

(a) *(b)*

(c) *(d)*

Figure 4.9: Optical microscope images of CR-39 samples exposed to alpha particles and chemically etched with NaOH. (a) unexposed 'control' (b) 1s exposure (c) 5s exposure and (d) 10s exposure. Many etch tracks are seen in (c) and (d).

Figure 4.10 below shows the areal density of the tracks formed as a function of the duration of exposure to the alpha source. The areal density was estimated by counting the number of tracks within a given area of the image (typically over a 100μm x 100μm field). It is evident that longer exposure time significantly increases the track density, with the value reaching approximately 4×10^5 tracks/cm^2 for the 10 second exposure.

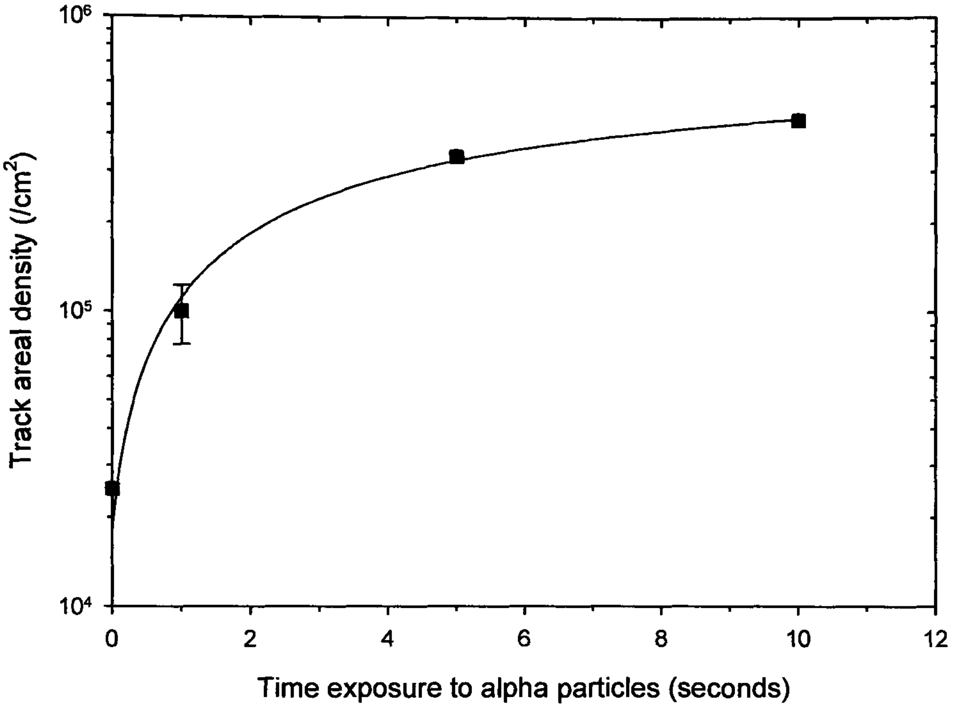

Figure 4.10: Variation of the areal density of tracks with time exposure to alpha particles for CR-39.

The CR-39 samples exposed for 5s and 10s to the alpha source were observed under the SEM in order to obtain a higher resolution view of the tracks. Figure 4.11a and b show the sample surface that was exposed for 5s. The etched holes are sharply defined and at the surface have cross-sections varying from circular to quasi-elliptical. This is because the radiation source emits over a wide range of angles and alpha particle damage tracks thus make various angles with respect to the surface normal. Those entering at an angle that exceeds the critical angle defined by equation 4.1, will be revealed by selective etching. Corresponding views for 10 second exposure, where the density of tracks is higher, are seen in Figure 4.11c and d. Here there is a higher statistical likelihood of particles overlapping, as is borne out by the close clustering of some groups of holes seen in Figure 4.11d. A close inspection of the deep tracks in the polymer reveals these have a conical shape, and also a step-like ring structure on their walls, possibly related to the etching process. The narrower width of the pores in these figures lies in the range 2-5μm and, as expected, they evidently penetrate quite deeply into the surface. An estimate of the maximum hole ellipticity in Figure 4.11c gives a value ~ 1:4, hence suggesting the critical angle is ≤ 14° and according to equation 4.1 that $V_T > 4V_G$.

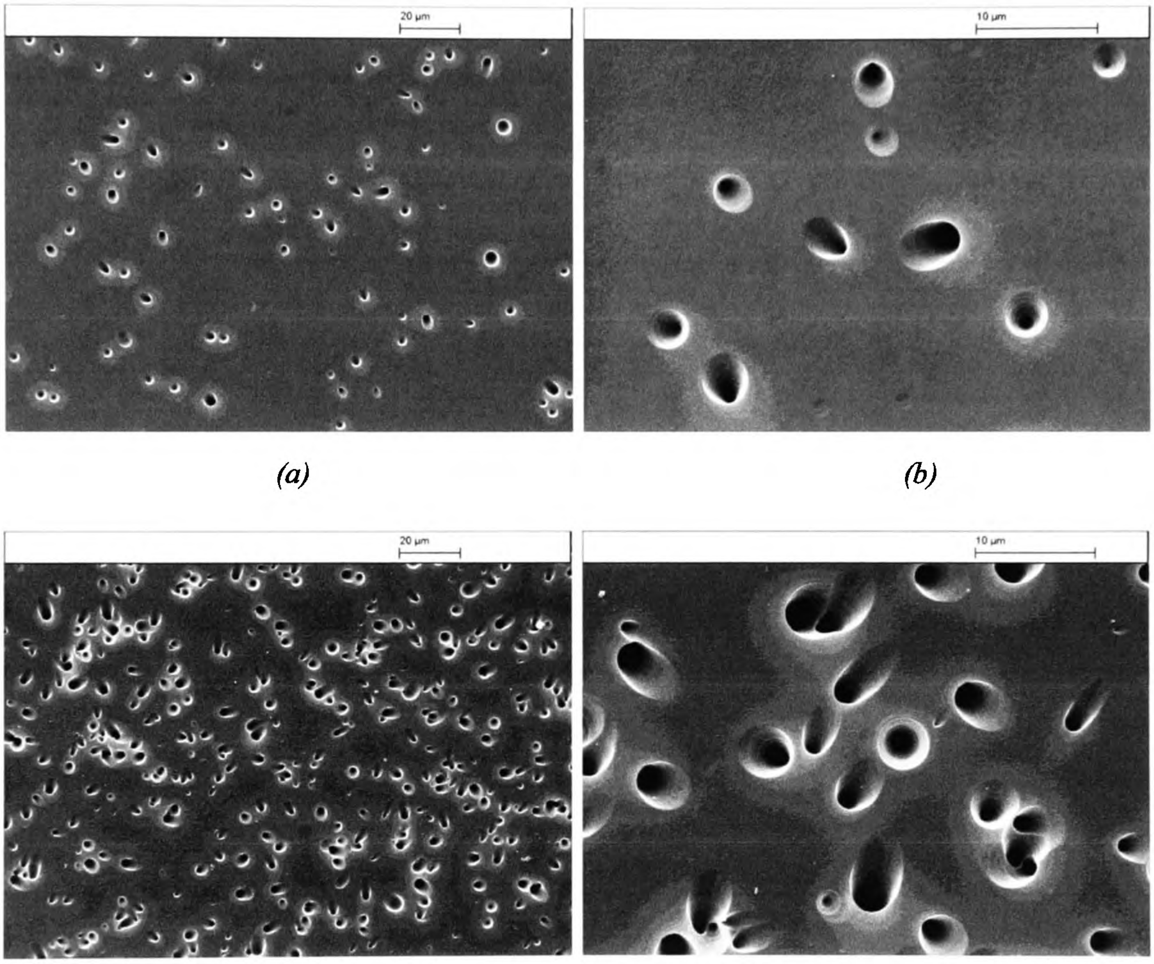

(a) *(b)*

(c) *(d)*

Figure 4.11: SEM images of the tracks etched in CR-39 exposed to the alpha source and chemically etched (a) and (b) 5s exposure, (c) and (d) 10s exposure.

A sample that had been exposed to alpha radiation for 10seconds but not chemically etched was ablated using the 157nm F_2 laser for different numbers of pulses and then viewed under the SEM. Figure 4.12 shows areas ablated at ~100mJcm^{-2} with 100 pulses on the right hand side of the micrograph and 500 pulses on the left hand side. The two irradiated areas overlap slightly, so the somewhat deeper region in the centre of the etch site has received 600 pulses in total. A careful inspection of the surface revealed no evidence for differential laser ablation associated with the alpha particle-induced damage tracks in these non-chemically etched surfaces. This is probably not surprising as the diameter of the radiation damaged zone along a track in the polymer is ~10nm [4] and hence would be unresolved at the 157nm laser wavelength even if there was selective removal. Cones are seen on the surface of the 100 pulse site and larger sized cones and also mounds with rounded tops in the 500 pulse site, but as has been seen earlier, these are also a feature of pristine samples that are neither seeded with particles or subject to radiation exposure.

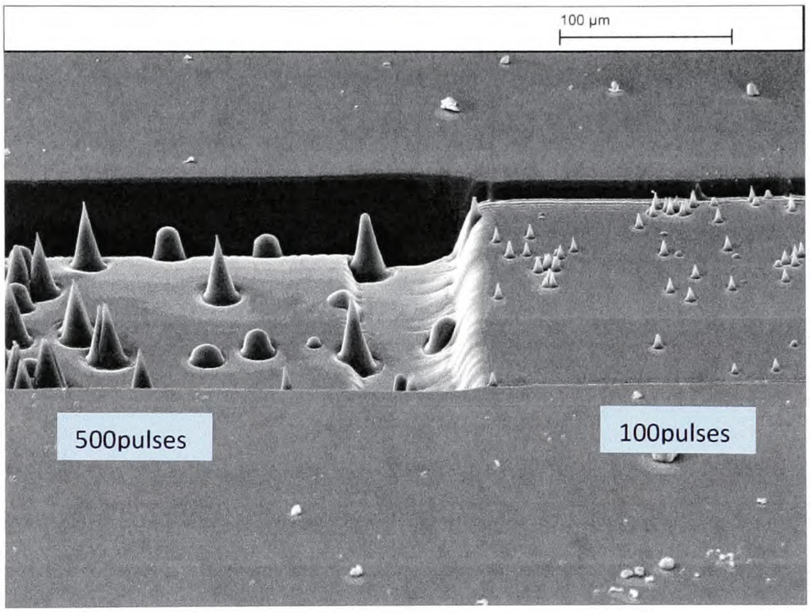

Figure 4.12: SEM images of CR-39 exposed to the alpha source for 10s, but not chemically etched and then ablated using the 157nm laser with 100 and 500 pulses at 100mJcm^{-2}.

Several changes have been observed on the CR-39 samples exposed for 10seconds to the alpha source, chemically etched in sodium hydroxide (NaOH) and then irradiated with 157nm F_2 laser. Results for fluence of ~130mJcm^{-2} with different pulse numbers applied to the surface are shown in Figure 4.13. With a single pulse (Figure 4.13a), the etch tracks can still be seen clearly and appear to have had their edges slightly rounded by the laser exposure. With 10 pulses the ablation site deepens and the tracks appear to be reduced in size and number and there is substantially more edge-smoothing than with just one pulse (Figure

4.13b). In some tracks, cones are starting to develop. In Figure 4.13c where 500 pulses were used tracks are no longer visible in the centre of laser region and a high density of cones has formed on the surface. As seen below the presence of the track-etch sites appears to provide 'nucleation' points for cone growth. Figure 4.14 shows normal incidence SEM views of the ablation area and the region adjacent to this that was not exposed to the laser. Figure 4.14(a) is the result for a single pulse, (b) for 10 pulses and (c) for 500 pulses applied on the CR-39 samples at ~130mJcm^{-2}. With a single pulse there is some rounding of the edge of the holes that is suggestive of softening of the polymer and melt flow having then occurred. With 10 pulses (Figure 4.14b), cones begin to form, some appearing to grow from the cone rim. These cones become much more pronounced with 500 pulses and nearly completely cover the track etch holes leaving only small openings where several cones have begun to coalesce as indicated in Figure 4.14c. It appears that the track etch sites provide nucleation points for the growth of conical structures and as a result the cone coverage of the surface increases significantly. This is seen clearly in on the right hand side of Figure 4.13c where there are many cones distributed across the surface. The reason for this is not fully clear but may stem from residual chemical deposits associated with the chemical etching or simply be a result of the non-uniformity of etching at the step at the rim of the hole. A contribution from radiation damaged polymer appears to be ruled out as this extends only over ~10nm diameter, so will have been stripped away in the early stage of chemical etching and will no longer remain when the surface is ablated.

The capability of producing small chemically etched holes in alpha-exposed CR-39 offers a simple way to explore basic mechanisms in F_2 laser polymer ablation such as resolution limits set by melt-flow on the heated surface and related surface smoothing effects. Though the preliminary work described here has used only one set of chemical etching parameters to generate track etch sites of a few microns size at the surface, it should be possible to produce sub-micron holes by reducing the etching time. This could form a means of studying how surface nano-features evolve under 157nm ablation and how and why cone growth is initiated at these sites. It has been reported that long wavelength lasers exposure can be used to strip away a surface layer of polymer that is hard to etch, speeding the chemical etching process. It would be interesting to see whether 157nm surface ablation prior to alpha-particle exposure can influence the subsequent chemical etching rate.

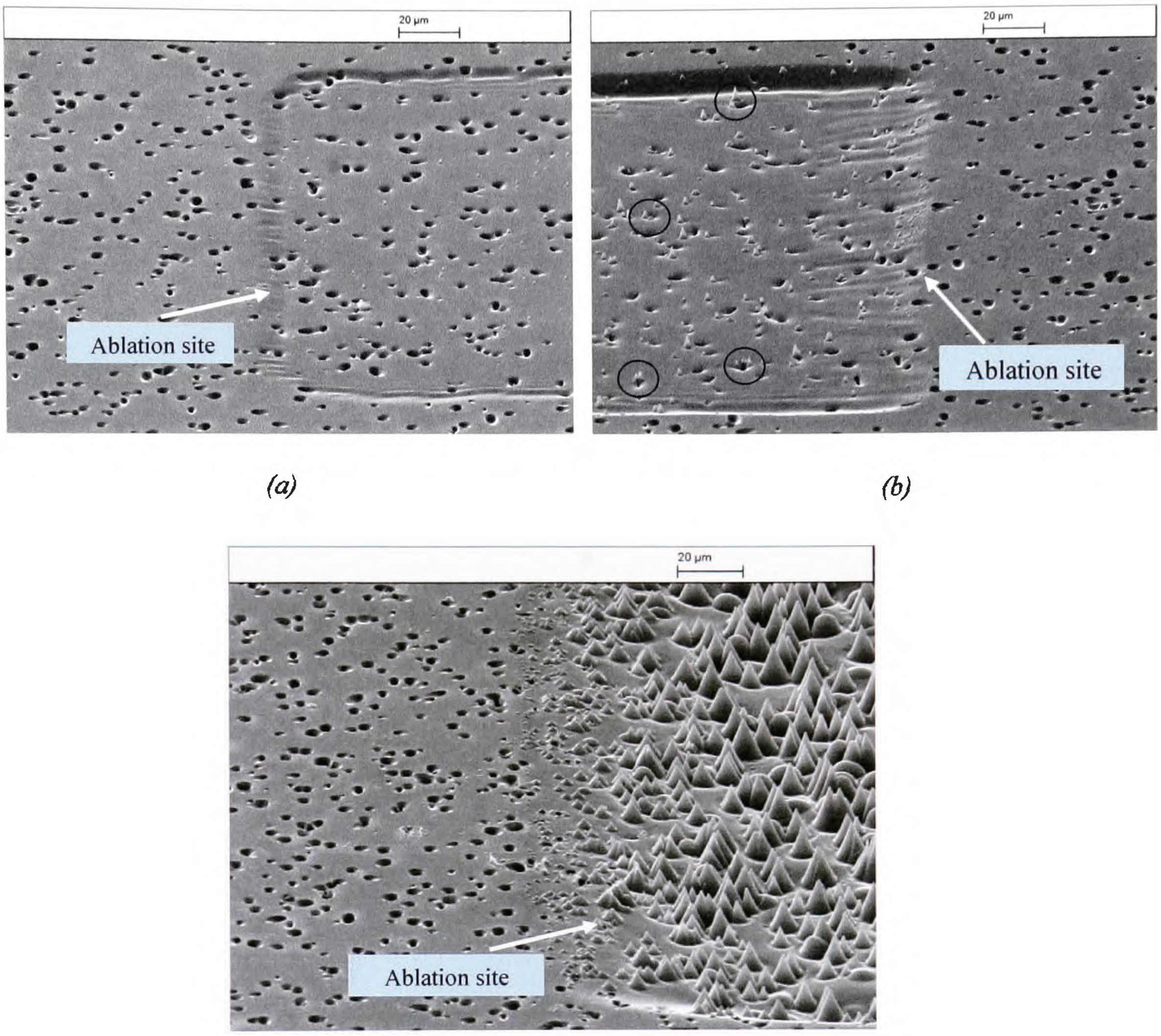

(a) (b)

(c)

Figure 4.13: SEM images on CR-39 exposed to alpha source for 10seconds, chemically etched and then ablated using the 157nm laser at ~130mJcm^{-2} (a) 1 pulse (b) 10 pulses and (c) 500 pulses with indicating arrow showing the ablation area, circles in (b) shows regions where cones have started to develop around the holes.

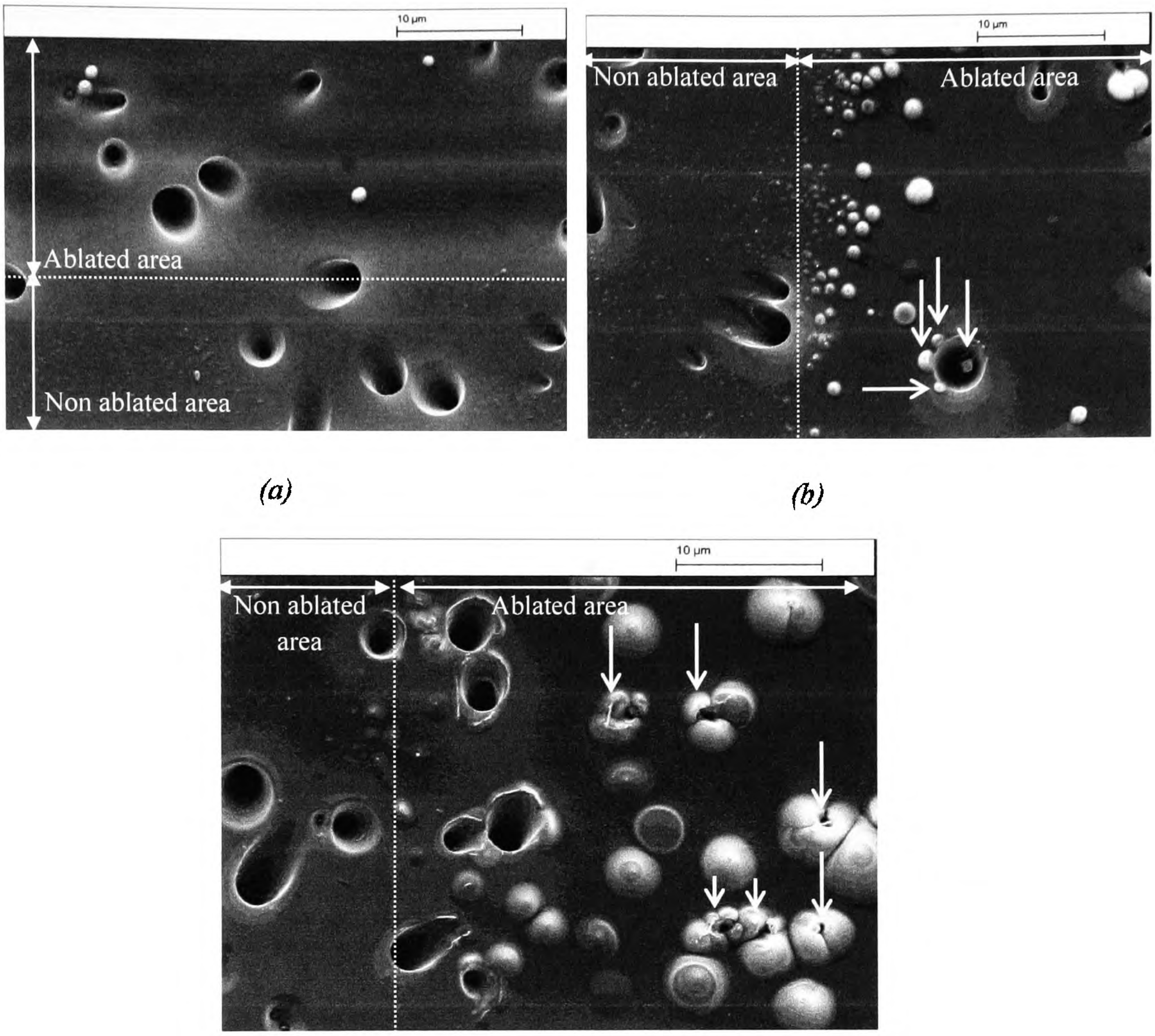

(a)

(b)

(c)

Figure 4.14: SEM images at normal incidence showing the tracks in the ablated and non-ablated region of CR-39. Exposure by 157nm laser with (a) single pulse (b) 10 pulses and (c) 500 pulses, at fluence of 130mJcm^{-2}. Arrows show the cones growing from around the rim a track etch holes.

References

[1] D.L.Henshaw, Physics Technology 13 (1982) 266.

[2] Giulio Croce, Paola D'Agaro, and F. D. Mora, in International Symposium on Advances in Computational Heat Transfer, Norway, 2004.

[3] L. M. Kukreja, Bull.Mater.Sci 11 (1988) 225.

[4] G. F. Knoll, Radiation Detection and Measurement, John Wiley and Sons, 2000.

[5] Mohd Abdul Malek, Abdullah Renreng, and C. S. Chong, Radiation Physics and Chemistry 60 (2001) 601.

[6] K.C.C.Tse, D.Nikezic, and K.N.Yu, Radiation Measurements 43 (2008) S98.

[7] M F Zaki, A Abdel-Naby, and A. A. Morsy, PRAMANA-Journal of physics 69 (2007) 191.

CHAPTER 5

SURFACE QUALITY OF POLYMERS ABLATED WITH THE 157nm F_2 LASER

5.0 Introduction

This chapter will describe theoretical and experimental studies of the surface quality of 157nm F_2 laser ablated polymers. Limitations set by statistical fluctuations in the multimode beam, and by stationary beam non-uniformity i.e. that is fixed from pulse-to-pulse, are explored together with material issues such as debris formation/re-deposition from ablation products where cones appear under F_2 laser exposure. Experimental work on ablating polydimethylsiloxane (PDMS), Lexan polycarbonate (PC) and the polymer CR-39 has been carried out by assessing the quality of the ablated surfaces using a white light interferometer (Wyko NT1100).

Theoretical consideration is given to the fundamental limitations that coherence effects have on the attainable smoothness of an ablated surface [1] i.e. arising from spatially varying statistical fluctuations that occur from pulse-to-pulse with the multi-mode beam, as well as practical aspects related to stationary beam non-uniformity [2]. The magnitude of statistical fluctuations is predicted to be a few percent, with associated roughness increasing as $m^{1/2}$, where m is the number of ablation pulses [1]. Beam characterization through use of VUV excited fluorescent from a glass plate recorded using a couple charge device (CCD) camera, as has been investigated to support this statistical fluctuation work will be described in the next chapter.

5.1 Theoretical Considerations of Ablation Uniformity

5.1.1 Multimode beam fluctuations

The free-running F_2 laser is usually operated with emission linewidths and a resonator Fresnel number that supports a vast number of electromagnetic modes (typically $\sim 10^7$) [1]. Highly multimode emission is attractive for certain applications as the many modes superimpose to produce very good spatial uniformity but with a low degree of coherence, greatly reducing speckle effects. Generally, the modes will have random relative phases on a pulse-to-pulse basis and interference among them can lead to small scale-size fluctuations in the local fluence. The presence of many modes makes possible a statistical argument with which to assess these fluctuations. When the output is averaged across all such mode groups within the lasing linewidth it should approximate to a Gaussian probability distribution for the fluence of the form:

$$dp = \frac{1}{\sigma\sqrt{2\pi}}\exp\left[-\frac{(F-\langle F\rangle)^2}{2\sigma^2}\right]dF \qquad (5.1)$$

Here dp is the probability that the fluence F will lie in the range F to $F+dF$, $<F>$ is the mean fluence (i.e. the long term average) and σ is the standard deviation of the distribution given by $\sigma = <F>\left(\frac{\tau_C}{f\tau_p}\right)^{\frac{1}{2}}$ where τ_p is the laser pulse duration and τ_c is the laser coherence time. For a Lorentzian lineshape, as assumed here, $\tau_C = \frac{1}{\pi\Delta\nu}$ where $\Delta\nu$ is the laser linewidth. If the laser emits a linearly polarized beam then $f=1$ but if the emission is unpolarised $f=2$ as twice as many independent modes makeup the output. This behaviour is confirmed later in the thesis by modelling the incoherent superposition of a large number of Hermite-Gaussian mode groups.

The coherence area A_C determines the transverse spatial extent over which the output beam retains coherence. For a rectangular beam this is given approximately by $A_C = \frac{\lambda^2}{\Delta\phi\Delta\theta}$ where $\Delta\phi$ and $\Delta\theta$ are the full-width beam divergence angles in its wider and narrow dimensions which are referred to as the x and y directions of the laser beam. The coherence fluctuations described by equation 5.1, will thus be uncorrelated and random between different coherence 'patches' in the beam. As an example, taking values of $\Delta\phi$ =2mrad and $\Delta\theta$ = 8mrad for the divergence angles of the F_2 laser gives $A_c \approx 1.5\times10^{-9}\text{m}^2$.

The effect of these fluctuations can now be assessed for material that has an assumed ablation rate per pulse, x, of the form:

$$x = \frac{1}{\alpha_{eff}} \ln\left(\frac{F}{F_T}\right) \tag{5.2}$$

Here α_{eff} is the effective absorption coefficient at the laser wavelength and F_T the fluence at the ablation threshold. Equation 5.2 has been found to be approximately useable for many laser material systems over a limited fluence range and has the advantage of analytical simplicity.

Suppose ablation of the material surface is a result of exposure to m laser pulses at an average fluence of $<F>$. It arises from the equations 5.1 and 5.2 that the ablation depth D will have an uncertainty between different coherence patches that can be determined from:

$$D = \frac{m}{\alpha_{eff}} \ln\left[\frac{<F> \pm \frac{\sigma}{\sqrt{m}}}{F_T}\right] \tag{5.3}$$

as $\frac{\sigma}{\sqrt{m}}$ is the standard error i.e. standard deviation of the mean. Assuming $<F>$ is large compared to $\frac{\sigma}{\sqrt{m}}$, equation (5.3) can be expanded as:

$$D = <D> \pm \frac{\sqrt{m}\sigma}{\alpha_{eff} <F>} \tag{5.4}$$

where $<D> = \frac{m}{\alpha_{eff}} \ln(\frac{F}{<F_T>})$ is the mean depth of material removed from the surface by ablation using m laser pulses. Equation 5.4 shows that the spatially varying fluence leads to an uncertainty in the ablation depth. Although the *relative* uncertainty in the depth, given by $\frac{\sqrt{m}\sigma}{\alpha_{eff} < F >< D >} = \frac{\sigma}{< F > \sqrt{m} \ln(F / F_T)}$, decreases with number of pulses as $\frac{1}{\sqrt{m}}$, a residual roughness is imposed on the surface of magnitude $r = \frac{\sqrt{m}\sigma}{\alpha_{eff} < F >}$ that increases as $\sqrt{m}$.

Evaluating σ in equation 5.1 using an estimate for the line width of ~8.8 GHz (0.82 pm) [3] for the main 157.63 nm transition of the F_2 laser and taking $\tau_p = 11 ns$, we obtain estimates of $\frac{\sigma}{< F >}$ = 5.7% for a polarised beam (f=1) and 4% for an unpolarised beam (f= 2). For the F_2 laser these 'mode speckle' fluctuations are predicted to be significantly larger than, for example, the free-running ArF or KrF laser because the latter have larger linewidths resulting in there being more independent modes involved in the spatial averaging.

If the surface roughness factor, r, is expressed in terms of $<D>$, we obtain,

$$r = \sqrt{\left(\frac{< D >}{\alpha_{eff} \ln\{\frac{< F >}{F_T}\}} \right)} \frac{\sigma}{< F >} \tag{5.5}$$

This indicates that when it is desirable to minimise roughness on the ablated surface, it is advantageous to have a high absorption coefficient, and to work well above the ablation threshold. In this respect the F_2 laser has an evident benefit for processing polymers, glasses and indeed, other insulator materials, as α_{eff} can be large in the VUV with correspondingly low thresholds, permitting 'well above threshold' ablation. Even so the roughness induced by 'mode speckle' can be important.

5.1.2 Stationary Beam Non-Uniformity

It is of interest to examine how stationary beam non-uniformity effects the ablation depth i.e. variations in $<F>$ that remain unchanged from pulse-to-pulse. Consider that the 157nm laser beam is nominally flat-topped and has a residual fluence variation of $|dF| \lll < F >$ superimposed on the profile. Then, from equation 5.2, we find that δD, the difference in the depth of ablated material when exposed to *m* pulse at fluence $<F>$ and at $<F>+dF$, is:

$$\delta D = \frac{mdF}{< F > \alpha_{eff}} = \frac{D(\frac{dF}{< F >})}{\ln(\frac{< F >}{F_T})} \qquad (5.6)$$

Equation 5.6 shows that the variation in depth or roughness of the ablated surface is now linearly dependent on the ablated depth D but is independent of the value α_{eff}, which differs from equation 5.5. For low roughness it is still, however, advantageous to work at high fluence above the ablation threshold.

Stationary beam non-uniformity even at a level as low as 1% can evidently produce significant difference in ablation depth and it is likely that random variation of this magnitude could easily be introduced by imperfection in the beam delivery components. As an example, an ablation depth of $D = 20\mu m$ produced with $<F>/F_T = 3$ and stationary non-uniformity of $dF/<F> = 0.01$ (1%) is predicted to lead to $\delta D = 180nm$. This depth uncertainty could present a significant problem if fabricating precision a optical surface by ablation and points to the need for good beam homogenisation in applications work. Stationary non uniformity may also appear from coherence effects in contact and projection imaging where diffraction patterns with significant fluence modulation are produced on the material surface [4]. This can be particularly problematic for the F_2 laser because of its relatively narrow line width and long coherence length.

In order to make quantitative characterisation of roughness, white light interferometry has been used to analyze the surface of ablated polymer samples, in terms of the average roughness *Ra* and the RMS roughness *Rq*. The surface roughness average is illustrated in Figure 5.1 where the parameter contains the variation in height from point to point on the surface, where the results can be elaborated further in terms of a statistical distribution that characterises the average roughness on the measured surface.

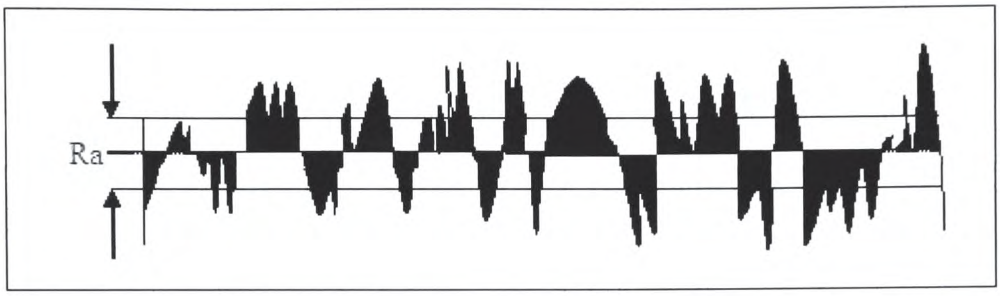

Figure 5.1: Derivation of the average roughness Ra on the measured surface.

The Gaussian distribution can be considered from the height *r(x)* at a point *x* and the probability density *p(r)* of a distribution of heights shown in Figure 5.2 below. The probability of a height lying in the *r* and *r+dr* range is *p(r)dr*, and the cumulative probability that a height will be below some level *h* defined as [5]:

$$P(h) = \int_{-\infty}^{h} p(r)dr \tag{5.7}$$

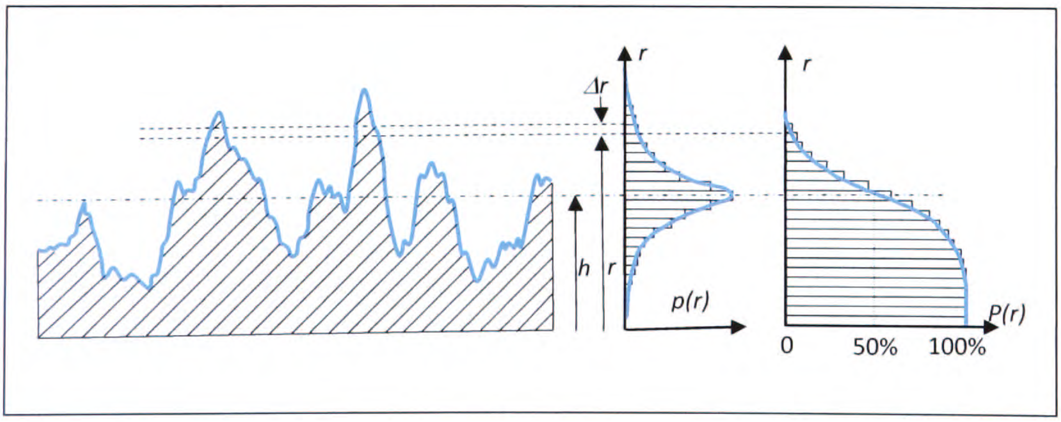

Figure 5.2: Profile height distribution p(r) and cumulative height distribution P(r)

The distribution *p(r)*, where the height of the mean line of the profile, can be characterised by its central moments of the profile:

$$\mu_n = \int_{-\infty}^{\infty} r^n p(r) dr \tag{5.8}$$

The variance *v* is in units of (height) squared; this is related to the square of the standard deviation of the distribution i.e. $v = \sigma^2$, and *Rq* is formally identical to the RMS roughness. Many surfaces have more or less symmetrical height distributions which can be represented as the Gaussian distribution:

$$p(r) = \left(\frac{\sigma}{\sqrt{2\pi}}\right) \exp\left[-\left(\frac{r^2}{2\sigma^2}\right)\right] \tag{5.9}$$

5.2 Experimental Techniques

Experiments on the surface quality of laser ablation were carried out using the Lambda Physik LPF 202 F_2 laser producing output energy of up to 35mJ at a pulse repetition rate ≤20Hz. Samples of PDMS, PC and CR-39 were used as ablation targets. The target samples were mounted on a stepper motor driven stage that allowed precision adjustment of their position. Laser interaction took place in the vacuum chamber with the pressure of $1\text{x}10^{-5}$ mbar. The chamber was connected to the laser by a 2m long beam delivery tube. The surfaces of the ablated samples were investigated using both scanning electron microscopy (SEM) and the white light interferometer to provide information on roughness.

5.2.1 White Light Interferometer Analysis of the Ablated Site

The use of the white light interferometer not only allowed for precise depth measurements to be made but also the profile of the etched surface could be determined. Generally, white light interferometer profilers provide three-dimensional measurements that represent undulations on the ablated surfaces. It is possible to use such measurements to determine various properties of interest such mean roughness and roughness distributions for ablated material surfaces.

The white light interferometer could be used to obtain information on the physical smoothness of the ablated polymer surface. It provided, for example, *Rq* the RMS surface roughness and Ra, the average roughness. The latter is defined by:

$$Ra = \int_0^L |r(x)| \frac{dx}{L} \tag{5.10}$$

The root-mean-square average of the surface measurement, *Rq* is defined as:

$$Rq = \sqrt{\int_0^L r^2(x) \frac{dx}{L}} \tag{5.11}$$

where *r(x)* is the deviation from the mean surface and *L* is some length measure along the surface.

5.2.2 PDMS

Figure 5.3 shows the image obtained from the white light interferometer crossing horizontally and vertically on the ablated area for the case where just 5 pulse exposures is used and the average depth removed is 0.6μm at ~100mJcm^{-2}. The profile in Figure 5.4 shows the ablated surface is relatively smooth and ablative removal is confined to a shallow skin on the surface, as indicated by the height, magnitude and spacing of the peaks and valleys.

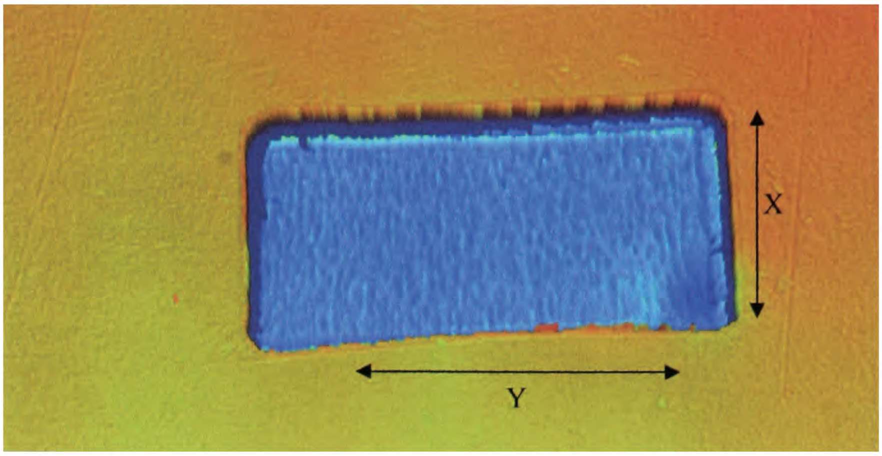

Figure 5.3: White light interferometer image of 5 pulses with arrows indicating the X and Y profile across the ablation site. X and Y are defined in Figure 5.4.

The white light interferometer is seen to provide excellent depth resolution and can be used to investigate not only removal but also material 'swelling' or reposition around the ablation site. The graph in Figure 5.4 shows the surface profile for 5 pulses at ~1000 $mJcm^{-2}$ fluence where the depth is 0.6μm, where it can be noted that the base relief of the irradiated area is not smooth but has significant undulations. These irregularities may well be a product from the way the PDMS material ablated, as opposed to the profile of the laser beam. As a result of the experiments where 100 pulses (Figure 5.5e) per sites were delivered, the increase in depth of the ablated sites also resulted in average roughness increasing. This may possibly have occurred due to the modifying of the molecular structure of the material. Figure 5.5 shows 3D images, produced from the white light interferometer data, where undulations on the base of the etch crater can be seen. Figure 5.5a shows the ablation site for a single pulse, (b) for 5 pulses, (c) for 10 pulses, (d) for 50 pulses and (e) for 100 pulses. From the images shown below, the depth of the ablation holes clearly increases with number of exposure pulses at 157nm.

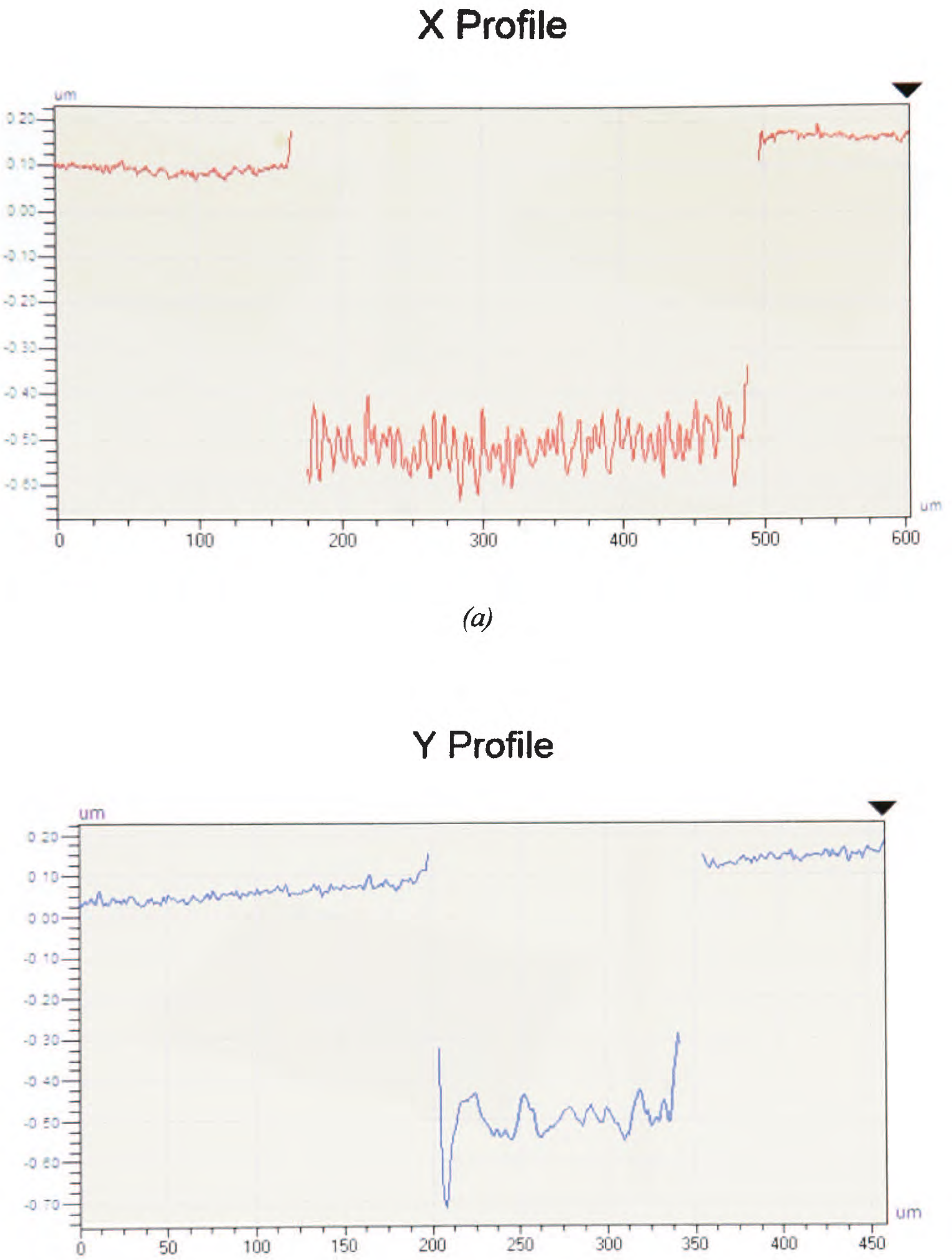

(a)

(b)

Figure 5.4: Etch depth profile along x-and y-direction of ablation site obtained using white light interferometer for PDMS. The average depth removed is ~0.6μm, after irradiation with 5 pulses from the 157nm laser at fluence of ~1000mJcm^{-2}.

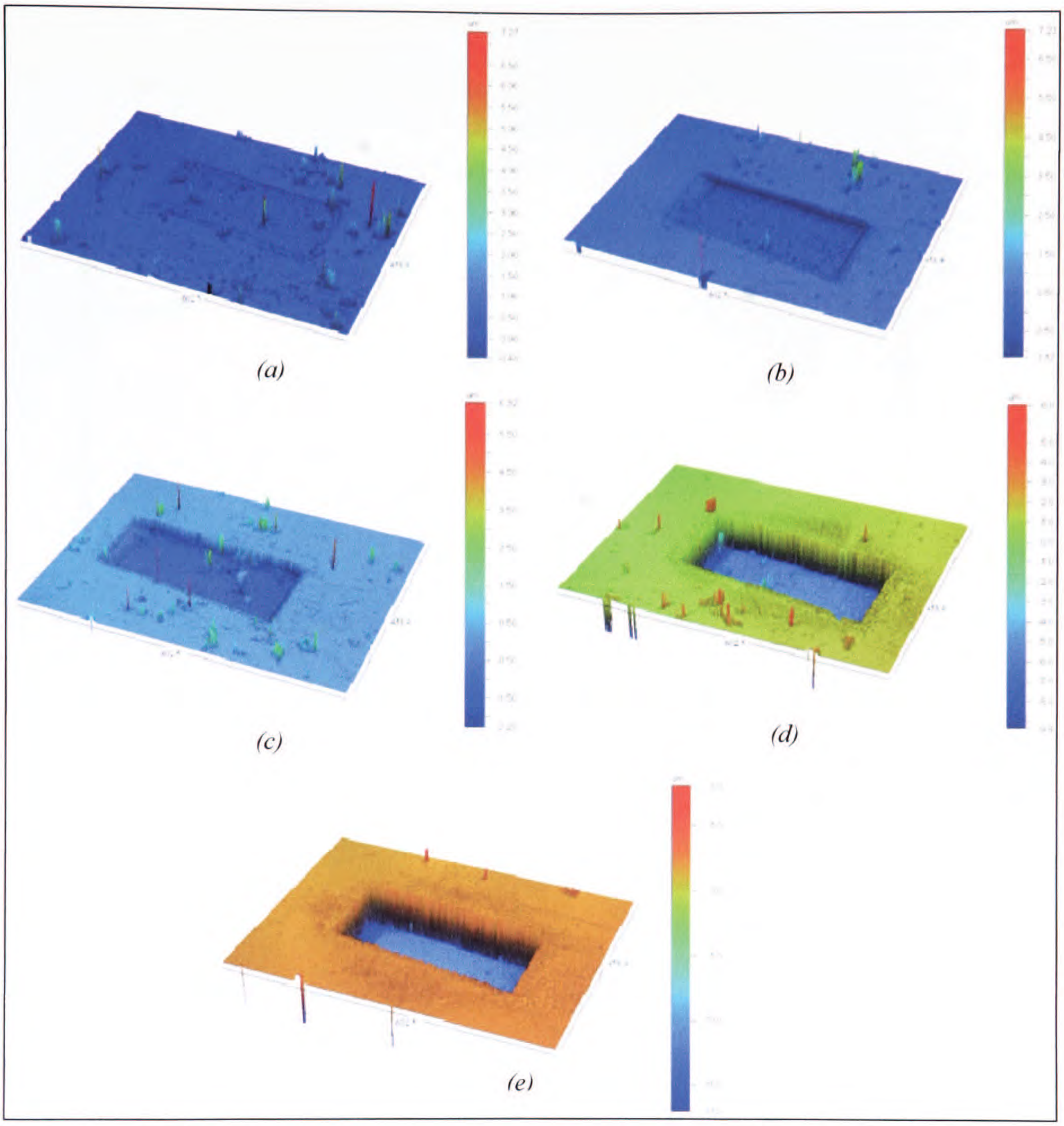

(a)

(b)

(c)

(d)

(e)

Figure 5.5: 3D images of ablation sites produced in PDMS, obtained using the white light interferometer. For (a) single pulse, (b) 5 pulses, (c) 10 pulses, (d) 50 pulses and (e) 100 pulses 157nm laser exposure at $1000mJcm^{-2}$.

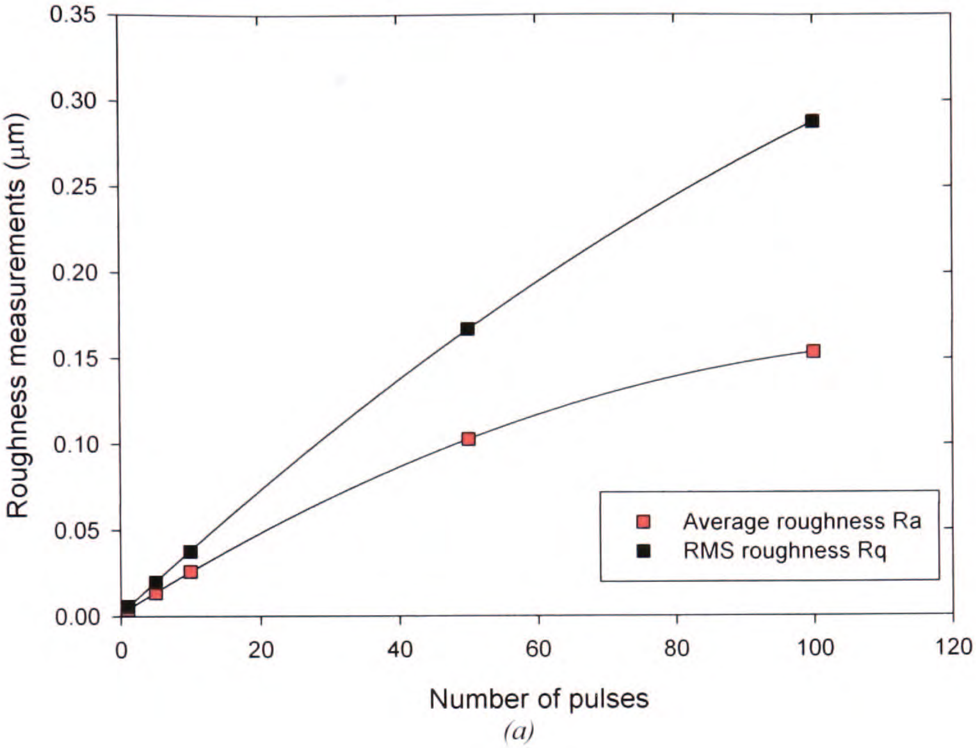

(a)

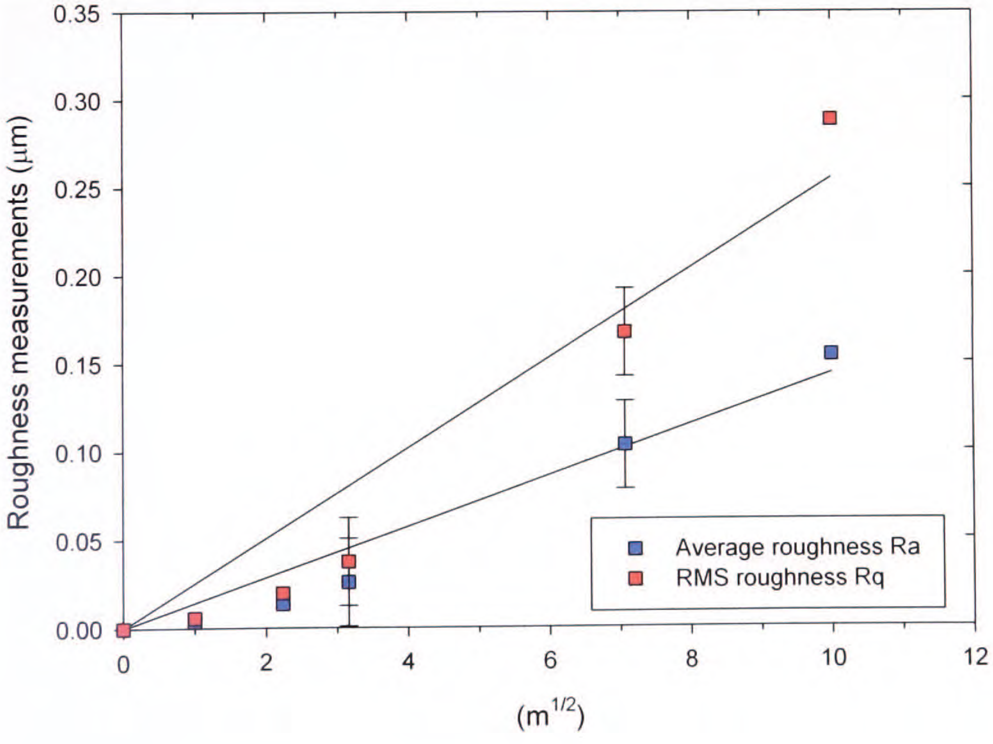

(b)

Figure 5.6: Roughness measurements, RMS (R_q) and average roughness (R_a) using the 157nm laser against (a)m the number of pulses and (b) $m^{1/2}$ for PDMS at a fluence of ~1000mJ cm^{-2}.

Figures 5.6a shows *Rq* and *Ra* as a function of the number of pulses using 157nm laser exposure delivered to the PDMS sample at a fluence of 1000mJcm^{-2}. These parameters were based on averages made using the white light interferometer over a width of $L \approx 300\mu m$ in the *X*-profile (equations 5.10 and 5.11). This corresponded to approximately the full-width of the crater and was acceptable in this case as its average base depth was nearly constant. *Rq* is seen to increase in a nearly linear fashion with increasing number of pulses *m*, and reaches up to *Rq* = 0.3µm for 100 pulses. Similar results can be seen for the *Ra* data in Figure 5.6 where *Ra* ≈ 0.15µm for 100 pulses. The ratio of *Ra* to *Rq*, has the mathematical significance that $\frac{R_q}{R_a} = 2^{\frac{3}{2}}\pi \approx 8.8$ for special case of a sinusoid and $\frac{R_a}{R_q} = \left(\frac{2}{\pi}\right)^{\frac{1}{2}} \approx 0.8$ for a Gaussian height distribution [5]. For the present results, the ratio of *Ra* to *Rq* can be seen in Figure 5.7, for 1, 5, 10, 50 and 100 pulses. This ratio has a value of ≈ 0.7, for 5 and 10 pulses but shows a slightly lower value for 1, 50 and 100 pulses. The average value is 0.634, which suggests that a Gaussian-like roughness distribution is produced on PDMS with the 157nm laser.

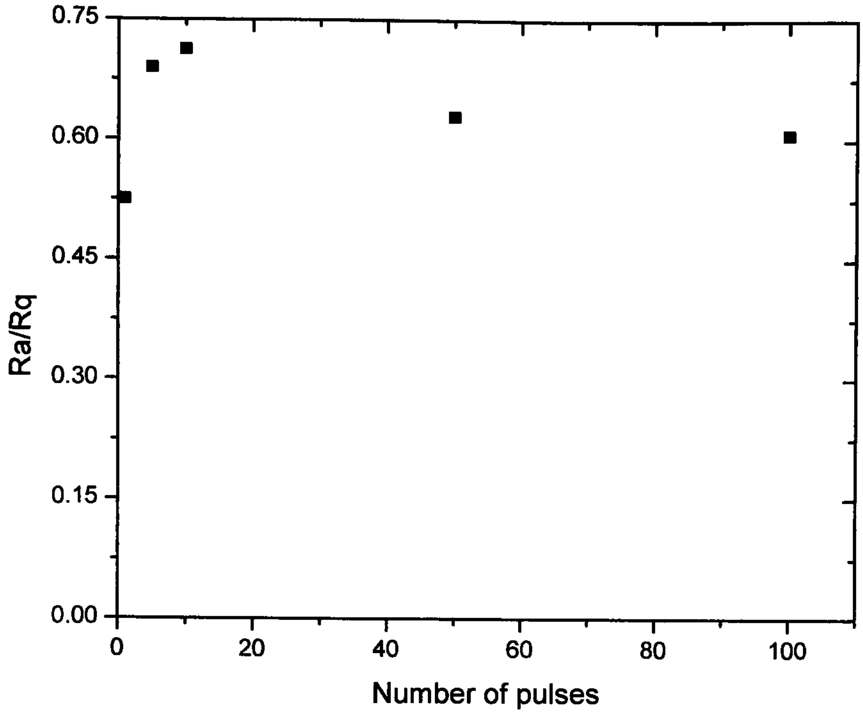

Figure 5.7: The ratio of the average surface roughness (R_a) to RMS surface roughness (Rq) against number of pulses for PDMS when ablated using the 157nm laser at a fluence of ~1000mJcm^{-2}.

The roughness data seen in Fig 5.6b do not show a particularly close fit to an $m^{1/2}$ dependence which suggest that statistical roughening related to mode fluctuations may not be significant and that other material related roughening effects are dominant. This is perhaps not unexpected as PDMS is a 'soft' rather than rigid polymer at room temperature and transient laser heating may play a role in deforming its surface.

5.2.3 Polycarbonate (PC)

To assess and evaluate the surface roughness produced using the 157nm F_2 laser, most of the work here was focussed on the Lexan polycarbonate ablated by exposure for up to 500 pulses at an average fluence of ~230mJcm^{-2}. In this case inspection of the SEM images of ablation sites such as shown in Figure 3.22 of Chapter 3 reveals several interesting findings. Firstly, the ablated PC is predominantly smooth and has a crack free surface. There is, nevertheless, a factor-of-two difference in the ablation depth of the near and far sides of the crater indicative of a relatively large variation in fluence across the beam. Secondly, at high fluence (~230mJcm^{-2}) and high number of pulses, it can be seen that the number of cones in the ablated area is reduced.

To correctly characterize roughness of the ablated PC surface at 157nm, it is crucial to eliminate cones in measurements. Cones were readily produced at fluences in the range 20-200mJcm^{-2}, whereas in general less cones develop at higher fluence. Hopp *et al* [6] reported that above 600mJcm^{-2} using 193nm laser, no conical structure was found. It believed that under these conditions small particulates impurities are removed from the surface, thus no cones develop from the shadow of the impurity, as noted in Chapter 3.

Figure 5.8(a-e) shows the white light interferometer surface images and the cross sections of X and Y profiles of the unirradiated PC surface and cross-section of X profiles after exposure to 1, 10, 50 and 100 pulses at a fluence of 230mJcm^{-2}. It is evident that there is a distinct growth in roughness with increasing number of pulses. Roughness was determined by averaging over regions of width L ~100μm that were selected to minimise contributions of low spatial frequency arising from beam non-uniformity (i.e. corresponding to stationary fluence variations) and that were free from cones. Figure 5.9 shows the surface of PC after irradiation with 1000 pulses, indicating after exposure at higher pulse number, the cones disappear resulting in an essentially smooth surface. Along the X profile there is a roughness of ~3μm for averaging over the full width of the ablation site.

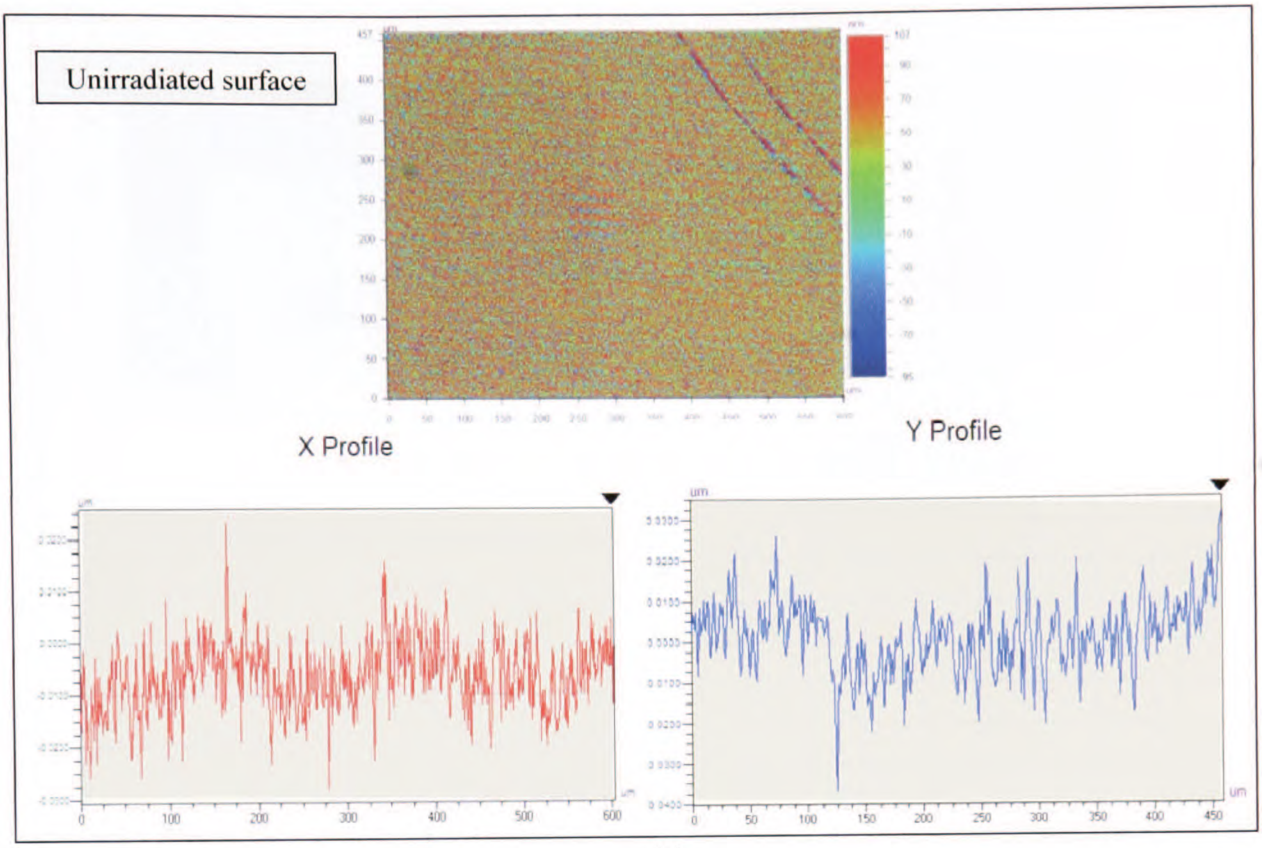

(a)

Figure 5.8(a): White light interferometer for analysis for PC using 157nm laser at ~ 237mJcm^{-2} for unirradiated surface. The above profiles shown are for the full width of the crater and for a restricted range of L = 100μm.

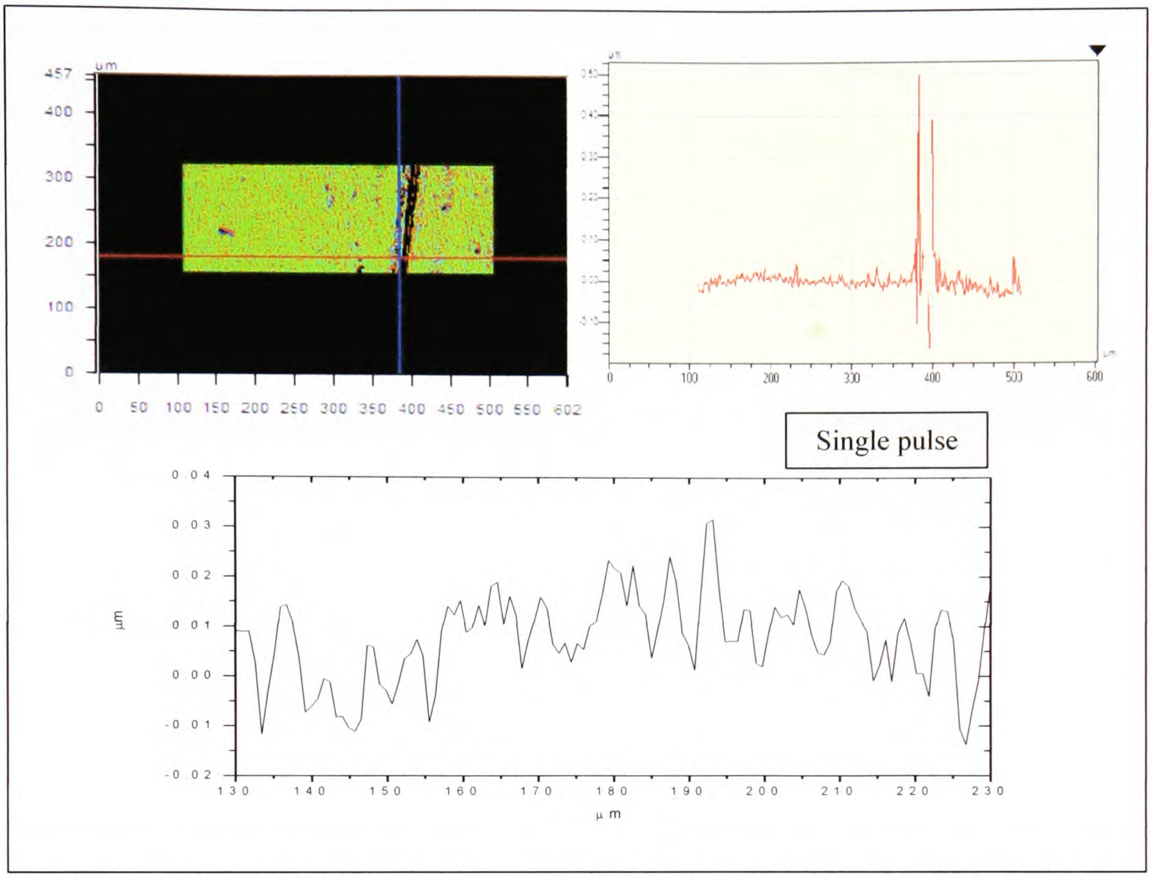

(b)

Figure 5.8(b): White light interferometer for analysis for PC using 157nm laser at ~ 237mJcm^{-2} for single pulse. The above profiles shown are for the full width of the crater and for a restricted range of L = 100µm.

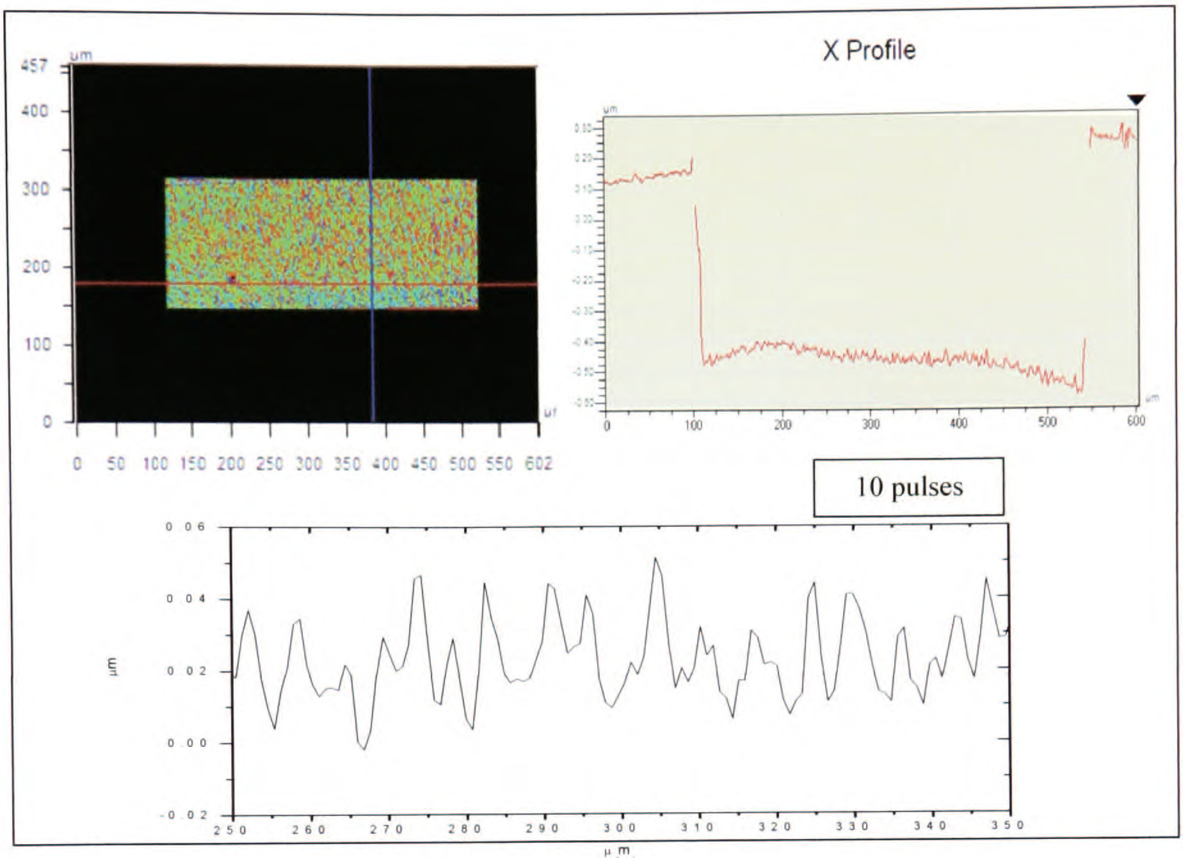
X Profile
10 pulses
μm
457
400
300
200
100
0
0 50 100 150 200 250 300 350 400 450 500 550 602
0 100 200 300 400 500 600
0.06
0.04
0.02
0.00
-0.02
250 260 270 280 290 300 310 320 330 340 350
μm

(c)

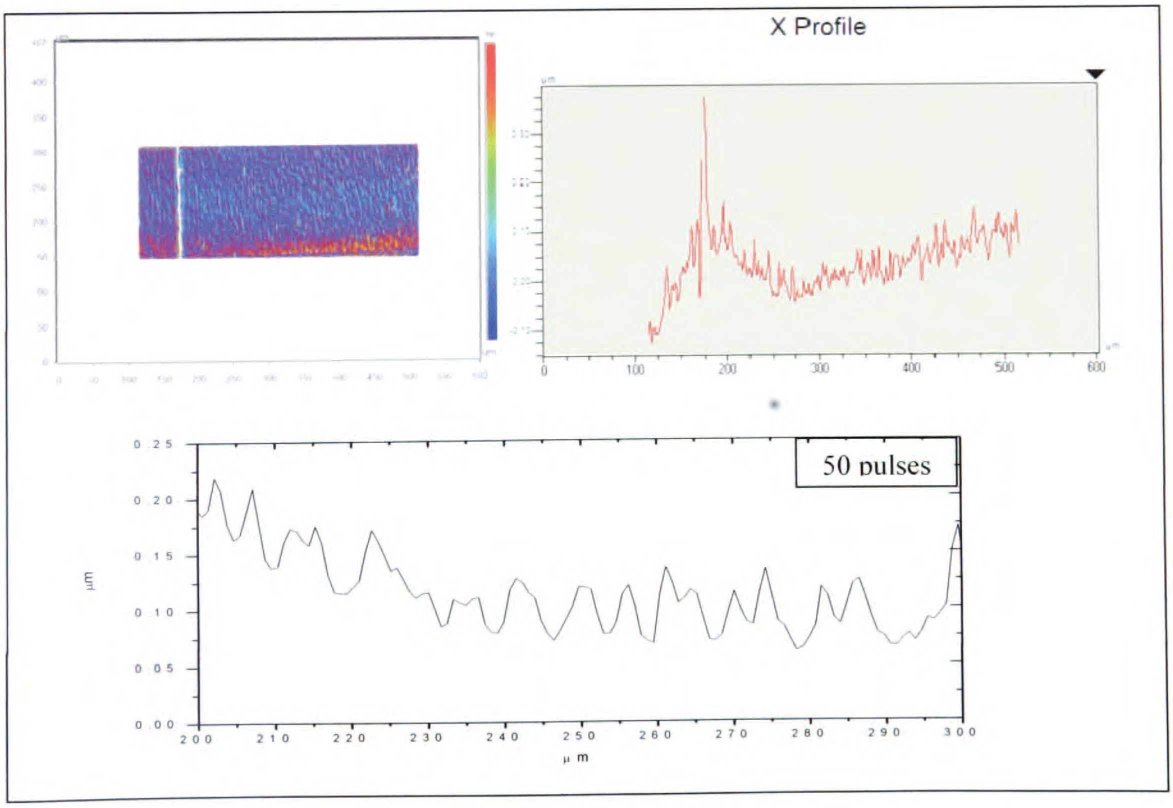
X Profile
50 pulses
μm
0 100 200 300 400 500 600
0.25
0.20
0.15
0.10
0.05
0.00
200 210 220 230 240 250 260 270 280 290 300
μm

(d)

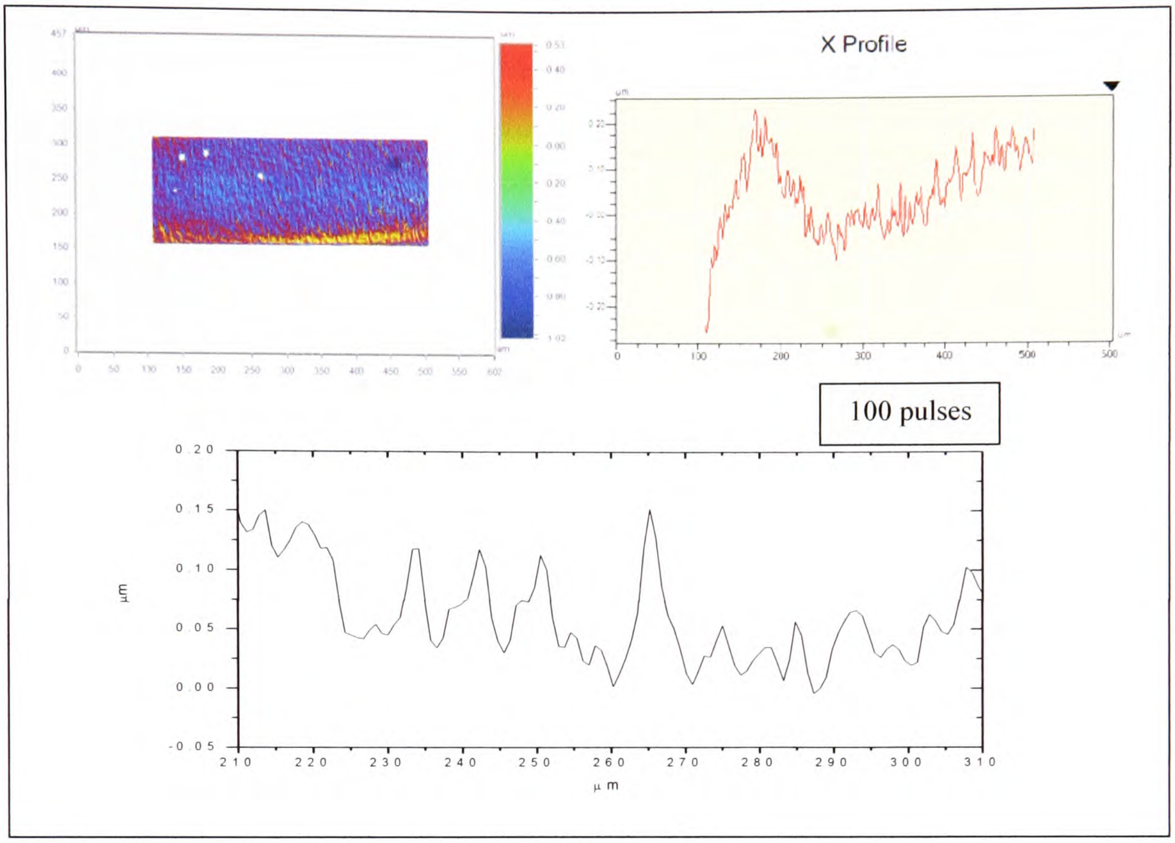

(e)

Figure 5.8: White light interferometer for analysis for PC using 157nm laser at $\sim 237 mJcm^{-2}$ (c) 10 (d) 50 and (e) 100pulse. The above profiles shown are for the full width of the crater and for a restricted range of $L = 100\mu m$.

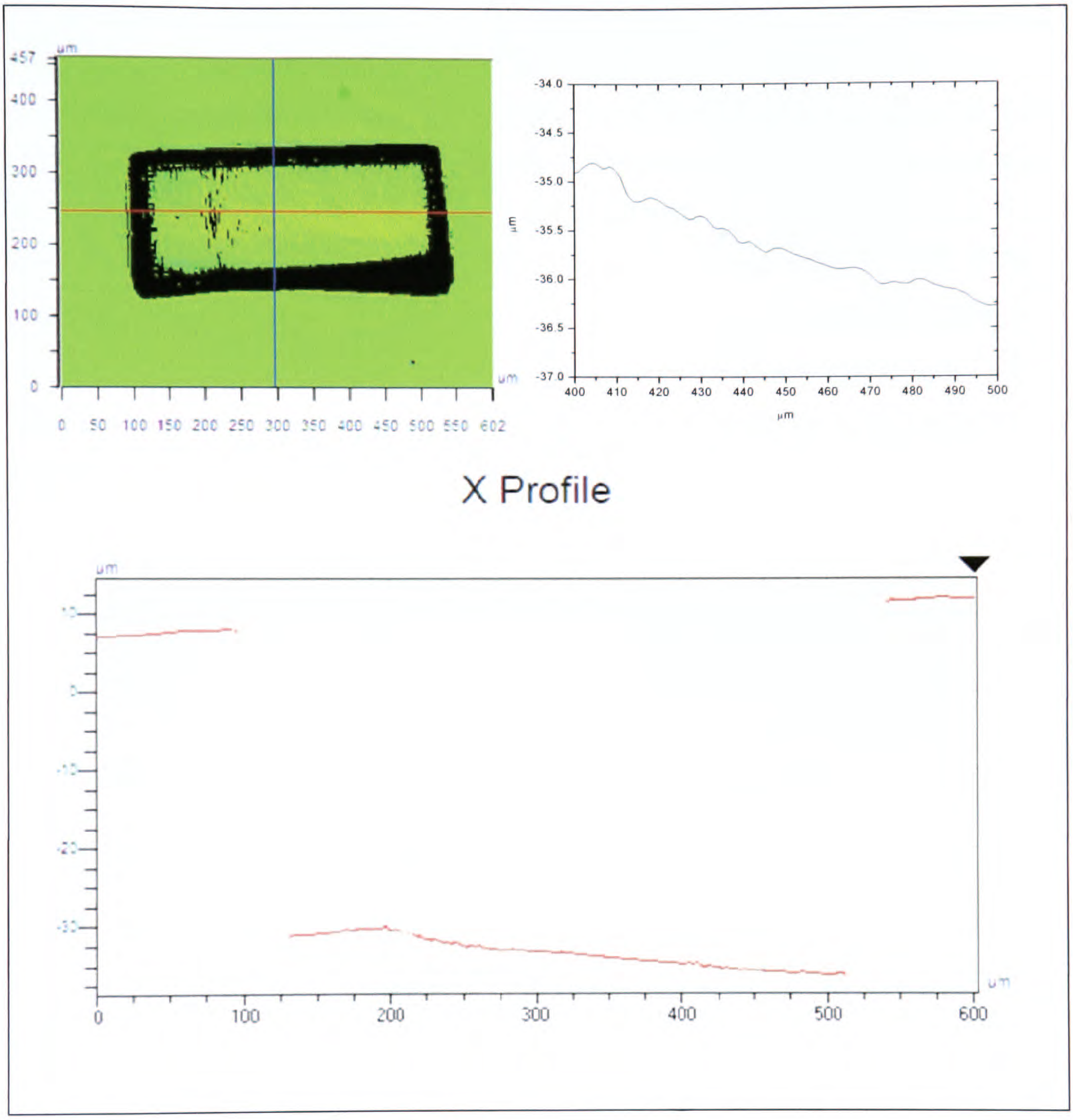

Figure 5.9: White light interferometer analysis for PC using 157nm laser at ~237mJcm^{-2}, 1000 pulses, The X profiles show profiles for the full width of the crater and for a restricted range of L =100µm.

Roughness measurements obtained for cone-free regions of PC surfaces using the Wyko interferometer are shown in Figure 5.10a and b. In Figure 5.10a, $(Rq^2\text{-}Rq_o^2)^{1/2}$ and $(Ra^2\text{-}Ra_o^2)^{1/2}$ are plotted versus number of pulses where Rq is the measured RMS roughness and Ra is average roughness where $Ra_o = Rq_o = 0.01\mu m$ is the corresponding roughness of the unirradiated polycarbonate surface. The data shows an increased roughness value with the number of pulses applied to the PC surface. For m pulses applied to the ablated surface, the modelling based on statistical (pulse-to-pulse) fluctuations predicts that the total depth ablated will have uncertainty that is a factor of $\sqrt{m}$ times larger than σ, giving a roughness $r = \sqrt{m}\sigma$ [1] i.e. increasing as $\sqrt{m}$. Figure 5.10b shows the roughness plotted versus $\sqrt{m}$ with a straight line fitted to the data. This gives a reasonable fit to the data when account is taken of the considerable uncertainty in the measurements.

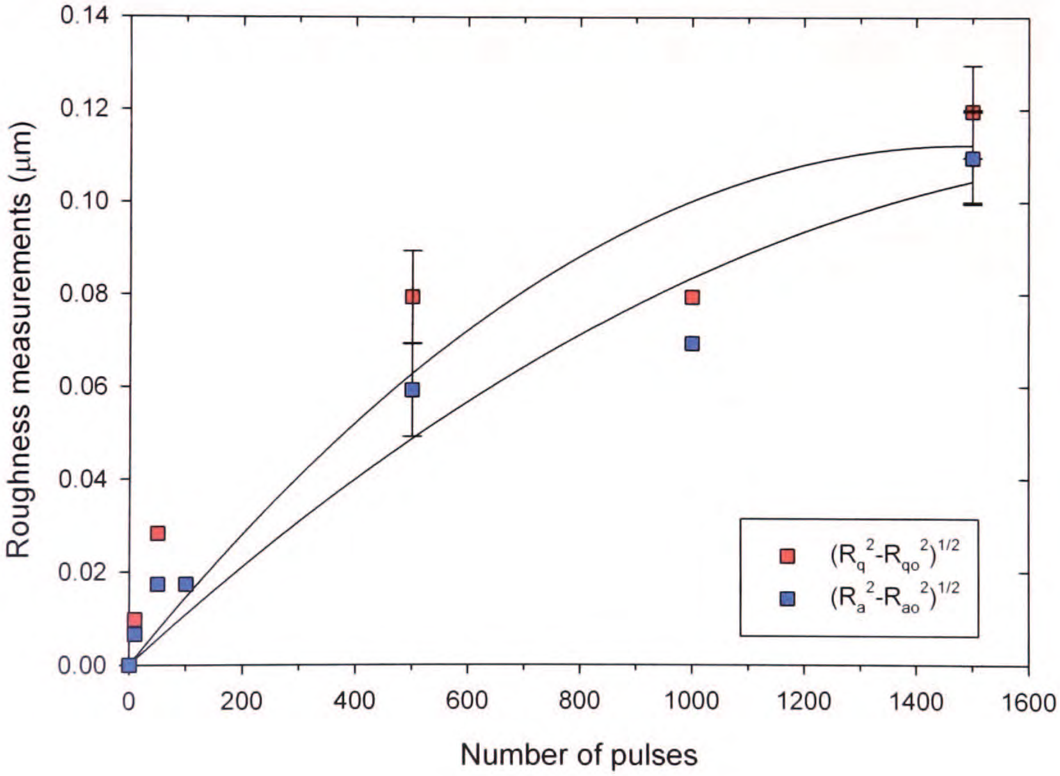

(a)

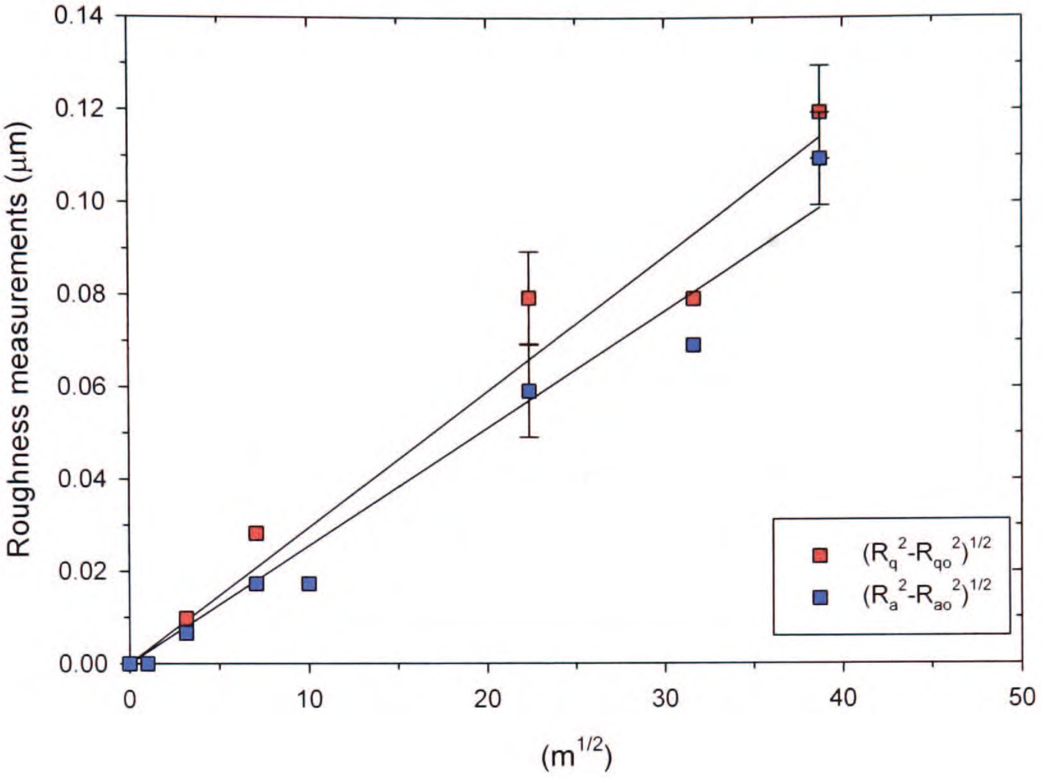

(b)

Figure 5.10: Average roughness $(R_a^2-R_{ao}^2)^{1/2}$ and RMS roughness $(R_q^2-R_{qo}^2)^{1/2}$ against (a) number of pulses m and (b) against $m^{1/2}$ for polycarbonate using 157nm laser exposure at a fluence of ~237mJcm^{-2}.

Figure 5.11 shows a magnified SEM image of an essentially cone-free region of the surface of polycarbonate at about ~2μm scale-size from which it is evident that a smooth surface texture remains after ablation using 157nm laser. This result and the extremely smooth walls seen on the micron scale size cones formed in PC (e.g. see Figure 3.30), suggest that F_2 laser processing could achieve roughness in the nano-meter range on a micrometer lateral scale. This gives this polymer laser combination good potential in lab-on-chip device development applications, for example, for genome analysis and biotechnology [7], and also for machining micro-optical components and other structures.

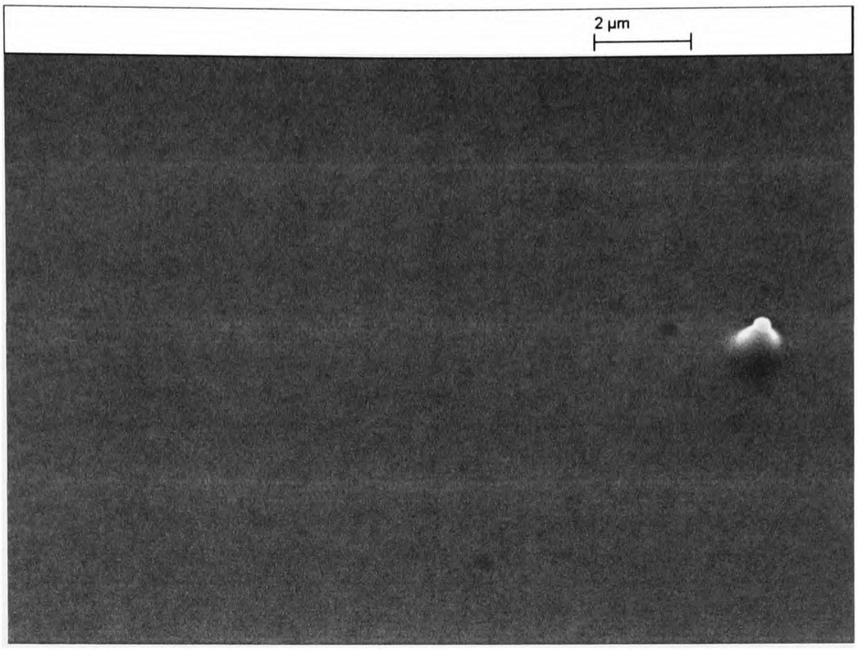

Figure 5.11: Magnified SEM image of the surface in the region of essentially cone-free area on polycarbonate (PC), at ~237mJcm^{-2}, 500 pulses.

Figure 5.12 shows the height distribution extracts from the white light interferometer analysis on the ablated polycarbonate from which can be deduced that the surfaces can be represented by the Gaussian-like distribution. Figure 5.12a is for the pristine surface before laser exposure; Figure 5.12b the distribution following of a single pulse on the PC surface, and Figures 5.12c and d for 50 pulses and 100 pulses respectively. The results have close to a Gaussian-like distribution, with $Ra/Rq \approx 0.8$ although it can be seen there is a small shift toward negative skew with an increasing number of pulses.

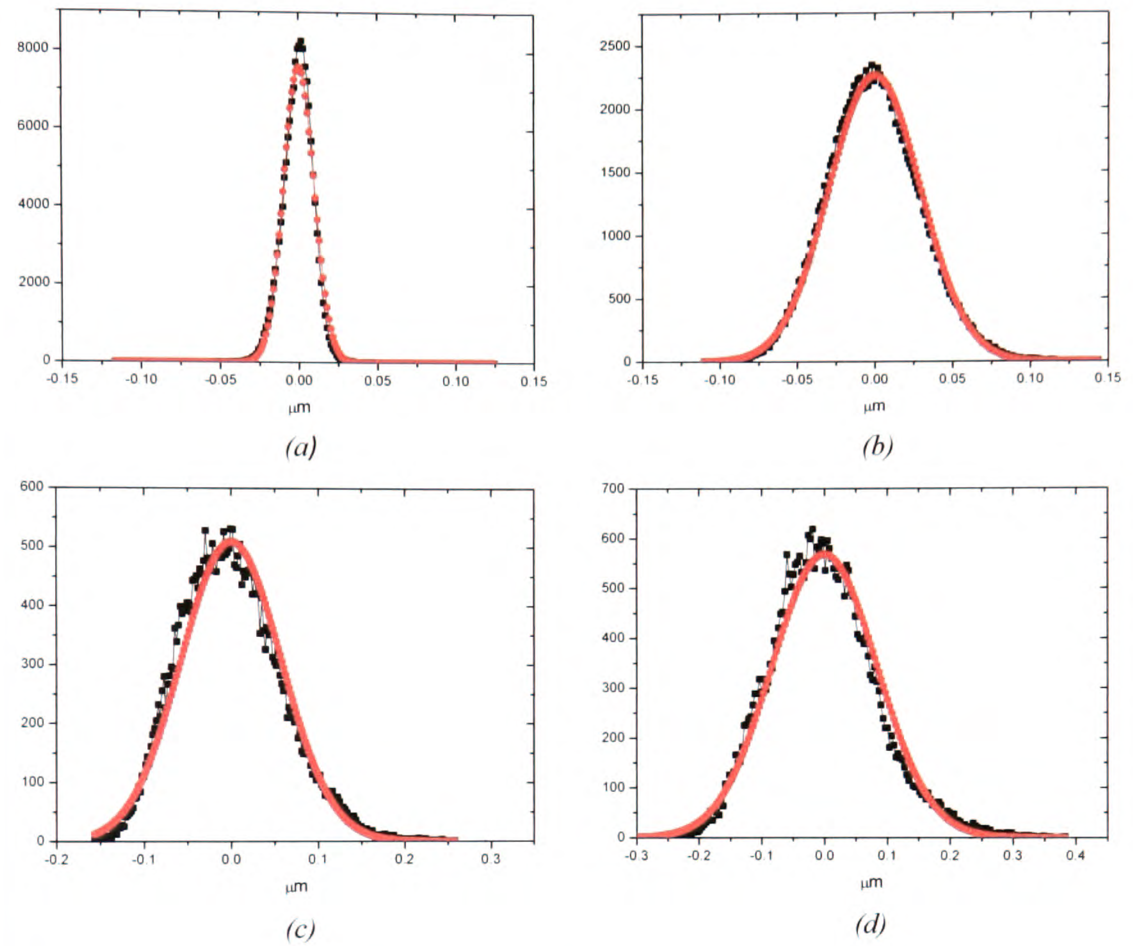

(a) (b) (c) (d)

Figure 5.12: Height distributions of the surface of the ablated polycarbonate samples: (a) unirradiated (b) single pulse (c) 50 pulses and (d) 100 pulses at a laser fluence of ~237mJcm^{-2}. Red lines show Gaussian fits to distributions.

5.2.4 CR-39

This section will describe the roughness analysis of CR-39 ablated using the 157nm beam. Figure 5.13(a-e) shows the white light interferometer images and the cross section of *X* and *Y* profiles of the unirradiated CR-39 surface, and *X* profiles after exposure to 1, 10, 50 and 100 pulses at a fluence of 182mJcm^{-2}. Roughness determination was again restricted to averaging over a scale length of $L = 100\mu m$ to minimise contributions from stationary fluence variations and to avoid contributions from cones if present. In Figure 5.13e where 100 pulses were applied on the CR-39 polymer, 'dark spots' appear, indicating cone formation, and bringing an increasing degree of uncertainty to the roughness measurements. From Figure 5.13(a-e) there is seen to be a distinct growth in roughness with increasing number of pulses. In Figure 5.14a $(Rq^2-Rq_o^2)^{1/2}$ and $(Ra^2-Ra_o^2)^{1/2}$ are shown plotted versus number of pulses, where Rq is measured RMS roughness and Ra is average roughness where $Ra_o = Rq_o \approx 0.01\mu m$ for the pristine surface of this polymer. The value of $(Rq^2-Rq_o^2)^{1/2}$ increases to ~0.04µm for exposure to 100 pulses, and average roughness $(Ra^2-Ra_o^2)^{1/2}$ increases up ~0.03µm for the same number of exposure pulses at a fluence of 182mJcm^{-2}. The roughness of ~0.04µm for CR-39 is slightly higher than that of ~0.02µm obtained on polycarbonate at 100 pulses exposure. In Figure 5.14b the measured roughness $(Rq^2-Rq_o^2)^{1/2}$and average roughness $(Ra^2-Ra_o^2)^{1/2}$, plotted against $\sqrt{m}$ in order to compare with the statistical roughness expression (equation 5.5), shows quite good agreement with a linear dependence over the range involved. Figure 5.15 shows the magnified SEM image of CR-39 on a 2µm scale for a cone-free zone. It is seen to have a relatively smooth surface texture after ablation. Figure 5.16 shows corresponding histograms of the surface height variation on the CR-39 surface. This remains close to a Gaussian-like distribution, with $Ra/Rq \approx 0.8$, though the plots have poorer overall symmetry for this polymer compared to polycarbonate and in this case a small positive skew.

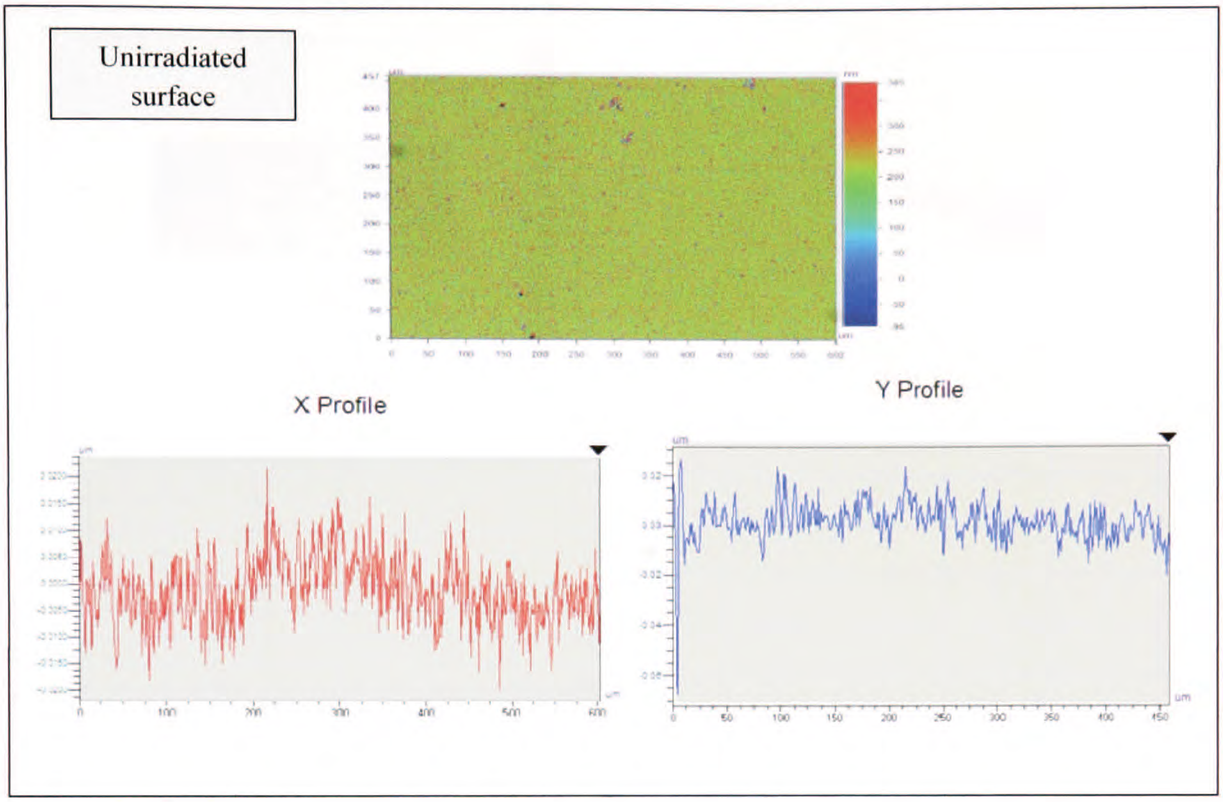
Unirradiated surface
X Profile
Y Profile
µm
0.02
0.00
-0.02
-0.04
-0.06
0
50
100
150
200
250
300
350
400
450
0
100
200
300
400
500
600
µm

(a)

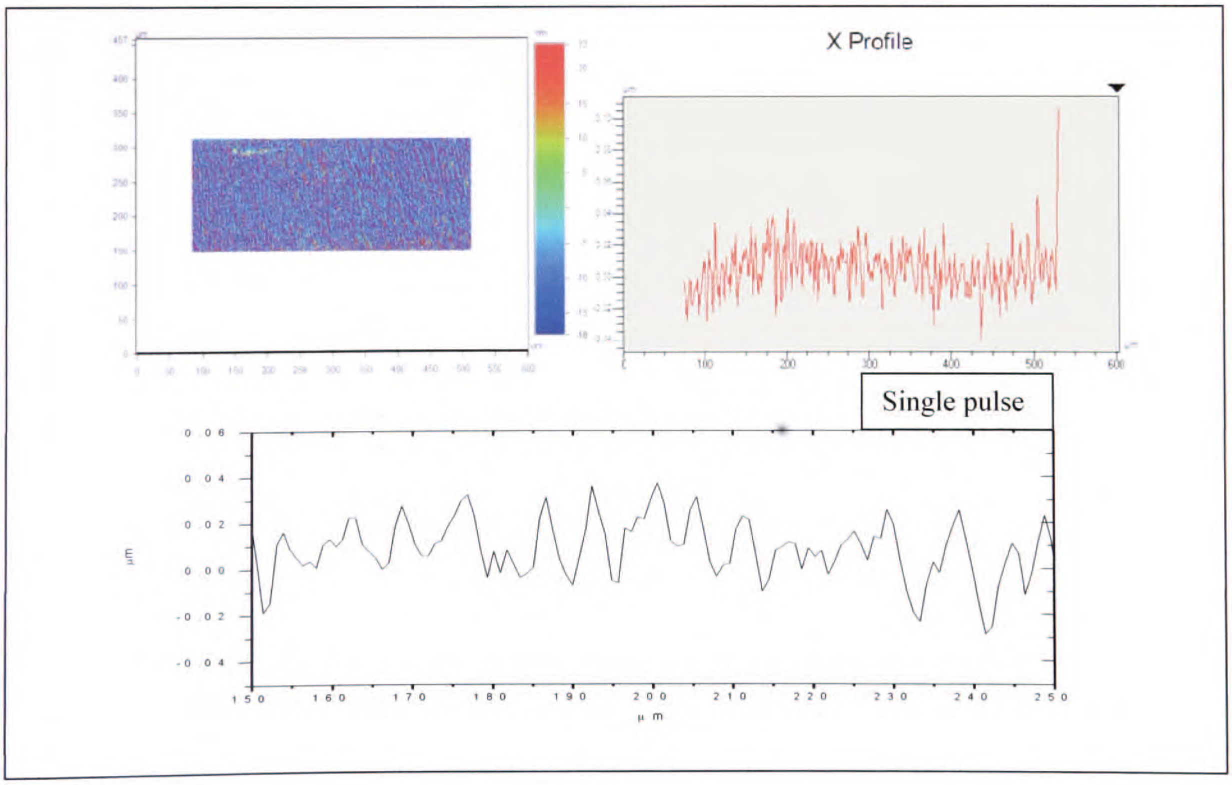
X Profile
Single pulse
0.06
0.04
0.02
µm
0.00
-0.02
-0.04
150
160
170
180
190
200
210
220
230
240
250
µm
100
200
300
400
500
600

(b)

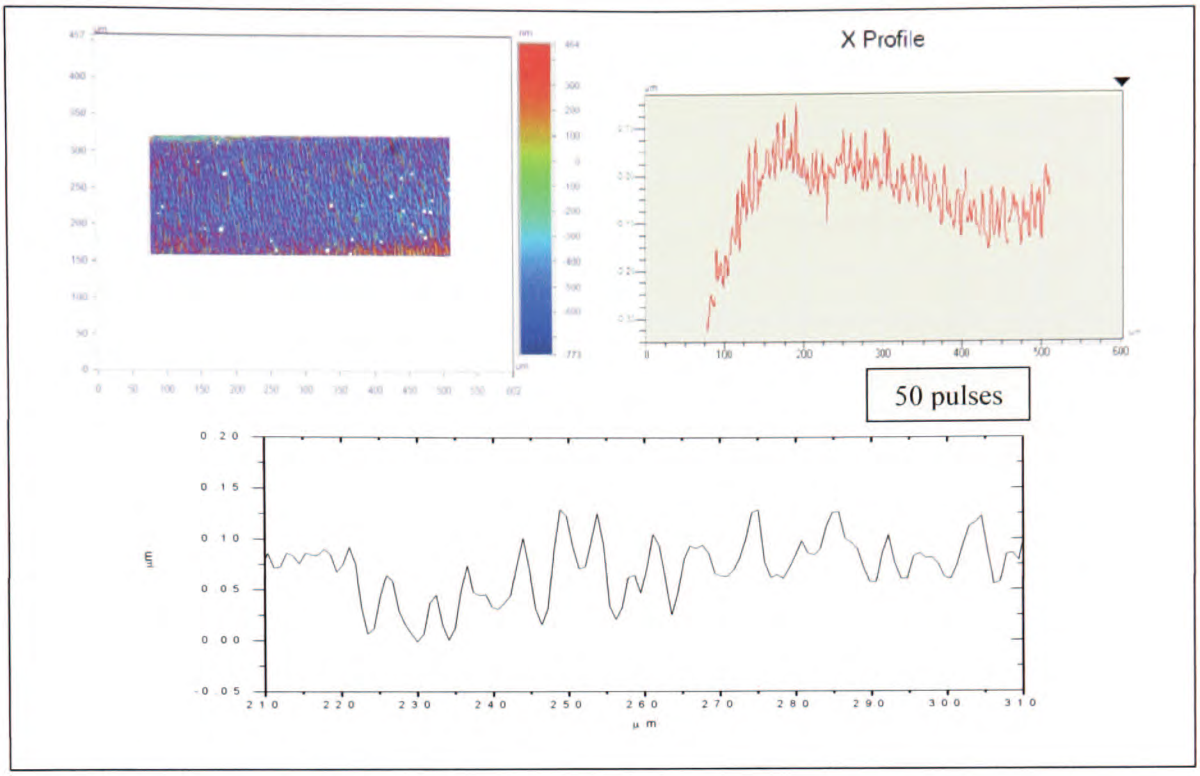

(c)

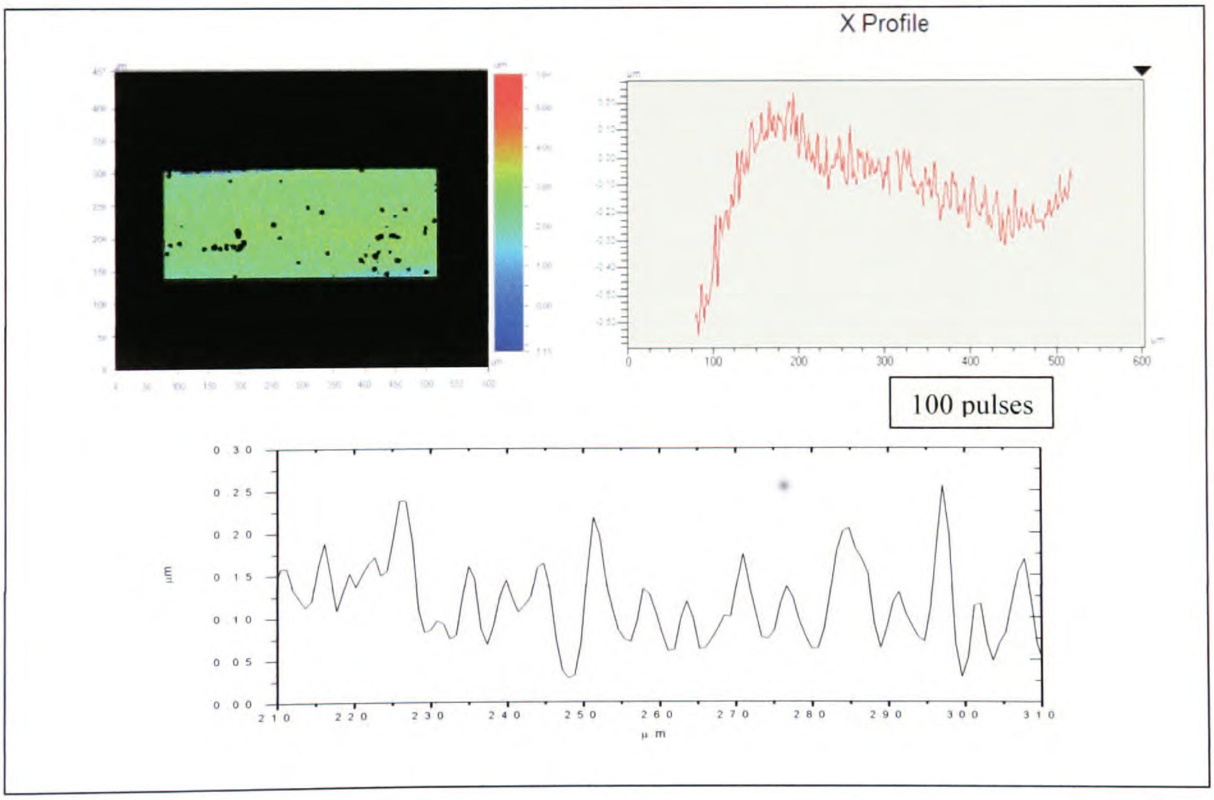

(d)

Figure 5.13: White light interferometer analysis of CR-39 surfaces ablated using the 157nm laser at~ 182mJcm^{-2}(a) unirradiated (b) single pulse (c) 50 and (d) 100 pulses. Full X profiles are shown together with those over a width range restricted to L = 100µm.

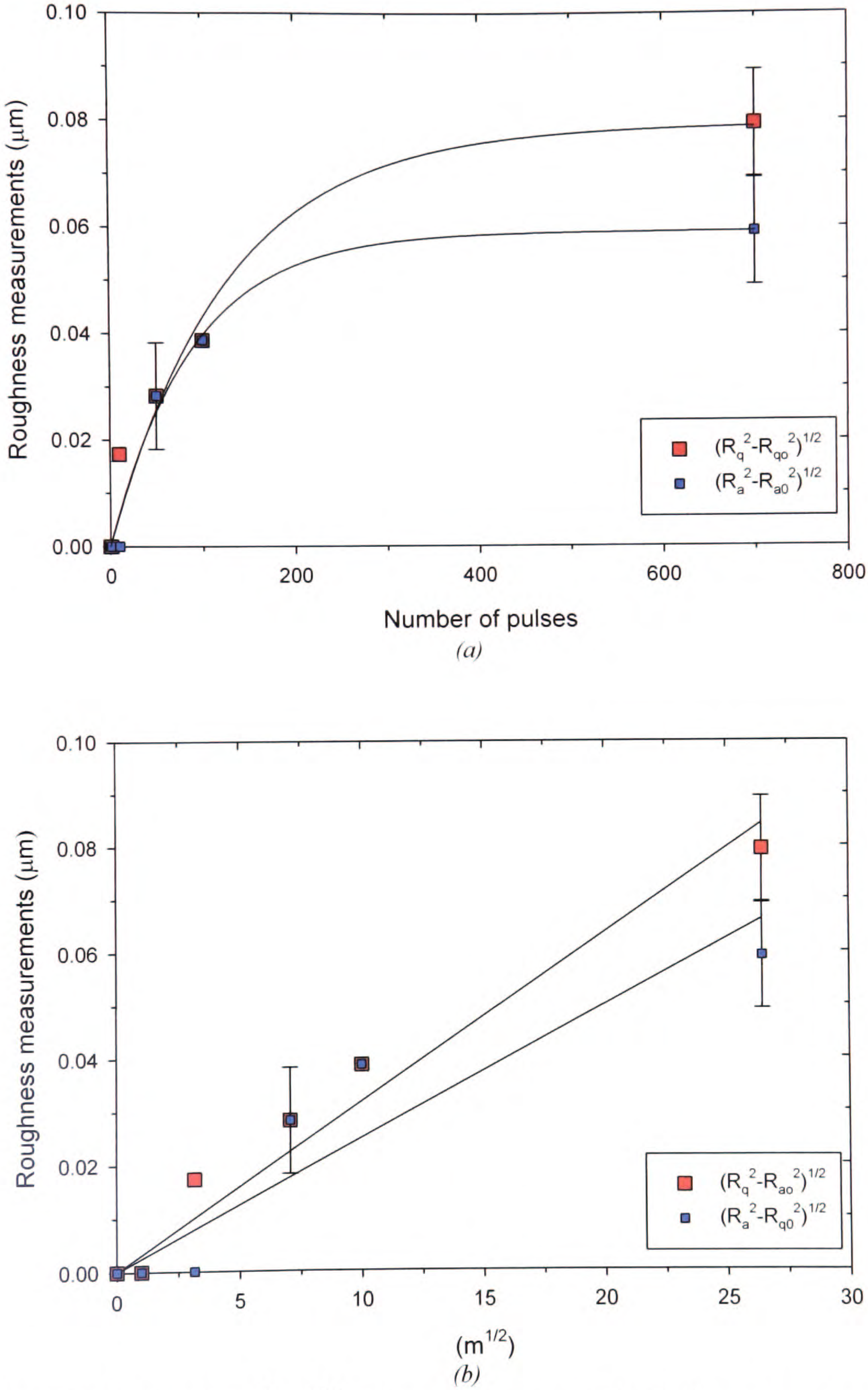

(a)

(b)

Figure 5.14: RMS roughness $(R_q^2-R_o^2)^{1/2}$ and average roughness $(R_a^2-R_{ao}^2)^{1/2}$ against (a) number of pulses m and (b) against $m^{1/2}$ for CR-39 using 157nm laser exposure at a fluence of ~182mJcm^{-2}.

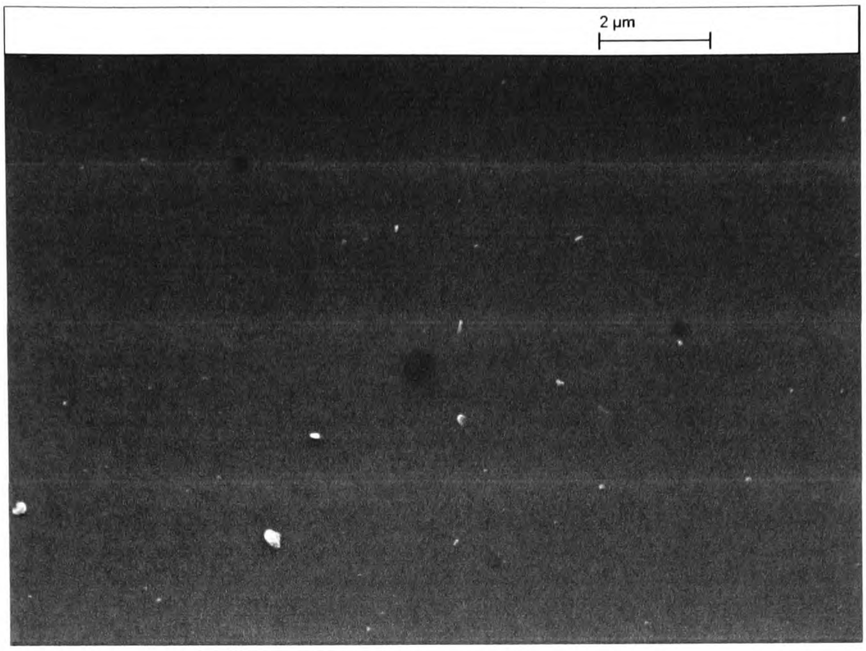

Figure 5.15: Magnified SEM image of the surface in the cone-free area on CR-39, at ablated at ~182mJcm^{-2}using 500 pulses.

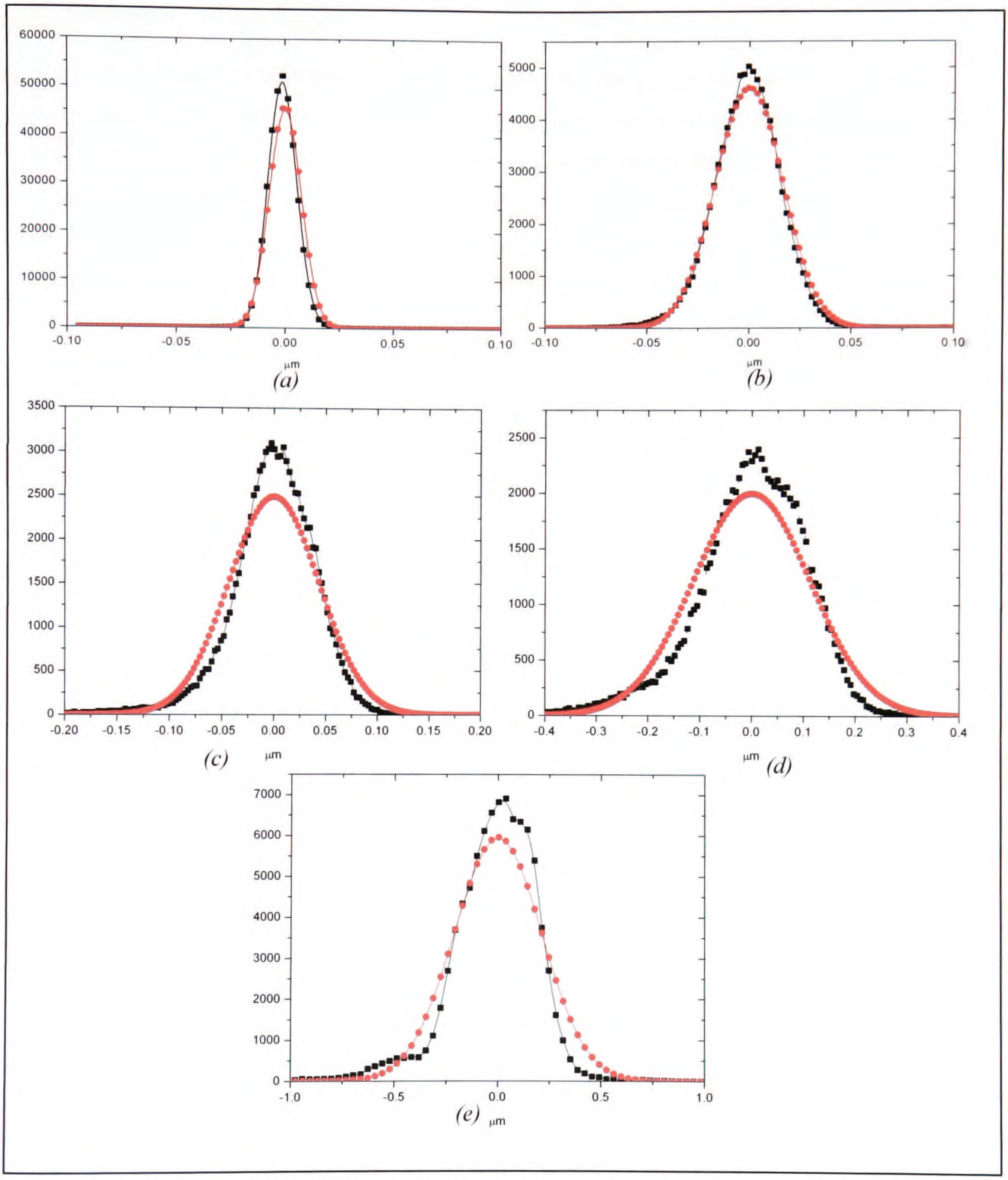

Figure 5.16: Height distributions for the surfaces of CR-39 samples ablated at a 157nm laser fluence of ~182mJcm^{-2} (a) unirradiated surface (b) single pulse (c) 10 (d) 50 and (d) 100 pulses. Red lines show Gaussian fits to distributions.

5.3 Discussion

It is of interest to compare the results obtained for the surface roughness of PDMS, polycarbonate (PC) and CR-39 ablated using the 157nm laser with the predictions of the roughening model based on laser mode fluctuations. Turning first to the scaling with number of pulses m, it is found that a reasonable fit to the results for PC and CR-39 is obtained using an $m^{1/2}$ dependence which is supportive of a statistical roughening model. For PDMS the fit is poorer, a result that may relate to the fact that this polymer is significantly different to PC and CR-39, both of which are rigid at room temperature, whilst PDMS is 'soft' (non-rigid). This could result in there being a degree of distortion associated with transient heating under laser exposure that amplifies or modifies induced the surface roughness. Relaxation of residual stress in aligned polymers is, for example, known to lead to one or two dimensional undulations depending on whether alignment is uniaxial or biaxial [8, 9].

The magnitude of roughening r predicted by the mode fluctuation model can be determined from

$$r = \frac{\sqrt{m}\sigma}{\alpha_{eff} < F >} \tag{5.12}$$

where α_{eff} is the effective absorption coefficient at 157nm, σ in the standard deviation of the fluence and $<F>$ the mean fluence. Based on the F_2 laser linewidth a value $\sigma/<F> = 4\%$ is obtained for the unpolarised beam giving for polycarbonate with $\alpha_{eff} \approx 3 \times 10^5$ cm^{-1}

$$r = 1.3m^{1/2} \text{ (nm)} \tag{5.13a}$$

and for CR-39 with $\alpha_{eff} \approx 2.9 \times 10^5$cm^{-1}.

$$r = 1.4m^{1/2} \text{ (nm)} \tag{5.13b}$$

From Figure 5.10b, the measured roughness for polycarbonate with $m^{1/2} = 10$ (100 pulses) is ~20nm compared with a corresponding predicted value of $r = 13$nm. Given various uncertainties discussed below this is reasonable agreement. For CR-39 experiments give ~40nm for 100 pulses (Figure 5.14), compared with a predicted roughness of 14nm showing that in this case there is a considerably larger difference between these values. Several factors may contribute to these differences: Firstly, use of an etch rate of the form in equation 5.2 to describe material removal is a simplification and the derived value of α_{eff} used in equations 13 can have considerable uncertainty. Secondly, in measuring surface roughness it is difficult to disentangle low spatial frequency variations arising from beam non-uniformity that is fixed from pulse-to-pulse ('stationary') with variations that are random from pulse to pulse. Use of a restricted spatial averaging range (here $L \sim 100\mu m$) helped minimise this, though low frequency depth changes may still remain that contribute to the roughness determination and thus result in an overestimate of statistical contributions.

Clear qualitative evidence of the surface quality attainable in 157nm ablation of both PC and CR-39 comes from SEMs of restricted regions of surfaces and from the high quality of the walls on conical structures that can form under multiple pulse exposure. As an example, Figure 5.17 shows a micron scale-size cone in CR-39, where both the cone wall and the surface surrounding the cone beyond the interference rings are seen to be very smooth. The fringes in Figure 5.17 have a spacing of only ~170nm, showing the excellent potential of CR-39 for recording nanometer microstructures by ablation with the 157nm laser. Similar conclusions can be drawn for polycarbonate as discussed in Chapter 3.

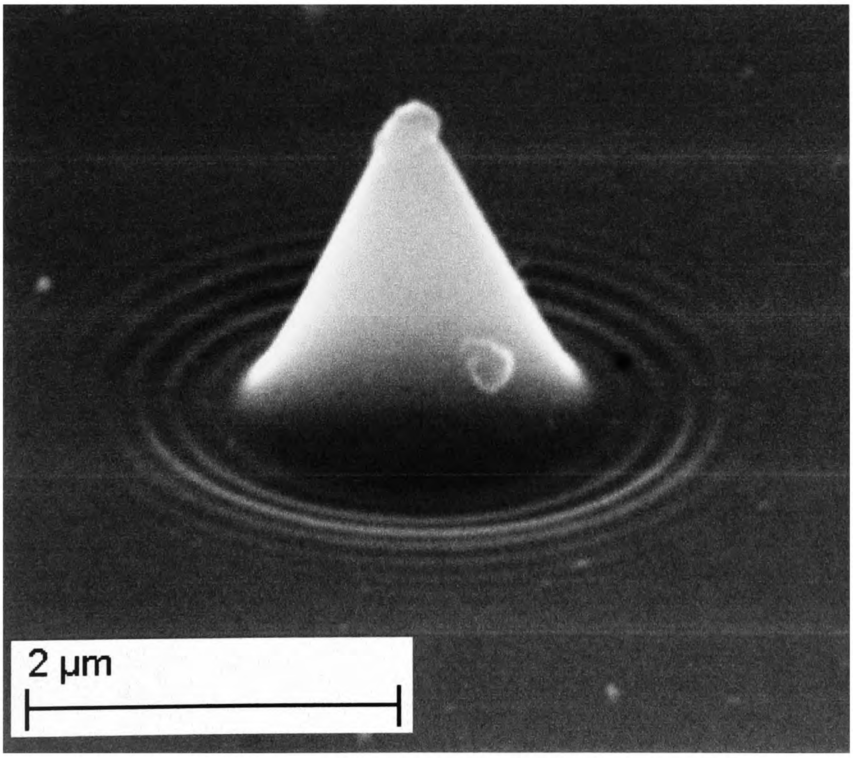

Figure 5.17: A cone developed on CR-39 at fluence of ~60mJcm^{-2}, single pulse using 157nm laser.

For PDMS the predicted statistical roughness is $r = 11m^{1/2}$ using $\alpha_{eff} = 3.5 \times 10^4$ cm^{-1} and $\sigma/\langle F\rangle = 4\%$. For 100 pulses this gives 110nm which can be compared with ~150nm found experimentally. Thus, though the scaling with pulse number is not in close agreement with the theoretical prediction, the magnitude of roughness is similar to that expected.

By using the optical system reduction of 15x for PC and 10x for CR-39, resulting spatial frequency for roughness of ~2μm for wider dimension of the beam (for examples Figure 5.8c and 5.8e) gives the spatial coherence as ~20μm for CR-39 and ~30μm for PC for wide dimension (*X*). Thus, this spatial coherence values obtained seems are consistent with the interference effects measured from the adjacent cone base reported [10].

Previous work on the surface quality using 157nm laser on the ablated glasses shows macroscopically smooth with no signs of cracks on the surface as it was found to have a low ablation threshold and relative freedom from spurious microstructures formation, not like the materials used induced on polydimethylsiloxane (PDMS), polycarbonate (PC) and CR-39 polymer is presumably are not as good as other material like glass as it found to be good physical and chemical homogeneity, thus minimizing possibly roughening associated with non-optical factors [1].

References

[1] P.E.Dyer, C.D.Walton, and K.A.Akeel, Optics Letters 30 (2005) 1336.

[2] P.E.Dyer, S.M.Maswadi, H.V.Snelling, and C.D.Walton, Proceeding SPIE 4637 (2002)

[3] C.J.Sansonetti, J.Reader, and K.Vogler, Applied Optics 40 (2001) 1974.

[4] P.E.Dyer, J.Mackay, and C.D.Walton, Optics Communications **240** (2004) 391.

[5] T.R.Thomas, Rough Surfaces, Imperial College Press, 1999.

[6] B.Hopp, Zs.Bor, E.Homolya, and E.Mihalik, Applied Surface Science 109 (1997) 232.

[7] Markus Lapezyna and M. Stuke, *Rapid prototype fabrication of smooth microreactor channel system in PMMA by VUV laser ablation at 157nm for applications in genome analysis and biotechnology,*Materials Research Society Symposium proceedings 526 (1998) 143.

[8] Y.Novis, J.J.Pireaux, A.Brezini, E.Petit, and R.Caudano, Journal Applied Physics 64 (1988) 365.

[9] T.Bahners and E.Schollmeyer, Journal Applied Physics 66 (1989) 1884.

[10] P.E.Dyer, C.D.Walton, and R.Zakaria, Applied Physics A 95 (2009) 319.

CHAPTER 6

157nm F_2 BEAM CHARACTERIZATION

6.0 Introduction

In industrial applications using excimer lasers, for example in photolithography or material processing, the process strongly depends on the stability and the precise control of the characteristics of the emitted radiation, such as pulse energy, beam width, divergence, pointing stability etc [1]. As such standardized methods for the evaluation of the beam are important. Whereas the output energy and power of the beam can be monitored by measuring tools such as joulemeter [1] whilst to record the spatial beam profiles, or more exactly the energy density distributions, requires specific instrumentation adapted to the output characteristics of the laser.

In this chapter, the main objective is to report an investigation of the 157nm F_2 laser beam characteristics using Lumilass G9 fluorescence glass plate as a transform medium from the vacuum ultra-violet to visible light spectral region. The plate is viewed and recorded using the CCD camera. This experimental work is complemented by modelling of the statistical fluctuations in the pulse-to-pulse spatial fluences distribution of the highly multimode of 157nm F_2 laser beam in an effort to assess the contribution of the coherence effects on ablated surface quality.

In the present work, many aspects have to be considered in recording the 157nm F_2 beam, especially the capability of the Lumilass G9 glass as a medium for transformation the UV radiation to visible, followed by capturing images onto a CCD chip as well as the sensitivity of the camera as a image recorder. A computer equipped with frame grabber software is used for the profile acquisition, real-time display and evaluation of the characteristics of the beam parameters. The other part which plays an important role in this experiment is the CCD camera which must be able to capture and record images adequately. The capability of the CCD camera has been described in the section below.

6.1 Fluorescent Materials for VUV

The use of a fluorescent material to convert the VUV to visible radiation is attractive for beam profiling the 157nm laser as a CCD (charge coupled device) can then be used to record the two-dimensional radiation irradiance/fluence distribution. For this application the fluorescent material should have good stability i.e. should not decompose rapidly under VUV exposure, achieve adequate spatial resolution for the proposed use, and provide a linear response over a useful dynamic range. In addition, a high efficiency of conversion (quantum efficiency for fluorescence) to a wavelength range where CCD's are sensitive is desirable. There is also potential advantage in terms of the spatial resolution if there is localization of emission to a shallow surface layer so as to avoid depth of focus effects with the CCD imaging (Figure 6.1). A material that is transparent to the fluorescent radiation is advantageous for use with the VUV laser as rear viewing could then allow the plate to act as a window and the CCD camera to work in air. It is also important that fluorescent species within the material are uniformly distributed and at a sufficiently high density so as not to compromise the spatial resolution.

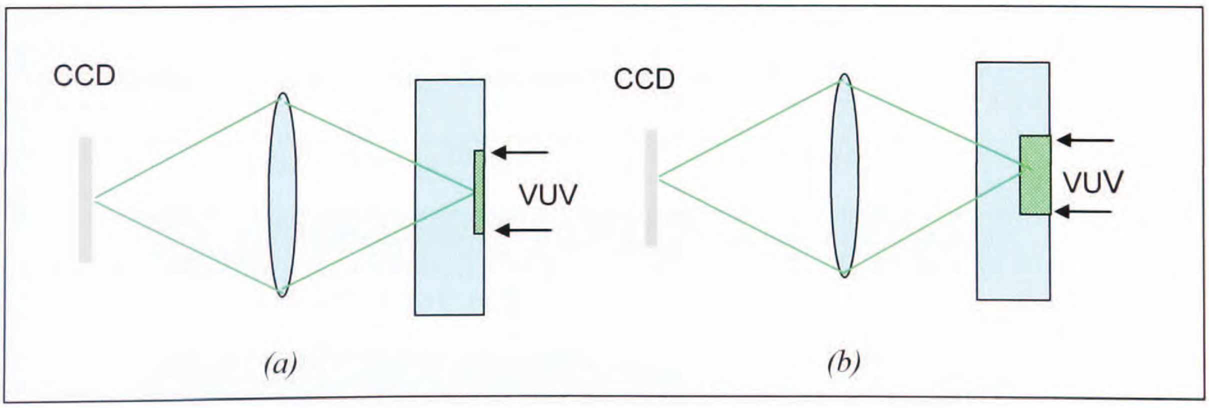

Figure 6.1: Fluorescence with (a) strong VUV absorption where emission is confined to a shallow layer and (b) weak VUV absorption in the fluorescent sample.

The capabilities of fluorescent glass under 157nm laser excitation described below were investigated first using several standard glasses (fused silica, soda glass, Pyrex glass and lead glass) of which fused quartz proved most suitable, though of poor emission efficiency. Attention then shifted to Lumilass G9, a special fluorescent glass. The fused silica was a standard material (VF-IR clear fused silica) and though no information was available on the origin of its fluorescence, this likely arises through impurities in the sample. As fused silica remains moderately transparent at 157nm, the emission will occur over a finite depth of material which limits resolution (Figure 6.1b).

The Lumilass G9 sample was obtained from Sumita Optical Glass Incorporation, Japan and was a plate of 70mm x 50mm and 3mm thick. This glass has a composition $B_2O_3.CaO.SiO_2LaO_3:Tb^{3+}$ and it is the rare earth Terbium ion that is the fluorescent species. It is highly transparent in the visible where its refractive index is 1.694; its thermal and mechanical properties are summarised in Table 6.1. According to the Sumita Optical Glass Incorporation, it has excellent properties for UV use;

- High sensitivity to UV radiation and conversion to visible radiation. A minimum sensitivity of $1\mu Wcm^2$ is quoted.
- High durability as it does not readily decompose under UV exposure since the light emission of the rare earth terbium ion is used which is much more stable than organic or other inorganic phosphors.
- A wide UV excitation range that extends into the VUV.

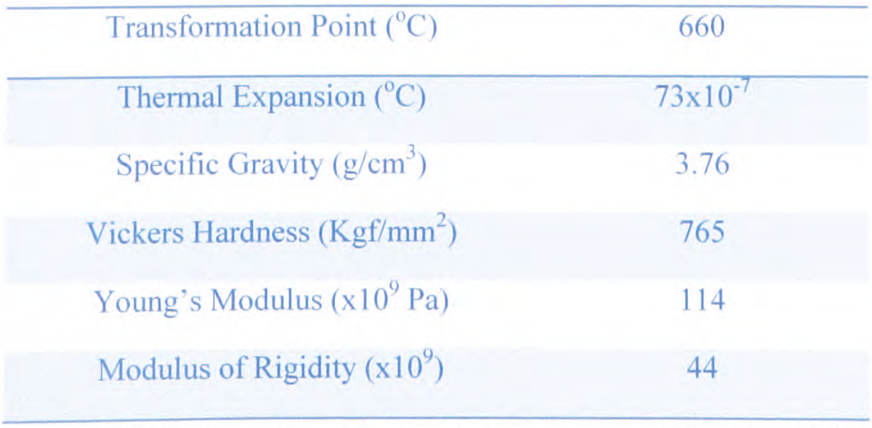

Transformation Point (^oC)	660
Thermal Expansion (^oC)	$73x10^{-7}$
Specific Gravity (g/cm^3)	3.76
Vickers Hardness (Kgf/mm^2)	765
Young's Modulus ($x10^9$ Pa)	114
Modulus of Rigidity ($x10^9$)	44

Table 6.1: Thermal and mechanical properties of Lumilass G9 glass

Efficient fluorescence emitters of this type are of interest in a number of areas including optical tagging technologies [2] and work on them has also extended into the VUV because of potential applications in Hg-free lamps and plasma display devices. For example, previous work on a similar glass has included 160nm VUV excitation where it has been concluded by Liu *et al* [3, 4] that absorption is likely due to the host glass, with subsequent energy transfer of excitation to terbium which then emits in several narrow visible bands, the strongest being around 540nm.

A conference report by Otani *et al* [5] describes preliminary studies of Lumilass G9 with 157nm laser excitation where use is made of this for beam profiling and for displaying fringes in a VUV Michelson interferometer. The linearity of response is reported, though not in terms of laser fluence or irradiance per pulse but 'average UV power'. The authors state that terbium is distributed as nanocrystals at a surface density of $10^{23}cm^{-2}$ with an average ion-ion spacing of 1nm, suggesting that spatial resolution will not be limited by the material itself. In other work Shivastava *et al* [6] have reported work on Lumilass G9 for fluorescence beam profiling of the 308nm XeCl laser. A good linearity of response was found and though their result is not quantified it can be assumed linearity extends at least to $100mJcm^{-2}$ for 308nm excitation. A measured emission lifetime of 18μs was obtained. They found the material was not damaged by ablation at fluencies up to a least $100mJcm^{-2}$. Exceeding the ablation threshold is clearly undesirable in an imaging application as this would irreversibly damage the surface. No studies of ablation were carried out in the present work but it can be conjectured that the damage threshold will be considerably lower at 157nm than 308nm because of stronger absorption. Saturation of the fluorescence emission (i.e. non-linearity) will anyway likely occur at fluencies well below the ablation level, so this aspect was not pursued further.

6.1.1 Experimental arrangement for the fluorescence study

The properties of the glass in responds to the emission at 157nm VUV laser were carried out using high resolution spectrometer ocean optics (HR2000CG-UV-NIR). The experimental set-up, shown in the schematic diagram in Figure 6.2 was used with fibre optic cable placed in front of the glass to record the intensity of the fluorescent light emitted by the glass.

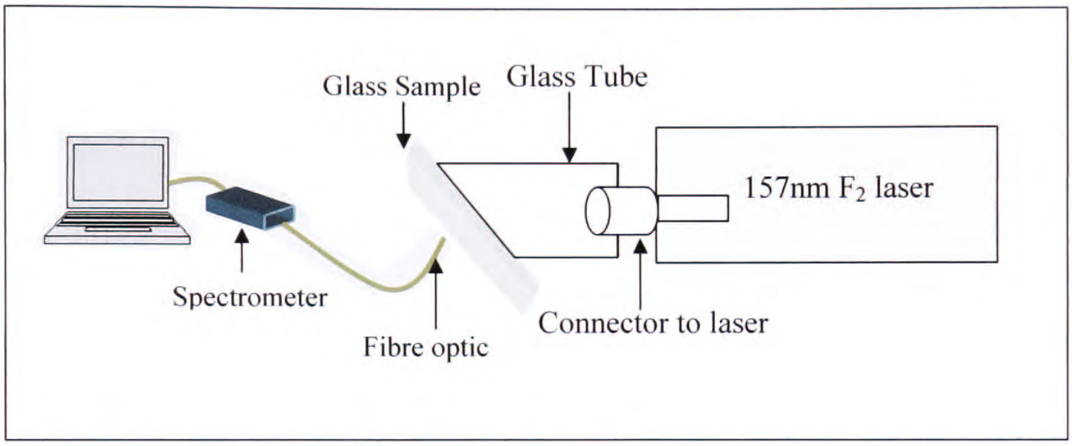

Figure 6.2: Schematic diagram for the emission spectroscopy measurement, with the spectrometer placed in front of the fluorescent glass.

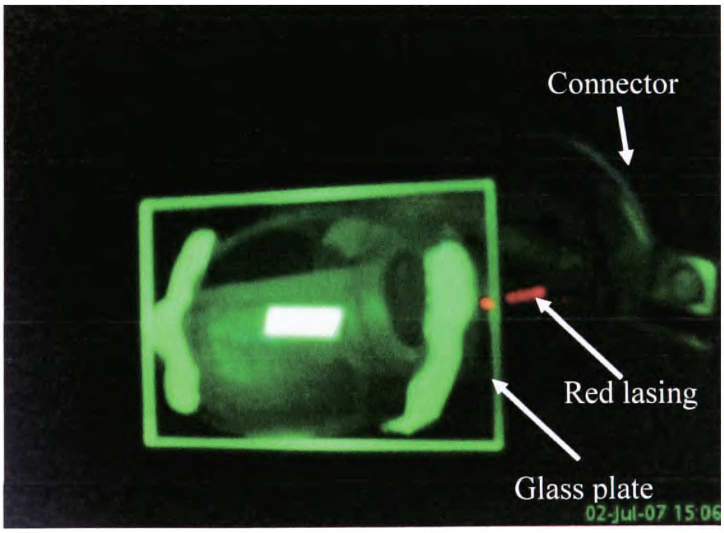

Figure 6.3: A Lumilass G9 glass fluoresce using argon flow F_2 laser in the dark.

The schematic diagram in Figure 6.2 shows the glass used was attached to the cylindrical glass tube at an angle of 45°. The cylindrical glass tube had a diameter of 4cm and upper length of 9cm was connected to the F_2 laser beam delivery tube. Flowing Argon gas was passed through the delivery tube to permit transmission of the VUV laser radiation shown in Figure 6.3 with sampling area fluorescence of 5mm x 10mm.

An optical fibre collected fluorescent emission from the plate and transmitted this to the spectrometer. The magnitude of specific emission feature was monitored and its variation with incident VUV laser energy was recorded.

6.2 Results and Discussions

6.2.1 Fused silica glass

Fused silica glass is a transparent material that exhibits a blue-violet fluorescence emission when irradiated at 157nm. The fluorescence arises because molecules absorb the high energy photons and then emit lower energy photons through transitions to different levels. The emission spectrum with varies in fluences from 1.7-4.3mJcm^{-2} is shown in Figure 6.4.For fused silica glass, no further investigations was carried out because of the quality of the glass in respect of the emission spectra results obtained gives low signal noise because of week fluorescence.

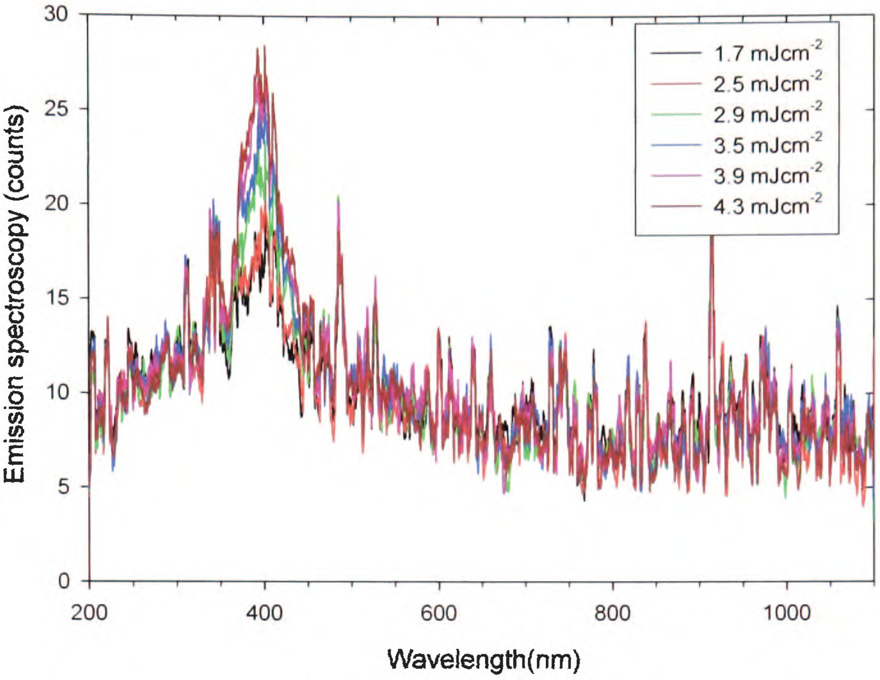

Figure 6.4: Emission spectrum of fused silica glass sample as a function of fluences with 157nm laser excitation.

Emission spectrum in Figure 6.4 shows the prominent blue-violet fluorescence light at about ~300nm to ~500nm wavelength. The spectra give low signal noise at this wavelength. The variation of signal strength (counts) of the fused silica glass plate in response to the fluence of the fluorescence light was plotted, shown in Figure 6.5, which shows the result obtained from the mean emission value from spectroscopy with the change in fluence of the laser. In Figure 6.5 the data produced inconsistent results for the mean intensity (counts) against the fluence. The data shows slight different with increasing fluences as ~20counts up to highest fluence for fused silica glass under 157nm excitation.

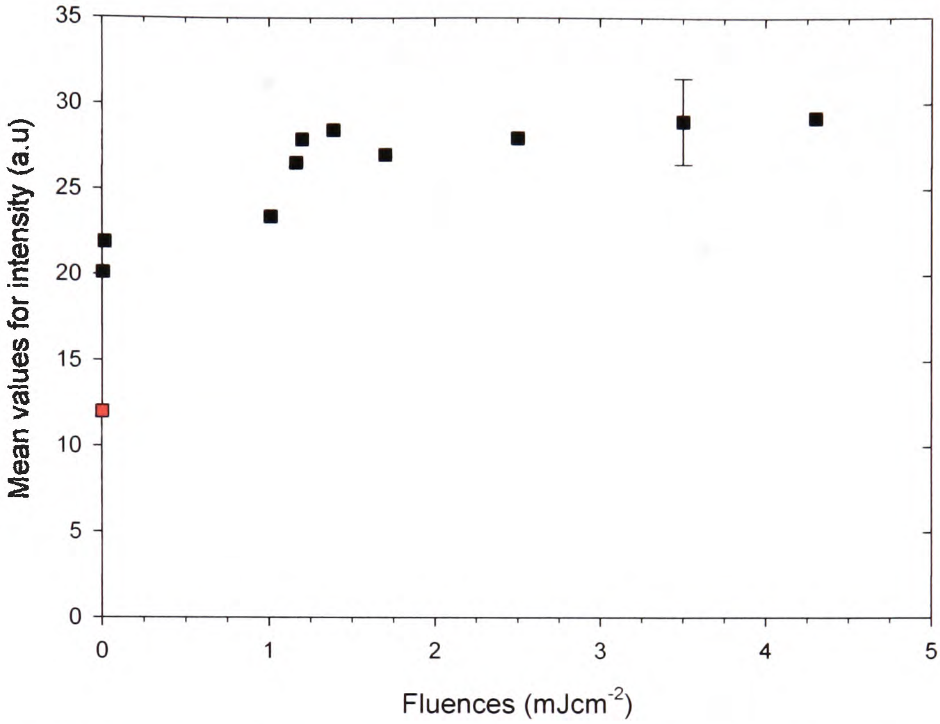

Figure 6.5: Fluorescence intensity of quartz glass as a function of fluence at 157nm laser with a red data point as background noise.

6.2.2 Lumilass G9 glass

Figure 6.6 shows the emission spectrum of Lumilass G9 glass under VUV excitation of 157nm. This glass obviously converts VUV to a predominantly green fluorescence light when the light incident on the glass plate. The graph shows how the strength of the bands varies with different excitation fluences from 1.0mJcm^{-2} to 5.3mJcm^{-2}. The prominent band of fluorescence is at 544nm, followed by the band peaks at 490nm, 588nm and 622nm.

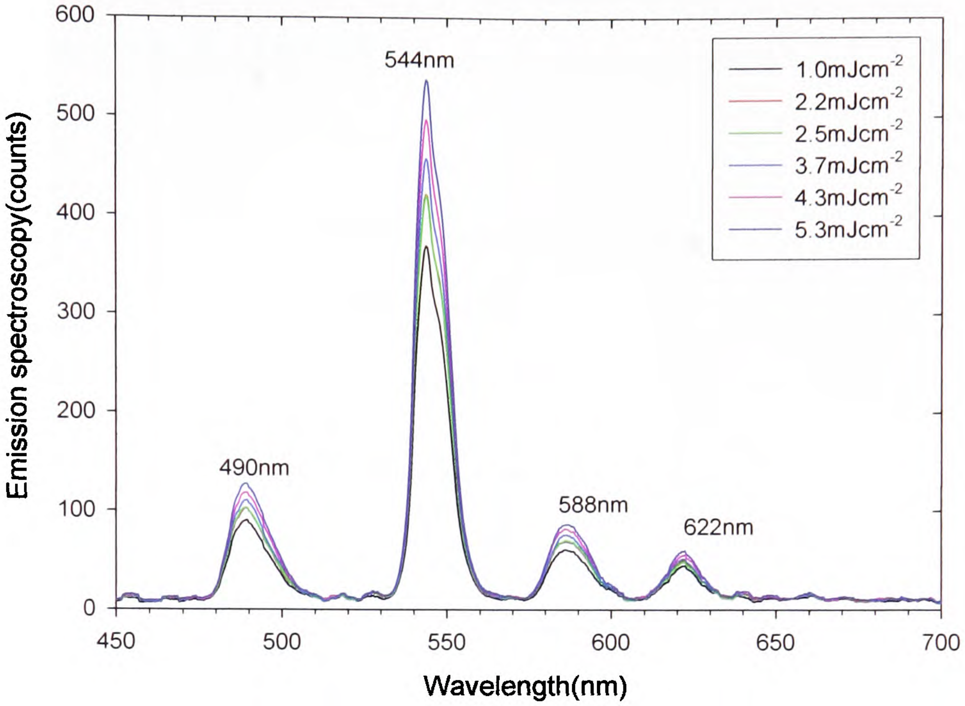

Figure 6.6: Fluorescence spectra of Lumilass G9 glass at 157nm excitation, which show main fluorescence wavelength at 544nm with varies in fluences.

Under vacuum ultra violet (VUV) the trivalent excitation rare earth Tb^{3+} ion clearly has the most intense band situated at 544nm, which corresponds to the $^5D_4 \rightarrow {}^7F_5$ transition. The configuration of the Tb^{3+} ion is $4f^8 5s^2 p^6$ [7]. The emission from the Tb^{3+} ion mainly originates from $^5D_4$ to ^7F_J where J = 6,5,4,3. From Figure 6.6, at 490nm, they belong to the transitions of the ground state $^7F_6$ to $^5D_4$. The most intense band at 544nm is the transition from $^5D_4 \rightarrow {}^7F_5$ based on lasing in $LiYF_4$ host emission at 544.5nm, terminal level is ~2000cm^{-1} and 5ms lifetime [7].

The designation in Figure 6.7 and Table 6.2 show $^{2S+1}L_J$ where S is the spin quantum number, L is the orbital quantum number and J=S+L. From the upper state level of ~20365cm^{-1}, shows the transitions of Tb^{3+} based on the fluorescence band in Figure 6.6 respectively.

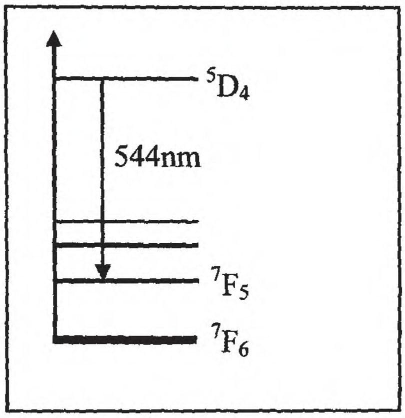

Figure 6.7: Tb^{3+} transition state from $^5D_4$ to ground state $^7F_6$

From the excitation state in Figure 6.6, Table 6.2 below shows the transition state of Tb^{3+} ion to the wavelength emission respectively [7].

Upper state	20365cm^{-1}
$^5D_4 \rightarrow {}^7F_6$	490nm
$^5D_4 \rightarrow {}^7F_5$	544nm
$^5D_4 \rightarrow {}^7F_4$	579nm
$^5D_4 \rightarrow {}^7F_3$	622nm
$^5D_4 \rightarrow {}^7F_2$	650nm

Table 6.2: Transition of electron state and related wavelengths.

Figure 6.8 shows the relation of the intensity of the luminescence on the glass to the fluence of the VUV laser. The minimum signal to noise ratio was 200:1: which resulted in the counting errors were always being less than 1% in this work. The intensity of luminescence increases linearly at lower fluence (~less than 1mJcm^{-2}) up to as high as ~ 500 count intensity, and shows saturation effects for the fluence higher than 1mJcm^{-2}. The details study (inset graph) at lower fluence (~less than 0.5mJcm^{-2}) confirms the intensity of this glass increases linearly at this region agreed with earlier work reported [5] that the fluorescent intensity of this glass is almost linear. The intensity of background noise recorded as much as ~12 counts. To obtain lower fluence, up to two attenuators (Shin-Etsu glass) with transmission loss as 72% were placed in front of the glass plate. The chemical composition in this fluorescent glass is based on optical glass which has high transparency for the visible light. However, the Lumilass G9 glass easily absorbs the vacuum ultra violet light used in this work, hence limits fluorescent emission to a thin surface layer [5].

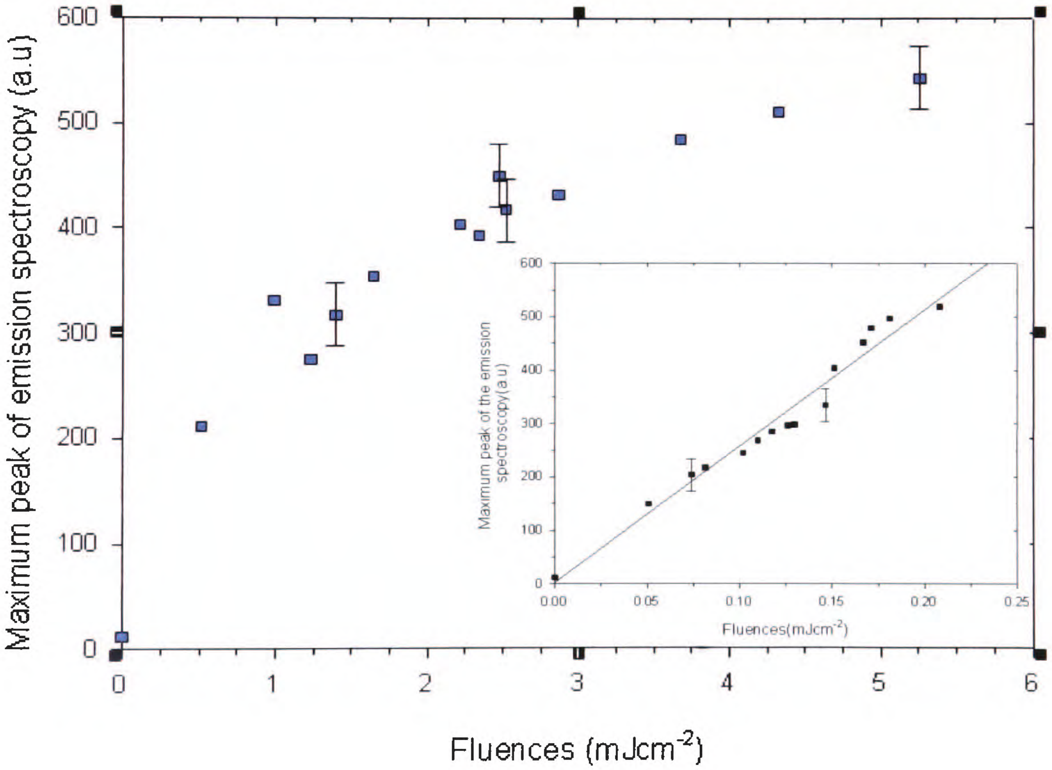

Figure 6.8: The fluorescence intensity of the Lumilass G9 glass as a function of fluence of the VUV excitation at 157nm F_2 laser.

6.3 Beam Diagnosis Experimental Arrangement

A photograph of experimental arrangement for the beam characterisation of the F_2 laser is shown in Figure 6.9 where the glass plate placed on the rail in the vacuum environment and schematically shown in Figure 6.10. The irradiance distribution of the output beam was measured using a CCD camera (OPHIR BeamStar profiler V-PCI), size aperture of 6.4mm by 4.8mm corresponding to 320 by 240 pixels at both dimensions respectively. The experimental arrangement used consists of the fluorescent glass plate that converts the VUV to visible emission when is then imaged using a lens and CCD array detector to obtain the two-dimensional profile of the beam. A trigger circuit sent signals to a computer that controlled the laser firing sequence, and also the framestore in the CCD profiler software that synchronized the capture of a video image to the start of the CCD camera. The CCD images using this software provided the information for recording the direct beam profile and also profiles of weakly focussed VUV laser spots. Intensity profiles were recorded as bmp format images and the images could be read into MathCAD for further characterisation and analysis.

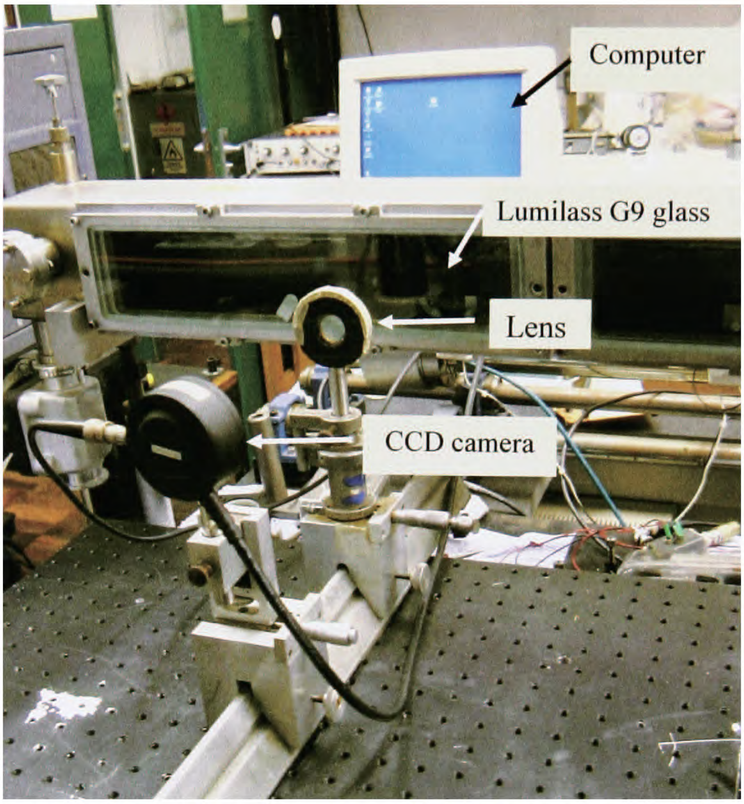

Figure 6.9: Picture of experimental arrangement for beam profiler using VUV F_2 laser.

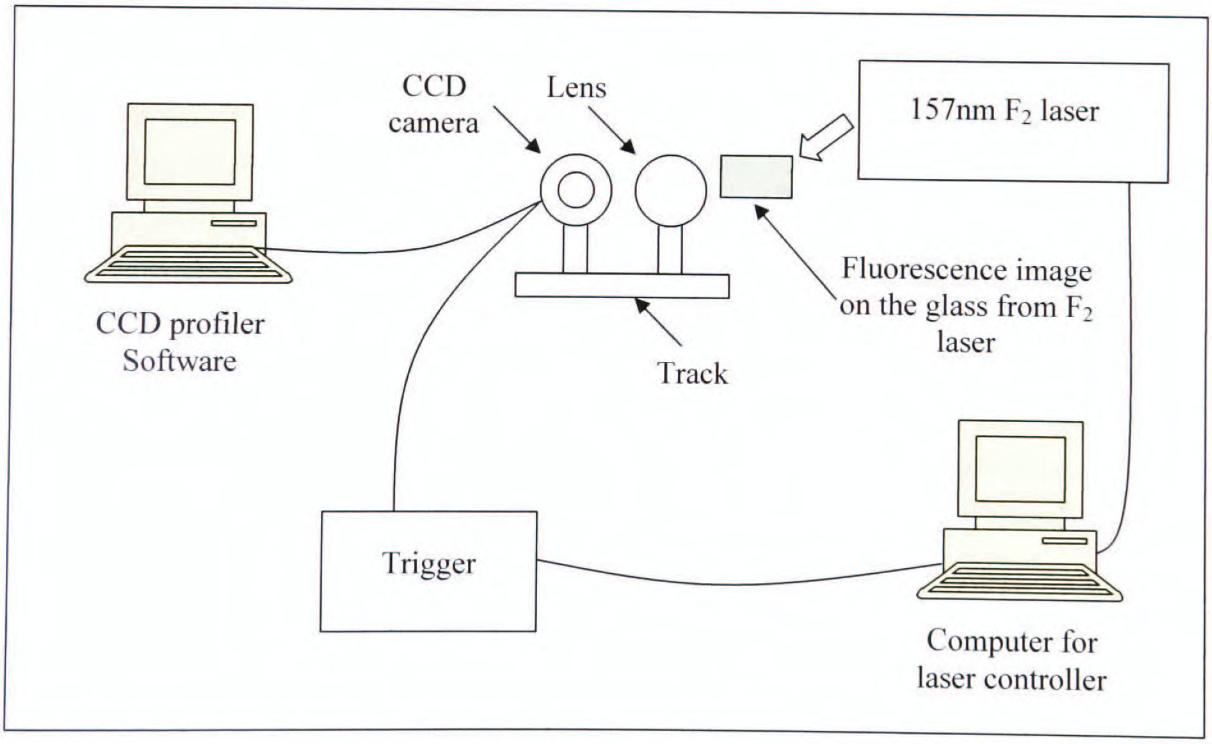

Figure 6.10: Schematic diagram of the experimental arrangement used for the process of recording the fluorescence images on the CCD profiler software.

Beam diagnostics systems for the VUV F_2 laser, require reasonably high spatial resolution [1] and thus the system must have an adequate detector adapted to the near-field cross section and, more importantly, the optics and sensors have long term stability under the pulse irradiation.

In the present work, the optical set-up was mounted in the air and the images were recorded through the 157nm coated radiation mirror placed on the vacuum tube rail. The far-field beam was produced using a CaF_2 lens with focal length of 200mm to minimize errors caused by spherical aberration. Filters were used to block red lasing emission from fluorine before the profiles of the distributions were recorded simultaneously on 6.4mm x 4.8mm size aperture of the CCD camera.

6.3.1 CCD camera

Charge couple device (CCD) camera consists of an array, which the element of the array is called a photo-detector junction or photosite. CCDs are compact and highly sensitive to light. Photosites on a CCD are composed in columns and lines which the size of photosites range between 3 to 25 microns depending on the design of the detector [8]. The CCD camera used in the system has 320 by 240 pixels on the size aperture of 6.4mm by 4.8mm. It is a serious matter to ensure the adequately used of the CCD camera relates to the pixels number. In this work, on the x dimension, this has 320 pixels at 6.4mm size of the CCD camera, giving 50 pixels per mm or 50 lines per mm. The minimum spacing to distinguishable lines or dots referred to the resolution of the image, that 50 lines or dots per mm is appropriate condition in obtaining and analyzing results by using this technique [9].

An enlarged image will show good resolution for example in the Figure 6.14, if the pixels are resolved to about 10 pixels per mm. Therefore, the analysis obtained from the MathCAD for Figure 6.14(a), one full period is 900μm in 50 pixels giving 20μm per pixels resolution which shown the adequate way to gain good resolution results by using CCD camera.

6.3.2 Background assessment for CCD

With the CCD under dark conditions there is a still a voltage level on pixels that can essentially be attributed to dark current. An example of the corresponding background (dark) image is seen in Figure 6.11, together with sample readout from pixels along a line in the X direction. The mean level in this example is 12.9 for the 320 pixels, with a standard deviation of 0.43 or uncertainty of approximately ±3.3%. As the manufacturer specifies a spatial uniformity of ±0.5% for the CCD it can be assumed that this arises from fluctuations in the dark level. Before analysing profiles recorded using the imaging system corrections were applied by subtracting the background from the recorded image.

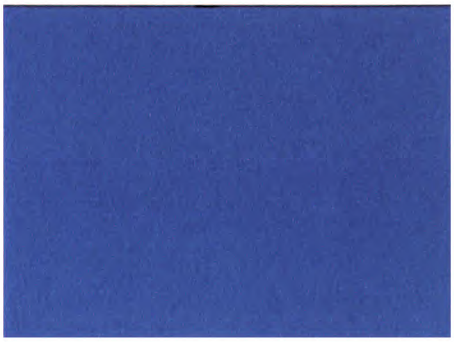

(a)

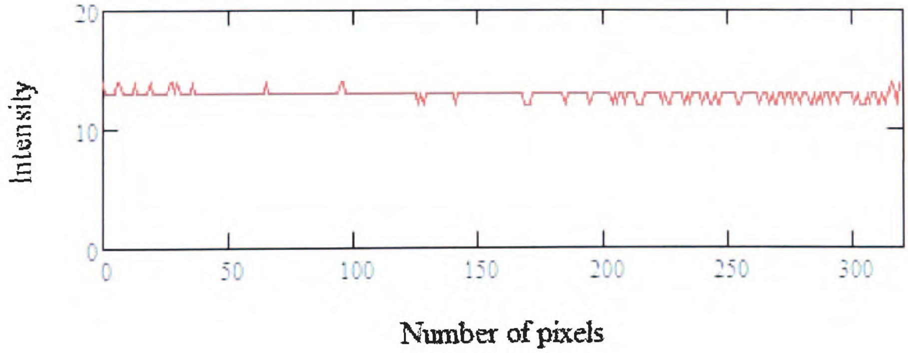

(b)

Figure 6.11: (a) Background recorded in the dark on the CCD camera and (b) MathCAD analyzed on the X direction.

6.3.3 Calibration of imaging system

To calibrate the CCD imaging system a copper grid (S450 B450) with 450μm wide openings and 450μm bars giving a period of 900μm (Figure 6.12), was contacted to the surface of the Lumilass G9 glass plate. The plate was mounted on the glass window on the beam delivery tube and a 157nm mirror oriented at 45° to the beam axis was used to turn the F_2 laser beam onto the grid/G9 plate. This excited fluorescence in a bar pattern that could then be imaged onto the CCD. A red filter was mounted in front of the CCD and a lens used to produce an image of the grid on the CCD at a magnification of 2× shown schematically in Figure 6.13. The images were recorded on the CCD profiler software in AVI and BMP files. The images on the AVI files for several shots were transferred to Video Decompiles application which extracted the video images of each shot of frames. These images were then read and analysed in MathCAD.

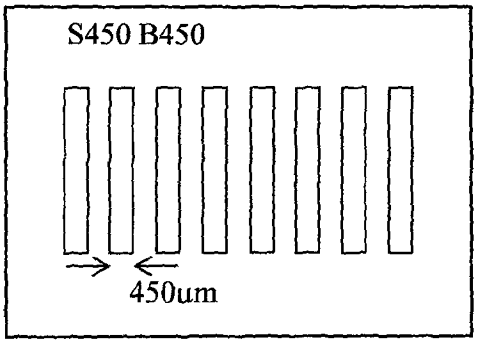

Figure 6.12: Grid of S450 B450 with the distance 450μm apart.

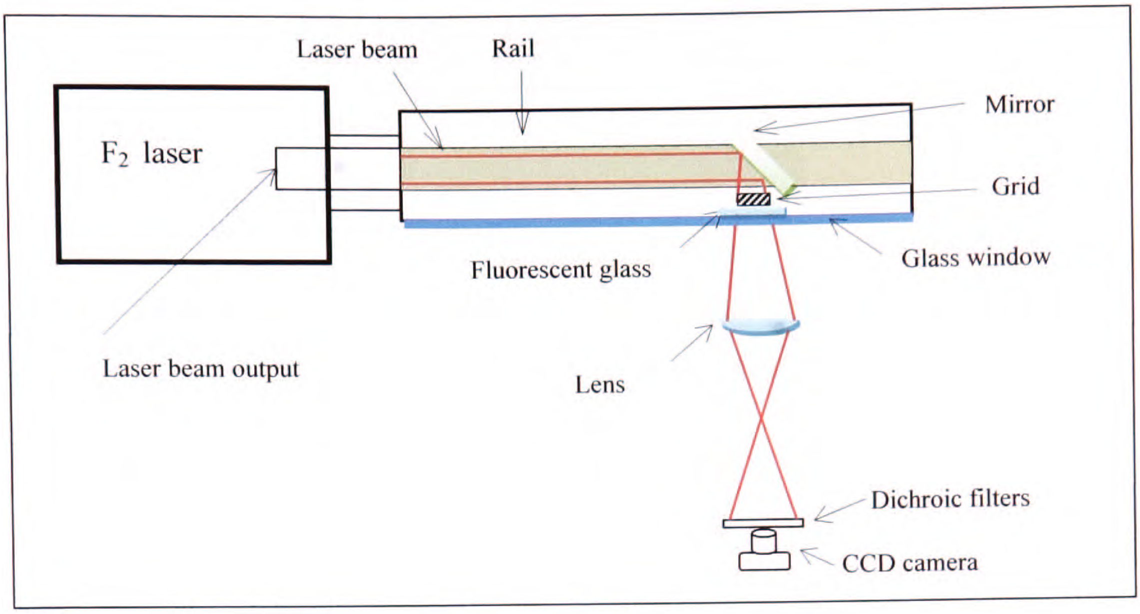

Figure 6.13: Schematic diagram for the calibration of the CCD camera with magnification by 2.

A 120mm focal length lens spaced a physical distance of 180mm from the grid was used for image formation on the CCD, and to minimise spherical aberration, its aperture was restricted to give an *f*-number of 6. This enabled relatively clear, sharp, images, Figure 6.14a, to be produced at nominally 2× magnification, neglecting optical shifts in the fluorescence plate and window glass on the beam delivery tube. The profile of the irradiance is seen in Figure 6.14b and whilst the spaces (bright regions) are well defined there is considerable light leakage in the regions that should be dark. This is well above the typical background for the CCD and may possibly arise because of reflections and scattering when fluorescence is viewed through the plate, Figure 6.15.

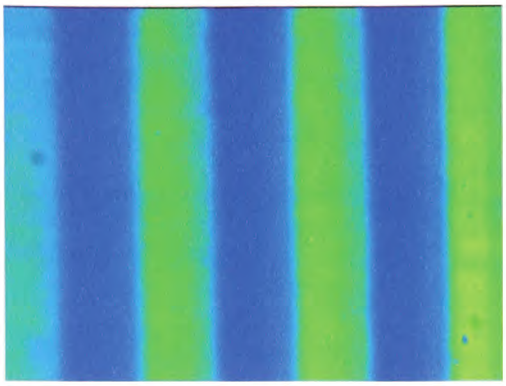

(a)

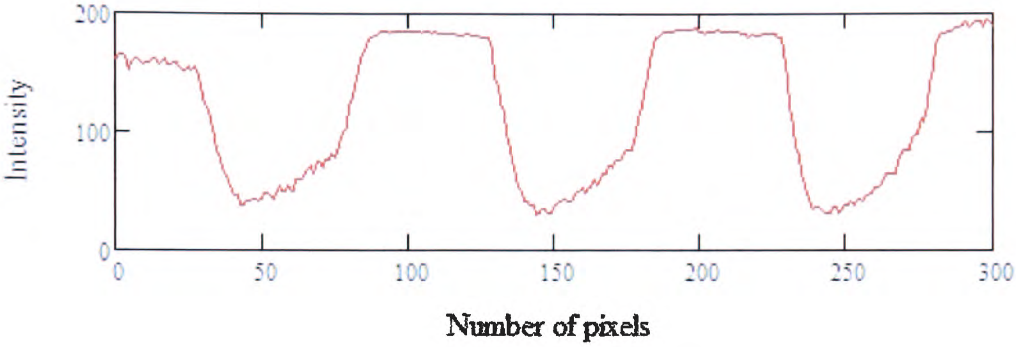

(b)

Figure 6.14: (a) Image taken at magnification of 2 by using 2cm diameter lens for better resolution with (f #6) and (b) profile of the grid read from the MathCAD across X dimension with background subtraction.

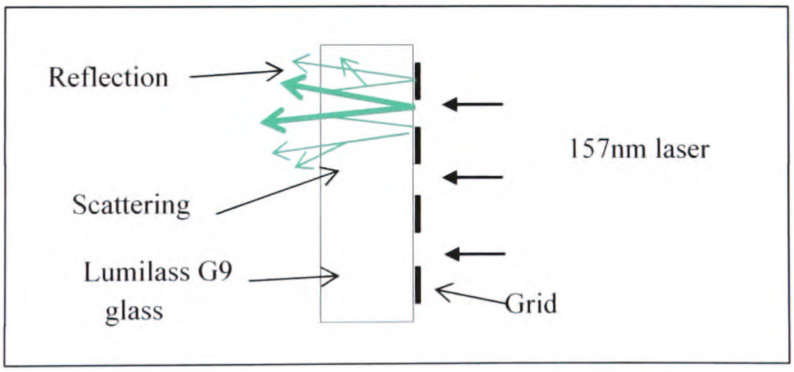

Figure 6.15: Reflection effects in Lumilass G9 glass plate that could influence image fidelity.

The magnification of the system was checked from the known grid period and the known spacing of 20 μm for pixels on the CCD. A value of 2.2× was obtained in this way compared with the calculated value of 2× based on the nominal focal length of the lens of 120mm. This true value is higher than that calculated because the latter neglected the refraction in the Lumilass G9 glass plate and optical window.

6.4 Experimental Arrangement and Results

6.4.1 Divergence Measurement

This section describes measurements of the divergence of the highly multimode F_2 laser, based on measuring the size of the output beam at various distances from the resonator output window. The beam divergence obtained experimentally from the F_2 laser was measured using beam patterns taken on the heat-sensitive paper or thermal paper at various distances from the output laser. The thermal paper used for this objective offers a convenient method for detecting the beam shape and it is more convenient to detect the alignment of the beam. However, thermal papers have small dynamic range and non-linear thermal properties which, means this method gives only a tentative idea of the shape of the incident radiation of the laser and is unable to provide qualitative intensity profiles for further analysis. Therefore, for the divergence measurement and to determine the intensity profile of the beam, the experiment was concentrated on recording the images of the beam via the Lumilass G9 fluorescent glass plate for the near-field profile.

For the far-field profile, the beam was brought to a focus using a CaF_2 lens with focal length of 200mm. The focal spot size of the beam provided information of determining the divergence (X: wider and Y:narrow directions) and hence an estimate of the spatial coherence of the beam [1]. The divergence measurement gives the spreading angle of the propagating beam i.e. how much it is diverging from a collimated parallel beam. Divergence is important because the lower its value, the longer the beam will remain at a given diameter. Nevertheless, beam divergence measurement is not providing the real characteristics of the beam, because the expanding beam will change the divergence value itself. For this objective, M^2 measurement can be supported in evaluating the performance of the beam [10].

Recording the beam profile distributions required a converter medium to enable conversion from VUV to visible light. Here, the Lumilass G9 glass plate described in the previous section was applied as a linear, uniform and UV-radiation-resistant converter medium. The optical set-up plays an important role here for the CCD camera to record adequately. Because of the sensitivity of the CCD camera, it is impossible for the CCD camera to sit parallel to the incident beam in the vacuum environment. Thus, the image of fluorescence beam was captured through the glass window on the CCD camera with the optical lens arrangement in air.

To determine the size of the direct output beam, the thermal paper was located at the distance of 800mm from the laser output, showing the direct output beam image of the 157nm F_2 laser. The burn pattern has shown (Figure 6.16) the beam to have a rectangular cross section at 800mm with dimension of 23mm and 7mm for the wider width (X) and narrow width (Y) respectively.

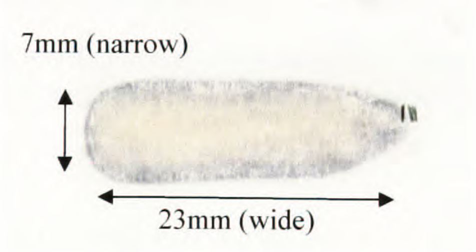

Figure 6.16: Burn pattern on the distance of 800mm away from the laser aperture with size of the direct output beam as 23mm (wide) and 7mm (narrow).

6.4.2 Beam divergence through the Lumilass G9 fluorescence glass

Figure 6.17 is shown the experimental arrangement for this experiment, where the beam image was captured by putting the fluorescence glass plate (Lumilass G9) parallel to the beam and the fluorescence light viewed through the glass window by using reflecting mirror in the vacuum chamber. The mirror was located at an angle of 45° behind the glass and the reflection of the beam was recorded through the glass window by using CCD camera. To read the image out from the CCD camera, it depends on the array of pixels, which produce output directly proportional to the amount of radiation they receive. By imaging on the aperture of the CCD camera array, and correlating the output of each pixel with their position in the array, the spatial distribution of intensity of the beam can be determined. The CCD camera based system enabled capture of intensity of the incident beam, in both the *X* and *Y* dimensions.

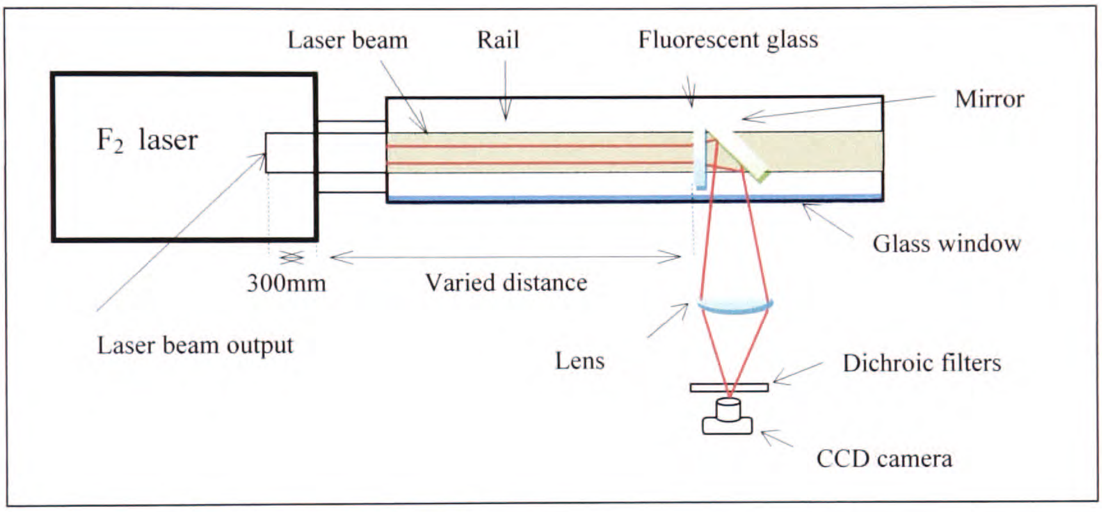

Figure 6.17: Schematic diagram of arrangement to capture images of the beam fluorescence at varying distance from laser output. Imaging onto the CCD used a demagnification a 7x.

CCD camera has limiting capability in capturing incident light, which at high intensity can cause saturation to occur. To overcome this problem, and for the CCD camera to capture only desired radiation from the fluorescent glass, it is necessary to eliminate any emission, which possibly more comes from the red lasing from fluorine. Figure 6.18a shows an example of a bright image captured on the CCD. Here, by keeping the CCD camera at low level intensity of light reached, the saturation effect from high intensity fluorescence can be seen when analyzing the bmp image read into MathCAD. The graph in Figure 6.18b shows the result from the bmp image in Figure 6.18a after subtracting the background value. From Figure 6.18a below, the saturation happen on the glass which provides evidence that this glass only linear at the certain energy as stated in the section 6.2.2.

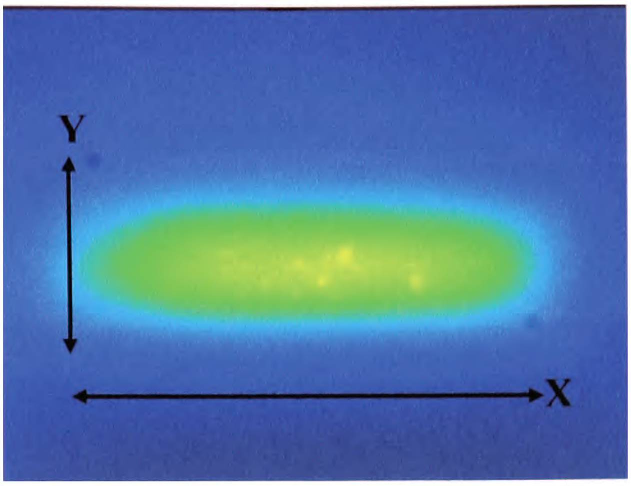

(a)

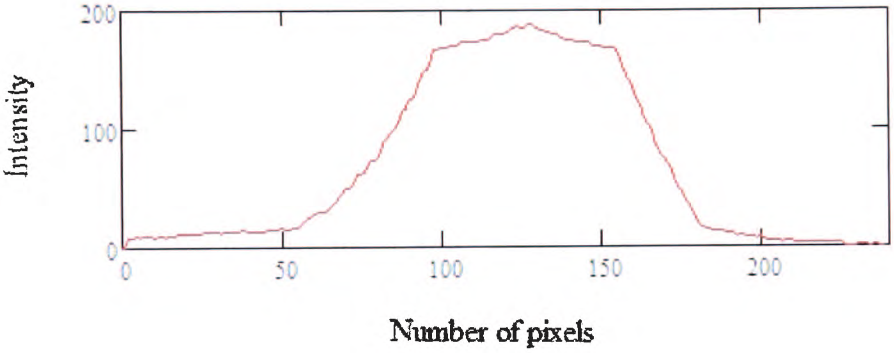

(b)

Figure 6.18: (a) Beam fluorescence image at 3.7mJcm^{-2} which gives bright image viewed on the CCD camera, arrows indicate the dimension for wider width (X) and narrower width (Y) and (b) graphical representation of intensity along Y dimension from the beam shown at (a), showing saturation occurred at high fluence.

To eliminate any red emission reaching the CCD camera, two dichroic filters (cyan and yellow subtractive filters) were placed in front of it. The images of the beam formed on the fluorescence plate were then recorded on the CCD camera attached to the computer. The fluorescent glass was then moved accordingly to the varied distance on the rail and the images were then recorded and analyzed. The distance ranged over 800mm, 900mm, 1000mm and 1100mm as measured from the laser output, where the shorter distance than 800mm were not possible because of constraint set by the beam tube.

The size of the direct output beam of the F_2 laser was 23mm by 7mm, which was too big to be captured by the size of the CCD camera aperture (6.4mm by 4.8mm), and thus the beam had to be de-magnified for the image to be recorded. The de-magnification was chosen to be by 7x, for the profile of the beam to be viewed. The distance from the fluorescence surface to the lens was 42cm (S_o) and the distance from the lens to the CCD camera (S_I) was 6cm with focal length of the lens was 5cm.

The images shown in Figure 6.19 (a -d) were taken and recorded on the software attached to the CCD camera at varying distances along the rail in the vacuum chamber. A measurement of the narrow and wider width of the beam was made from the profile analyzed in MathCAD. The example of the beam profile extract from MathCAD is shown only for the distance 800mm in Figure 6.19a. The demagnification of the CCD camera was set to ~7x. At the distance of 800mm from the laser output, the size of the beam on the narrow width is 7.2mm and wider width is 31.5mm. At 900mm, the narrow width is 7.6mm and wider width is 31.8mm is shown in Figure 6.19(b-d). At 1000mm away from laser output with narrow width is 7.7mm and wider width is 33.2mm and at 1100mm, the narrow width 8.03mm and the wider width 33.7mm.The images shown are based on a single laser pulse. To measure the size of the beam from the profile shown in Figure 6.19a, the widths were defined in terms of the full-width at half maximum points.

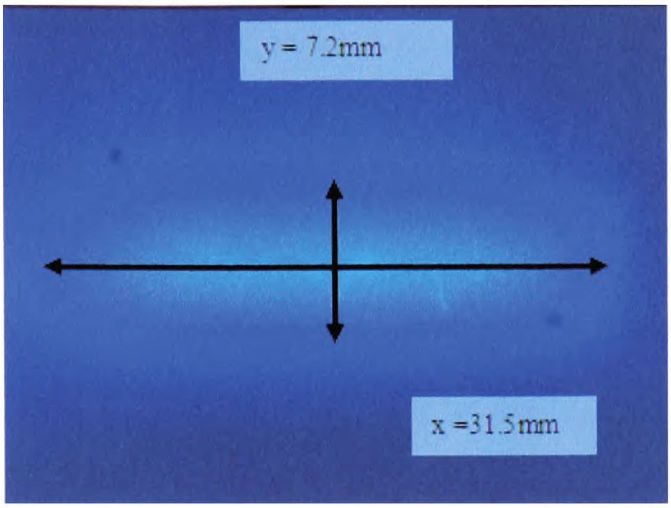

Figure 6.19(a): Beam image shown in the distance of 800 mm away from the laser output with Y (narrow width) of 7.2mm and X (wider width) of 31.5mm.

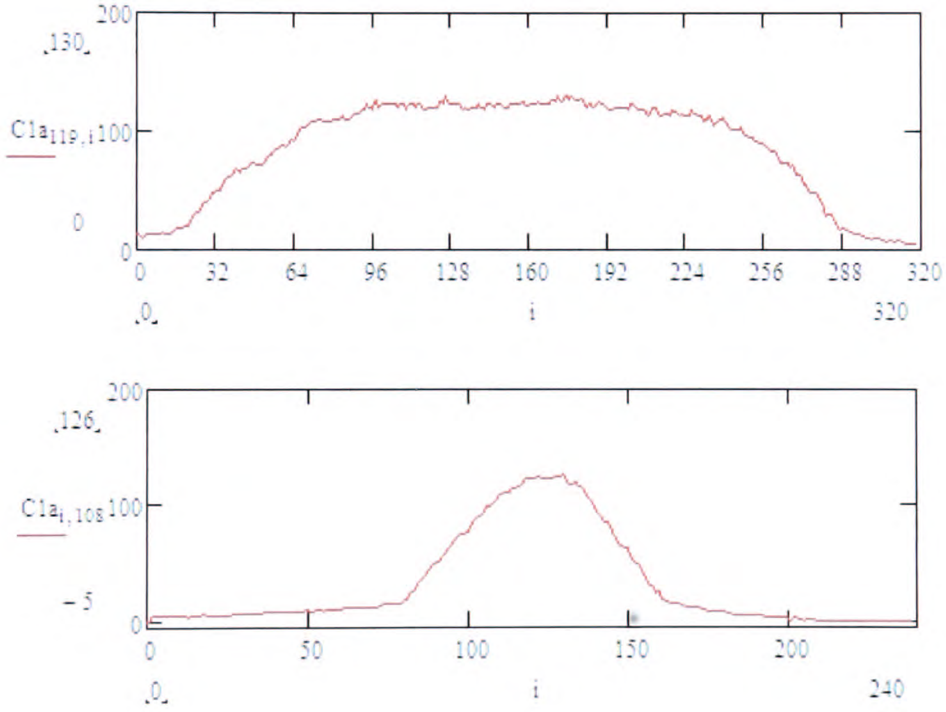

Figure 6.19: Cross sections of wider (top) and narrower width (bottom) for the beam extracts from Figure 6.19(a).

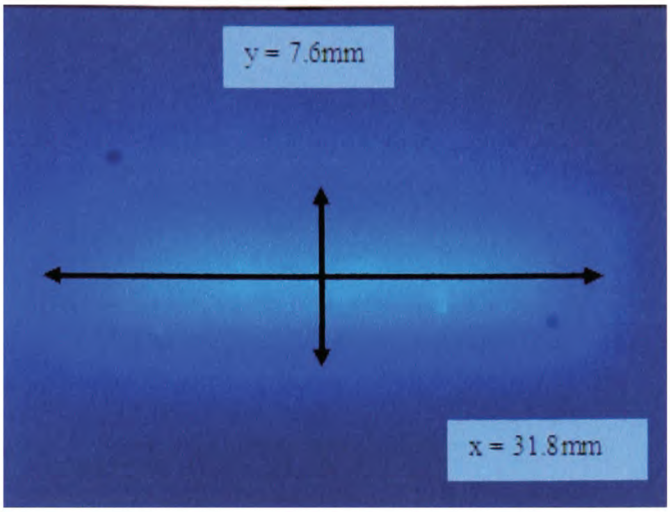

Figure 6.19(b): Beam image shown at a distance of 900mm from the laser output with Y (narrow width) of 7.6mm and X (wider width) of 31.8mm.

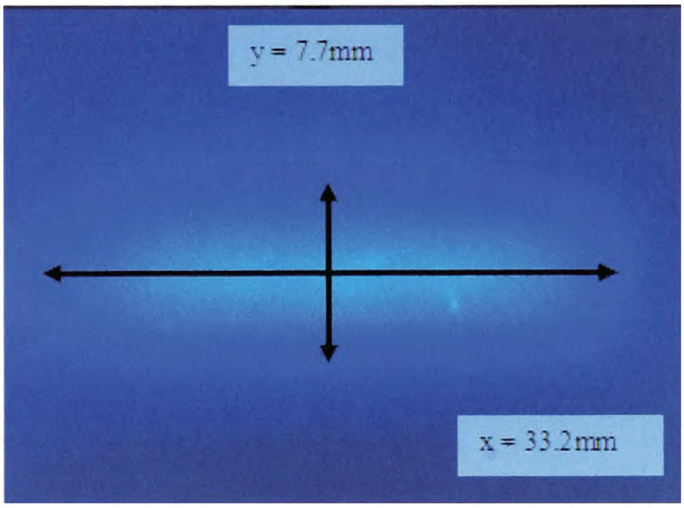

Figure 6.19(c): Beam image shown at a distance of 1000mm from the laser output with Y (narrow width) of 7.7mm and X (wider width) of 33.2mm.

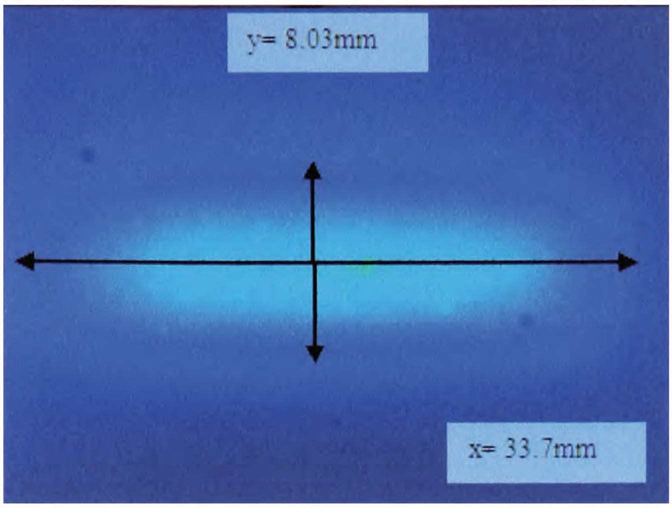

Figure 6.19(d): Beam image shown at a distance of 1100mm away from the laser output with Y (narrow width) of 8.0mm and X (wider width) of 33.7mm.

The beam sizes at various distances are plotted in Figure 6.20 enabling the divergence of the beam to be determined from the resultant slope of the graph. For the beam width (FWHM) values on the narrow width (*Y* dimension), the value of the divergence is 2.7mrad. The divergence for the orthogonal direction is shown in Figure 6.21 and gives a divergence of 7.9mrad.

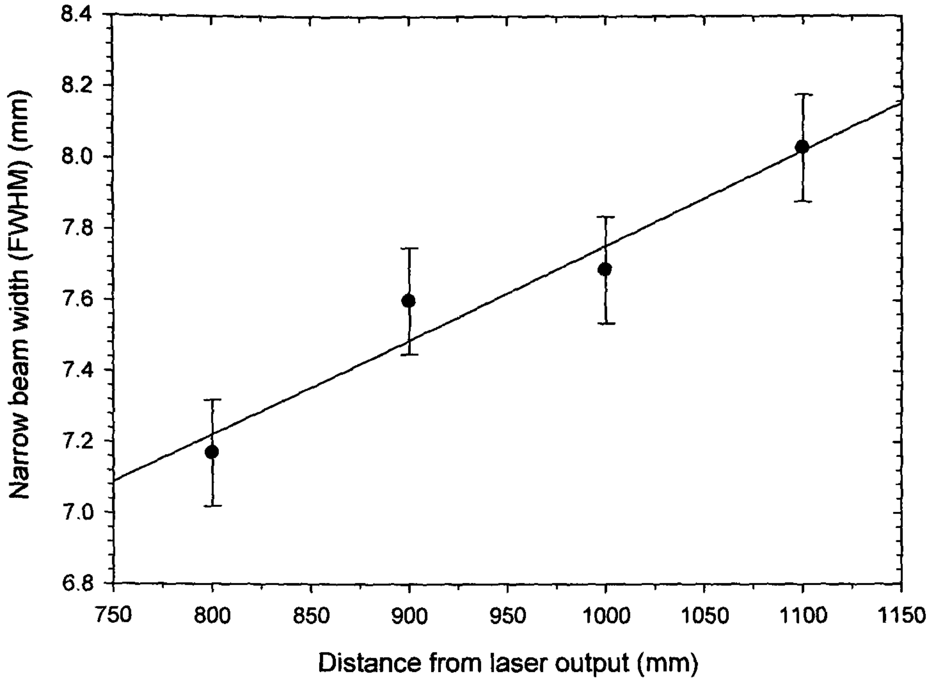

Figure 6.20: Narrow width of beam plotted versus distance giving a divergence of 2.7mrad for the 157nm laser.

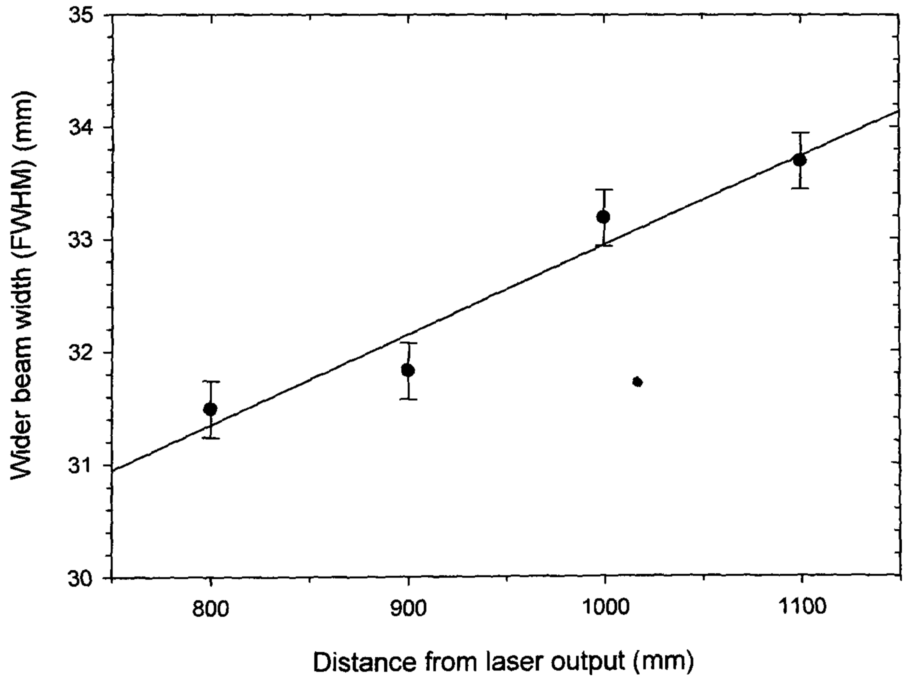

Figure 6.21: Wider width of beam plotted versus distance from which a divergence of 7.9mrad is found for the 157nm laser.

6.5 Analysis of Beam Fluctuations

In the present work one of the matters of specific interest was the extent to which surface roughness on ablated materials is influenced by intrinsic mode fluctuations with the 157nm laser i.e. coherence effects. Previous work [11] has reported a preliminary attempt to measure such fluctuations using a small diameter aperture to sample a fixed point on the output beam so as to allow a measurement of pulse-to-pulse fluctuations. With this approach it is difficult to correct for pulse-to-pulse fluctuations in laser output that are unconnected to mode 'noise' e.g. possibly arising from changes in excitation voltage, discharge quality of the laser etc. In the present studies the objective was to use the fluorescence plate imaging technique to characterise the magnitude of spatial fluctuations on the multimode beam for images acquired using single pulses.

To do this a region of dimensions 10mm × 10mm was selected the F_2 laser beam by use of an aperture and this region was reflected onto the Lumilass G9 plate using a mirror as illustrated in Figure 6.22. The fluorescence image was then recorded using the CCD with a 2× magnification being used to improve the spatial resolution. The two-dimensional spatial image was captured as a bmp image for a single pulse, imported into MathCAD and, after correction for background noise, analysed statistically.

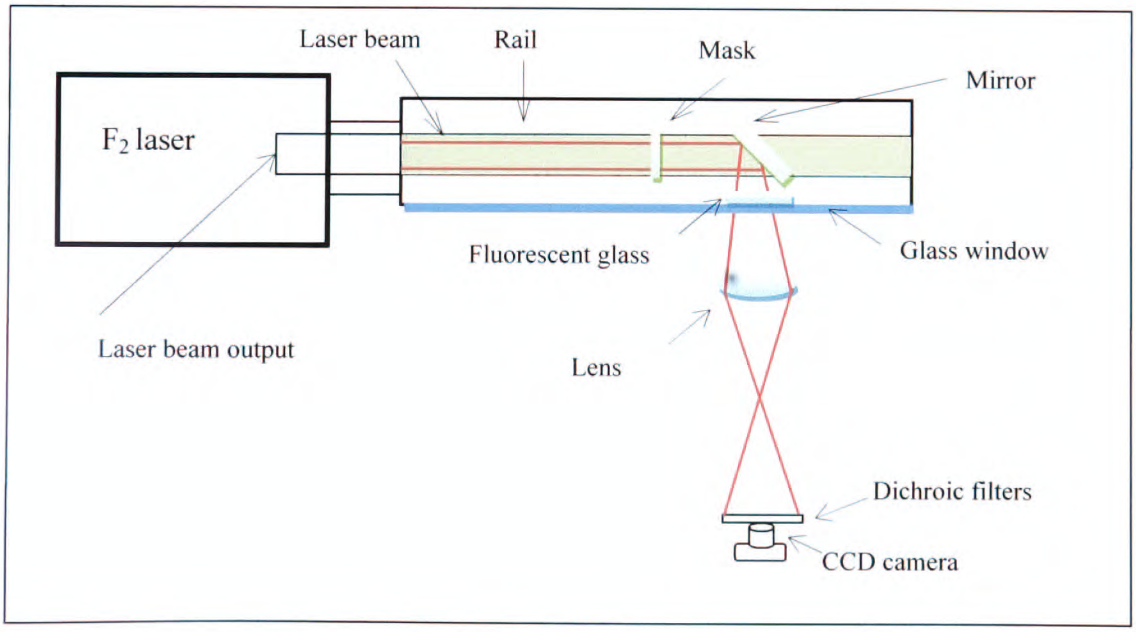

Figure 6.22: Schematic diagram of the fluctuations analysis which 10mm by 10mm mask placed on the rail.

Visually the images acquired in this way appeared quite uniform as is evident from the example shown in Figure 6.23a for the selected region involved. The quantified pixel levels, however, showed a degree of fluctuation as seen from the examples in Figure 6.23 b and c for pixel rows in the direction of *X*, the wider dimension and *Y*, the narrower dimension, of the F_2 laser beam.

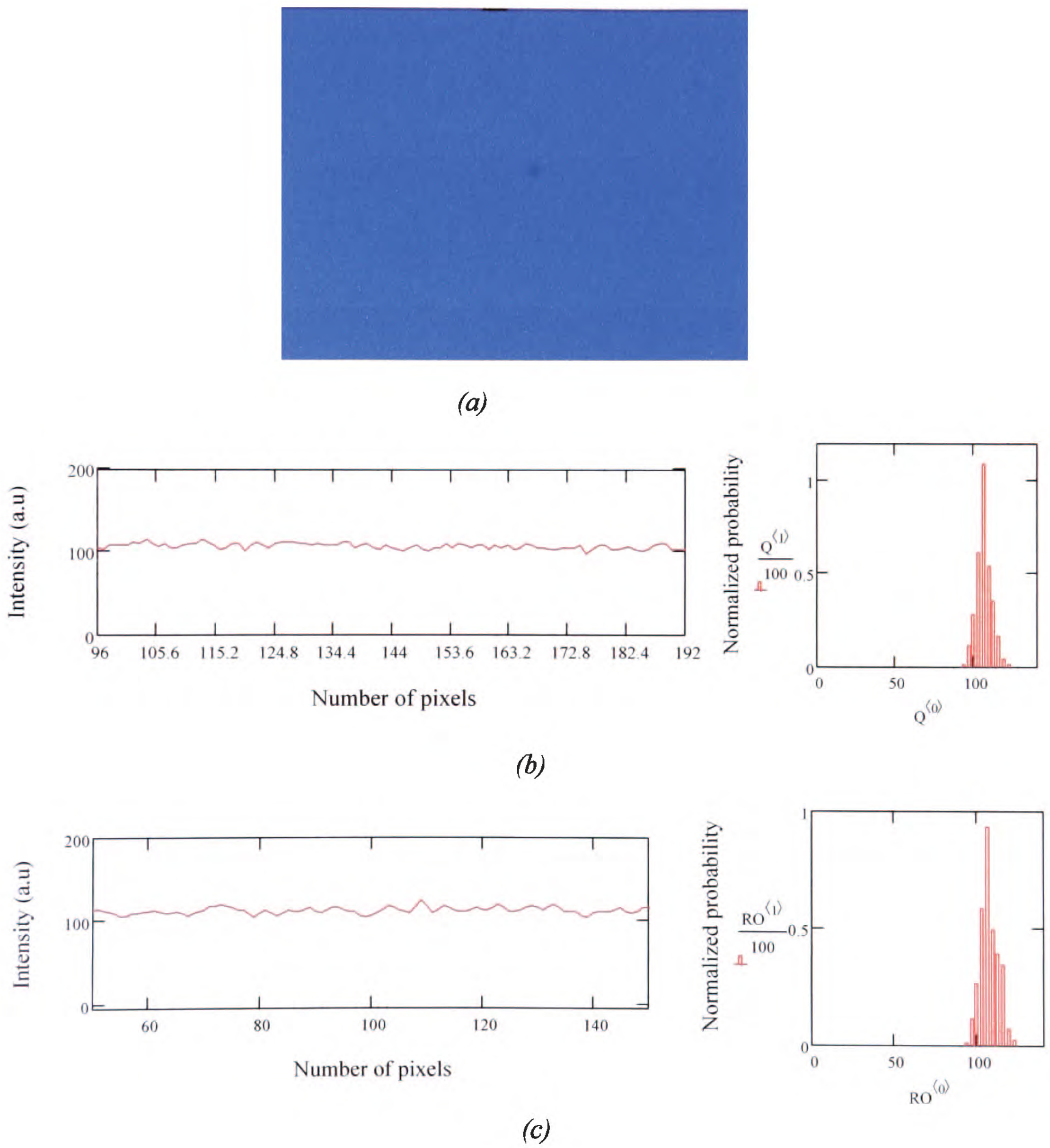

(a)

(b)

(c)

Figure 6.23:(a) Bmp image of the selected area beam captured onto the CCD camera from the fluorescent glass (b) Fluctuations profile of the cross section for the wider width (X) and (c) cross section for narrow width (Y) and histograms show the spatial fluctuations where Q and RO are only mathematical symbols.

Also shown is a histogram representation of the spatial fluctuations. Fluorescence images were recorded for various laser output energies and thus fluence on the plate. To minimise the contributions from the small but significant change in mean laser fluence and hence fluorescence amplitude over the image at the CCD, averaging and statistical characterisation was carried out on restricted groups of adjacent pixels and the ratio $\sigma/<m>$ = (standard deviation/mean) was obtained. This was repeated over typically 5 intervals across the CCD image and these were then used to produce an average value for $\sigma/<m>$. The several data points show at different points of the beam. For an F_2 laser fluence of ~0.5mJcm^{-2}, a level at which the Lumilass glass should remain essentially linear in its fluorescence response, the averaged single-pulse spatial fluctuation was $\sigma/<m> = 3.1\%$ (standard deviation /mean). The plot in Figure 6.24 show $\sigma/<m>$ for the X and Y directions of the beam with various F_2 laser operating voltages to change the fluence on the fluorescent plate. It appears there is little change in the average $\sigma/<m>$ as the fluence is raised; it should be kept in mind, however, that at the higher fluencies a degree of fluorescence saturation is likely which could act to compress the amplitude of fluctuations. The use of attenuator plates was deliberately avoided in this part of the work because of concerns that they could introduce fluctuations that would be difficult to characterise i.e. through inhomogenieties, scattering etc.

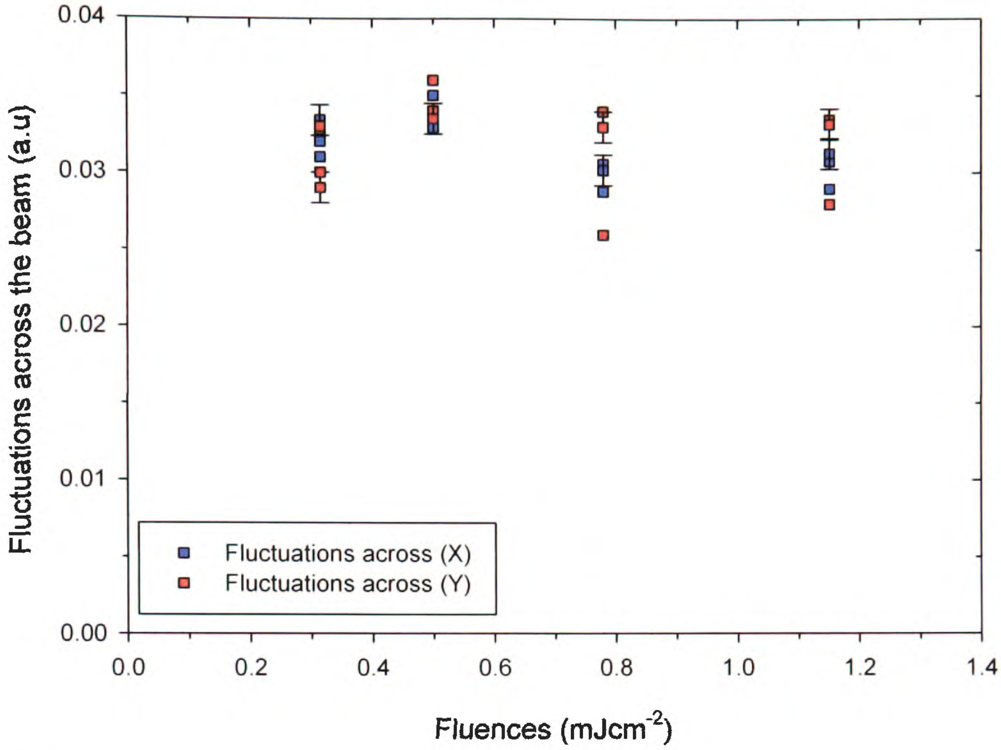

Figure 6.24: Fluctuations (σ/<m>) against fluences for X and Y directions across the F_2 laser beam, the data points are average of 5 groups of 64 pixels with different points on the beam.

6.6 Coherence Width from Focal Distribution

A focal plane measurement of the irradiance distribution allows the coherence function (mutual intensity function) to be found at the input plane of the lens. The theoretical basis for this has been given by Beran and Parrent [12]. They show that the intensity (irradiance) distribution *I(x)* in the focal plane i.e. image of the effective source at infinity, is related to the mutual intensity function Γ(ρ,*0*) in the input plane of the lens by

$$I(x) = \text{constan.} \int_{-\infty}^{+\infty} \Gamma(\rho,0) \exp \frac{2\pi i \rho x}{\lambda f} d\rho \tag{6.1}$$

Here x is the position variable in the image plane and $\rho = \xi_1 - \xi_2$ the difference between two points ξ_1 and ξ_2 in the lens aperture in the one-dimensional case. It is seen from this equation that *I(x)* is the Fourier transform of Γ(ρ,0) so that the inverse Fourier transform of

I(x) gives $\Gamma(\rho,0)$, allowing the coherence function to be found. It is to be noted that there are several restrictions for this approach to be valid [12]. Firstly, the intensity across the lens input should be constant which, in general, is not the case with laser illumination is. However, provided the intensity is essentially constant over distances greater than those for which $\Gamma(\rho,0)$ shows significant variation this should not influence the findings. Secondly, the theory breaks down near the edge of a source. Finally, it is assumed the lens point-spread-function makes no contribution, which will be justifiable provided the lens aperture is much greater than the coherence interval involved.

A simple view of this relation has been given by Berant and Parrent and we give an example here to support the link between *I(x)* and $\Gamma(\rho,0)$. Suppose, as shown in Figure 6.25, an incoherent slit source is positioned at a distance from the lens that is much greater than its focal length. The lens then forms an image of the source that is essentially in its focal plane. The van Cittert-Zernike theorem relates $\Gamma(\rho,0)$ at the lens to the Fourier transform of the source intensity distribution, which for the slit is a sinc function. As, according to equation (a), the intensity distribution in the focal plane image is the Fourier transform of $\Gamma(\rho,0)$ this will hence be a rectangular function i.e. the transform of sinc. This is consistent with the expected image of a slit produced by the lens.

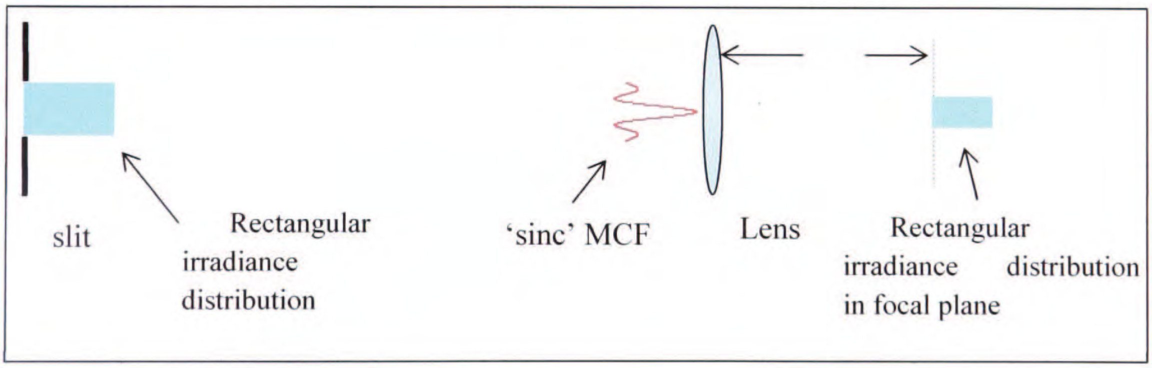

Figure 6.25: Lens producing image of distant, finite size, incoherent slit source. The mutual coherence function (MCF) at the lens is a sinc function and the irradiance in its focal plane is the Fourier transform of the MCF. This is a rectangular function and is the image of the slit.

To measure the focal spot distribution the output from the F_2 laser was focussed onto the Lumilass G9 plate using a 200mm focal length calcium fluoride lens as seen in the set up in Figure 6.26. Figure 6.27 shows a photograph of a lens, fluorescent glass and a mirror in the vacuum tube. A turning mirror oriented at 45° directed fluorescence from the plate to a lens which imaged the spot onto the CCD array. The magnification was one-to-one. To avoid saturating the fluorescent glass several attenuators were placed in front of the lens, and to eliminate red emission from the laser discharge a red filter was positioned in front of the CCD camera. The output from the camera was read into MathCAD so that the spatial irradiance distribution could be analysed.

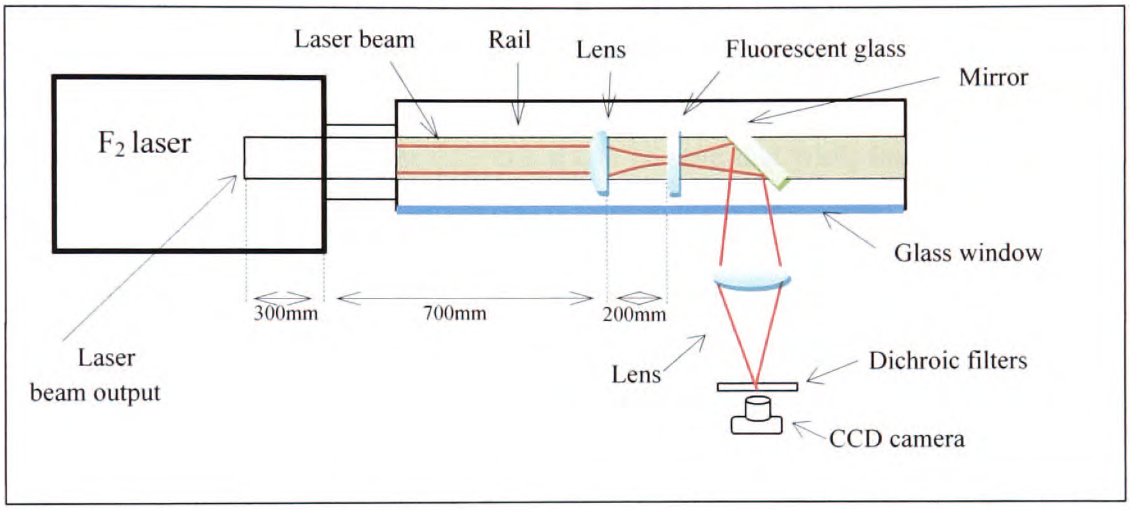

Figure 6.26: Schematic diagram of the experimental set-up for focal irradiance distribution.

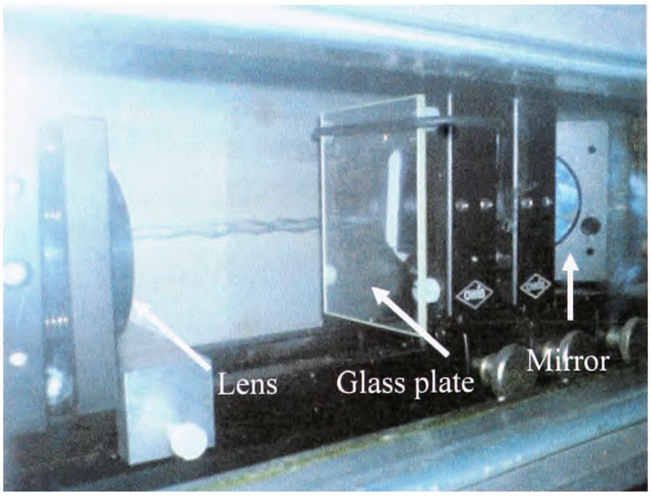

Figure 6.27: A photograph of lens, Lumilass G9 glass and a mirror sitting at 45° on the rail track.

Figure 6.28 shows the focal irradiance distribution along the direction of the narrow dimension of the laser. Calibration showed that 50 pixels on the camera corresponded to 1000μm giving a spatial scale of 20μm per pixel. As seen in Figure 6.29, both a Gaussian and a Lorentzian function give a reasonable description of the focal distribution in the narrow direction. The empirical forms derived for these were

$$\text{Gaussian} \quad I(x') = 67\exp-\left(\frac{x'-128}{\sigma}\right)^2 \quad \text{with } \sigma = 16 \tag{6.2}$$

$$\text{Lorentzian} \quad I(x') = \frac{67}{1+\left(\frac{x'-128}{\varepsilon}\right)^2} \quad \text{with } \varepsilon = 10 \tag{6.3}$$

where x′, σ and ε are in units of numbers of pixels. These are compared with the experimental distribution in Figure 6.29 and it can be seen that while both are reasonable in the central region, the Lorentzian decays less rapidly in the wings.

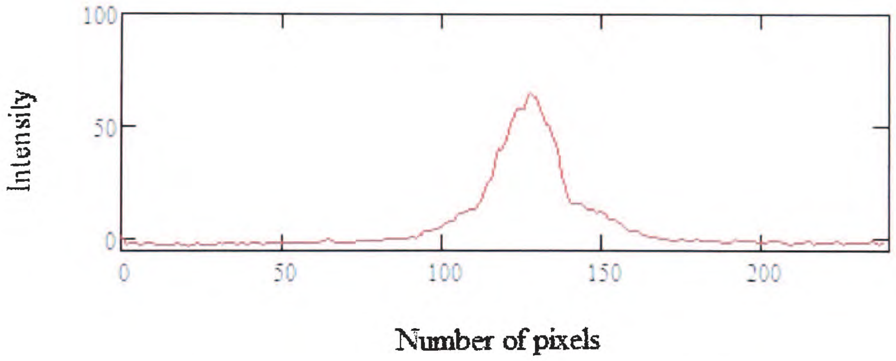

Figure 6.28: Cross section profile of the narrow width (Y) beam according for the focal spot irradiance.

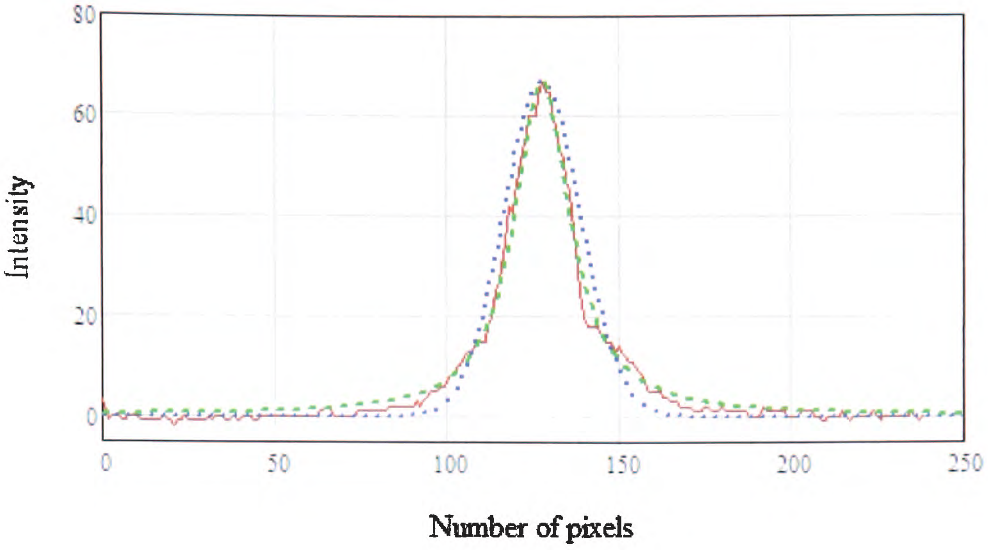

Figure 6.29: Focal irradiance graphs show the fit between Gaussian (---) and Lorentzian (---) for the beam intensity (___).

The inverse Fourier transform of a Gaussian distribution of the form exp $-\pi g\, x^2$ is:

$$A(\xi) = \int_{-\infty}^{+\infty} \exp - \pi g x^2 \exp(-2\pi i \xi x)\, dx = \frac{1}{\sqrt{g}} \exp - \frac{\pi \xi^2}{g} \tag{6.4}$$

If in equation (6.2) a new variable $\xi = \rho / \lambda f$ is defined and in equation (6.3) a change in variable made to $x = x' - 128$ and we set $\pi g = 1/\sigma^2$, the inverse transform of the experimental distribution becomes

$$\Gamma(\rho, 0) = \frac{1}{\sqrt{\pi\sigma}} \exp - \frac{\sigma^2 \pi^2 \rho^2}{\lambda^2 f^2} \tag{6.5}$$

The mutual coherence function is thus a Gaussian with a 1/e width ρ_w given by

$$\rho_{GW} = \frac{\lambda f}{\sigma \pi} \tag{6.6}$$

Using the calibration of 20μm per pixel gives $\sigma = 16 \times 20\mu m$, so with f=200mm and λ = 157nm the 1/e width is found to be $\rho_{GW} = 3.1 \times 10^{-5}$m or 31μm. This is plotted in Figure 6.30.

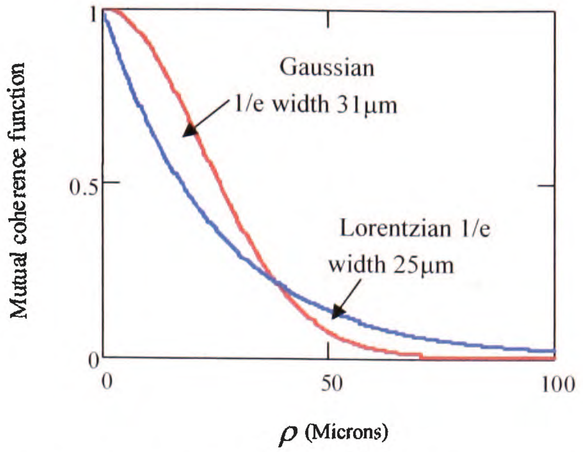

Fig 6.30: Mutual coherence function derived from experimental focal irradiance distribution in direction of the narrow dimension of the F_2 laser output beam. Results shown for Gaussian and a Lorentzian fit to the irradiance distribution. The coherence function is shown as a function of ρ, the separation of two points on the beam at the input plane of the lens. Gaussian 1/e width = 31μm, Lorentzian 1/e width = 25μm.

In similar fashion the inverse Fourier transform of equation (6.2) for the Lorentzian irradiance function $I(x')$ defined by equation (6.3), is an exponential

$$\Gamma(\rho,0) \approx \exp-\frac{2\pi\varepsilon|\rho|}{\lambda f} \tag{6.7}$$

This has a 1/e width of $|\rho_{LW}| = \lambda f/2\pi\varepsilon$, and with $\varepsilon = 10\times20\mu m$, $f = 200mm$ and $\lambda = 157nm$, gives $|\rho_{GW}| = 25\mu m$. This is shown in Figure 6.30 for comparison with the Gaussian fit.

Though neither the Gaussian nor Lorentzian fits in Figure 6.29 give exact correspondence with the experimental distribution, they bound the result in a reasonable way. It can thus be argued that the exact coherence function likely falls between those shown in Figure 6.30. The advantage of this approach is that a quantitative form for the coherence function is obtained rather than simply an estimate of its width being determined from a measurement of the divergence. The main experimental uncertainty is in ensuring that the fluorescent plate surface is located in the focal plane, which becomes more problematic if short focal length lenses with limited depth of focus are used. It is also important to avoid saturating the fluorescence emission by using appropriate attenuation so that the profiles are not distorted. The width of the plots in Figure 6.30 is dependent on the criterion applied and if, for example, the $1/e^2$ width is taken it is 44μm for the Gaussian and 51μm for the Lorentzian. As these are much smaller than the dimension of the beam at the lens, the restrictions noted above on uniformity of irradiance and the influence of edge effects should be satisfied. Further work on Fourier analysing the full focal spot distribution to obtain the two-dimensional coherence function would be of interest but time constraints prevented this in the present studies.

6.7 Modelling of Mode Coherence Fluctuations

To theoretically determine spatial fluctuations in the highly multimode output beam of the F_2 laser a numerical model has been used based on a set of Hermite-Gaussian modes with weightings chosen to simulate the beam profile. Fluctuations are assumed to arise because the modes have differing frequencies as set by the constraints of the laser optical resonator and laser line-width. Those lying sufficiently close in frequency may remain coherent over the duration of the emission pulse. If their relative phases are fixed then interference effects will remain unchanged from pulse-to-pulse. However, in a free-running laser it is more realistic to assume that the relative phase of modes varies randomly from pulse-to-pulse, so interference effects will fluctuate resulting in changes in the fluence at a fixed point in the beam.

This can be illustrated by a simple example where two optical fields with unity amplitude, angular frequencies ω and $\omega + \delta\omega$, and phase difference ϕ are added, producing a resultant:

$$E_R = \sin\omega t + \sin[(\omega + \delta\omega)t + \phi)] \tag{6.8}$$

The time averaged irradiance, found from E_R^2, can be expressed as

$$I = \langle E_R^{\,2} \rangle = \int_0^{\tau} \frac{\{\sin^2 \omega t + \sin^2[(\omega + \delta\omega)t + \phi] - \cos[(2\omega + \delta\omega)t + \phi] + \cos(\delta\omega t + \phi)\}dt}{\tau} \tag{6.9}$$

If the averaging time, τ, is considerably longer than $1/\nu$ where $\nu = \omega/2\pi$ is the optical frequency, the two sine squared terms in the integral each average to ½ and the cosine in the third term to zero. Assuming $\delta\omega << \omega$, the fourth term remains so that

$$I = \langle E_R^{\,2} \rangle = 1 + \int_0^{\tau} \frac{\cos(\delta\omega\, t + \phi)dt}{\tau} = 1 + \frac{\sin\frac{\delta\omega\tau}{2}}{\frac{\delta\omega\tau}{2}}\cos(\frac{\delta\omega\ \tau}{2} + \phi) \qquad (6.10)$$

Defining the coherence time as $\tau_c = 1/\delta\nu = 2\pi/\delta\omega$ this becomes

$$I = 1 + \frac{\sin\frac{\pi\tau}{\tau_c}}{\frac{\pi\tau}{\tau_c}}\cos\left[\frac{\pi\tau}{\tau_c} + \phi\right] \qquad (6.11)$$

The following observations can be made:

(i) If $\tau >> \tau_c$, it follows from equation (6.10) that $I = 1$ and the resultant irradiance is simply that for incoherent addition of the two waves.

(ii) The difference between the irradiance averaged over a finite time and the long-term average is

$$I - 1 = \sin c\frac{\pi\tau}{\tau_c}\cos(\frac{\pi\tau}{\tau_c} + \phi) \qquad (6.12)$$

Suppose now the waves are emitted as a series of pulses each of duration τ. If the phase difference ϕ remains constant then, according to equation (6.12), I will, in general, differ from the long-term average but this difference will be the same from pulse-to-pulse. However, if the phase difference varies randomly from pulse-to-pulse then I will fluctuate over a range $\pm \sin c\frac{\pi\tau}{\tau_c}$, as the cosine term is bounded by ± 1.

This is illustrated in Figure 6.31 where I is plotted with a ratio of 'pulse' duration to coherence time set at $\tau/\tau_c = 4.5$ and ϕ is varied randomly from 0 - 2π for a sequence of 100 pulses. I is seen to fluctuate about the average value of unity in a noise-like manner.

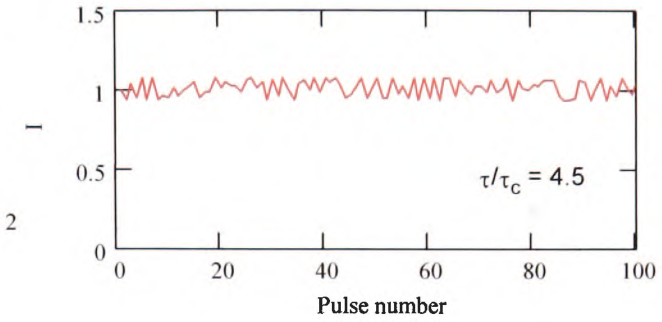

Figure 6.31: Run of 100 values for I with the phase difference ϕ in equation (a) set to a random value in the range 0-2π on each calculation.

A highly multimode laser will have a very large number of modes with slightly different frequencies that interfere and the following approach was used to model fluctuations. For a laser pulse of duration τ, modes within a frequency interval of $1/\tau$ are assumed to remain coherent and hence their fields can be added coherently in order to determine the irradiance. If the laser linewidth is $\Delta\nu$ there will be $\Delta\nu/(1/\tau) = \Delta\nu\tau$ such coherent mode groups that are independent of one another that can then be added incoherently to produce the laser output beam profile.

6.7.1 Implementation

The calculations described below were carried out using the MathCAD software package. A function producing a flat-topped Gaussian for *incoherently* added modes was chosen to represent the F_2 laser beam, as the mathematical basis exists for determining its mode content [13]. Additionally, a flat-topped profile provides a convenient reference level against which to measure spatial fluctuations. The flat-topped Gaussian is made up of Hermite-Gaussian functions $E_m(x)$ weighted by a coefficient c_m. These are defined by

$$E_m(x) = Herm[m, \sqrt{2}x/v_o]\frac{\exp - x^2/v_o^2}{(2^m m!)^{1/2}} \tag{6.13}$$

where $Herm(m\sqrt{2}x/v_o)$ is the value of the Hermite polynomial of degree m at x and v_o is the spot size of the fundamental Gaussian mode. The weighting coefficient is [13]

$$c_m = \left(\frac{2\pi}{N+1}\right)^{1/2} (-1)^N \int_0^\infty \frac{Her[2(N+1),t]Lag(m,2t^2)\exp-2t^2 dt}{N!2^{2N-1}} \tag{6.14}$$

where $Lag(n,2t^2)$ is the value of the Laguerre polynomial of degree n at $2t^2$. The width ω_o of the flat-topped Gaussian is determined by N through the relationship $\omega_o = \left(\frac{N+1}{2}\right)^{1/2} v_o$. The irradiance profile $I(x)$ of the beam along x is then the incoherent addition (long-term average);

$$I(x) = \sum c_m E_m(x)^2 \tag{6.15}$$

the summation being taken over all modes with a non-zero coefficient c_m.

In the present studies 90 Hermite-Gaussian transverse modes giving $N = 89$, and a value of $v_o = 301\,\mu m$ to give a divergence characteristic of the F$_2$ laser beam in a direction parallel to its narrow width, were used. The mode weightings are shown in Figure 6.32. It is noted that the contributions above $m \sim 60$ becomes increasingly small for the parameters chosen.

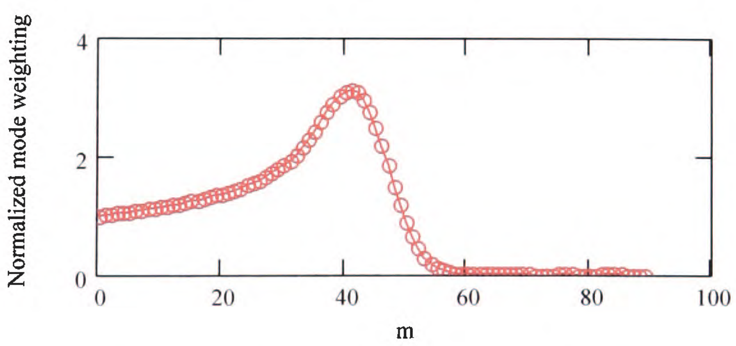

Figure 6.32: Mode weightings for a flat topped Gaussian calculated using equation (6.14) with N = 89.

The resulting profile and underlying lowest order Hermite-Gaussian mode for these parameters is seen in Figure 6.33.

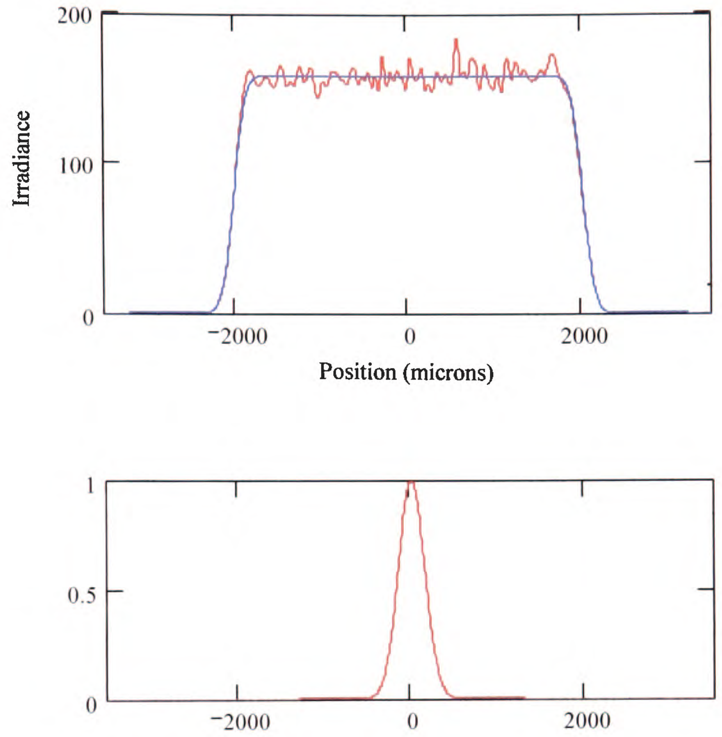

Figure 6.33: (a) Flat-topped Gaussian distribution with beam width of 2019μm simulated with m = 90 Hermite-Gaussian modes. Blue line – fully incoherent addition of modes giving long-term average irradiance (fluence). Red line – partial coherence where it is assumed there are 600 independent groups of 90 transverse modes, each group being coherent but with random phases. (b) Irradiance profile of underlying fundamental Gaussian distribution, spot size v_o *= 301μm.*

To treat the partially coherent case the number of coherent mode groups within the laser linewidth was estimated from the coherence time and the averaging time, the latter taken as the emission pulse duration τ. Assuming a Lorentzian line shape of width $\Delta\nu$ fwhm (full-width at half-maximum) the coherence time is $1/\pi\Delta\nu$ and the number of mode groups is $j = \tau/\tau_c = 2\tau\pi\Delta\nu$, the factor of two arising for an unpolarized beam [14]. With $\Delta\nu = 8.8$GHz for the F_2 laser [15] and a pulse width of $\tau = 11$ns (fwhm), $j = \tau/\tau_c = 608$. Each coherent mode group is then formed from

$$E_j(x) = \sum_m \sqrt{c_m}\, E_m(x) e^{i\phi} \tag{6.16}$$

where the phase ϕ takes a random value between 0 and 2π. The irradiance of the j^{th} mode group is found from

$$I_j(x) = \sum E_j(x)E_j(x) \tag{6.17}$$

and the total irradiance (equivalently fluence) profile of the beam obtained by summing over all independent randomly phased groups

$$I(x) = \sum_j I_j(x) \tag{6.18}$$

The result for partial coherence with $j = 600$ is seen in Figure 6.33 and it is evident that significant spatial fluctuation occurs when compared with fully incoherent addition.

The corresponding probability distribution for the time-averaged irradiance (fluence) across the profile is shown in Figure 6.34 and has a good fit with a Gaussian. The ratio of the standard deviation to the mean is 0.038, which compares closely with a value of $1/\sqrt{j} = 0.041$ expected using a simple statistical argument that has previously been used to estimate mode fluctuations [14]. A statistical optics treatment of this problem has also been reported independently by Rydberg *et al* [16]. They analyse mode coherence effects in optical projection lithography using excimer laser sources and have used the term 'dynamic speckle' [16] to describe spatial fluctuations that vary with each pulse.

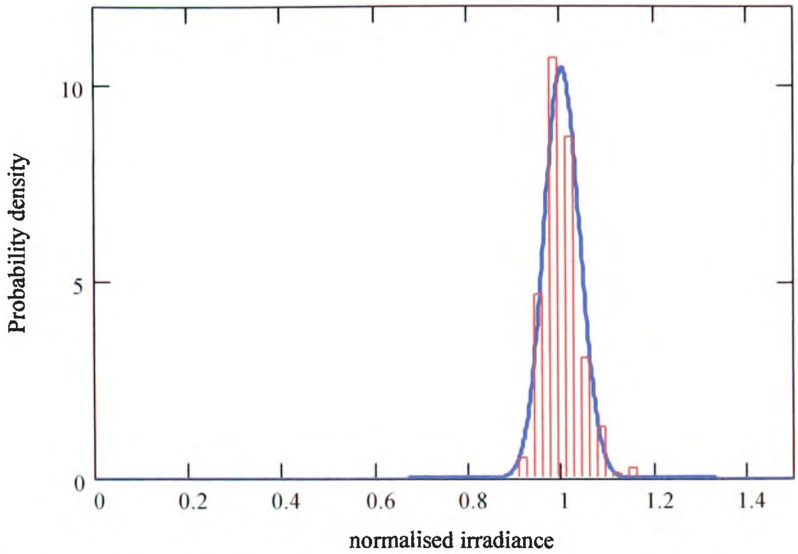

Figure 6.34: Probability distribution of normalised time-averaged irradiance (fluence) over the flat-topped Gaussian profile in Figure 3, for partially coherent mode addition with j = 600. The solid line is a Gaussian fit to the distribution with a standard deviation of 0.038.

The scale size over which these variations occur is governed by the spatial coherence width as this determines the range over which correlations are maintained across the beam. Figure 6.35 shows the real and imaginary parts of the normalized correlation function γ [17] and $|\gamma|$ calculated from the results for the partially coherent case in Figure 6.33. Taking the spatial coherence width as the spacing between two points on the beam where $|\gamma|$ falls to its first minimum, a value of ~60µm is found from Figure 6.35. Estimates of the lateral scale of fluctuations in figure 6.33 are consistent with this finding.

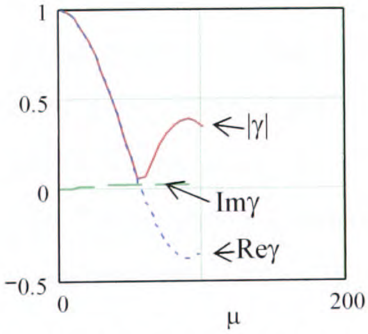

Figure 6.35: Normalized correlation function γ versus spacing between points on beam profile for partially coherent case in Figure 6.33(a).

These theoretical results give a magnitude of 3.8% for mode coherence fluctuations which compares quite closely to a value of ~3.3% obtained from the fluorescence imaging measurements described in section 6.4. It should be noted that the modelling is a simplification in that

(i) It neglects gain saturation effects which can act to reduce fluctuations over the 'cold cavity' case (i.e. resonator without gain medium) [14].

(ii) It does not take account of the shape of the laser pulse

(iii) The spectrum of the F_2 emission is assumed to be Lorentzian and to occur on a single line; whereas it is known [15] that weak lasing may also occur on other adjacent transitions.

The fluctuations found in this way are larger than expected for other excimer because the relatively narrow linewidth of the 157nm F_2 laser means fewer incoherent mode groups are involved in the averaging. This effect can play a role not only in materials processing by ablation, as was of interest here, but also in lithography [16].

6.8 Summary of Coherence Measurements

Three experimental approaches have been used to estimate the spatial scale length over which coherence is maintained in the F_2 laser output beam. The beam has a quasi-rectangular profile, with greater divergence in the long dimension than in the narrow dimension on account of the difference in the maximum transverse mode numbers in this asymmetric profile.

In Chapter 3, micron sized cones formed in ablated polycarbonate were shown to produce interference by reflection in a two-dimensional analogy of the Lloyd's mirror geometry. From the range over which fringes remained visible, estimates of the spatial coherence lengths of ~54μm along the *Y* axis (narrow dimension) and ~21-24μm along the *X* axis (wide dimension) of the beam were obtained (Table 6.3).

The second approach is to use the full-width at half-maximum divergence angle, $\Delta\theta$, obtained from the fluorescence imaging of the direct output beam at increasing distance from the laser output as described in section 6.3.2. On the assumption of a uniform one-dimensional irradiance distribution the spatial coherence width, Λ, is related to $\Delta\theta$ by

$$\Lambda = \lambda / \Delta\theta \tag{6.19}$$

This expression gives the spacing between two points on the beam at which the coherence first falls to zero. This is clearly at best an approximation for the actual beam profile generated by the laser, particularly in the X direction. Values obtained from equation 6.19 in this way are 58μm along the Y axis and 20μm along the X axis.

The third method, described in section 6.5 is based on a Fourier transform of the focal irradiance distribution. This has the potential to provide quantitative information on the form of the mutual intensity function and as such it is more powerful than the two other methods above, neither of which can provide such information. A preliminary measurement based on fluorescence imaging of the F_2 laser focal plane irradiance distribution was made for the Y axis (narrow direction) of the beam. The resulting coherence function appeared to fall between the transform of a Gaussian and Lorentzian, giving a coherence width in the range 44 - 55μm based on the distance over which the mutual intensity function dropped from 1 to $1/e^2$. This value differs somewhat from that found using the other methods (Table 6.3) but this is not surprising given that these are estimates based on simplifying assumptions about the beam profile.

Method	Spatial coherence Λ in narrow beam direction (Y)	Spatial coherence Λ in wide beam direction (X)
Interference fringes produced by cones	54μm	21-24μm
Direct beam divergence (full-width at half maximum)	58μm	20μm
Fourier transform of focal irradiance	44 - 51μm	Not measured

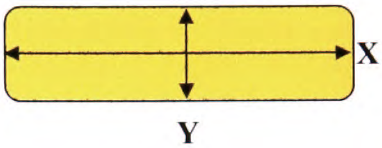

Table 6.3: Summary of spatial coherence widths of the F_2 laser output beam determined by three techniques. X and Y define orthogonal directions in the rectangular output beam.

References

[1] K.Mann, Excimer Laser Technology, Springer Berlin Heidelberg, *New York*, 2005.

[2] AMR Ackermann, T.J.Drummond, J.P.Wilcoxon, and P.A.Cahill, Sandia Laboratories Report,'*A brief examination of optical tagging technologies*' SAND2003 (2003-2004) 2204.

[3] W.Liu, D.Chen, H.Miyoshi, K.Kadono, and T.Akai, Journal of Non-Crytalline Solids 352 (2006) 2969.

[4] W.Liu, D.Chen, H.Miyoshi, K.Kadono, and T.Akai, Chemistry Letters 34 (2005) 1176.

[5] Y.Otani, M.Takahashi, L.Jin, H.Kowa, and N.Umeda, Proceeding SPIE 5188 (2003) 134.

[6] B.B.Shrivastava, N.S.Benerji, P.Bhatnagar, HS Vora, and U.Nundy, in International Conference in Photonics, Institute of Photonics, Cochin University,Cochin (Kerala),India, 2004.

[7] M.J.Weber, Handbook of Laser Science and Technology, CRC Press, *London*, 1982.

[8] R.Berry and J.Burnell, The Handbook of Astronomical Image Processing, Willmann-Bell,Inc, *United State of America.*, 2006.

[9] D. C.Giancoli, Physics for Scientist and Engineers, Pearson Prentice Hall, *London*, 2008.

[10] H.L.Offerhaus, C.B.Edwards, and W.J.Witteman, Optics Communications 151 (1998) 65.

[11] P.E.Dyer, A.M.Johnson, S.Maswadi, and C.D.Walton, Lasers in Manufacturing (2003) 27.

[12] M.J.Beran and G.B.Parrent, Theory of Partial Coherence, Prentice-Hall, Inc, *New Jersey*, 1964.

[13] M.Santarsiero, F.Gori, R.Borghi, and G.Guattari, Applied Optics 38 (1999) 5272.

[14] P.E.Dyer, C.D.Walton, and K.A.Akeel, Optics Letters 30 (2005) 1336.

[15] C.J.Sansonetti, J.Reader, and K.Vogler, Applied Optics 40 (2001) 1974.

[16] C.Rydberg, J.Bengtsson, and T.Sandstrom, Journal Microlithography Microfab Microsys 5 (2006) 033004.

[17] G.R.Fowles, Inttroduction to Modern Optics, *Holt, Rinehart Winston, New York*, 1975.

CHAPTER 7

CONCLUSIONS

7.0 Main Findings and Conclusions

During the course of the research in this thesis experiments were carried out using 157nm F_2 laser radiation on the ablation properties of polymers that included polydimethylsiloxane (PDMS), SU-8, Nylon 66, ultra-high molecular weight polyethylene (UHMWPE), Lexan polycarbonate (PC) and allyl-diglycol CR-39 polymer. The ablation thresholds of these polymers obtained from etch rate measurements are summarised in Table 7.1. These range from ~10mJcm^{-2} for polycarbonate to 105mJcm^{-2} for PDMS, the differences probably being largely traceable to their differing VUV effective absorption coefficients. Here, most of the work was subsequently concentrated on the Lexan polycarbonate and CR-39 polymer.

Polymer	Experimental ablation threshold fluence (mJcm^{-2})
PDMS	105 ± 10
SU-8	90 ± 5
Nylon 66	27 ± 3
UHMWPE	28 ± 3
Lexan polycarbonate	10 ± 5
CR-39 polymer	50 ± 10

Table 7.1: The ablation threshold from the etch rate measurements for PDMS, SU-8, nylon 66, UHMWPE, Lexan polycarbonate and CR-39 polymer.

Previous research has shown that the photoetching of polymers can produce a variety of morphological features on the ablated surface e.g. well-organized laser-induced periodic structures, one and two-dimensions ripples driven by relaxation of stress in aligned polymers, and micro-scale cones. In the course of the studies, it was observed that very well defined cones could be produced on ablated Lexan polycarbonate surfaces that were either seeded with small particles or were un-seeded. In a similar fashion it was found that certain ablation parameters led to exceptionally well defined cones forming on CR-39 polymer. These conical microstructures proved useful as they permitted an estimate of the ablation threshold (F_T) to be determined from the apex angle of the cones. This gave F_T = 25mJcm^{-2} with 20% uncertainty in the calculation for Lexan polycarbonate using a refractive index μ= 1.463 to determine reflection loss at the sloping wall. The corresponding value was 58mJcm^{-2} for CR-39 though this remains an estimate as the 157nm refractive index was not available for this material. The cones developed on the CR-39 were exceptionally good, having very straight smooth walls and extremely sharp tips. The cones that developed on the surface led to interference effects that resulted in fringes forming in the region adjacent to their base. The characteristics of the interference fringes can be related to the divergence of the laser, thus allowing spatial coherence to be determined. The spatial coherence calculated from interference effects produced by cones of a few microns dimensions on polycarbonate was found to be ~21-24μm based on wide dimension of the beam with an 8 mrad divergence value, and 54μm on the orthogonal dimension with an 3 mrad divergence value.

The morphology of cones on polycarbonate and CR-39 polymer indicated that a very smooth surface can be produced on microstructures produced by 157nm ablation. The surface roughness of these polymers was characterised using white light interferometry (VEECO-Wyko NT1100) on regions free of cones and compared with the value predicted using a theoretical model based on mode related coherence fluctuations. Based on the F_2 laser linewidth a value $\sigma/<F>$ = 4% is obtained for the unpolarised beam giving for polycarbonate with $\alpha_{\text{eff}} \approx 3 \times 10^5$ cm^{-1} and for CR-39 with $\alpha_{\text{eff}} \approx 2.9 \times 10^5$cm^{-1}, the measured roughness for polycarbonate with $m^{1/2} = 10$ (100 pulses) is ~20nm compared with a corresponding predicted value of r = 13nm, with various uncertainties explained in this chapter. For CR-39 experiments give ~40nm for 100 pulses, compared with a predicted roughness of 14nm showing that in this case there is a considerably larger difference between these values.

A preliminary study was made of CR-39, a track-etch material for heavy ionising particles, by exposing it to a 226 Ra alpha source (~5MeV) and then using chemical etching (NaOH 6.25N for 1.5hour) to reveal the alpha tracks. Various pulse numbers of 157nm laser pulses were used to ablate these samples and then optical and scanning electron microscopy (SEM) employed to view changes to the morphological structure of the etched tracks. As radiation damage alters the properties of the polymer it was conjectured that laser etching might be a possible route to revealing tracks. However, the samples exposed to alpha particles and then laser etched *without* prior chemical etching showed no morphological evidence of tracks after ablation at 157nm. This is possibly because the latent radiation damage sites initially extend over a diameter of only about 10nm and hence would be 'un-resolvable' at this wavelength. However, interesting effects were observed in radiation exposed samples that were chemically etched in NaOH to reveal deep tracks of 2-3μm diameter and then ablated using 157nm laser. Smoothing of the edges tracks due to melt flow relaxation and, under multiple numbers of exposures, a significantly increased density of cones structures was seen, evidently their growth being seeded by edges of the tracks.

In the final part of this work a technique was developed for characterising the VUV F_2 laser beam using a fluorescence glass plate (Lumilass G9). This approach was found to be technically quite useful as several important characteristics of the laser beam could be determined. Using this fluorescence technique, two-dimensional beam profiles could be recorded using a CCD camera and subsequently analyzed using MathCAD software allowing indirect measurements of spatial coherence, and beam fluctuations to be assessed. The saturation effects on the fluorescent glass were also investigated. The beam divergence of the laser measured using this technique was 2.7mrad in the narrow and 7.9mrad in the orthogonal wide direction. From focal spot irradiance, focal spot found to be as 0.42mm on narrow width (Y) gives the divergence of 2.1mrad. Using a low laser fluence of 0.5mJcm^{-2}, the fluctuations value calculated in MathCAD (Section 6.5) shows a value of ~3.3%. The coherence width derived from fluorescence focal irradiance the 1/e width is found to be 31μm for Gaussian fit and 25μm for Lorentzian fit. From modelling of fluctuations using the Hermite-Gaussian simulation, the theoretical results give a magnitude of 3.8% for mode coherence fluctuations which compares quite closely to a value of ~3.3% obtained from the fluorescence imaging measurements described in section 6.5.

7.1 Summary

A summary of spatial coherence measured in this chapter from the interference fringes produced from cones and fluorescence method based on the *X* and *Y* direction of the laser beam can be concluded in Table 6.3, reproduce below as convenience.

Method	Spatial coherence Λ in narrow beam direction (Y)	Spatial coherence Λ in wide beam direction (X)
Interference fringes produced by cones	54μm	21-24μm
Direct beam divergence (full-width at half maximum)	58μm	20μm
Fourier transform of focal irradiance	44 - 51μm	Not measured

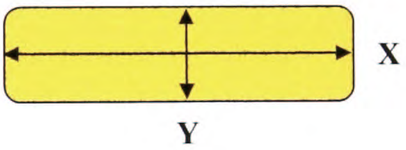

Table 6.3: Summary of spatial coherence widths of the F_2 laser output beam determined by three techniques. X and Y define orthogonal directions in the rectangular output beam.

7.2 Future work

A preliminary study was made of CR-39 polymer exposed to alpha radiation, chemically etched and then ablated at 157nm. For future work, it could be of interest to extend this to investigating the effects of NaOH etching in increasing normality or etching time for radiation exposed samples and how this influences the ablation properties of the material. The potential for high quality 157nm ablation of CR-39 polymer has been seen in the exceptionally well defined straight, smooth walls and sharp tips that are formed on cones in this material. This points to an opportunity for further studies on using this material as a substrate for defining various micro-structures by VUV ablation e.g. using nano- and micro-particles to seed cones in a controlled way, and micro-whiskers to generate analogous prismatic structures on CR-39.

APENDIX A

PROFILE OF THE CONE

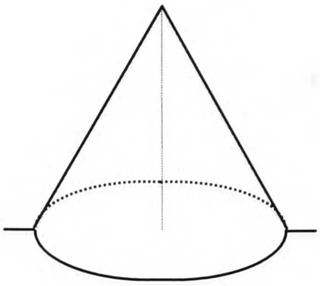

(1) Profile of the cone viewed tilted based on the stage.

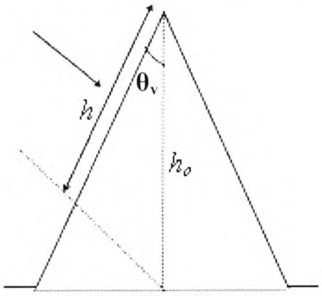

(2) Viewed of the cone based on the half angle viewed (θ_v), height perceived (h) and height of cone (h_o)

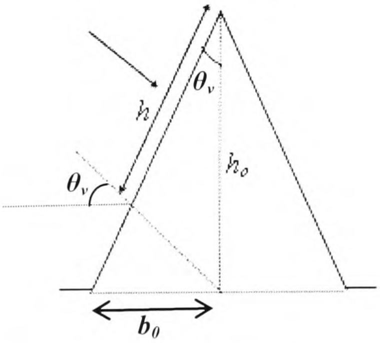

(3) Viewed of the cone based on the half angle viewed (θ_v), height perceived (h) and height of cone (h_o) and half base of the cone (b_0)

The height perceived is *h*, giving:

$$\cos\theta_0 = \frac{h}{h_0}$$

$$h = h_0 \cos\theta_0 \tag{i}$$

Then by substituting (*i*) and considering the half base of the cone as b_0, the perceived angle (θ_p); with viewing angle as (θ_v) giving:

$$\tan\theta_p = \frac{b_0}{h}$$

$$\tan\theta_p = \frac{b_0}{h_0 \cos\theta_V} \tag{ii}$$

From equation (ii), if viewing angle (θ_v) is 0, then equation (ii) become:

$$\tan\theta_P = \frac{b_0}{h_0} \tag{iii}$$

And if viewing angle (θ_v) is 90°, equation (iii), become $\tan\theta_p = \infty$, and $\theta_p = 90^o$, so for the half true angle (θ_t) for each of the angle applied, if $\tan\theta_t = \frac{b_0}{h_0}$, giving

the equation below:

$$\tan\theta_p = \frac{\tan\theta_t}{\cos\theta_v}$$

$$\cos\theta_0 . \tan\theta_p = \tan\theta_t$$

$$\theta_0 = \tan^{-1}(\tan\theta_p . \cos\theta_V) \tag{iv}$$

Viewing angle (θ_v) viewed from horizontal, thus for the viewing angle from the vertical, giving:

$$\theta_t = \tan^{-1}\left[\tan\theta_p . \cos(\frac{\pi}{2} - \theta_V)\right] \tag{v}$$

List of publications

1. P.E.Dyer, C.D.Walton, R.Zakaria, ***'Interference effects in 157nm laser ablated cones in polycarbonate and application to spatial coherence measurement'***, Applied Physics A (2009) 319.

2. P.E.Dyer, M.Pervolaraki, C.D.Walton, D.Waugh, R.Zakaria, ***'Ablation and material modification with micro-lasers'***, Presented in Conference on Laser Ablation 2007 (COLA 07), Tenerife, Spain.

3. S.Cockcroft, P.E.Dyer, C.Moore, C.D.Walton, R.Zakaria, ***'Ablation of pristine and radiation exposed CR-39 polymer using a 157nm laser'***, will be presented in CLEOEUROPE 2009, Munich, Germany.

4. D.Waugh, J.Lawrence, C.D.Walton, R.Zakaria,***'Investigation into the efficiacy of CO_2 lasers for modifying the factors influencing of polymeric biomaterial in comparison with F2 excimer laser***, ICALEO 2008, Los Angeles, United States.

Appl Phys A (2009) 95: 319–323
DOI 10.1007/s00339-009-5102-9

Applied Physics A
Materials Science & Processing

INVITED PAPER

Interference effects in 157 nm laser ablated cones in polycarbonate and application to spatial coherence measurement

P.E. Dyer · C.D. Walton · R. Zakaria

Received: 21 November 2008 / Accepted: 21 November 2008 / Published online: 29 January 2009

Abstract Conical structures formed in 157 nm laser-ablated polycarbonate exhibit a well-defined fringe structure with a period of a few 100 nm surrounding the cone base. Experiments and modelling studies of the interference produced by these micro-conical mirrors are shown to provide a means of measuring the spatial coherence of the highly multi-mode 157 nm laser.

PACS 42.55.-f · 52.38.Mf

1 Introduction

Conical structures formed in laser-ablated polymers, semiconductors and metals have been investigated quite extensively since the 1980's [1–4]. Evidence suggests these cones are initiated by particulate inclusions either inherent to the material, generated via the ablation process itself or deliberately added to the surface [1]. The role of diffraction, reflection and interference effects has been considered by a number of authors [1, 3, 4], as these influence the evolution of the cone structure.

In this paper we report on cones of microscopic dimensions (a few microns) that develop in polycarbonate when ablated using the 157 nm F_2 laser. There is interest in the ablation of polycarbonate [3, 5], as laser machining permits components such as micro-lenses [6] and large-area lens arrays [7] to be fabricated in this high optical quality material, as well as micro-channels to be defined for use in 'lab-on-chip' micro-reactors [8]. In previous work, Hopp et al. [3] have reported on conical microstructures formed in polycarbonate ablated in a fluence range between about 20 and 600 mJ cm^{-2} at 193 nm and observed their symmetry is influenced by the laser polarisation. Lapczyna and Stuke [8] have presented 157 nm VUV laser etch rate measurements for polycarbonate, in relation to micro-channel fabrication. Of specific interest in the present work is that cones with an appropriate apex angle develop distinct fringes with a period of a few 100 nm in the region adjacent to the edge of their base. Modelling confirms these fringes arise through interference of the direct beam with the beam reflected from the cone wall and provides a reasonably good description of the surface depression and fringes around the base. The cones effectively form a micro-conical mirror that produces circular fringes in a manner akin to the linear fringes with the Lloyds *mirror arrangement* [9]. From the radial extent of the fringes it is shown that the spatial coherence width of the 157 nm laser can be found for orthogonal directions of the rectangular output beam.

2 Experimental arrangement

A Lambda Physik F_2 laser producing up to 35 mJ per pulse at ≤ 20 Hz was used to ablate samples of polycarbonate (Lexan, supplier Goodfellow Cambridge Ltd) in the form of 3 mm thick sheets. The output beam from the laser was passed through a rectangular aperture to extract a region of quasi-uniform fluence and a CaF_2 lens used to produce a $15\times$ demagnified image of the aperture at the surface of the sample. The full-angle beam divergence of the direct output beam was $\sim$3 mrad in its narrow dimension and $\sim$8 mrad in its long dimension. Ablation was carried out in vacuum (10^{-5} mbar) at a laser pulse repetition rate of $\sim$10 Hz. Cones were readily produced at fluences in the

---

P.E. Dyer (✉) · C.D. Walton · R. Zakaria
Physics Department, University of Hull, Hull, HU6 7RX, UK
e-mail: p.e.dyer@hull.ac.uk
Fax: +44-01482-465606

range 20–200 mJ cm^{-2} without deliberate particulate seeding, although in some cases alumina powder (0.05 µm diameter) was applied to the surface to increase their areal number density. Following exposure to a given number of pulses and fluence, the depth of material removed was determined using a white-light interferometer (VEECO-Wyko NT1100) allowing the average etch depth per pulse and the ablation threshold to be obtained. Surface features were imaged using a scanning electron microscope (SEM, Carl Zeiss SMT Ltd, Model EVO 60), and the measured wall angle of cones was used to make an independent estimate of the threshold [2].

3 Results

The average etch depth per pulse d as a function of fluence F for polycarbonate ablated at 157 nm based on 100 and 500 pulses is shown in Fig. 1. A linear fit of the form $d = k^{-1} \ln F/F_T$ gives an ablation threshold of $F_T \approx 11$ mJ cm^{-2} and an effective absorption coefficient of $k = 3.0 \times 10^5$ cm^{-1}. The latter is considerably higher than a value of 1.14×10^5 cm^{-1} at 157.4 nm for Lexan polycarbonate as determined by the conventional measurement of optical constants [10]. An estimate of the threshold was also made using the limiting angle of the apex of conical structures formed in the polymer [2]. This calculation took account of the angular dependence of the surface energy loading and gave a somewhat higher value for the threshold of $F_T \approx 25$ mJ cm^{-2}. For comparison, a threshold value of $F_T \sim 20$ mJ cm^{-2} is estimated from data in [8].

Figure 2a shows a group of conical structures formed on a polycarbonate surface subjected to 100 pulses at a fluence of 81 mJ cm^{-2}. The SEM viewing angle is 60° from the vertical. The surface well away from these structures is seen to be

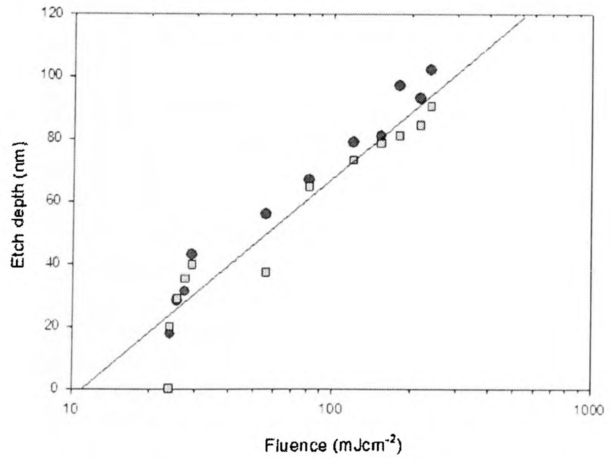

Fig. 1 Average etch depth per pulse versus fluence for polycarbonate ablated at 157 nm using, ■ 500 laser pulses, and • 100 laser pulses

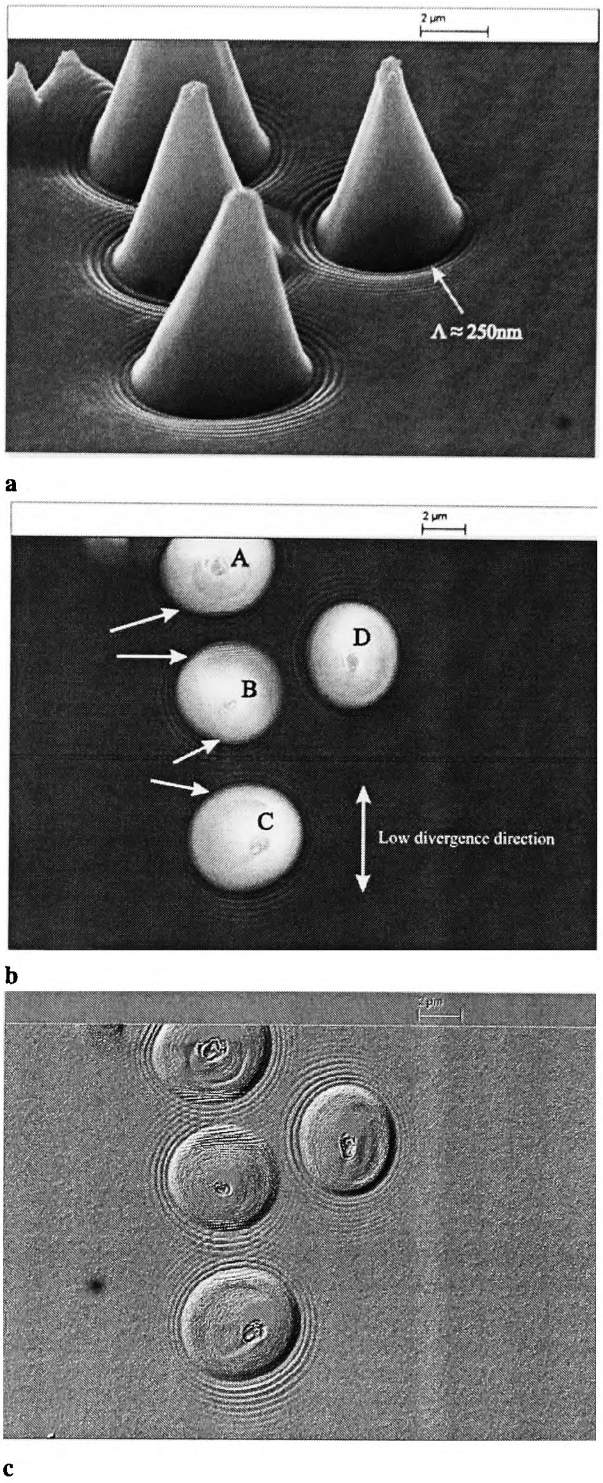

Fig. 2 (**a**) Cones in polycarbonate ablated with the 157 nm laser (100 pulses, 81 mJ cm^{-2} per pulse). SEM viewing angle = 60° from vertical. (**b**) As (**a**), but viewing angle = 0°. *Arrows* indicate fringes on cone wall. (**c**) Viewing angle = 0° with convolution bas-relief filter applied to enhance fringes

smooth and devoid of significant debris, indicating the good surface quality attainable in this material when ablated with the 157 nm laser. The micron-scale cones in the main group have smooth, relatively straight, walls and there is substantial depression formed adjacent to the base, where the etch depth is greater than the mean surface. A well-defined set of circular fringes arising from interference between the direct beam and that reflected from the cone wall [3] also surrounds each base, the fringe period being ~250 nm. A pair of partially evolved cones is evident in the top left-hand corner of the SEM, the initiating particulates presumably only having become present near the end of the pulse sequence. When viewed from above (Fig. 2b and 2c), a careful examination of these structures shows that the fringes exhibit an asymmetry. They are visible over a greater distance along the direction of the narrow dimension of the F_2 laser output beam than in the orthogonal direction. This is attributed to the difference in spatial coherence widths in the low- and high-divergence directions of the beam and is discussed further below. Additional support for this observation comes from the fact that cones A, C and D, which approximately lie along the high-coherence direction, are seen to imprint fringes on the walls of their neighbour. In contrast, cone D, lying to the right of cone B, i.e. being displaced along the low-coherence direction, has no fringes on its wall; neither does it appear to produce fringes on B.

4 Interference model

We assume that radiation reflected from the cone wall interferes with the direct beam producing a set of circular fringes on the flat surface beyond the cone base. For this geometry, straightforward analysis gives for the fringe period, Λ,

$$\Lambda = \frac{\lambda}{\sin 2\theta_t}, \tag{1}$$

where λ is the laser wavelength and θ_t is the half-angle of the cone apex.

To quantify the fringe system, the amplitude reflection coefficients R_s and R_p for s- and p-polarised radiation, respectively, were calculated using the Fresnel equations [11], assuming the incident 157 nm beam to be unpolarised. These were based on the real refractive index $\mu = 1.463$ for polycarbonate at 157.4 nm [10], as estimates showed that including the extinction coefficient (≤ 0.37 based on the effective absorption coefficient) had a negligible influence on their value. A vector sum of the field for the independent s- and p-components of the direct and reflected beams was formed and the irradiance along x (Fig. 3) determined. The line width of the F_2 laser is sufficiently small [12], so that temporal coherence can be assumed over the optical path differences involved.

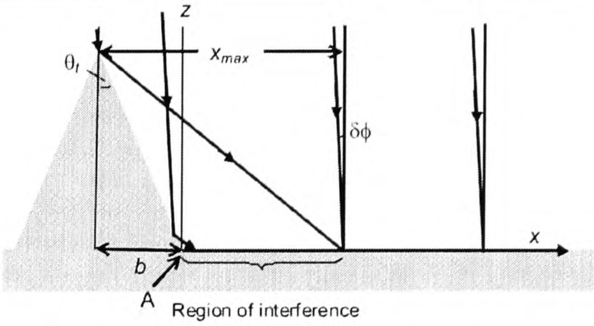

Fig. 3 Schematic diagram showing region of interference of the incident beam with that reflected from the cone wall

A plane wave description was used but with the reflected field reduced to correct for the 3D beam expansion from the conical surface. The sum of the incident and reflected fields for the s- and p-polarised components is, respectively,

$$\begin{aligned}E_s = &\left(\frac{1}{\sqrt{2}}\right) \exp -i(kx \sin\delta\phi + kz\cos\delta\phi)\\ &+ \left(R_s\sqrt{\cos(2\theta_t - \delta\phi)}\sqrt{I_x}/\sqrt{2}\right)\\ &\times \exp -i\left(kx\sin[2\theta_t - \delta\phi] + kz\cos[2\theta_t - \delta\phi]\right),\end{aligned} \tag{2a}$$

$$\begin{aligned}E_p = &\begin{pmatrix}\frac{1}{\sqrt{2}}\\ 0\end{pmatrix} \exp -i(kx \sin\delta\phi + kz\cos\delta\phi)\\ &+ \begin{pmatrix}R_p\cos(2\theta_t - \delta\phi)\sqrt{I_x}/\sqrt{2}\\ R_p\sin(2\theta_t - \delta\phi)\sqrt{I_x}/\sqrt{2}\end{pmatrix}\\ &\times \exp -i\left(kx\sin[2\theta_t - \delta\phi] + kz\cos[2\theta_t - \delta\phi]\right).\end{aligned} \tag{2b}$$

Here $I_x = \frac{(b - x\cos 2\theta_t)\cos[2\theta_t - \delta\phi]}{(x+b)}$ accounts for the irradiance reduction at x produced by expansion of the reflected beam from the cone wall, where b is the radius of the cone base. The incident beam is nominally normal to the surface, but with a small spread of angles, $\delta\phi$, with respect to the z axis (Fig. 3) to allow account to be taken of beam divergence. The average amplitude of the incident wave is unity.

The fluence F is given by the product of irradiance and pulse duration and hence is proportional to the scalar product, $F_{s,p} \propto E_{s,p} \cdot \overline{E_{s,p}}$. To account for finite spatial coherence $F_{s,p}$ was integrated over $\Delta\phi$, the full divergence angle of the laser, with the simplifying assumptions that the source was spatially incoherent and had a uniform irradiance distribution,

$$F_{\text{full},s,p} = \int_{-\Delta\phi/2}^{\Delta\phi/2} F_{s,p}\frac{d\delta\phi}{\Delta\phi}.$$

For multiple-pulse exposure the fringe system does not remain stationary along x, because the cone height and base radius progressively increase as ablative etching proceeds. This leads to a spatial shift of the fringes and, over a number of pulses, effectively results in a loss of fringe visibility.

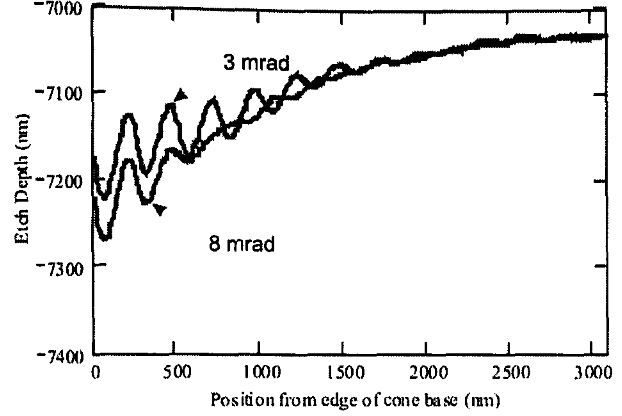

Fig. 4 Modelled interference fringes produced in the region adjacent to the base of a cone in polycarbonate with cone half-angle = 0.337 rad (19.3°) and base radius of 2461 nm. The cone edge is at the origin $x = 0$. 100 pulses at 81 mJ cm^{-2} per pulse and effective absorption coefficient $k = 0.024$ nm^{-1} and ablation threshold $F_T = 15$ mJ cm^{-2}. Refractive index $\mu = 1.463$

Assuming the cone height increases at a uniform rate from pulse to pulse and that $d = k^{-1} \ln F/F_T$ describes the etch rate per pulse, the removed depth of surface d_m for m pulses is

$$d_m = \sum_{n=1}^{m} \frac{1}{k} \ln\left[F_{\text{tot}}(x, n)\gamma\right].$$

Here

$$F_{\text{tot}}(x, n) = F_{\text{full},s}\big(x + b(m) - b(n)\big) + F_{\text{full},p}\big(x + b(m) - b(n)\big) \quad \text{for } 0 \le x \le x_{\max}$$

and

$$F_{\text{tot}} = 1 \quad \text{for } x > x_{\max}.$$

$x_{\max} = b(n)/\cos 2\theta_v$ is the maximum value of x for which the reflected beam overlaps the incident beam on the nth pulse when the cone has a base radius $b(n)$ (Fig. 3). $\gamma = F/F_T$ is the ratio of the incident to the threshold fluence. In this simplified picture the cone-initiating mechanism, which is thought to initially depend on diffraction at a particulate inclusion [1, 3], is neglected.

Figure 4 shows the calculated surface profile beyond the base of a cone produced in polycarbonate ablated with $m = 100$ pulses, $F = 81$ mJ cm^{-2}, $F_T = 15$ mJ cm^{-2} ($\gamma = 5.4$). The cone angle was set at $\theta_t = 19.3°$ and the pulse number chosen to produce a cone base radius of 2.5 μm to allow for comparison with the result in Fig. 2a and b. A value of $k = 0.024$ nm^{-1}, some 20% lower than deduced from Fig. 1, was used to provide a cone depth consistent with experiment. It is evident that the simulated profile is in good qualitative agreement with the etched region containing the fringes seen adjacent to the cone base in the SEM. The peak-to-peak depth modulation reaches ~95 nm near the base edge. An interference minimum is placed at $x = 0$ as there is a π phase shift for the reflected s-component, and, with $\mu = 1.463$, when $\theta_t < 34.4°$ for the p-component. This minimum location likely plays a role in the cone development but was not investigated further here. The fringes have a period of ~252 nm, in good agreement with (1). The etch depth outside of the reflected beam zone is 7031 nm, but it is deeper by ~150–195 nm at the edge of the cone base (depending on beam divergence) because of the reflected contribution. The fringe amplitude is limited by the spatial shift from pulse to pulse. Further, fringe visibility falls as x increases both because of the finite spatial coherence of the beam and the reflected beam expansion factor I_x.

The etch-depth curves in Fig. 4 are for intrinsic beam divergences of 3 mrad and 8 mrad as estimated for the narrow and long dimension, respectively, of the rectangular output beam of the 157 nm laser. In the simulation these divergences have been increased by 15× because of the projection image demagnification factor. The range over which fringe visibility is maintained is lower for the larger divergence as the corresponding spatial coherence width is reduced. This is borne out by the experimental results in Figs. 2b and 2c, where the fringes in the direction of low spatial coherence extend over a considerably smaller distance than those in the orthogonal direction.

In the low-coherence direction an estimate of the spatial coherence width l can be made from the observation that fringes persist out to $x_i \sim 800$–900 nm from the cone edge. The direct and reflected rays that meet at this limiting point are spaced laterally by $w = 2x_i \cos^2\theta_t$, giving $w \approx 1.43$–1.6 μm for a cone half angle $\theta_t = 19.3°$. Multiplying this by the image reduction factor of 15, the spatial coherence width in the wide dimension of the 157 nm laser beam is $l \approx 21$–24 μm, which is consistent with $l = \lambda/\Delta\phi \approx 20$ μm based on full-angle divergence of $\Delta\phi = 8$ mrad. For the narrow dimension a similar estimate gives $l \approx 54$ μm.

Other evidence for the difference in spatial coherence widths is seen in Fig. 2b. Cones A, B and C, aligned along the high-coherence dimension, imprint fringes on each others' walls. In contrast, cones B and D, aligned roughly in the low-coherence direction, do not, because of the lower coherence width.

5 Conclusions

The period of fringes formed around the base of micron-scale size cones produced in 157 nm laser ablation of polycarbonate is consistent with these arising through interference of the incident beam with a component reflected from the cone wall. These structures form good-quality micro-conical mirrors and effectively provide a two-dimensional

Lloyd mirror interferometer. Modelling shows that an observed asymmetry in the spatial extent of the fringe system is related to the spatial coherence of the laser, which differs in the two orthogonal axes of the output. Good qualitative agreement is found with the observed etching in the vicinity of the cone base. An estimate for the spatial coherence of ~22 μm and 54 μm in the high- and low-divergence axes, respectively of the VUV beam, has been derived from the fringes. These values are consistent with expectation based on the source divergence. The results also show indirectly that the quality of etching in polycarbonate with the 157 nm laser is suitable, in principle, for use in fabricating micro-optical components.

References

1. P.E. Dyer, S.D. Jenkins, J. Sidhu, Development and origin of conical structures on XeCl laser ablated polyimide. Appl. Phys. Lett. **49**, 453 (1986)
2. P.E. Dyer, S.D. Jenkins, J. Sidhu, Novel method for measuring excimer laser ablation thresholds of polymers. Appl. Phys. Lett. **52**, 1880 (1988)
3. B. Hopp, Z. Bor, E. Homolya, E. Mihalik, Investigation of conical structures created by ArF excimer laser irradiation of polycarbonate. Appl. Surf. Sci. **109/110**, 232–235 (1997)
4. J. Zhu, Y. Shen, X. Chen, G. Yin, D. Chen, L. Zhao, Effect of polarization on femtosecond laser pulses structuring silicon surfaces. Appl. Surf. Sci. **252**, 2752–2756 (2006)
5. M. Devalckenaere, A. Jadin, K. Kolev, L.D. Laude, Excimer ablation of polycarbonate-based plastic substrates. Nucl. Instrum. Methods Phys. Res. B **151**, 263–267 (1999)
6. K. Naessens, H. Ottevaere, R. Baets, P. Van Daele, H. Thienpont, Direct writing of micro-lenses in polycarbonate with excimer laser ablation. Appl. Opt. **42**, 6349–6359 (2003)
7. K.L. Boehlen, I.B. Stassen Boehlem, R. Allot, Advanced laser micro-structuring of super large area optical films. Proc. SPIE **5720**, 204–211 (2005)
8. M. Lapczyna, M. Stuke, Rapid prototype fabrication of smooth microreactors channel in PMMA by VUV laser ablation at 157 nm for applications in genome analysis and biotechnology. Mat. Res. Symp. Proc. **526**, 143–148 (1998)
9. F.A. Jenkins, H.E. White, *Fundamentals of Optics*, 3rd edn. (McGraw-Hill, New York, 1957)
10. H.R. Philipp, D.G. Legrand, H.S. Cole, Y.S. Liu, The optical properties of bisphenol-A polycarbonate. Polym. Eng. Sci. **27**, 1148–1155 (1987)
11. M. Born, E. Wolf, *Principles of Optics*, 7th edn. (Cambridge University Press, Cambridge, 1999)
12. C.J. Sansonetti, J. Reader, K. Vogler, Precision measurement of wavelengths emitted by a molecular fluorine laser at 157 nm. Appl. Opt. **40**, 1974–1978 (2001)

Ablation of pristine and radiation exposed CR-39 polymer using a 157nm laser

Stephanie Cockcroft[1], Peter E Dyer[1], Craig Moore[2], Christopher D Walton[1] and Rozalina Zakaria[1]
1. Department of Physics, University of Hull, Hull, HU6 7RX, UK
2. Radiation Physics Department, Castle Hill Hospital, Cottingham, HU16 5JQ, UK

The polymer CR-39 (allyl diglycol carbonate) finds application in optical components because of its excellent transparency in the visible region and its good scratch resistance. It is also widely used as a detector for heavy ionizing particles, based on revealing their damage tracks by selective chemical etching ('track-etch' detector). The influence of coherent and incoherent radiation on the polymers chemical etching properties have been reported previously [1], principally in relation to track-etch detection. Here we describe an investigation of the ablation of CR-39 using 157nm F_2 laser radiation, motivated by an interest in producing optical microstructures and the possibility of revealing radiation damage tracks by photoablation.

Initial experiments on clean CR-39 surfaces involved measurements using a white light interferometer of the depth of material removed and surface roughness induced by the VUV laser radiation over a range of fluences and exposure pulses. From etch depth-fluence plots the threshold fluence was estimated to be $\leq 50\text{mJcm}^{-2}$ and the effective absorption coefficient approximately $3\times10^5\text{cm}^{-1}$. Ablation surfaces were found to be of good quality, with little re-deposited debris evident, although over most of the fluence range studied there was a propensity for conical structures to develop. The cones were extremely well defined compared with those seen in other UV laser-polymer ablation experiments, having straight, smooth walls and very sharp tips. Those of a few micron-scale size with appropriate apex angle, exhibited a well-defined circular fringe system surrounding their base, with a period consistent with them arising though the interference between the direct beam and that reflected from the cone wall. This is confirmed by modelling which provides a good description of the fringes and the 'scalloping' effect that the wall reflection produces in the vicinity of the base. Experiments using nano- and micro-particles to seed cones, and micro-whiskers to generate analogous prismatic structures on CR-39 are currently underway.

CR-39 samples exposed to α particles (primarily 4.87 and 4.61MeV) from a ^{226}Ra source showed no morphological evidence of radiation damage tracks when etched using the F_2 laser. This is likely because the radius of damage tracks in the polymer is typically ~5nm and hence 'un-resolvable' at a wavelength of 157nm. However, interesting effects have been seen in radiation-exposed samples that were chemically etched in NaOH to reveal deep tracks of a few microns diameter and then ablated at 157nm. These include smoothing of the edges of tracks due to melt flow relaxation and, under multiple pulse exposure, a significantly increased density of conical structures, apparently seeded by the edges of tracks.

[1] N. Dwaikat, T. Iida, F. Sato, Y. Kato, I Ishikawa, W. Kada, A. Kishi, M. Sakai and Y. Ihara, "Study etching characteristics of a track detector CR-39 with ultraviolet laser irradiation", Nucl. Instr. and Meth. in Phys. Res, A 572, 826 (2007).

INVESTIGATION INTO THE EFFICACY OF CO_2 LASERS FOR MODIFYING THE FACTORS INFLUENCING BIOCOMPATIBILITY OF A POLYMERIC BIOMATERIAL IN COMPARISON WITH AN F_2 EXCIMER LASER

Paper (M604)

D. G. Waugh[1], J. Lawrence[1], C. D. Walton[2] and R. B. Zakaria[2]

[1] Wolfson School of Mechanical and Manufacturing Engineering, Loughborough University, Leicestershire, LE11 3TU, UK
[2] Department of Physical Sciences, Physics, University of Hull, Kingston-Upon-Hull, HU6 7RX, UK

Abstract

Enhancement of the biocompatibility of a material by means of laser radiation has been amply demonstrated previously. Due to efficient absorption of the energy, short wavelengths and energies per pulse, polymers are usually processed using UV lasers, but the processing of polymers with IR lasers has also been demonstrated previously. In this work a comparative study for the surface modification of nylon 6,6 has been conducted in order to vary the parameters driving biocompatibility (surface topography, hydrophobic reactions, hydrophilic reactions and surface chemistry) using CO_2 and excimer lasers. Topographical changes were analysed using white light interferometery which indicated that both laser systems could be implemented for modifying the topography of nylon 6,6. Variations in the surface chemistry were evaluated using EDX and XPS analysis and showed that the O_2 increased and decreased for the CO_2 and F_2 laser irradiated samples, respectively. Modification of the hydrophobic and hydrophilic reactions was quantified by measuring the contact angle, which was found to increase in all instances for both laser systems. It is proposed that the increase in contact angle, especially for the CO_2 laser irradiated samples, is due to a change in wetting regime as a result of the surface pattern produced.

Introduction

It has been demonstrated previously by others that nylon can be utilized within the biomaterial industry [1] as sutures [2], vascular grafts and other hard tissue implants [3]. However, the common theme emanating from past work is that the polymer surface does not give rise to adequate cell adhesion and proliferation. As a result of this one can see that it may be an advantage to devise a technique which would allow the bioactivity of the nylon to be increased. Numerous techniques have been developed to produce surfaces that have the ability to do this. Some of these methods are radiation grafting [4], plasma surface modification[5,6] and using various coatings [7]. Laser surface modification [8,9] is another method which has the ability to improve bioactivity and offers a number of benefits:

- Relative cleanliness.
- Accurate processing.
- Allows much control over the heat affected zone (HAZ) due to the ability of relative precise control over the thermal profile and thermal penetration/absorption.
- Precise placement of the beam onto the target material allowing user specified areas of the target material to be processed.
- Non-contact processing.

The CO_2 laser is one of the most used lasers throughout the scientific world and within many industries because it is one of the most versatile. It is capable of emitting radiation within the infra-red (IR) region of the electromagnetic spectrum on rotational-vibrational transitions with wavelengths ranging from 9 to 11μm [10]. Due to the versatility and high powers that these lasers can achieve they have been implemented for many years in the general field of materials processing. Specific to polymers, IR lasers give rise to resonant coupling in the form of bond and lattice vibrations allowing for the processing to be thermolytical. This is due to the fact that the photon is only weakly absorbed by the polymer, with the energy that has been absorbed being distributed to vibrational modes [11].

Ultraviolet (UV) excimer lasers have also been seen to be an extremely versatile tool. Since they offer relatively small operating wavelengths and have high energies per pulse, these lasers have also been employed for materials processing over a number of years. They also have other applications in areas such as medicine [12-14], photolithography and the pumping of dye lasers [10]. With regards to the processing of polymers, UV lasers tend to give rise to the absorption of the light through electronic excitation which is often within delocalized electron configurations. In consequence polymers can have broad absorption features and directly break the polymer bonds as a result of the high photon energy [15]. With most lasers it is seen that the smallest possible features that can be achieved are on the micron scale; however, nano-structures have been achieved using a laser emitting at a wavelength of 157nm [16].

Previous and current research has shown that it is imperative that any biomaterial should be optimized such that it can function appropriately and efficiently within the desired biological environment. In many applications it is seen that the bulk properties of a biomaterial are decided upon such that the surface properties are compromised [17,18]. For instance, this is seen throughout the use of polymeric biomaterials as they offer excellent bulk properties for biological applications; however, they possess surface properties that do not lend themselves to high performance in regards to cell adhesion and proliferation [19]. As a result of this, one can see that it would be necessary to attempt and vary the surface properties of the material without changing the bulk properties in order to influence the wettability and biocompatibility characteristics. The role of wettability in biomaterials science has been one of the most interesting subject areas in biomaterials surface science for a number of years and has allowed many to endeavour to determine the complex links between surface wetting and bioactivity [20]. A number of theories have been put forward in order to explain this phenomenon in which they usually fall into two basic categories. The first attempts to correlate the surface energy with the biomimetic properties whilst the second involves water solvent properties near the surface in which a correlation between the contact angle and biocompatibility is strived for. It should be noted; however, that in both of these categories arises a fundamental factor in which the surface energy/wetting is related somewhat to the biological response [21]. Many researchers have taken various approaches as to ascertain quantitative reasoning to bioactivity such as Van Oss *et al.* [22] by utilizing the 'equation of state' approach to calculate interfacial tensions from previously measured contact angles in order to attempt and predict cell adhesion. Such approaches have been found to fall short for determining a quantitative theory regarding the bioactivity of a material. Through the available literature it can be seen that extensive research is now being carried out regarding this in the attempt to link wettability and bioactivity of materials [23,24].

Both CO_2 and excimer lasers can be employed to produce variations in surface characteristics which can lead to a manipulation of the bioactivity of a material with regards to cell adhesion and proliferation [9,18]. In this paper, two very different laser systems are used and compared to produce surface variations in nylon 6,6 with the wettability characteristics being quantified.

Experimental Technique

CO_2 Laser System

The 10.6μm wavelength Synrad cw 10W CO_2 laser system, with a spot size of the order of 100μm, is housed at Loughborough University and uses a galvanometer scanner to scan the beam directly across the target material. The target material and laser system was held in a laser safety cabinet in which the ambient gas was air. An extraction system was used to remove any fumes produced during laser processing. In order to generate the required marking pattern the Synrad Winmark software version 2.1.0, build 3468 was used. In addition, the software was capable of using images saved as .dxf files which can be produced by using CAD programs such as, in this case, Licom AutoCaM

F_2 Excimer Laser System

The Lambda Physik LPF 202 F_2 excimer laser system with a wavelength of 157nm is housed at the University of Hull and utilizes a projection etching system to irradiate the target material. The beam outputting from this laser had to be fully encased in a vacuum chamber running at pressure of around 2×10^{-3} mbar. This is due to the fact that 157nm light is highly absorbed in ambient air over a few cm. A diagram of the projection etching system can be seen in Figure 1.

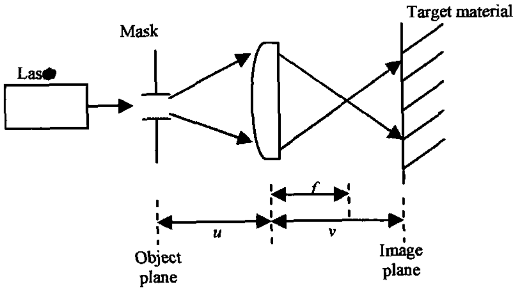

Figure 1 – Schematic diagram showing the projection etching system used

With u being the object distance, v being the image distance and f the focal length of the lens. Prior to any experimentation being carried out it was necessary to determine the required image plane.

In order to achieve the required trench dimensions an aperture projection mask was produced (Laser Micromachining, Ltd) using SS316 foil. The mask was 30mm×30mm and consisted of an array of five apertures with a diameter of 0.5mm in a straight line spaced by 1mm centre to centre. This allowed 50μm wide trenches to be etched, spaced by 50μm upon using a demagnification of 10.

Laser Irradiation Procedures

The nylon 6,6 was sourced in 100mm×100mm sheets with a thickness of 5mm (Goodfellow Cambridge, Ltd). To obtain a conveniently sized sample for experimentation, the as-received nylon sheet was cut into 30mm diameter discs using a 1kW cw CO_2 laser (Everlase S48; Coherent Ltd). No discernible HAZ was observed under optical microscopic examination.

For the Synrad CO_2 laser system, trenches were produced with spacings of 50 and 100μm (sample C10 and C9, respectively) by scanning the beam across the target material. To produce these spacings, each experiment was carried out twice: firstly using a power of 50% (5W) with a velocity of $1000mms^{-1}$ and secondly using a power of 80% (8W) with the same velocity.

The Lambda Physik LPF 202 F_2 excimer laser system was used to produce two areas of etched trenches by traversing the stage and keeping the beam stationary. The first of these being to achieve an etch depth of approxiamately 1μm (sample F3) and the second giving a depth of approximately 10μm (sample F4). In order to achieve these depths each site required 1,000 and 10,000 pulses, respectively, as the etch depth per pulse was approximately 1nm per pulse. With this in mind it was possible to determine the traverse velocities, v_t, by using Equation (1).

$$v_t = \frac{DR}{N} \qquad (1)$$

Where D is the diameter of one of the apertures in the mask, R is the repetition rate (which was 20Hz) and N is the number of pulses. Upon using this equation it was determined that for 1μm and 10μm deep trenches velocities of 0.01 and $0.001mms^{-1}$ was to be used, respectively.

Mechanical Roughening Procedure

For further verification of laser induced contact angle modification two samples were roughened manually using DA-F P220 emery paper. One sample was roughened using a zig-zag motion traversing from the top to the bottom of the sample (sample R1). The second sample (sample R2) was roughened by carrying out the same technique as the first sample, with the addition of rotating the sample through 90° and repeating the roughening method with the emery paper.

Topography, Wettability Characteristics and Surface Chemistry Analysis

After the laser irradiation of the nylon 6,6 samples they were analysed using a number of techniques. An optical microscope (Flash 200 Smartscope; OGP Ltd) was used to obtain optical micrographs of the samples. The surface profiles were determined using a white light interferometer (WLI) (NewView 500; Zygo, Ltd) with MetroPro and TalyMap Gold Software. The Zygo WLI was setup using a ×10 Mirau lens with a zoom of ×0.5 and working distance of 7.6mm. This system also allowed Sa, Ra and Wa roughness parameters to be determined for each sample.

The samples were ultrasonically cleaned in isopropanal (Fisher Scientific, Ltd) for 3 minutes at room temperature before using a sessile drop device to determine various wettability characteristics, in accordance with the procedure detailed by Rance [25]. This was to allow for a relatively clean surface prior to any contact angle measurements being taken. The sessile drop device used was a Dataphysics OCA20 with SCA20 Software. This allowed the recent advancing and receding contact angles for triply distilled water and the recent advancing angle for diodomethane to be determined for each sample. By achieving the advancing and receding contact angles the hysteresis for the system was determined. In addition, by knowing the advancing contact angles for the two liquids it was possible to use the software to draw a Owens, Wendt, Rabel and Kaeble (OWRK) plot to determine the surface energy of the samples. For the two reference liquids the SCA20 software used the Ström et al. technique to calculate the surface energy of the material. It should be noted here that 10 contact angles, using 2 droplets, in each instance was recorded to achieve a mean contact angle for each liquid and surface.

Selected samples were analysed using X-ray photoelectron spectroscopy (XPS) and were also sputter coated with Au to attain adequate conductance and analysed using scanning electron microscopy

(SEM) and energy dispersive X-ray (EDX) analysis. This allowed any surface modifications in terms of chemical composition due to the laser irradiation to be revealed.

Results and Discussion

Optical Microscopy Analysis

In order to effectively and completely compare the laser irradiated samples an optical micrograph of the non-irradiated material was obtained, as can be seen in Figure 2.

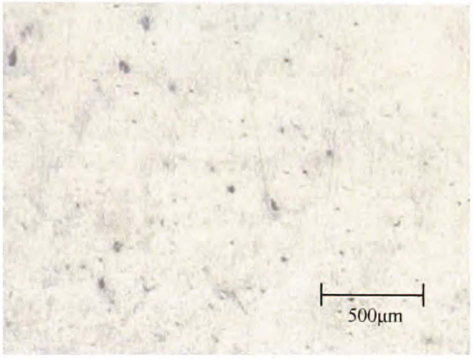

Figure 2 – Optical micrograph of the non-irradiated nylon 6,6 sample (Sample N6).

The optical micrograph of the non-irradiated sample shown in Figure 2 appears to have a minimal surface topography. The black dots on the image arise from the debris from the cutting of the samples. This debris was removed during the ultrasonic cleaning.

It was seen that both laser systems gave the ability to produce relatively good quality μm features in the nylon 6,6 samples. With regards to the trenches produced by the CO_2 laser, with a distance of 50μm between each trench, it can be seen in Figure 3 that no distinct trench lines had been produced.

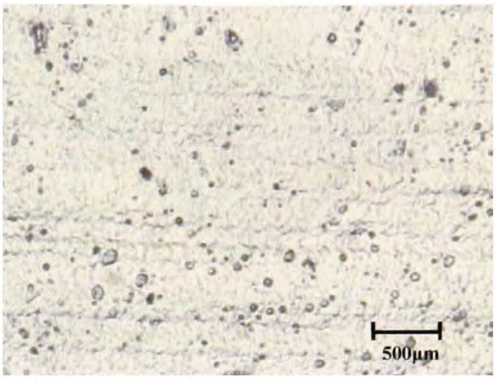

Figure 3 – Optical micrograph of nylon 6,6 CO_2 laser irradiated sample using 8W, $1000mms^{-1}$.

From Figure 3 it is possible to visualize that the CO_2 beam was scanned horizontally across the sample. However, as the spot size of the CO_2 laser was of the order of 100μm the scan overlaped itself so that no distinct grooves are left in the material. In addition to this, gas bubble rupture sites can be seen on the surface which is considered to be as a result of the melting and re-solidification of the nylon 6,6 following CO_2 laser irradiation. Also, as a consequence of the melting it appears that the material does not ablate with the CO_2 laser and as the material re-solidifies it produces a protrusion away from the surface. Owing to this phenomenon any trenches produced would arise due to two straight parallel protusions, with the unirradiated part of the sample being the bottom of the trench. In comparison, the F_2 excimer laser produces grooves that are considerably better defined, as can be seen in Figure 4. One other major difference that the F_2 excimer laser offers is that the trenches are ablated and etched into the nylon 6,6 sample.

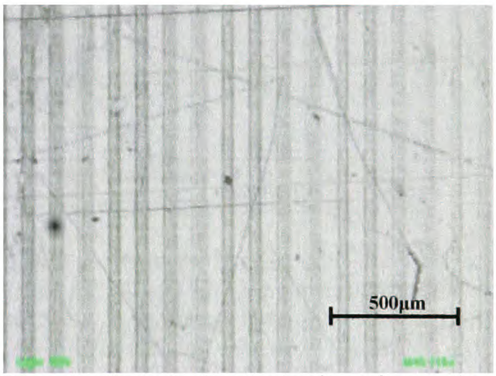

Figure 4 – Optical micrograph of trenches produced using the F_2 excimer laser using 1000 pulses per site, a fluence of $40mJcm^{-2}$ and a repetition rate of 20Hz (Sample F3).

White Light Inteferometry Analysis

The Zygo WLI and TalyMap Gold software were employed to elucidate the surface properties of the laser irradiated surfaces. Figure 5 shows the continuous axonometric with regards to the non-irradiated nylon 6,6 sample.

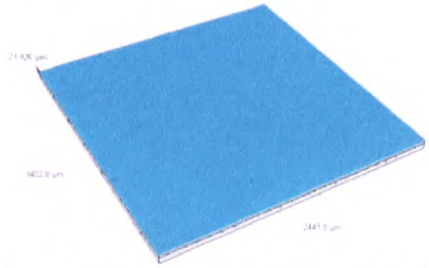

Figure 5 – Continuous axonometric image for the non-irradiated reference sample. (Sample N6)

Figure 5 shows how much smoother the surface of the nylon 6,6 is prior to laser irradiation, having an Sa value of only 0.038μm. This smoothness is also confirmed by taking a profile extraction of the surface, which can be seen in Figure 6.

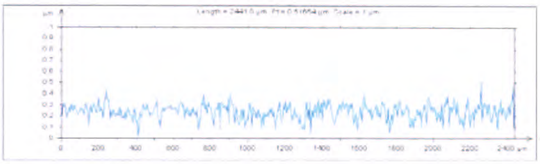

Figure 6 – Profile extraction of the surface shown in Figure 5.

The graph shown in Figure 6 allows one to see that maximum peak heights of the surface topography is approximately 0.3μm. In comparison, the CO_2 laser irradiated samples are considerably rougher than the reference sample indicating that considerable surface topography changes of nylon 6,6 are possible by this means. Figures 7 and 8 show continuous axonometric images for the CO_2 laser irradiated samples.

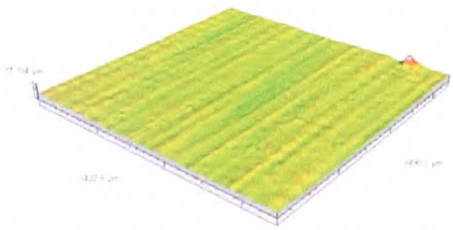

Figure 7 – Continuous axonometric for CO_2 laser irradiated nylon 6,6 at 5W, 1000mms^{-1} (Sample C10).

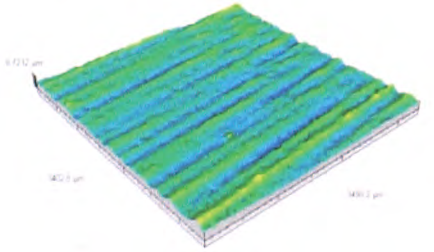

Figure 8 – Continuous axonometric for CO_2 laser irradiated nylon 6,6 at 8W, 1000mms^{-1} (Sample C9).

The surface roughness parameter Sa was determined for each of the surfaces. The Sa roughness value for the 5W CO_2 laser irradiated nylon surface was 0.262μm, whereas the higher power of 8W gave rise to a slightly rougher surface with an Sa value of 0.358μm. In addition, the effect the beam has had on the surface topography can be seen more prominently in Figures 7 and 8. However, by taking a profile extraction (Figures 9 and 10) of the surfaces perpendicular to the direction of the grooves, it can be seen that there is no fixed periodicity to the surface pattern. This is due to the fact that the spot size is larger than the intended surface pattern and the irradiation lines overlap.

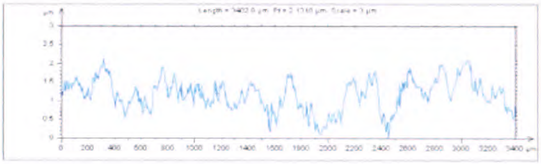

Figure 9 – Profile extraction of the surface shown in Figure 7, perpendicular to the grooves.

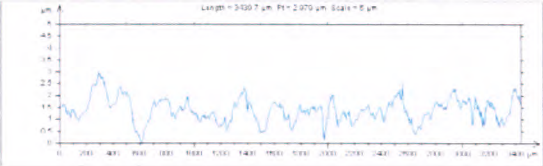

Figure 10 – Profile extraction of the surface shown in Figure 8, perpendicular to the grooves.

Figures 9 and 10 show that the maximum peak height observed for 5W and 8W laser powers were 2 and 3μm respectively. Even though there is no fixed periodicity for the irradiated samples shown in Figures 9 and 10, it can be seen that there are distinct grooves produced in the nylon 6,6 as a result of the CO_2 laser processing. This is more discernible when comparing the continuous axonometric images shown in Figures 7 and 8 with that of the non-irradiated reference sample shown in Figure 5, along with the relative profile extraction curves.

Figures 11 and 12 show the continuous axonometric images for the F_2 excimer laser irradiated nylon surfaces for different pulse numbers per site.

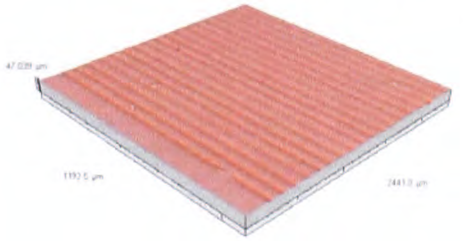

Figure 11 – Continuous axonometric image for F_2 excimer laser irradiated nylon 6,6 at 1,000 pulses per site (Sample F3).

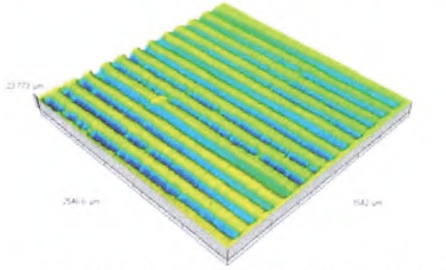

Figure 12 – Continuous axonometric image for F_2 excimer laser irradiated nylon 6,6 at 10,000 pulses per site (Sample F4).

The etched trenches using the F_2 excimer laser shown in Figures 11 and 12 are considerably more defined than the CO_2 laser irradiated samples (see Figures 7 and 8). In comparison to the CO_2 laser irradiated samples the pattern etched into the sample as shown in Figures 11 and 12 have a more distinct periodicity and can be easily identified with profile extractions as shown in Figures 13 and 14.

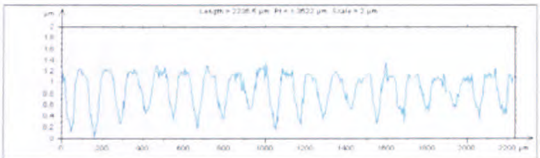

Figure 13 – Profile extraction of the surface shown in Figure 11, perpendicular to the grooves.

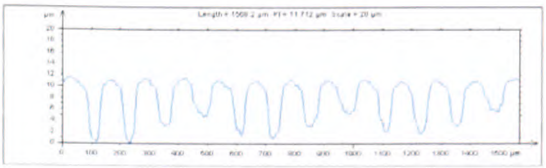

Figure 14 – Profile extraction of the surface shown in Figure 12, perpendicular to the grooves.

The roughness parameter for the surface shown in Figure 11 was found to be Sa = 0.248µm, whereas the roughness for Figure 12 was found to be Sa = 2.647µm which is considerably greater than the other three samples due to the depth of the trenches being approximately 10µm. It should be noted that for the other three samples the surface features were around 2 to 5µm as can be seen in the other profile extractions (Figures 9, 10, 13 and 14). Using the non-irradiated sample as a reference it can be seen that both lasers are capable of increasing the roughness of the surface of nylon 6,6; however, as the F_2 excimer laser offers better precision and accuracy due to the etch rate for this particular system being of the order of 1nm per pulse it can be seen that the roughness can be more accurately controlled. This is contrasted with the CO_2 laser system as the surface pattern is dependant on the surface melting and resolidifying to produce a protrusion out of the surface which gives rise to a level of inaccuracy for the surface pattern.

Effects of Laser Irradiation on the Wettability Characteristics

As it has already been discussed, it is believed by many that the characteristic contact angle for a material is the potential driving force in regards to the prediction of how a biomaterial will perform within a biological environment. The dynamic advancing contact angles and hysteresis for triply distilled water for each of the samples can be seen in Table 1, along with the recorded three roughness parameters Sa, Ra and Wa for each sample.

Table 1 – A summary of the results for the seven samples along with their characteristic contact angle and hysteresis with triply distilled water.

Sample ID	Sa (µm)	Ra (µm)	Wa (µm)	Contact Angle (°)	Hysteresis (°)
CO_2 Laser Irradiated Samples					
C10	0.262	0.346	0.118	53.91	17.22
C9	0.358	0.256	0.190	52.36	19.82
F_2 Excimer Laser Irradiated Samples					
F3	0.248	0.253	0.021	66.67	31.05
F4	2.647	2.947	0.978	72.92	40.97
Emery Paper Roughened Samples					
R1	3.104	2.368	1.862	43.95	26.01
R2	3.735	3.055	3.568	38.37	22.25
Non-Irradiated Reference Sample					
N6	0.038	0.043	0.020	49.34	19.98

The surface roughness shown in table 1, has been considerably increased, by up to an Ra of 2.904µm, in comparison to the non-irradiated sample using both laser systems. It can also be seen that the contact angle for each laser irradiated sample was increased with the F_2 excimer laser irradiated samples giving the largest change with a contact angle of 72.92° for the roughest sample. This does not concur with current theory as the contact angle should decrease with increasing surface roughness [18,26]. Further studies of the surfaces were required in order to explain these results. The contact angles determined for the emery paper roughened surfaces were decreased in comparison to the non-irradiated sample and will be discussed in more detail later.

Using the SCA20 software the surface energy and components for each sample were obtained to try to explain the variation in contact angle and can be seen in Table 2.

Table 2 – Surface energies and components of each of the five samples.

Sample ID	Contact Angle (°)	Polar Component (mJm^{-2})	Dispersive Component (mJm^{-2})	Total Surface Energy (mJm^{-2})
CO_2 Laser Irradiated Samples				
C10	53.91	20.75	27.38	48.13
C9	52.36	24.27	23.90	48.17
F_2 Excimer Laser Irradiated Samples				
F3	66.67	9.78	37.19	46.98
F4	72.97	8.46	28.44	36.90
Emery Paper Roughened Samples				
R1	43.95	22.57	34.86	57.43
R2	38.37	24.68	36.85	61.53
Non-Irradiated Reference Sample				
N6	49.34	20.15	36.12	56.27

The data given in Table 2 shows significant changes within the surface energy components in comparison to the non-irradiated reference sample used. After CO_2 laser irradiation the total surface energy is slightly reduced due to a change in polar and dispersive components. It can be seen that the polar component increases by up to $4.12mJm^{-2}$ for the rougher sample, whereas the dispersive component is reduced by $12.22mJm^{-2}$. As it is the polar component of the surface energy that plays the major role in determining the contact angle it can be seen that these results do not correspond with existing theory. For instance, Lawrence and Li [17] state that a laser-induced increase in the polar component, along with an increase in O_2 content, would give rise to a reduction in the contact angle.

Following on, subsequent to F_2 excimer laser irradiation the polar component of the surface energy is considerably reduced by up to $10mJm^{-2}$. This substantial reduction in polar component could be seen to be the main reason as to why there is a significant increase in the contact angle. The dispersive component is quite inconclusive due to the fact that both results lay either side of the value determined for the reference sample. As a result of this, further research may be required to determine the trend of the dispersive component in this case and could be used as a further study to confirm the results achieved here. However, it still can be seen that the total surface energy determined for the F_2 excimer laser irradiated samples is somewhat lower with $36.9mJm^{-2}$ for sample F4.

In order to determine if these changes in surface energies were as a result of variations in surface chemistry three samples where chosen for XPS and EDX analysis. Table 3 shows the surface O_2 content for selected samples.

Table 3 – Surface O_2 content for selected samples

Sample ID	Surface O_2 Content (%)	Contact Angle (°)
C10	22.23	53.91
F3	17.48	66.67
R1	20.70	43.95
N6	20.76	49.34

The non-irradiated reference sample showed that, in terms of weight, 79.24% was carbon and 20.76% was oxygen. In comparison with the CO_2 laser irradiated sample the oxygen content had risen slightly to 22.23%, whereas the F_2 excimer laser irradiated sample was found to have less oxygen content with only 17.48%. The oxygen in the ambient air of the CO_2 system could have possibly allowed oxidation of the surface to occur as the molten nylon re-solidified.

Additionally, as the F_2 excimer laser system was under vacuum, there would have been a reduction in oxygen and as a result the surface would not oxidize and could potentially lose oxygen content during the laser ablation process.

Due to the ability of using these laser systems to manipulate the wettability characteristics further research can also be made by carrying out biological testing of the laser irradiated samples. This would determine if cell adhesion and proliferation can be optimized by using these lasers to produce surface modification in terms of surface chemistry and surface topography. In addition, as nylon 6,6 has a high water absorption rate it may be possible to identify, through extended research, whether surface modifications using laser technology allows this parameter to be reduced. By experimenting with different ambient gases it may also be possible to inflict greater chemical changes on the surface of the material allowing for further studies of how the chemical nature of the surface gives rise to the variation in contact angle and surface energy.

Determination of Active Wetting Regime

As it has already been shown, surface energy, XPS and EDX analysis for the CO_2 laser irradiated samples should allow the samples to have a contact angle that is lower than the contact angle determined for the non-irradiated sample. To clarify this, two samples were roughened using emery paper, of which the continuous axonometric images can be seen in Figure 15 and 16, in order to find some explanation for this phenomenon.

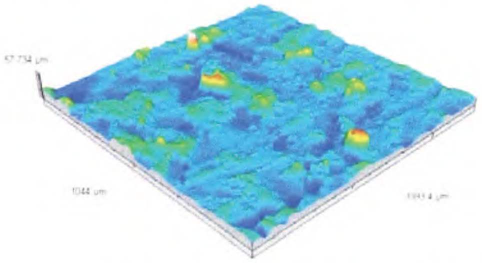

Figure 15 – Continuous axonometric image of the first emery paper roughened sample (Sample R1).

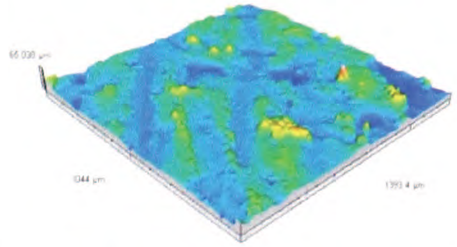

Figure 16 – Continuous axonometric image of the second emery paper roughened sample (Sample R2).

As a result of the mechanical roughening of the samples it can be seen in Tables 1 and 2 that an increase in polar component and roughness has given rise to a significant reduction in contact angle, which agrees with Lawrence and Li [17]. It must be stated at this point that the images shown in Figures 15 and 16 give an indication that no periodic pattern has been induced on the surface of the nylon 6,6 samples. In contrast, the laser irradiated samples have more periodic patterns relative to the manually roughened surfaces. These periodic patterns appear to have an extremely large affect on the wettability of the samples. As discussed by Jung and Bhushan [27] there are two regimes in which a material can wet; these being the Cassie-Baxter and Wenzel regimes. In which the Wenzel regime, shown in Figure 17, allows the whole sample to be wetted such that the droplet is in complete contact with the surface.

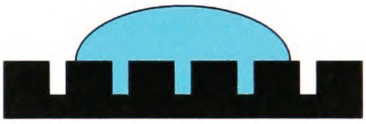

Figure 17 – Schematic diagram showing a droplet of water on a patterned surface giving rise to the Wenzel wetting regime.

On the other hand, the Cassie-Baxter regime, shown in Figure 18, allows the droplet to rest upon the roughenedsurface peaks forming air gaps between the droplet and the surface.

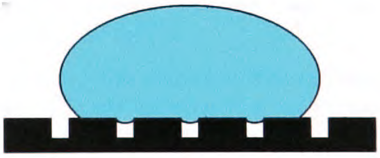

Figure 18 – Schematic diagram showing a droplet of water on a patterned surface giving rise to the Cassie-Baxter wetting regime.

It is proposed here that a change from the Wenzel regime to the Cassie-Baxter regime was the likely reason for the observed increase in the contact angle for the CO_2 laser irradiated samples and the F_2 excimer laser irradiated samples. This would be due to the fact that the Cassie-Baxter regime inherently gives rise to larger contact angles in comparison to the Wenzel regime. Therefore, it is also proposed that the surface pattern is the main driver for the manipulation of the wettability characteristics, implying that the surface roughness (Table 1), surface energy components (Table 2) and surface O_2 content (Table 3) do not play a governing role. In order to confirm this proposal more research into which wetting regime takes place is required.

Conclusions

It has been demonstrated that both the CO_2 and F_2 excimer laser systems that have been employed in this study have the ability to modify the surface of nylon 6,6. The CO_2 laser couples into the material via resonant coupling which gives rise to bond vibrations allowing the temperature to rise and melt the material. Upon cooling the molten material re-solidifies and a protrusion away from the surface becomes evident on the surface. This is contrasted with the F_2 excimer laser as it ablates the nylon 6,6 allowing the required pattern to be etched into the material. As a result the F_2 excimer laser system offers a major advantage over the CO_2 in the fact that it ablates approximately 1nm per pulse, with the fluence used in this instance, allowing the user to be precise and accurate with the surface topography they require. However, the amount of time it takes to pump the F_2 vacuum system to operating pressure and the amount of time it takes to produce a number of few µm deep trenches is considerably greater than the CO_2 laser system employed in this study.

Both of the laser systems affect differently the nylon 6,6 samples with regards to wettability and surface energy parameters – two major factors which are believed to manipulate the bioactivity of a material in regards to cell adhesion and proliferation. The CO_2 laser has been seen to be capable of producing contact angles slightly larger in comparison to an unirradiated reference sample. This does not agree with current theory as the increased polar component and increased O_2 content should give rise to a reduction in contact angle. For instance the F_2 excimer laser irradiated samples gave larger contact angles which seems to be the result of a decrease in polar component and decrease in O_2 content. However, it has been proposed here that the increases in the contact angle for both laser systems could also be due to the fact that the sample surfaces are patterned, such that they give rise to a change in wetting regime from Wenzel type to the Cassie-Baxter regime. This may allow one to see how the CO_2 laser irradiated samples would give a larger contact angle in comparison to the non-irradiated sample. This would imply that the surface pattern dominates the wettability characteristics of the material. In order to confirm this proposal much more research is required into how the droplet forms on the sample surface.

Acknowledgements

We would like to thank Matthew Gibson, Peter Wileman and David Britton for all of their much appreciated support. This study is financially supported by the EPSRC (No. EP/E046851/1).

References

1. Mao, C. et al. (2005) In vitro studies of platelet adhesion on UV radiation-treated nylon surface. Carbohydrate Polymers, 59, 19-25.

2. Karaca, E. et al. (2008) Analysis of the Fracture Morphology of Polyamide, Polyester, Polypropylene, and Silk Sutures Before and After Implantation In Vivo. Journal of Biomedical Materials Research Part B: Applied Biomaterials.

3. Makropoulou, M. et al. (1995) Ultra-viole and Infra-red Laser Ablation Studies of Biocompatible Polymers. Lasers in Medical Science, 10, 201-206.

4. Benson R. S. (2002) Use of Radiation in Biomaterials Science. Nuclear Instruments and Methods in Physics Research B, 191, 752-757.

5. Arefi-Khonsari, F. et al. (2005) Processing of Polymers by Plasma Technologies. Surface and Coatings Technology, 200, 14-20.

6. Pappas, D. et al. (2006) Surface Modifcation of Polyamide Fibers and Films using Atmospheric Plasmas. Surface and Coatings Technology, 201, 4384-4388.

7. Harnett E.M. et al. (2007) The surface energy of various biomaterials coated with adhesion molecules used in cell culture. Colloids and Surfaces B: Biointerfaces, 55, 90-97.

8. Yu, F. et al. (2005) Laser interference lithography as a new and efficient technique for micropatterning of biopolymer surface. Biomaterials, 26, 2307-2312.

9. Mirzadeh H. et al. (2003) Influence of laser surface modifying of polyethylene terephthalate on fibroblast cell adhesion. Radiation Physics and Chemistry, 67, 381-385.

10. Silfvast W. T. (1996) Laser fundamentals. Cambridge, UK. Cambridge University Press.

11. Skordoulis, C. D. et al. (1995) Ablation of nylon-6,6 with UV and IR lasers. Applied Surface Science, 86, 239-244.

12. Duncan, A. C. et al. (2002) Laser Microfabricated Model Surfaces for Controlled Cell Growth. Biosensors & Bioelectronics, 17, 413-426.

13. Pfleging, W. et al. (2007) Laser-Assisted Modification of Polystyrene Surfaces for Cell Culture Applications. Applied Surface Science, 253, 9177-9184.

14. Callewaert, K. et al. (2003) Excimer Laser Induced Patterning of Polymeric Surfaces. Applied Surface Science, 208-209, 218-225.

15. Tiaw, K. S. et al. (2007) Precision Laser Micro-Processing of Polymers. Journal of Alloys and Compounds.

16. Sarantopoulou, E. et al. (2007) Polymer Self-Assembled Nano-Structures and Surface Relief Gratings Induced with Laser at 157nm. Applied Surface Science, 253, 7884-7889.

17. Lawrence J. et al. (2001) Modification of the Wettability Characteristics of Polymethyl Methacrylate (PMMA) by Means of CO_2, Nd:YAG, Excimer and High Power Diode Laser Irradiation. Materials Science and Engineering A, 303, 142-149.

18. Hao L. et al. (2005) Laser surface treatment of bio-implant materials. New Jersey, USA: John Wiley & Sons Inc.

19. Lai, J. et al. (2006) Study on Hydrophilicity of Polymer Surfaces Improved by Plasma Treatment. Applied Surface Science, 252, 3375-3379.

20. Ma Z. et al. (2007) Surface modification and property analysis of biomedical polymers used for tissue engineering. Colloids and Surfaces B: Biointerfaces, 60, 137-157.

21. Vogler E. A. (2004) Role of water in biomaterials. In: Ratner, B. D. et al., editor. Biomaterials Science. Second ed. San Diego, California, USA. Elsevier Academic Press.

22. Van O. et al. (1975) Phagocytic engulfment and cell adhesiveness. New York, USA. Marcel Dekker.

23. Kim, M. S. et al. (2007) Gradient polymer surfaces for biomedical applications. Progress in Polymer Science.

24. Ball M. D. et al. (2004) Cell interactions with laser-modified polymer surfaces. Journal of Materials Science: Materials in Medicine, 15, 447-449.

25. Rance D. G. (1982) Chapter 6 - thermodynamics of wetting: From its molecular basis to technological application. In: Brewis DM, editor. Surface Analysis and Pretreatment of Plastics and MetalsEssex, UK. Applied Science Publishers.

26. Lawrence J. et al. (2001) Laser modification of the wettability characteristics of engineering materials. Suffolk, UK. Professional Engineering Publishing Limited.

27. Jung Y. C. et al. (2007) Wetting transition of water droplets on superhydrophobic patterned surfaces. Scripta Materialia, 57, 1057-1060.

Meet The Author

David Waugh is currently undertaking a Ph.D at the Wolfson School of Mechanical and Manufacturing Engineering, Loughborough University, UK under the supervision of Dr. Jonathan Lawrence. His research is focusing on using laser surface treatment of polymeric biomaterials for enhanced cell response. He obtained his MPhys Hons. in Physics with Lasers and Photonics and MSc in Laser Applications in Micro-Machining and Processing from the University of Hull, UK.